Low Conductivity Thermal Barrier Coatings

A Dissertation

Presented to

The Faculty of the School of Engineering and Applied Science

University of Virginia

In Partial Fulfillment

of the Requirements for the Degree

Doctor of Philosophy (Materials Science and Engineering)

Approval Sheet

This Dissertation is submitted in partial fulfillment of the

requirements for the degree of

Doctor of Philosophy, Materials Science and Engineering

Author, Hengbei Zhao

This dissertation has been read and approved by the examining committee:

Dissertation Advisor, H. N. G. Wadley

Co-Advisor, C. G. Levi

Chairman, D. M. Elzey

P. Reinke

J. F. Groves

Accepted for the School of Engineering and Applied Science:

Dean, School of Engineering and
Applied Science
May 2009

Abstract

The dissertation begins by exploring the growth of 7YSZ coatings on vapor deposited NiCoCrAlY bond coats at different substrate rotation rates. The experiments show that as the rotation rate was increased, the texture changes from <111> to <100> and the total pore fraction slowly decreased. Inter- and intra-columnar pores were found to be present in the coatings. The intercolumnar pores (Type I) are perpendicular to the coating surface and are very effective at strain accommodation during thermal cycling. The intra-columnar pores (Type II and III) appear the most effective for the reduction of thermal conductivity of the coatings. The minimum thermal conductivity occurs at a low rotation rate and is 0.8 W/mK, which is ~50% below that of conventional EB-PVD deposited 7YSZ coatings.

The failure modes and mechanisms of 7YSZ coatings during thermal cycling have been investigated. The primary mode of failure on rough bond coat surfaces involves delamination within the ceramic coating, just above the thermally-grown oxide (TGO). It was initiated by a bond coat rumpling mechanism. The delaminations were initiated preferentially at “corn kernel” growth defects in the coating. The coating lifetime increased to 600 cycles as the pore fraction increased. Ceramic coatings applied to smooth (polished) bond coat surfaces had much longer spallation lifetimes and the delamination fracture shifted to the interface of TGO/bond coat. These delaminations were extended by a mechanism involving the formation and coalescence of interfacial voids. The lifetime again increased to 1250 cycles as the coating density was decreased. The lifetime of both coatings significantly exceeded that of coatings applied to the same bond coats using the traditional EB-PVD method. The enhanced coating life is shown to be a consequence of their lower density and hence, lower elastic modulus. This reduces the elastic strain energy stored in the ceramic layer and thus the driving force for interfacial delamination.

Efforts to enhance engine efficiency by raising gas turbine engine operating temperatures have exposed a potential weakness of the YSZ coating system. Rare earth zirconates appear to be a promising candidate due to their reported low intrinsic thermal conductivity, good phase stability and greater resistance to sintering and CMAS attack compared to 7YSZ. The growth of $Sm_2Zr_2O_7$ (SZO) coatings by EB-DVD and the effect of deposition conditions upon their thermal conductivity and cyclic durability have been investigated. Coatings grown from a single SZO source were found to exhibit significant fluctuations in composition because of differences in the vapor pressures of the constituent oxides. They also were found to have a metastable fluorite structure that resulted from kinetic limitations that hindered the cation ordering needed to form the equilibrium pyrochlore structure. The SZO coatings had as-deposited conductivities of 0.5±0.1 W/mK, about one-half of their DVD 7YSZ counterparts grown under similar conditions. The conductivity difference is primarily associated with the lower intrinsic conductivity of this zirconate. When these SZO coatings were subjected to thermal cycling, it was found to have a much shorter lifetime (on both rough and smooth bond coats) than similarly deposited 7YSZ material. It was also found that samaria tended to react with alumina to form a $SmAlO_3$ interphase of the TBC/TGO interface which appears to significantly lower the interface toughness.

To improve the durability of SZO coatings, 7YSZ/SZO bilayer coatings were grown by the DVD method so that a thin 7YSZ layer separated the SZO from the TGO layer. During the deposition the SZO layer continuously regrew on YSZ column tips and grew along the original YSZ column direction. The SZO layer was found to thermochemically compatible with YSZ without the degradation during the cycling exposure. It was also found that the thickness of 7YSZ layer is a critical parameter for a diffusion barrier layer against samaria interaction with alumina. Sm was detectable near the TGO when the bilayer with 10 μm of 7YSZ was subjected to thermal cycling for more than 1000 hours. This appeared to have contributed to a reduced coating life during thermal cycling.

This dissertation has shown that thermal barrier coatings with controllable coating morphology, texture, density and thermal conductivity can be grown rapidly and efficiently using the EB-DVD approach. The durability of the coatings can be greatly improved by manipulation of the growth conditions to increase the pore fraction in the coatings.

Acknowledgments

First and foremost I would like to thank my advisor, Professor Haydn Wadley, for his support, guidance, inspiration and especially his patience throughout this research program. I would also like to express my gratitude to my co-advisor, Professor Carlos Levi for his invaluable suggestions and discussions. I sincerely appreciate the comments, suggestions, and thoughtful review of this work by my dissertation committee members: Professor Dana Elzey, Professor Petra Reinke, and Professor James Groves.

Secondly, I would like to thank my fellow IPM members who have helped me with my research. They are George (Zhuo) Yu, Yoongu Kim, Aarash Sofla, Sang-wan Jin, Pimsiree (Ming) Moongkhamklang, Scott Kasen, Brian Gillespie, Junjie Quan, Jiani Yu, Kevin West, Tochukwu George and Toni Kember. I am also grateful to the research staff of the IPM lab including Dr. Phillip A. Parrish, Tommy Evans, David Glover, Rich Gregory, and Sherri Sullivan for their support and lab management.

Thirdly, I greatly appreciate Dr. Fengling Yu and Dr. Rafael Leckie at UCSB, who provided help with sample preparation and thermal conductivity measurements. I wish to thank my friends Li He and Wenbin Fan for their help during my experimental work. Also, my thanks to John Gaskins in the mechanical engineering department at UVA for the measurement of elastic modulus. Additionally, I am grateful to the present and past MSE lab staff, Shiahn Chen, Richard White and Tim Herlihy for training on various instruments. Special thanks to Boris Starosta for his numerous drawings during my research work. In particular, David Wortman of GE Aviation deserves special mention for kindly providing the substrates.

Finally, I want to thank my family for their life-long love, encouragement and support on this endeavor. Without their sacrifices and efforts, I could never have been able to complete my work.

This work is funded by the Office of Naval Research under Contract #N00014-03-1-0297 monitored by Dr. David Shifler.

Table of Contents

Chapter 1. Introduction

Chapter 2. Background

Chapter 3. Directed Vapor Deposition

Chapter 4. Experimental Methodology

4.3 Coating Characterization Methods

Chapter 5. Morphology, Texture and Thermal Conductivity of DVD YSZ

5.6 Discussion

Chapter 6. Thermal Cycling of DVD YSZ Coatings

6.3 Cycling Test

Chapter 7. Morphology and Texture of DVD $Sm_2Zr_2O_7$ Coatings

7.3 Results

7.4 Discussion

Chapter 8. Thermal Cycling of DVD $Sm_2Zr_2O_7$ Coatings

8.2 Thermal Cycling Results

Chapter 9. 7YSZ/$Sm_2Zr_2O_7$ Bilayer Coating

9.4 Thermal Cycling

Chapter 10. Discussion

List of Figures

List of Tables

Chapter 1

Introduction

1.1 Design of Turbine Engines

The design of modern turbine engines has been enabled by the development of high temperature engineering alloys. The thermodynamic foundation of engine design holds that increasing turbine entry operation temperature can lead to concomitant improvement in its power and efficiency. During operation, the engine blades/vanes in the gas turbine engine are exposed to hot engine gasses, an oxidative and corrosive environment, and high velocity foreign object impacts. Therefore, the material of these components should have the requirements of high temperature strength, toughness, resistance to oxidation and hot corrosion. Fig. 1-1 shows the chart of evolution of the superalloy high temperature capability and cooling technology over almost 60 years [6]. These developments result in very significant improvements in increasing engine operating temperature. Continued improvements in engine performance have been slowed in the mid 1990's as superalloys approached their theoretical limits.

For further improvement, ceramic component engines (especially silicon nitride [7, 8]) have received more attention for use in internal combustion engines and turbines. They have good thermal shock resistance and good creep resistance. However, their low fracture toughness has precluded their use in load-bearing applications. Thus, the current approach is the use of a thermal barrier coating (TBC) system to protect the superalloy components and allow them to use at higher engine gas temperatures.

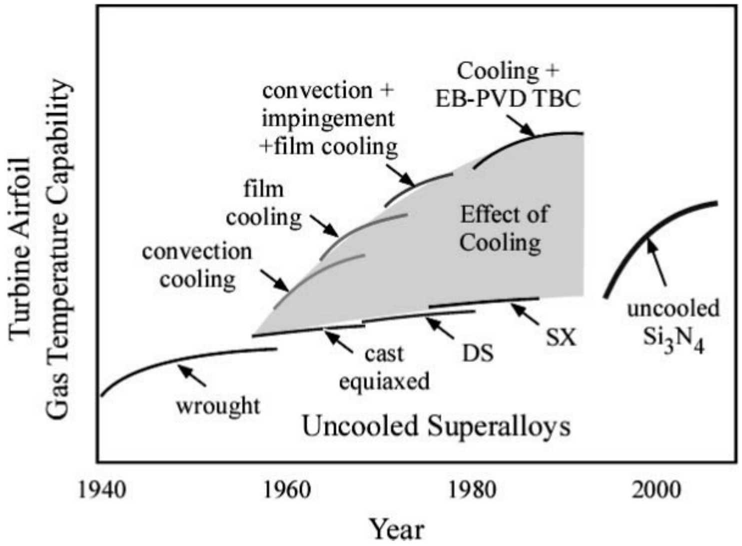

Figure 1-1. The development of high temperature superalloys and cooling technology over the last six decade [6]

1.2 Thermal Barrier Coatings

Thermal barrier coatings (TBCs) are widely used in the hot gas path of advanced aero-engines and land-based gas turbines [9, 10]. They protect the engine blades and vanes from exceeding their maximum use temperature. They also improve the operational lifetime while facilitating continued increases in turbine efficiency [11]. The TBC system applied to gas turbine usually consist of a ceramic top coat that reduces the metal temperature; a metallic bond coat to enhance the bonding between the top coat and the underlying superalloy and to also protect the superalloy from oxidation and hot corrosion; a thermally grown oxide layer (usually α-Al_2O_3) that forms on the bond coat surface to reduce the rate of its oxidation. Yttria stabilized zirconia containing 6-8 wt% Y_2O_3 (7YSZ) is the most widely used ceramic material for the TBC top coat because of its low thermal conductivity, high melting point, phase compatible with alpha alumina, and combination of its good resistance to erosion and damage from large particle impacts. These coatings are commonly applied by electron-beam physical vapor deposition (EB-PVD) or air-plasma spray (APS). The EB-PVD TBC is of particular interest for coatings used in aero engine airfoils. In this application, the coatings are severely thermally cycled and its columnar structure provides a means of strain accommodation as the different materials in the coating/substrate system thermally expand/contract during heating/cooling.

The current TBC system suffers from a number of limitations. First, there is still a relatively poor understanding of the relations between the coating structure, conditions used for its synthesis and its performance. Secondly, the costly and ineffective EB deposition process is a major concern for the further use in the EB-PVD process because of the relatively low deposition rate. Finally, 7YSZ has reached its maximum temperature that it can be exposed up to 1300 °C without incurring deleterious phase changes. The requirement of future engine designs is driving a search for materials that further reduce the temperature of the metal surface while concomitantly facilitating increased gas path temperatures. A new generation of TBC material deposited in a manner that maximizes their lifetime during aircraft engine operation is required.

1.3 Goals of the Dissertation

In this dissertation an electron beam directed vapor deposition (EB-DVD) method [12] has been explored to apply thermal barrier coatings onto superalloy substrates. In this process, an electron beam is used to evaporate a ceramic source material and a supersonic gas jet is used to entrain the vapor atoms and efficiently transport them to a substrate for deposition. It is anticipated that this approach can have high deposition efficiency (deposit a much higher fraction of the evaporated flux on the component) and reduce equipment cost due to the resulting higher deposition rate. Previous results [13] have shown that the coating morphology can be manipulated by altering the deposition conditions. It is a key goal of this dissertation to investigate relations between coating structure and deposition conditions, thermal cyclic durability and thermal conductivity. Due to the limitations of current YSZ system identified above, a new material, samarium zirconate, is investigated as a potential candidate for higher temperature TBC system. Finally, these investigations are combined to propose a new TBC system design.

The thesis is organized as follows: Chapter 2 provides a background for TBC selection, TBC microstructure, TBC spallation, limitation of current TBC system, as well as the search of new materials. This is followed by a review of the EB-DVD approach (Chapter 3) and the experimental methodology used for coating characterization and property measurements (Chapter 4). Chapter 5 examines TBC morphology, texture, density and thermal conductivity for coatings grown under different rotation rates and investigates their relationships. A thermal cycling lifetime test was used to explore the failure mechanism of this coating system and their relation to coating lifetime and coating morphology in Chapter 6. A new material, samarium zirconate was studied for its morphology and texture which was effected by deposition conditions (rotation rate and substrate temperature) (Chapter 7). The cycling lifetime and its failure modes of this coating system are discussed in Chapter 8. Chapter 9 develops a new bilayer system and examines its lifetime. Chapter 10 discusses the pore morphology, texture, density and thermal conductivity relationships and trade-off with coating failure life. The dissertation closes with a series of conclusions and remarks about future directions (Chapter 11).

Chapter 2

Background

Improving gas turbine engine efficiency is generally achieved by maintaining the gas path temperature of the combustor and turbine engines as high as possible. For almost 50 years following the invention of the gas turbine engine, the primary driver for the increase of the operating temperature has been the development of high temperature superalloys [6]. This has become especially critical for the engine blades and vanes in the hot section of modern gas turbine engines. The nickel-based superalloy usually used as a blade/vane is internally cooled by the flow of cool air through internal, serpentine cooling passages, in Fig. 2-1. Small holes allow this air to form a cool air film on the blade surface. The superalloy is subjected to high centrifugal loads and must be very creep resistant. It is usually made as a single-crystal that contains from 5 to 12 elements (in addition to the Ni base element) to optimize high-temperature strength, ductility, oxidation and hot-corrosion resistance [14]. Examples of commonly used superalloys for cyclically loaded components are Rene alloys and CMSX single crystal alloys. These components must survive extremely hot engine gases, and an oxidative and hot corrosive environment. These components are also subjected to occasional high velocity impact by small foreign objects [15, 16] and to erosion by fine airborne dust particles [17, 18].

Modern gas turbine engines have driven and exploited advanced superalloy technology and have also evolved to rely on highly engineered cooling strategies to prevent load-bearing components from exceeding their maximum use temperatures. These developments resulted in very significant improvements in both the power and efficiency of aero gas turbines. Continued improvements in engine performance by these routes slowed in the mid 1990’s as superalloys approached their theoretical limits. The search for alternative materials for the vanes and blades of aero gas turbines has been constrained by the need for high temperature thermochemical stability, excellent oxidation and hot corrosion resistance and good toughness. Other relevant properties are erosion resistance, resistance to chemical reactions with impurities such as sulfur and vanadium, or with deposits like molten salts [19]. With little prospect for significant improvement in alloy performance, the community shifted its interest to multilayered thermal barrier coating (TBC) systems that can be applied to hot section super alloy components to meet these needs.

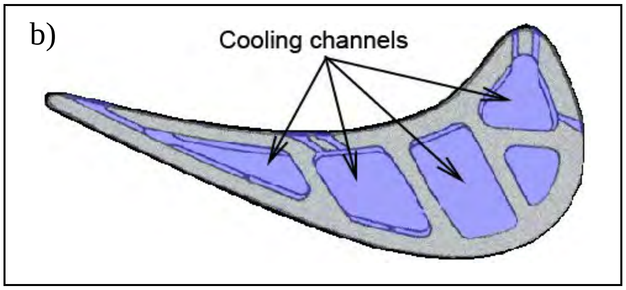

Figure 2-1. (a) A high pressure gas turbine blade (Photo courtesy of S. Tin, Rolls-Royce UTC.) and (b) a cross-section showing its cooling channels (image courtesy of Michael Cervenka, Rolls-Royce Plc)

2.1 Thermal Barrier Coating System

Thermal barrier coating systems consist of a low thermal conductivity ceramic layer and a metallic bond coat. They are now widely used in gas turbine engines to increase airfoil component life and engine performance. They provide a thermal transport and oxidation barrier (between the hot engine gases and air cooled turbine blades/vanes) that can reduce the metal surface temperature by 100-300 °C [20]. This, in combination with internal blade cooling can enable modern gas-turbine engines to operate at gas temperature well above the melting temperature of the superalloy (~1300 °C) [6], thereby improving engine efficiency and performance. To further reduce the thermal transport to the substrate, improvements to a TBC system could be achieved by the development of materials with lower thermal conductivity. However this results in higher ceramic layer surface temperatures so this in turn leads to a requirement for high temperature phase stability [21, 22] and sintering resistance [23]. In addition, the coating must have excellent spallation resistance under cyclic thermal loading and resistance to the damaging effects of “glassy” Calcium-Magnesium-Alumino-Silicate (CMAS) deposits which are likely to become a serious issue as ceramic layer surface temperatures increase [24]. To better understand these issues, this section investigates today’s state of the art coatings and the potential of new material solutions.

A schematic illustration of a typical TBC system is shown in Fig. 2-2. The current TBC system consists of three layers (a bond coat, thermally grown oxide and a ceramic layer) made of different materials with specific properties and functions. The bond coat is applied to the superalloy airfoil. A thermally grown oxide (TGO) then forms on the exterior surface of the bond coat. A ceramic top layer is then finally applied to the TGO covered bond coat [25]. Typical bond coats for TBCs are based on either a platinum modified nickel aluminide (NiAl+Pt) diffusion coating [26, 27] or a MCrAlY (M refers to one or more of the elements Ni, Co or NiCo) overlayer [28]. The primary function of the bond coat is to provide substrate oxidation and hot corrosion protection, which can be achieved by the oxidation of aluminum and other reactive elements (such as Cr and Y) that lead to the formation of a protective thermally grown oxide adherent to the bond coat. This (ideally α-Al_2O_3) TGO layer grows on the bond coat during top coat deposition and component service. The interconnected porosity that always exists in the top-coat allows easy diffusion of oxygen from the engine environment to the bond coat. Moreover, even if the top coat were fully dense, the extremely high ionic diffusivity of oxygen in ZrO_2-based ceramic top coat makes it “oxygen transparent” [29].

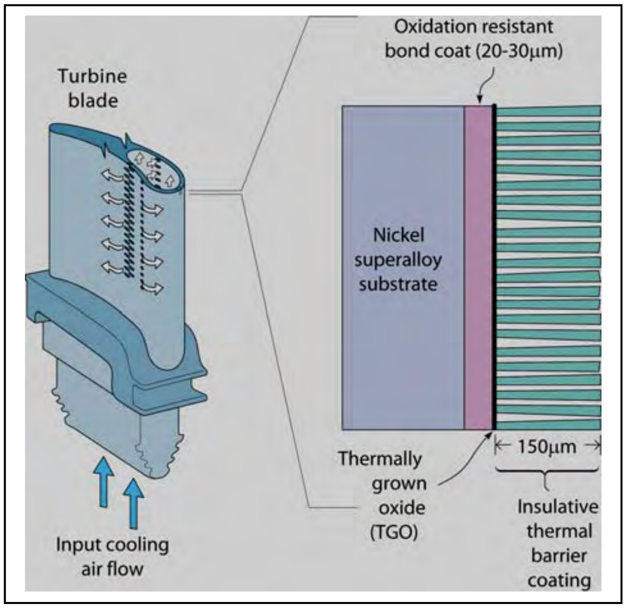

Figure 2-2. Illustration of TBC microstructure [13]

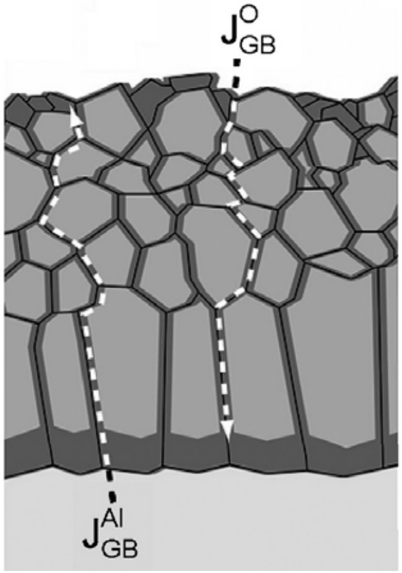

Figure 2-3. Schematic illustration of the diffusion of oxygen and aluminum to form alumina, reproduced from ref. [33].

The growth rate of the TGO is usually well fitted by the parabolic growth law of $h^2 = 2k_p t$ [30], where h is the thickness, t time and k_p the parabolic rate constant. Generally the TGO growth involves counter-diffusion of oxygen and aluminum along the α-Al_2O_3 grain boundaries (Fig. 2-3): inward diffusion of oxygen and outward diffusion of aluminum from the bond coat [31-33]. The diffusion flux and the parabolic TGO growth rate is determined by the grain size of α-Al_2O_3, as well as by impurities and by dopants that diffuse to the TGO from the bond coat and substrate [33]. At the initial stage of oxidation, transient metastable alumina (gamma and theta) may generally form and then transform to the stable α-Al_2O_3 [34-36]. This transformation is greatly affected by certain dopants (such as Hf and Y) because of the significant solubility of these dopants in gamma and theta alumina, but not in alpha. Consequently, doping with Hf and Y will retard the growth rate of the α-Al_2O_3. On the contrary, other dopants, Cr and Fe, that are soluble in alpha, can accelerate the growth rate of α-Al_2O_3 [33]. Finally, the transformation rate of $\gamma \rightarrow \alpha$ will be compromised by these dopant levels. The composition of the bond coat also has an important effect on the adhesion with TGO layer. It is known that the segregation of S at the bond coat/TGO interface reduces the TGO adhesion dramatically [37] because the interfacial covalent-ionic Ni-O bonds are replaced with weaker ionic-covalent S-Al bonds. To mitigate this adverse effect, either the S content in the superalloy should be kept very low (less than 1ppm) or Hf can be added to inhibit the diffusion of S [33].

The new α-Al_2O_3 can form either at the bond coat interface if the inward diffusion of oxygen is rapid or at the surface of prior TGO if the outward diffusion of aluminum is fastest. The ensuing volume change can be accommodated by both upward and lateral deformation. A small compressive growth stress is thus developed at the oxidation temperature and has been measured to be of order, $\sigma_{growth} \approx -300$ MPa [38]. Upon cooling, the compression increases dramatically due to the thermal expansion mismatch with the substrate. At ambient temperature, the compressive stress in a non rumpled TGO layer is in the -3.5 ~ -6 GPa range [39]. This large strain energy can be partially released by bond coat rumpling which facilitates elongation of the TGO, but in turn contributes to the potential TBC failure.

2.2 Yttria Stabilized Zirconia

The primary requirements of the ceramic TBC layer in the protection system are a low thermal conductivity and phase stability at the peak use temperature. The current ceramic 7YSZ top coat is based upon zirconia, which has a high melting point (~ 2700 °C), making it suitable for high-temperature applications. From the phase diagram Fig. 2-4, it can be seen that pure zirconia (ZrO_2) has a monoclinic (m) structure at room temperature. Upon heating, it transforms to a tetragonal (t) structure at ~1300 °C and then to cubic fluorite (F) phase at ~ 2340 °C [40]. These transitions are accompanied by a significant molar volume change. The monoclinic to the tetragonal transformation is especially problematic. The monoclinic phase has a 4% greater molar volume than the tetragonal structure [41]. Upon cooling from the t region, this transformation can lead to such high stresses that the coating will fracture [21]. For this reason, yttria is typically added to zirconia in order to stabilize the t phase upon cooling. In practice, 7±1wt % yttria stabilized zirconia (7YSZ, Fig. 2-4) is generally used since the metastable supersaturated t′ phase forms in the range of this composition [21]. This metastable t′ phase can exist over the temperature range from ambient to 1300 °C. The high temperature stability of the t′ phase of the yttria stabilized zirconia system then maximizes the spallation life of this coating material [42].

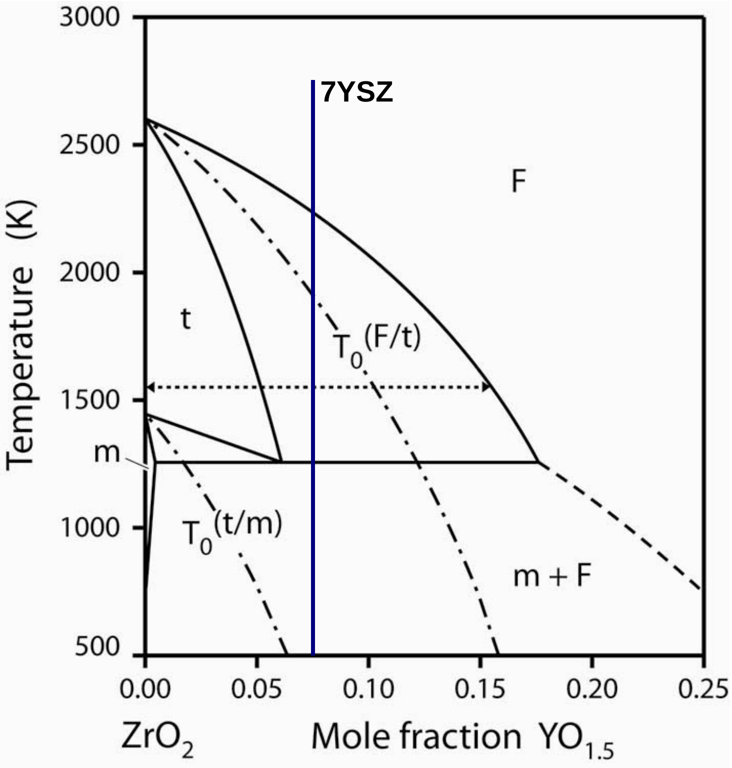

Figure 2-4. Phase diagram of $YO_{1.5}$-ZrO_2 adapted from [40]. The composition of the metastable t′ 7YSZ is shown in the dark blue line. The t′ 7YSZ will undergo a compositional partition into the equilibrium tetragonal (t) and cubic fluorite (F) phases when it reaches to the horizon dashed line.

The bulk fully dense form of 7YSZ is reported to have an intrinsic thermal conductivity of 3.0 W/mK at 25 °C [43]. However, it can be manipulated by varying the phase, porosity content and temperature [44]. It can also be influenced by incorporation of phonon scattering defects in addition to yttrium [45]. In absence of any defects in a solid, the intrinsic conductivity is ideally proportional to T^{-1}. In a real solid, the thermal conductivity can be reduced by the introduction of phonon-scattering lattice imperfections. The common point defects in the solid solutions are [46, 47]: (i) substitutional atoms, (ii) vacancies, and (iii) interstitial atoms. When yttria is added to zirconia, Y^{3+} cations substitute for the Zr^{4+} cations in the zirconia structure. To maintain overall charge neutrality, oxygen (O^{2-}) vacancies will be then created in the lattice. These oxygen vacancy point defects decrease the phonon mean free path, but the thermal conductivity cannot continue to decrease in this manner indefinitely. It will become temperature independent and plateau out at very high temperature [48]. The magnitude of the phonon mean free path reduction depends on (i) the point defect concentration and (ii) the scattering strength of the point defect, which is proportional to the square of the atomic weight difference between the solute and the host (Zr) cations [43, 46]. Considering 7YSZ, the scattering strength of the substitutional Y^{3+} cation is negligible because of the little atomic weight difference of yttrium (89) and zirconium (91). However, the scattering strength of oxygen vacancies is larger than the substitutional atoms because of the missing anion mass and the missing interatomic linkages associated with the vacancies.

Besides a low thermal conductivity, the top coat must have a relatively high coefficient of thermal expansion (CTE) that approaches that of the superalloy in order to reduce the thermal mismatch strain between the coating and the underlying alloy during thermal cycling. Yttria stabilized zirconia has a high CTE of 11.0 x 10^{-6}/K [49], which is still slightly lower than that of nickel-based superalloys (14.0-16.0 x 10^{-6}/K) [50]. This difference results in significant misfit stress in the TBC system. The EB-PVD TBCs have the feature of "columnar structure" and thus accommodate the strain induced by the misfit, as discussed in more detail later.

The coating material must exhibit good thermodynamic compatibility with the TGO layer. Generally zirconia and alumina are thermochemically compatible (Fig. 2-5, [1]), i.e., they do not form interphases and their mutual solubility is very limited although zirconia is soluble to some extent in the metastable transient theta or gamma alumina under some circumstances [51, 52]. As mentioned previously, the initial alumina scale formation usually involves transient phases: metastable θ- or γ-Al_2O_3 or oxides of other elements present in the bond coat/substrate. Transient oxides are also believed to promote the formation of the Al_2O_3 + ZrO_2 "mixed zone" in some systems [53]. The possible mechanism was proposed in the literature [51]. ZrO_2 is much more soluble in metastable alumina than stable α-Al_2O_3, up to ~17 mol% in γ-Al_2O_3 and ~40 mol% in θ-Al_2O_3 [51]. It is also known that the incorporation Y or Zr into the metastable alumina retards its transformation to α. When an initial metastable alumina layer induced by outward Al diffusion is in contact with YSZ, this metastable alumina tends to dissolve some YSZ and becomes resistant to the transformation to α-Al_2O_3 [34]. Then this layer may continue to grow outward and dissolve more YSZ. Concurrently, the inward diffusion of oxygen may also lead to the formation of new metastable alumina on the bond coat surface, which is depleted of ZrO_2 and is susceptible to the transformation to α-Al_2O_3. The metastable alumina may then slow its growth until the dense and thick α-Al_2O_3 block the outward diffusion of Al. Eventually the metastable solid solutions transforms to α-Al_2O_3 with the precipitation of ZrO_2 along the transformation front, which forms the mixed zone layer.

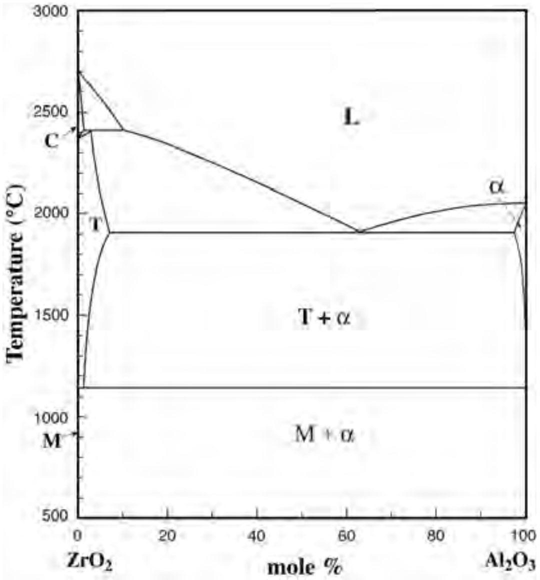

Figure 2-5. The phase diagram of ZrO_2-Al_2O_3 [1]. M, T and C represent monoclinic, tetragonal and cubic zirconia, representatively. α represents α-Al_2O_3.

Finally, the coating material applied to rotating components should have a low density to minimize centrifugal loads, a good resistance to erosion and to hot corrosion. Fully dense YSZ material has a relatively low density of 6.0 g/cm^3 which basically satisfies the density requirement. The EB-PVD 7YSZ also has a relatively good resistance to the erosion and its high toughness helps to mitigate foreign object damage [20, 54]. Experiments on hot corrosion tests [55] demonstrate that YSZ are more susceptible to vanadate attack. Even though it can not ideally satisfy all the requirements, 7YSZ is still successful for the TBC application due to its effective balance of properties.

2.3 TBC Microstructure

2.3.1 Pore morphology

The ceramic layer is applied either by EB-PVD [56, 57] or by APS [54, 56, 58]. Both processes result in the entrainment of porosity in the coating which dramatically modifies the coating's functionality. These two deposition processes result in quite different coating (pore) morphologies as shown in Fig. 2-6. APS is based on ceramic particles that are accelerated and melted by a plasma arc, and then solidify into splats upon contact with the substrate. In air plasma-sprayed coatings, inter-splat pores are roughly aligned parallel to the substrate surface and are accompanied by micro-cracks and a fine grain size [54]. This pore orientation is highly effective for impeding the flow of the heat through the coating. APS coatings therefore have low through thickness thermal conductivities of 0.8–1.1 W/mK [59]. However, this coating has less in-plane strain tolerance to accommodate the strain difference between the metallic bond coat and the ceramic top layer during thermal cycling [54, 56]. This constrains their use to low thermal cyclic environments such as land based power generation turbines. Modifications to the APS deposition conditions have enabled dense, vertically cracked (DVC) coatings to be deposited [60]. The roughly equally spaced vertical cracks enable the coating to expand with the metal during heating and they may become important for aero gas turbine applications in the years ahead. A new, potentially lower-cost, solution precursor plasma spray (SPPS) deposition process has also been recently proposed [61]. It is claimed to have the potential for creating more durable TBCs with reduced strain compatibility limitations compared to conventional APS TBCs.

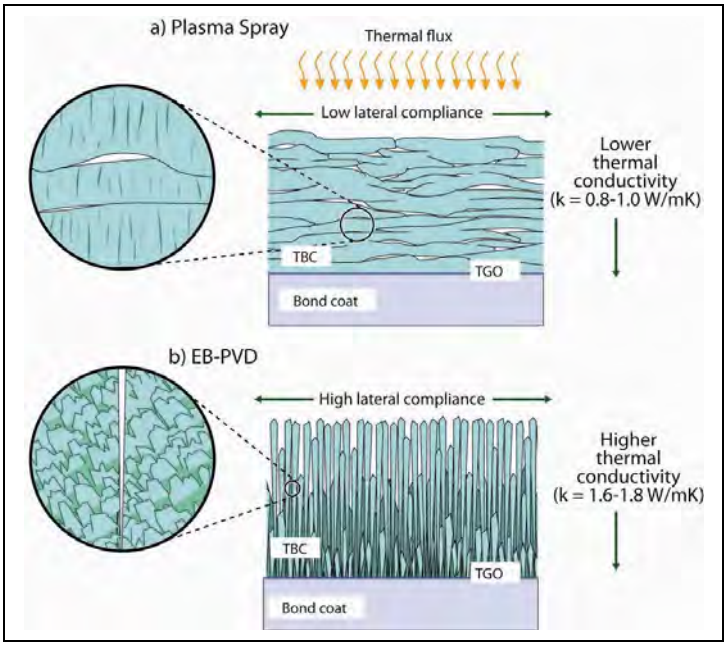

Figure 2-6. Schematic illustration of the microstructure of YSZ coatings [13] formed by (a) APS and (b) EB-PVD

The competing deposition approach, and the one normally used for aero gas turbine blade coatings is based upon the electron beam evaporation of 7YSZ ceramics and the controlled condensation of this vapor on a component. The electron beam melts a ceramic source rod fed into a high vacuum chamber to create a vapor plume. This vapor is then transported to the surface of a component and condenses upon the component which is rotated during the deposition. The typical chamber pressure during the deposition must be low (~10^{-4} torr) to enable propagation of the electron beam and relatively collisionless transport of the vapor to the substrate. The vapor is emitted with a $\cos^n\theta$ (n=2-5) angular distribution where θ is the angle from the normal to the source surface. The vapor that strikes the substrate is therefore a small fraction (~2%) of that emitted. By using high power EB gun technology, the deposition rate can be increased to 0.5-1.5 μm/min range. EB-PVD coatings consist of collinear elongated columnar structure with a predominantly <100> orientation, in Fig. 2-7(a) [62]. They contain a small volume fraction of intercolumnar pores which are orientated perpendicular to the coating interface [63]. Due to these elongated (Type I) intercolumnar pores, the EB-PVD coating is more strain tolerant in directions normal to the columns (in-plane directions) and they are much more resistant to spallation than APS coatings [54]. A finer distribution of intracolumnar Type II and III pores, Fig. 2-7(b), is present within the columns [63]. Thermal transport modeling has shown that these intracolumnar pores are much more effective at impeding heat flow through the coating as they are generally inclined to the heat flow direction [63].

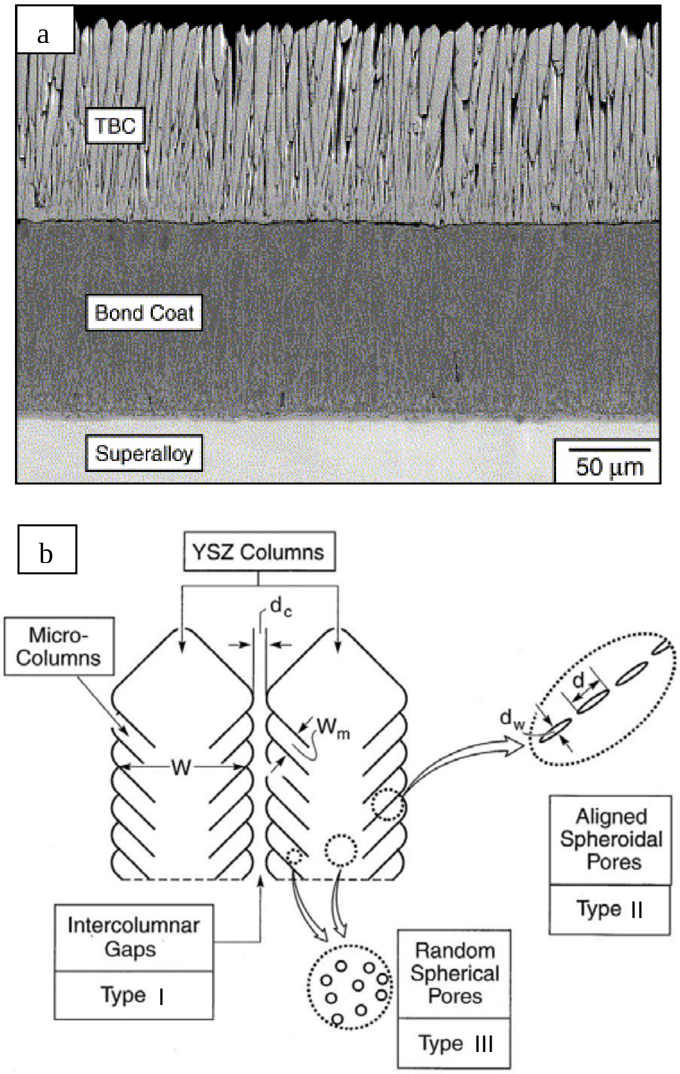

Figure 2-7. Typical microstructure of EB-PVD TBCs [41], (a) columnar structure and (b) illustration of pore morphology [63]

Porosity in PVD films generally forms through a combination of flux shadowing coupled with insufficient surface diffusion [64]. Geometric features in the path of vapor cast shadows on the growing film surface due to the line-of-sight nature of the EB-PVD process. The growth of the voids created by the shadowing process is dependent on the competition with the void elimination by surface diffusion [65]. Columns and intercolumnar gaps (Type I pore, Fig. 2-7b) originate from vapor phase condensation and operation of macroscopic shadowing caused by the column tips, triggered by rotation of the parts during deposition. Since shadowing occurs primarily along the plane of vapor incidence, columns have significant anisotropy in the direction parallel to the rotation axis and in the direction perpendicular to it. Another microstructural feature, “the feathery pores” (Type II, Fig. 2-7b), is a consequence of shadowing by growth steps on the column tips near the center of a column. The growth steps of the column tips act as shadowing centers, leading to mostly open porosity aligned under angles between 35-50° towards the main column axis. Sintering during deposition usually results in these open feathery pores partly transforming into rows of closed nano-sized spheroid pores (Type III). These nano pores are found more often near the center area of a column.

Both experimental [65-69] and recent atomistic modeling [70-73] studies of vapor deposited coatings indicate that the pore morphology can be influenced by many process variables which effect the vapor atoms incidence angle and the mobility of condensed species on the solid-vapor interface. These variables include the substrates temperature, the deposition rate, the background gas pressure, the vapor plume composition, the substrates initial roughness and the incidence direction of the flux which can be modified by rotation of the component. Experimental studies indicate that highly porous columnar morphologies are associated with low kinetic energy, oblique vapor incidence angles, low substrate temperatures, high deposition rates, rough substrates and high chamber pressures [65-69]. Atomistic models [70-73] of coating growth support these observations and link pore formation to flux shadowing under conditions of restricted adatom mobility on the coating surface.

Access to the conditions that produce optimal pore structures may be limited by the design of current EB-PVD systems. Low chamber pressures are usually needed to facilitate electron beam propagation and this results in less collisional vapor transport to the substrate. Oxygen is usually deficient in the coating due to the dissociation of the constituent oxides in the source material during the evaporation. This deficiency in the coating is also a significant issue. Hence, a partial pressure of oxygen flow into the chamber is maintained to compensate this deficiency during the growth. A narrow range of flux incidence angles is produced when the vapor impacts a flat, stationary substrate. Flux shadowing can then only be promoted by substrate rotation, which broadens the effective flux incidence angle distribution leading to increases in porosity [73]. This rotation also has a practical value. It enables uniform coating of complex shaped components such as the airfoils and guide vanes used in gas turbine engines.

There are many other ways besides rotation in which the incidence angle of a condensing flux (and thus a coating's pore morphology) can be manipulated. Hass et al. [74] inclined a substrate between two fixed angles to produce a symmetrical coating with zigzag shaped columns over the entire thickness, in Fig. 2-8. The measured thermal conductivity depended upon the zig-zag structure but was in some cases as low as 0.8 W/mK. In this structure, the intercolumnar gaps (primary, Type I pores) were orientated obliquely to more effectively impede the heat transport across the coating. Twisting a flat substrate as this is done will produce columns that have a spiral shape [75]. A second approach is to use high pressure environments to broaden the incidence angle distribution of the flux [12]. In directed vapor deposition (DVD) [12, 76], the evaporant flux is entrained in a

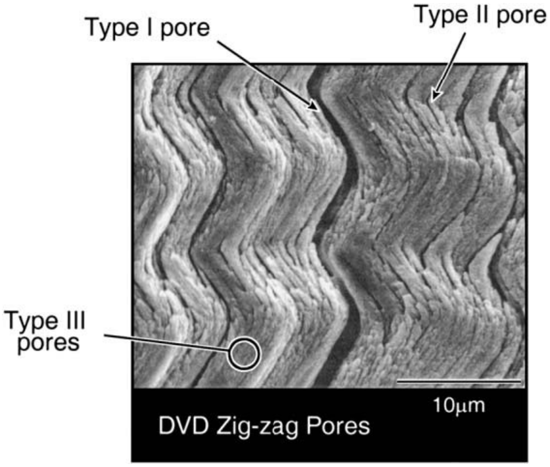

Figure 2-8. Zigzag pores of a EB-DVD coating [13]

supersonic gas jet that is directed towards the substrate. With the jet present, chamber pressures are much higher and the mean free path is greatly reduced so that many vapor phase collisions occur. Multiple scattering events during the transport of vapor towards the substrate, and especially during its passage above the surface, broaden the angular incidence distribution significantly. It can also increase the frequency of three body collisions and the probability of nucleating vapor phase clusters. The deposition of these nanoclusters provides a different mechanism of coating morphology manipulation. Previous preliminary studies have indicated that YSZ layers deposited by DVD onto stationary substrates have highly porous, columnar morphologies with hierarchical pore distributions which could be manipulated by the jet flow conditions [74]. Their through thickness thermal conductivities have been measured to be ~1.9 W/mK [74]. The reduced thermal conductivity of porous coatings is mitigated to some extent by sintering (densification) during use of the components at high temperatures. This can also eliminate the desirable vertical pores providing in-plane strain tolerance.

2.3.2 TBC texture

When 7YSZ grains first start to grow on the substrate, the first thin layer consists of equiaxed grains of about 30 nm in diameter, forming the so-called equiaxed zone [77].

The grains are randomly orientated and the thickness of the equiaxed zone varies from sample to sample. A model has shown that the equiaxed zone is formed exclusively during the very first rotation of the sample [57]. Continued growth leads to a columnar structure with an out-of-plane texture that increases in intensity with increasing thickness. An "evolutionary selection" growth mechanism has been proposed to explain this preferential orientation from the initially randomly oriented grains in the film [78]. The most favored orientation with the fastest growth rate will be left over during the film growth, all other orientations gradually dying out, shown in Fig. 2-9. Finally, a selection of the crystallographic orientation with the most favored growth rate takes place resulting in a strong texture of the TBCs with a {100} plane parallel to the substrate.

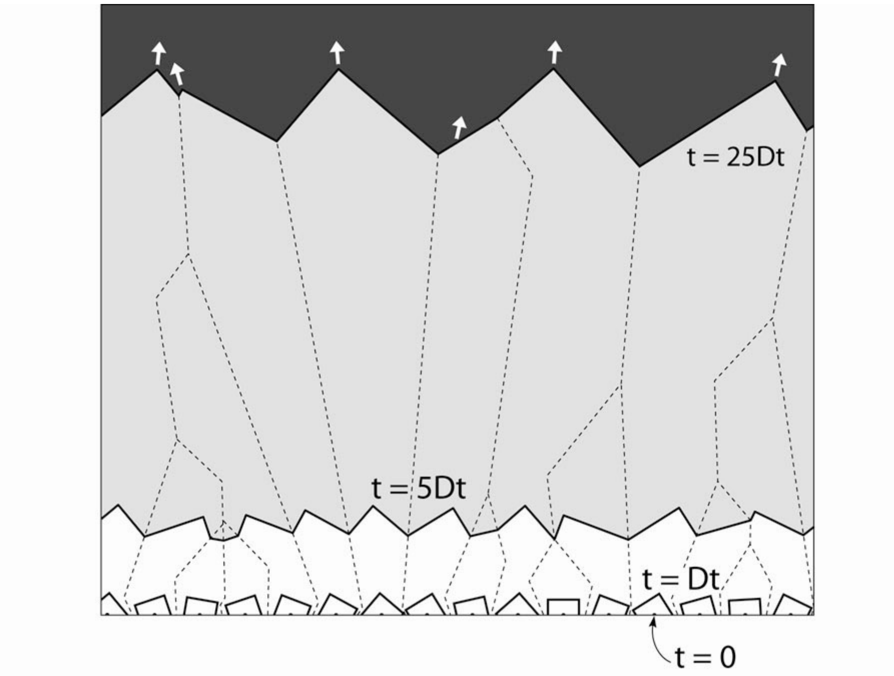

Figure 2-9. The 2-D illustration of the evolutionary selection [78]. The crystal grows with most preferred direction, starting from randomly orientated nuclei.

The TBC texture is also influenced by the rotation speed, substrate temperature and vapor incidence angle, etc. Experiments have shown that the YSZ coatings had a favored <111> column growth direction when grown without substrate rotation during deposition [65, 79]. This is consistent with a periodic bond chain (PBC) theory originally formulated by Hartman and Perdok [80]. According to the PBC theory, crystal growth proceeds by the formation of consecutive unique bonds between molecules, which are repeated throughout the crystal structure. In some directions, certain combinations of these bonds are repeated forming what is known as periodic bond chains. Some of them are strong and others weak. PBC theory assumes that for crystal growth the formation of strong PBCs are favored over the weak ones. This PBC analysis predicts {111} habit to be the preferred growth facets of the fluorite crystal structure [81], which is consistent with the experimental observation. Under stationary deposition, increasing the substrate temperature from 900 to 1000 to 1100 °C causes the column growth direction to change from <111> to <111> + <110> to <110>, respectively [65]. When the vapor incidence angle is changed from 0 to 45°, the dominant column growth direction is transformed from <111> to <110>.

2.3.3 Thermal conductivity

7YSZ has a low intrinsic thermal conductivity primarily due to phonon scattering by the oxygen vacancies in the structure. The thermal conductivity of the TBC can be further manipulated by varying the pore morphology in the coating. As mentioned above, the pores in the coating can be categorized in the following manners: inter-columnar pores

(Type I), aligned open pores between the feathery microstructures (Type II) and intra-columnar elongated nano-sized spheroid pores (Type III) in the center of a column. Type I pores are almost perpendicular to the substrate and very effective at accommodating the strain tolerance. However, this structure is less effective at impeding the heat flux to the below substrate. A model developed by Lu et al. [63] has shown that the low aspect ratio spheroidal (Type III) pores are most effective at impeding the heat flux at a fixed porosity level. They also demonstrated that the reduction of thermal conductivity is strongly dependent upon the orientation and aspect ratio of the Type II pores. If they have a low inclination angle (with the horizontal axis) and low aspect ratio (oblate and elongated), the Type II pores also result in a substantial reduction of thermal conductivity. This implies that the flat oblate pores are the most effective at reducing the axial conductivity. Finally, the column inclination is also associated with the thermal conductivity. The smaller the column inclination angle to the horizontal, the larger the decrease in thermal conductivity. It is for this reason that the zigzag structure of DVD YSZ has such a low thermal conductivity.

The results and models discussed above clearly indicate that the thermal conductivity of a ceramic coating can be varied by change of its pore morphology. A lower density, high pore fraction coating promotes a lower thermal conductivity. Density is mainly determined by the substrate temperature as well as the chamber pressure. The lower the substrate temperature, the lower is the ability for diffusion of the condensed particles into stable lattice positions, leading to an imperfect microstructure having a low density. The pore morphology of EB-PVD TBCs can to some extent, therefore, be tailored by manipulating process parameters, such as pressure, temperature and rotation speed. Inclining the vapor incidence angle can also change the pore shape in a coating and thus reduce the thermal conductivity, but it may be challenging to implement this strategy in practice because of the difficulty of also uniformly coating on a complex shaped component.

2.4 TBC Spallation

During operation of aero gas turbine engines, the coating system is subjected to thousands of thermal cycles that elevate the bond coat surface to ~1000 °C [82]. The outer surface of the top coat may experience temperatures more than 100 °C higher than this. At these temperatures, significant densification of the YSZ (sintering) and creep of the bond coat occurs and is accompanied by temperature dependent TGO layer growth. Moreover, the thermal expansion misfit results in larger compressive stresses upon cooling. The stresses developed by these processes eventually cause spallation of the TBCs which usually occurs at the TBC-BC interface [30, 83, 84]. An example of such a mechanism is shown in Fig. 2-10. In this system, the TGO develops instabilities enabled by elongation of the TGO as it thickens. The rumpling is allowed by the relative low resistance of the bond coat to high temperature yield strength. The spallation results from the linkage of the cracks formed in the TBC above the TGO.

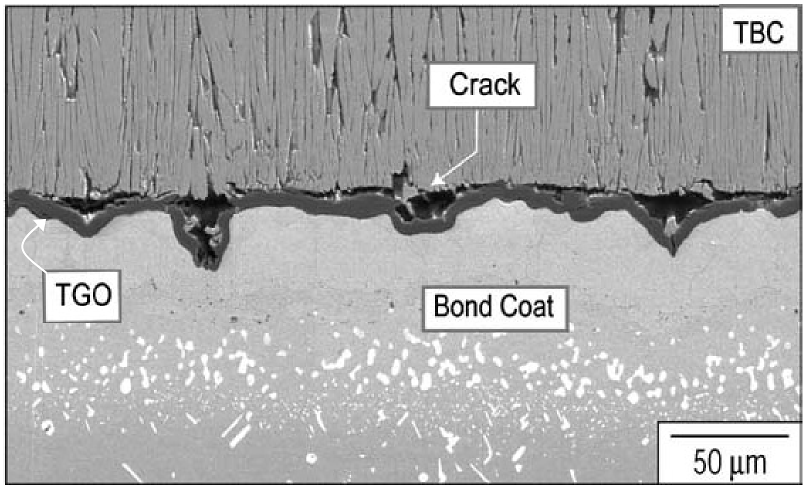

Figure 2-10. Crack coalescence leads to the failure of EB-PVD TBC on a PtNiAl bond coat [30]. TGO layer rumpling is also evident in the figure.

Ideally the TGO formed on the bond coat is pure α-alumina but oxides of other components such as yttria (the oxidation of Y diffused from the bond coat) have also been observed to form. When yttria domains are incorporated into the TGO, it thickens more rapidly in these regions and produces thickness imperfections. Simultaneously, the yttria reacts with the surrounding alumina to form yttrium aluminum garnet (YAG) [30, 85]. The interface properties of TBC/TGO and TGO/BC determine the failure mode.

Extensive experiments have been performed on investigating the spallation of EB-PVD thermal barrier coating deposited on different processed substrates [27, 86, 87]. These studies have indicated that the bond coat processing can influence the crack path and the time to failure. Grit-blasting and polishing (media or manually) are commonly used for bond coat surface processing. Results have shown that TBC deposited on polished substrates have longer lifetime to failure than that grown on grit-blasted substrates [87]. Grit-blasting of substrate surface prior to the TBC deposition may have a detrimental effect on the TBC lifetime because of defects and surface contaminations introduced by the grit particles [27]. The surface roughness of the bond coat also has a profound effect on the adhesion of the alumina scales with MCrAlY alloy during cyclic oxidation.

Based on the observations found in many experiments, some important principles govern the failure of TBC systems as follows:

i. The TGO experiences large in-plane compressions, especially upon cooling. As with any compressed thin film, it attempts to release the stress by lengthening itself which here can occur by rumpling. The normal tensile stresses induced by the TGO displacements motivate the delamination mechanism.

ii. During the TGO growth, imperfections exist (or developed) around the TGO. Tensile stresses are induced normal to the TGO/bond coat interface. Cracks will be initiated in this vicinity. These cracks link together and lead to failure.

The undulation growth is driven by the lateral growth strain in the TGO and governed by many factors, including the bond coat creep strength and the TGO yield strength. It is also reported that PtNiAl bond coats undergo a martensite transformation between 600 and 700 °C accompanied by nearly a 1% linear expansion during heat-up and the reverse transformation between 550 and 450 °C on the cool-down [88]. Balint and Hutchison [89] have developed an analytical model that predicts the TGO rumpling on PtNiAl bond coat. Their simulations have shown that the combination of thermal expansion misfit and the martensite transformation produces a relatively large equi-biaxial stress in the bond coat at high temperatures. The bond coat is susceptible to the undulation growth until this stress is relaxed. The TGO attached to the bond coat must also deform concurrently. In this way, the TGO length increases and it remains attached to the bond coat. According to this “ratcheting” mechanism, this undulation is accommodated by plastic deformation of both the TGO and bond coat during thermal cycling. This model has been substantiated by some experiments [90, 91]. In this case, system durability is dominated by cracks evolving in the TBC and at the TBC/TGO interface.

Initial non-planarities act as imperfections that initiate displacement instabilities. Removal of these imperfections by polishing inhibits instability formation, changing the failure mechanism to interface delamination. The interface between the TGO and the bond coat degrade with exposure, such as the segregation of impurities, which lower the interface toughness of TGO/BC. This degradation has negligible effect on life when the TGO instability dominates, but becomes important when the instabilities are suppressed and failure occurs by edge delamination mechanism. In summary, the bond coat properties are an important factor to determine the failure. The resultant properties by polishing suppress the TGO instabilities and enhance the durability.

2.5 Limitations of 7YSZ

Interest in raising the gas turbine engine operating temperatures (to enhance engine cycle efficiency) has exposed a potential weakness of the YSZ system. If 7YSZ is heated up to 1300 °C, it undergoes a phase transformation from the metastable *t′*-phase to a mixture of the equilibrium tetragonal (t) and cubic (c) phases [21]. During subsequent cooling, the t phase transforms to a monoclinic (M) structure with a significant (~4.5 vol.%) volume expansion which causes the large stresses and promotes coating failure [21]. New ceramic compositions that do not suffer phase changes over the temperature range of this future applications are therefore of interest.

It has also been realized that the sintering rate of ytrria stabilized zirconia rapidly increases with temperature [21]. This facilitates diffusion bonding of the vertical cracks and pores [50]. These effects increase the coatings thermal conductivity and its in-plane modulus. The former leads to a more rapid TGO growth and the latter to an increase in the strain energy within the TBC layer which is then available to drive interfacial (delamination) failure [23].

Another factor is that 7YSZ is vulnerable to CMAS penetration at high temperature. At temperature in excess of 1150 °C, sand particles and debris ingested during operation become molten and adhere to TBC surfaces. YSZ is readily wetted by molten CMAS deposits. These deposits rapidly infiltrate the coating via its porosity. Thereafter, upon cooling, the CMAS layer solidifies into a fully dense stiff domain [92], which results in the loss of strain tolerance of the coating, and delamination of the underlying TBC. Another consequence is that 7YSZ is dissolved in the molten CMAS and re-precipitated as Y-depleted zirconia which can transform to the monoclinic phase upon cooling [24]. The associated volume change could then contribute to the strains that cause coating failure during thermal cycling.

These issues have motivated a search for alternative ceramics with improved high temperature phase stability, better sintering and CMAS attack resistance, and improved toughness to reduce the erosion and foreign object impact comparable to the current material [43, 93].

2.6 The Search for New Materials

The first consideration for a new coating material is a low thermal conductivity (κ). Many low κ ceramics have been proposed for TBC applications [50, 94, 95]. They include mullite [94], CeO_2-doped YSZ [96, 97], Sc_2O_3-doped YSZ [98, 99], garnet [100], Y_2O_3-doped HfO_2 [9, 101], CaO-SiO_2-ZrO_2 system [102], zircon [103], lanthanum aluminates [104], pyrochlore $La_2Zr_2O_7$ and two perovskites ($SrZrO_3$ and $BaZrO_3$) [105]. Most of them are eliminated due to too high a thermal conductivity, phase instability or inadequate thermal and chemical stability.

An approximate expression has been deduced to estimate the minimum thermal conductivity, $\kappa_{\min}$, of a material based on Debye equation [50, 106-108]:

$$\kappa_{\min} \to 0.87 k_B N_A^{2/3} \frac{m^{2/3} \rho^{1/6} E^{1/2}}{M^{2/3}},$$

where M is the molecular weight, m is the number of atoms per molecule, ρ is the density of the crystal structure, E is the Young's modulus. And k_B and N_A are Boltzmann's constant and Avogadro's number. If it is assumed that heat is predominantly transferred by a conductive mechanism, comparisons of the acoustic phonon contribution to thermal conductivity, provide a fundamental approach for an initial identification and screening of the candidate materials. The lowest thermal conductivity occurs when the mean free path between phonon scattering events is comparable with the ceramic materials interatomic spacing [48, 109]. According to this approximation, the minimum thermal conductivities of rare earth (RE) zirconate pyrochlores were calculated and shown to have a lower κ_{min} than 7YSZ [48]. Experiments have also found that the thermal conductivities at temperatures between 700 and 1200 °C for zirconates of Gd, Eu, Sm, Nd and La lie between ~1.1 to ~1.7 W/mK [105, 110-112]. This is significantly below that of 7YSZ.

The data in Table 2-1 summarizes this and some of the other TBC related properties for fully dense (sintered) 7YSZ and three of the rare-earth zirconates. All of these zirconates have a significantly lower thermal conductivity than YSZ and a potentially much higher use temperature [43, 105, 111, 113]. Using molecular dynamics simulations, Schelling et al. have examined most of the pyrochlores (with the general formula $A_2B_2O_7$) and show that the B ions more strongly effect the thermal conductivity, the thermal expansion coefficient and the bulk modulus than the A ions [114]. The zirconate data in Table 2-1 appears to be consistent with this observation. All three of the zirconates possess a similar thermal expansion coefficient to 7YSZ but all their conductivities are significantly less.

Table 2-1. Thermophysical properties of fully dense rare-earth zirconates and 7YSZ, adapted from [43].

Ceramic Material	Thermal conductivity at 700 °C (W/mK)	Thermal expansion coefficient (× 10^{-6}/°C)	Maximum use temperature (°C)	Hardness (GPa)	Density (g/cm^3)
7YSZ	2.3 [43]	11 [30]	1425	13±1 [105]	6.0 [105]
$Gd_2Zr_2O_7$	1.6 [113]	11.6	1550	10	7.0 [112]
$La_2Zr_2O_7$	1.5 [113]	9.1-9.7 [115]	2300	9.9±0.4 [105]	6.05 [105]
$Sm_2Zr_2O_7$	1.5 [111]	10.8 [116]	2200	11	6.7 [111]

The maximum use temperature of a zirconate coating is dictated in part by high temperature phase stability considerations. The phase diagrams of several $REO_{1.5}$ - ZrO_2 ceramic alloys are shown in Fig. 2-11 [117]. At elevated temperatures, the stable phase of an equi-molar ZrO_2 and $REO_{1.5}$ ceramic alloy is a disordered fluorite (F) phase, shown in Fig. 2-12(a) for ZrO_2 [111]. The pyrochlore structure can be thought of as an ordered, defective fluorite solid solution (shown in Fig. 2-12b), which remains thermodynamically stable (without order-disorder transitions) up to the fluorite transformation temperature. This occurs at 2300 °C for $La_2Zr_2O_7$, 2200 °C for $Sm_2Zr_2O_7$ and 1550 °C for $Gd_2Zr_2O_7$ [116]. Phonons in these materials can also be scattered by oxygen vacancy defects in the pyrochlore structure resulting in additional lowering of the thermal conductivity. The presence of these vacancy type defects is thought to also contribute to the high thermal expansion coefficient of the zirconates [118]. Finally, ordering of oxygen vacancies in the zirconates may significantly increase their sintering resistance [43, 111]. Leckie et al. [119] have recently reported the deposition of $Gd_2Zr_2O_7$ coatings with morphologies well suited for TBC applications using EB-PVD. Maloney [110, 120] has patented and developed a low thermal conductivity gadolinia zirconate for gas turbine applications. His patents have identified all the rare earth zirconates as potential TBC candidates.

Samarium zirconate (ZrO_2-33 mol% Sm_2O_3) is of particular interest since its pyrochlore phase is thought to be stable up to its melting point 2200 °C [121]. Its thermal conductivity at 700 °C is reported to be ~1.6 W/mK [43] which is lower than that for 7 wt% Y_2O_3 stabilized zirconia (~2.3 W/mK). The thermal expansion coefficient is 10.8×10^{-6}/C [43] which is comparable with that of 7YSZ. Preliminary experimental studies of sintering also indicate it has a low sintering rate up to temperature of 1400 °C [122]. This combination of properties suggests samarium zirconate might also therefore be a promising candidate material for higher temperature TBC systems. However, the primary drawback with the zirconate systems is their low toughness and incompatibility with α-alumina. Levi has shown that all the zirconates are likely to be unstable when placed in contact with alumina at high temperatures [95]. Leckie et al. [119] and Wu et al [47] have found that a $GdAlO_3$ phase is formed at the contact between $Gd_2Zr_2O_7$ and α-Al_2O_3 after heat treatment at 1200 °C. Since all the pyrochlore zirconates are prone to degrade the TGO by interdiffusion [95], practical implementations of $Gd_2Zr_2O_7$ and other zirconate coatings may therefore require either maintenance of a low interface temperature (say below 1100 °C) or deposition of an intermediate barrier layer (such as 7YSZ) to impede the reaction with the TGO during service. Bilayer 7YSZ/$Gd_2Zr_2O_7$ has been investigated for the TBC application by Leckie [123]. The YSZ layer has been successfully used as a diffusion barrier against gadolinia interaction with alumina. The

$Gd_2Zr_2O_7$ layer also shows a potential resistance to CMAS attack [123]. Neither the thermal cyclic lifetime nor a resistance to erosion and foreign object impact has been reported for this or any of the zirconates.

Samarium zirconate (SZO) has received little attention by now and its behavior has not been well documented. In this dissertation, the SZO coating is deposited using DVD and the effect of substrate rotation and deposition temperature on the coating microstructure, texture and pore morphology is investigated, as well as their influence upon coating density, thermal conductivity and thermal cycling performance.

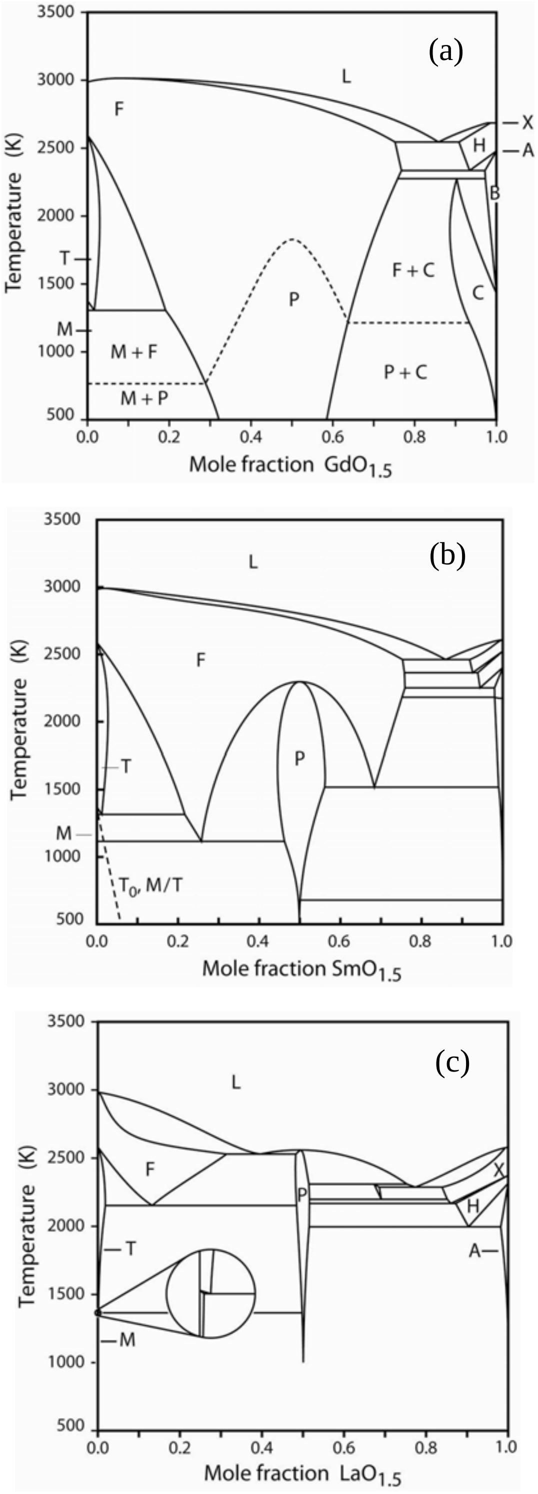

Figure 2-11. Experimental phase diagram for ZrO_2 and $REO_{1.5}$ of binary systems, where RE is either (a) Gd, (b) Sm and (c) La. F = Fluorite, L = Liquid, M = Monoclinic, P = Pyrochlore and T = Tetragonal. A, B, C, H and X represent some different types of rare earth oxides [117].

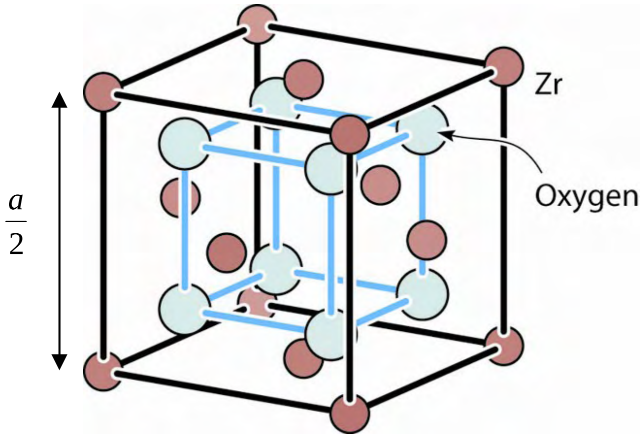

(a) Fluorite structure of stabilized ZrO_2

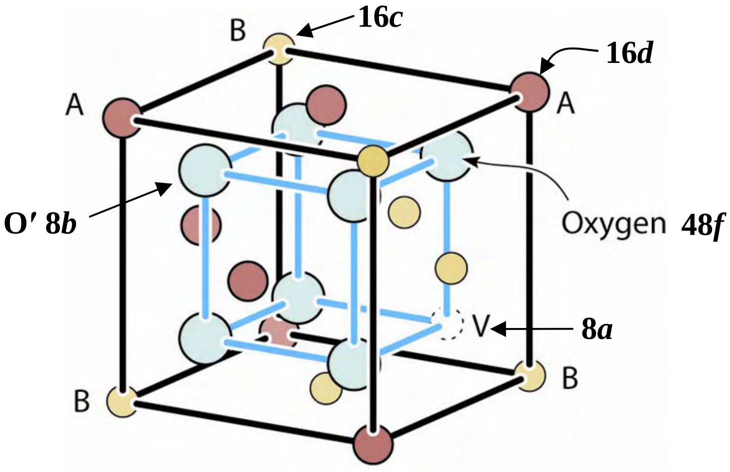

(b) One-eighth of the pyrochlore structure of an $A_2B_2O_7$ compound

Figure 2-12. The crystal structures of: (a) The fluorite structure of stabilized ZrO_2 and (b) the one-eighth of the pyrochlore structure of an $A_2B_2O_7$ compound. A is selected from the group of rare earth elements (La, Nd, Sm, Eu and Gd) and B represents either Zr or Hf. V is a missing oxygen atom (an oxygen vacancy). In the pyrochlore structure, the A^{3+} cations occupy the 16d site (A site) while the Zr^{4+} occupy the 16c site (B site). The oxygen vacancy is in the 8a and the two independent O^{2-} are located at the 48f and 8b. Now there are three distinct tetrahedral sites: 8a, which has four B nearest atoms; 8b, which has four A nearest atoms; and 48f, which has two A and two B nearest neighbours.

Chapter 3

Directed Vapor Deposition

3.1 Overview

Directed vapor deposition (DVD) is an electron beam physical vapor deposition technique that utilizes a supersonic gas stream to entrain a thermally evaporated vapor flux and transport it to a substrate with high material deposition efficiency [76, 124]. The combination of a high deposition pressure and the potentially high deposition rate is anticipated to facilitate the deposition of porous coatings by altering the angle of incidence and mobility of the vapor species on the substrate. Dense films can also be synthesized by a plasma-assisted directed vapor deposition approach [125]. The applications of the DVD technique are therefore ranging from thermal barrier coating deposition (porous structures) to the solid electrolyte of a thin film battery (dense film structures).

3.2 Electron Beam Technology

Electron beam technology has been developed for the material evaporation for many years. The electron beam gun and processing chamber are usually maintained at medium or high vacuum on the order of 10^{-2}-10^{-4} Pa. Beam generation takes place in an electron gun which is based on the thermionic emission of free electrons from a heated filament, their acceleration and shaping into a beam in an electrostatic field, and beam focusing and deflection via magnetic and electric field [126]. Then the beam is guided into the work chamber and impinged on the source material. During travel path from emission point to target, the electron beam energy losses occur by impinging inside the gun, scattering by gas and vapor atoms, electron backscattering from the evaporated material surface, thermal conduction and heat radiation and convection in the melt etc. Therefore, a very small fraction of initial beam power can be transformed to evaporate the material due to these losses. Compared to other losses, losses due to beam guidance in the gun can be neglected. In addition, the interaction between beam electrons and gas molecules is dependent upon gas pressure, gas type, acceleration voltage and beam current. In an adequately low pressure system of 10^{-2} Pa, the mean free path of electrons in a gas is approximately 3000 mm. Hence, the effects of collisions of vapor particles and electrons with gas particles are insignificant. At high pressure of 10 Pa, the mean free path would reduce to 3 mm and the interactions and collisions between the electron flow and the vapor stream cause the vapor particles and electrons depart from their initial trajectories. Energy losses of the electrons due to vapor collision are further accompanied by vapor excitation and ionization. Therefore, the requirement for maximum electron beam gun power in a low vacuum has been explored. It is noted that increasing the accelerating voltage and thereby decreasing the scattering cross-section of the atoms in the chamber would increase beam propagation through the low vacuum. Moreover, it is predicted from Arata’s equation [127] that beam propagation through the lower atomic number inert gas (helium) is superior because of the shorter range electron/atom interaction potential in that system [12].

3.2 Directed Vapor Deposition

In the configuration of the first DVD I approach investigated by Groves, the vapor was redirected toward a substrate (located 90° from the vapor source) by an inert carrier gas, shown in Fig. 3-1. In DVD I system, to ensure an ability to evaporate rapidly even high melting point materials, an accelerating voltage of 60 kV and carrier gas (helium) have been chosen which will transmit as much as possible of the beam's initial energy to the source material. The need for a redirection of vapor atoms limited DVD I when films needed to be deposited at a low gas flow or when a high deposition rate was required. To fully exploit the approach, a second generation DVD II system was designed and has been used extensively for experimental research. It is shown schematically in Fig. 3-2.

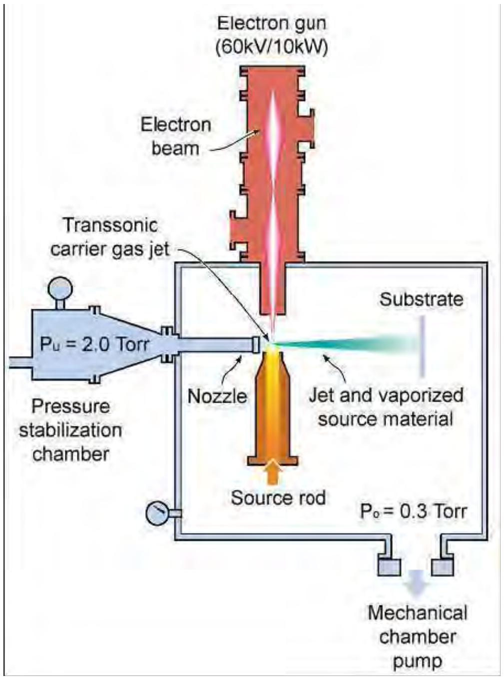

Figure. 3-1 Directed vapor deposition (DVD I) system. The supersonic gas jet redirects vapor atoms to a 90° angle toward the substrate during DVD deposition.

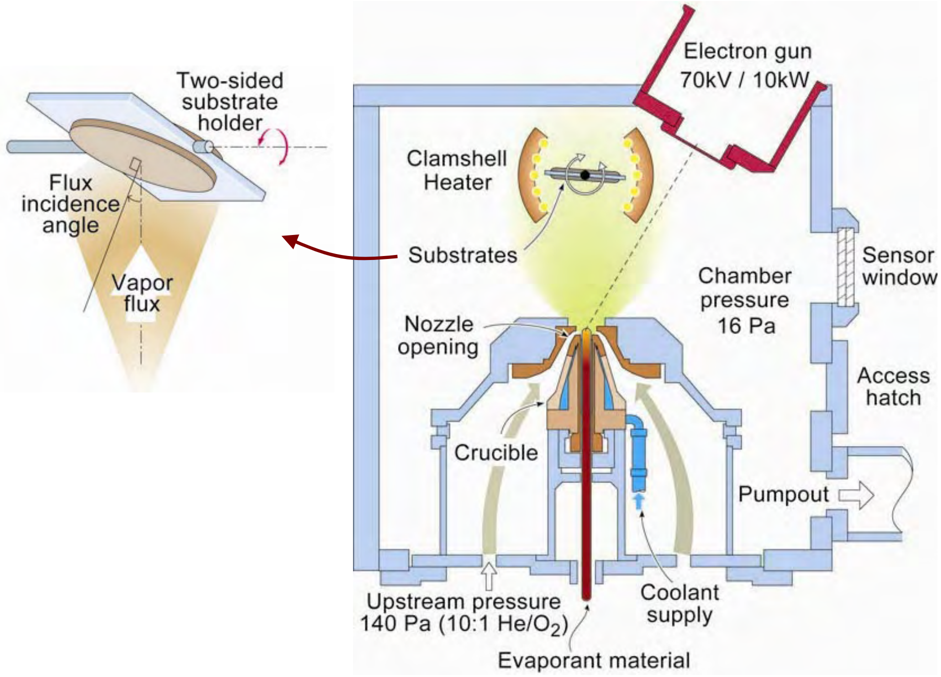

Figure 3-2.Illustration of DVD II system

In the DVD II system, the electron beam gun operates with the maximum power of 10 kW and a beam accelerating voltage of 70 kV. This high voltage is used to reduce the electron scattering cross-section with background gas atoms permitting focused penetration of the beam over considerable distance in low vacuum (high pressure) conditions. Even the source material with a very high melting point can be thermally vaporized by the bombardment of the electron beam with high power. In the DVD process, typical operating pressures are in the 10 to 200 Pa range. High-speed beam scanning with a frequency of 100 kHz has been incorporated in the electron beam gun to control the source melting more precisely. Multi-source crucible can be available for different purposes. In order to co-evaporate multiple source materials with a single electron beam, the electron beam scan pattern can be programmed to rapidly jump the electron beam between the multiple sources [128]. Each individual source material could be evaporated with different rates by controlling the dwell time of electron beam on each molten source pool. The ability to evaporate each individual source material with an independently controllable rate enabled a coating with a precise composition to be synthesized. Moreover, multilayer deposition can be easily operated by moving the beam between the source materials alternatively without breaking the vacuum.

During the deposition process, the upstream pressure (P_u) is higher than the downstream pressure (or chamber pressure P_o), creating a supersonic gas jet through an annular nozzle near the source rod. The vapor atoms from the source material will be entrained in the supersonic carrier gas jet which rapidly transports them to the substrate. The gas jet flow speed and density can be controlled by the choice of upstream pressure (P_u) and downstream pressure (chamber pressure, P_o) ratio and the nozzle dimensions. The speed of a supersonic gas jet, U, can be estimated from the following equations [12]:

$$U = M\sqrt{\gamma R_s T} \qquad (3\text{-}1)$$

Where γ = Ratio of specific heats (5/3 for helium),

M = Flow’s Mach number, T = Absolute temperature (K), and

R_s = Specific gas constant (2077 J/kg/K) for Helium.

The Mach number is determined by a pressure ratio (P_u/P_o) [129]:

$$\frac{P_o}{P_d} = \left[1 + \frac{\gamma - 1}{2} M^2\right]^{\gamma/(\gamma-1)} \qquad (3\text{-}2)$$

These two equations indicate that the speed of the supersonic gas jet can be increased by increasing the pressure ratio (P_u/P_o). In the practical deposition, the reactive gas oxygen mixed with carrier gas helium will be flowed into the chamber, which will increase the pressure difference and therefore the gas speed. Meanwhile, the use of supersonic gas jet also promotes the deposition rate and material utilization efficiency by focusing more vapor flux towards the substrate.

3.3 High Pressure Vapor Deposition

When vapor deposition is performed in a high chamber pressure, there is more chance of collisions between vapor atoms and gas particles. These collisions can affect the coating morphology in two ways. First, the flux shadowing can be altered in high pressure. Binary collisions scatter the vapor onto different trajectories resulting in changes to the vapor incidence angle distribution (IAD) of the depositing flux. A direct simulation monte carlo (DSMC) technique was used to simulate binary collisions during transport of the vapor to the substrate thus estimate IAD. The effect of chamber pressure on IAD is shown in Fig. 3-3 [130]. Higher chamber pressures result in broader distributions and peak positions close to the substrate normal. The results also show that many of the particles impinge the substrate at oblique angles of incidence, which enhances the shadowing effect. Flux shadowing results in porosity when oblique atom arrivals are shadowed by fast growing grains or surface asperities. A high fraction of oblique adatom arrivals and a low surface mobility promote porosity. Thus, an increased chamber pressure during DVD deposition changes the coating microstructure by altering the distribution of incidence angle.

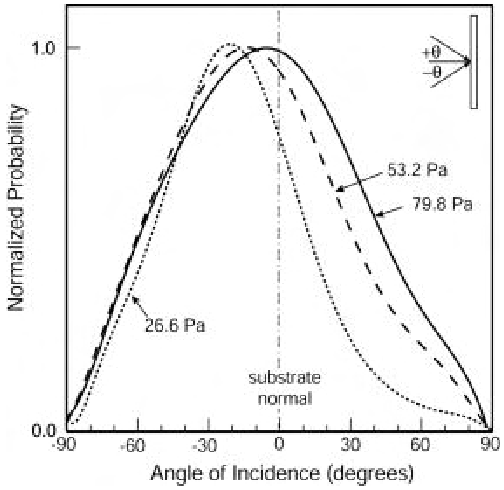

Figure 3-3.The effect of chamber pressure on the vapor incidence angle distribution

Secondly, the binary and ternary collisions during vapor deposition during vapor transport will, in some cases, promote gas phase clustering. The formation and ensuing deposition of clusters is important as they can affect the pore morphology and texture of vapor deposited films [131, 132]. High energy cluster impacts lead to denser coating morphologies and lower energy cluster result in porous, granular coatings with equiaxed grain structures. The cluster formation in a DVD environment has been investigated by Hass et al. [130] using a kinetic approach. The result shows that increased chamber pressure leads to larger cluster impact. For the DVD case, the clusters have a low kinetic energy per atom and low energy cluster impacts are resulting in small mounds on the surface.

Any changes caused by the deposition conditions such as gas speed, gas atom flux, nozzle parameters, chamber pressure and substrate temperature etc. are expected to effect the morphology of coating structures. Fig. 3-4 shows a Thornton diagram which indicates that the film structure is varied with the chamber pressure and substrate temperature [66]. The diagram is for sputtered thin films and shows the second axis as pressure. In this case, the sputtered material leaves the sputter source with relatively high energies (several electron volts). As the sputtering pressure is increased, then more scattering occurs and the arrival energy of the sputtered material decreases. For evaporated films the arrival energies are low and the thin film structure would follow the high pressure side of this diagram (porous structure). If ion and plasma assist is added then the energy per arriving atom increases the thin film structure will be improved and move towards the low pressure side of this diagram (dense structure).

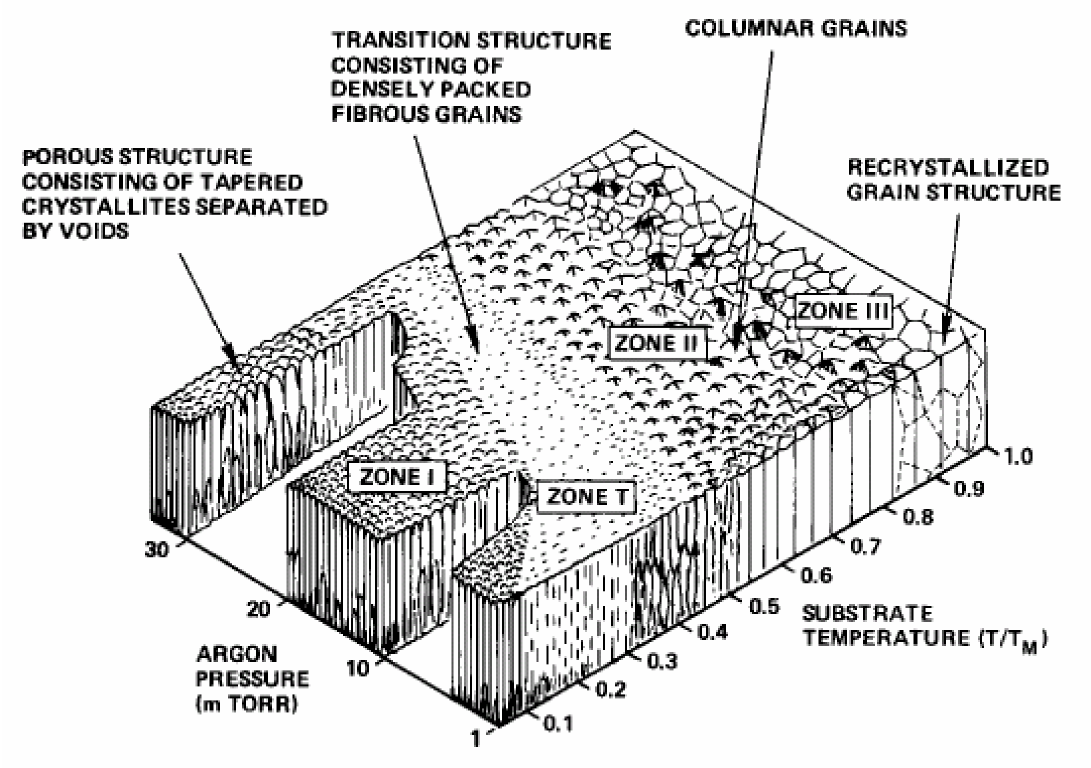

Figure 3-4. Thornton structure zone diagram [133] showing the effect of substrate temperature and chamber pressure on the morphology of coatings.

Chapter 4

Experimental Methodology

Previous studies have indicated that YSZ layers with porous, columnar morphologies can be produced using DVD [74, 134], however, a systematic study of the effect of substrate rotation on the morphology of YSZ layers, and a detailed understanding of how coating morphology depends on process conditions and affects spallation resistance has not been conducted. This dissertation begins with an exploration of how the morphology of a 7YSZ ceramic top coat is affected by the rotation rate. Since porosity in the coatings is usually formed by a flux shadowing mechanism, the initial roughness of the substrate is an important variable. In addition, different coating characterization techniques have been used to determine the morphological changes. Coating deposition technique, substrate and characterization methods are described below.

4.1 Coating Growth Methodology

In this study, The EB-DVD approach was used to deposit TBCs on stationary and rotated substrates as shown in Fig. 3-2. The disc shaped substrates were mounted on a holder rotating around a horizontal axis normal to a 12.5 mm diameter source ingot (and vapor plume) axis. 7YSZ and $Sm_2Zr_2O_7$ coatings were evaporated from single rod crucible and the bilayer 7YSZ/SZO coatings were grown using a two-rod crucible. Both 7YSZ and SZO rods have a diameter of 12.5mm and were supplied by TCI Ceramics, Inc.

(Hagerstown, MD). The 7YSZ source rod had a composition of 93wt%ZrO_2-7wt%Y_2O_3. A 2.45 kW power electron beam with a 0.5 mm beam spot size and a 100 Hz scan rate was used for evaporation. A scanning pattern was chosen from a programmed pattern library that enabled complete source rod evaporation without ejection of source droplets. The gas jet used in this process was created by maintaining a high upstream pressure P_u (140 Pa) of a nozzle opening and a lower downstream (or chamber) pressure P_o (16 Pa). The pressure ratio, P_u/P_o, was set at 8.75. The evaporated flux was entrained in a 10.0 standard litre per minute (slm) helium- 1.0 slm oxygen gas flow. The oxygen in the gas flow compensated for oxygen depletion in the ceramic source during evaporation. The evaporated 7YSZ vapor flux was entrained in a rarefied, supersonic jet and directed towards the substrate. A high carrier gas flow condition was chosen to both increase the deposition rate [76] and the pore fraction [13]. The resulting deposition rate was around 4±1 $\mu m\ min^{-1}$ during experiments with substrate rotation. It was higher (~10±2 $\mu m\ min^{-1}$) when the substrate was stationary. The substrate temperature was monitored and maintained at 1000±20 °C during deposition using a thermocouple placed very close to the substrate. Similar deposition parameters were used for all the experiments in this work.

For the bilayer deposition, 7YSZ and $Sm_2Zr_2O_7$ rods were placed in the crucible at the same time, shown in Fig. 4-1. The electron beam can jump to the second rod after finishing the deposition of one material by the input of the position parameters in the control software.

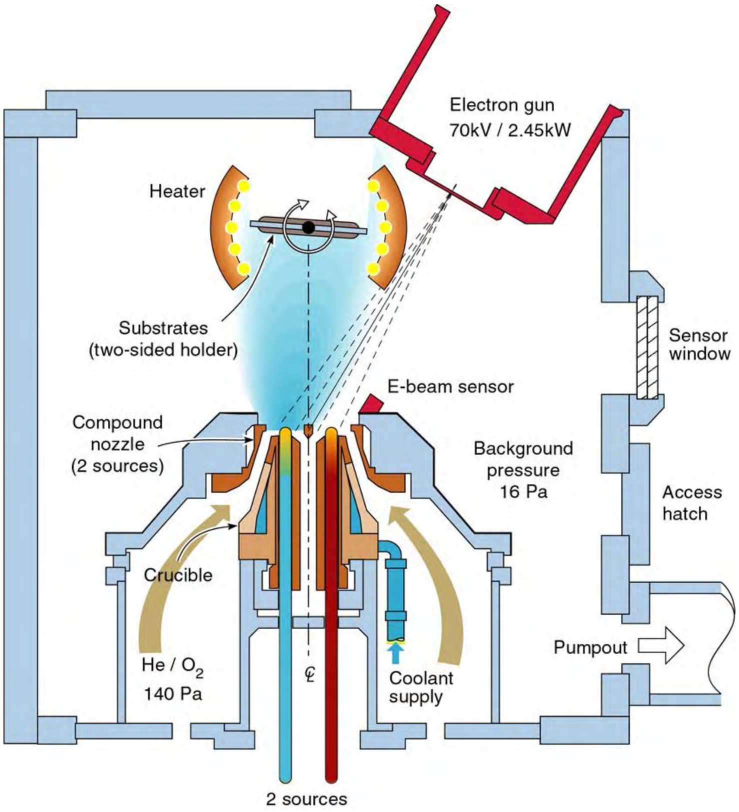

Figure 4-1. Experimental setup for bi-layer coating deposition

4.2 Substrate Material

The substrates used here consisted of a nickel-based Hastelloy-X superalloy base (Ni-22Cr-18Fe-9Mo-1.5Co-0.6W-0.1C-1*Mn-1*Si-0.008*B (in weight percent, *Maximum) and a NiCoCrAlY bond coat layer. It is not well documented about its cycling behavior of this bond coat on the Hastelloy-X superalloy. These substrates were kindly provided by GE Aviation (Evendale, OH). The Hastelloy-X buttons have dimensions of 25.4 mm in diameter and 3.175 mm in thickness. Prior to the deposition, these coupons were coated with a 100-200 μm thick Ni-22Co-20Cr-10Al-0.5Y (in weight percent) alloy using EB-PVD. Recently studies in the thermal cycling experiments have shown that the surface roughness of substrates has an important effect on the life time. Therefore, the effect of different surface processing techniques on the cycling performance will be discussed in the subsequent chapters. Here, these substrate coupons were processed with two kinds of surface treatment: hand polishing and grit blasting. In this work, the coupons were grit blasted with medium (#220) grits at the pressure of 30-40 psi. Other coupons were ground using up to #1200 grit paper and followed by polishing with 3 μm and 1 μm diamond suspensions. Subsequently, these surface-prepared substrates were ultrasonic cleaned with acetone and then rinsed with de-ionized water.

The surface roughness was measured by Veeco Dektak 6M stylus surface profilometer at DVTI. A roughness profile for both surfaces is shown in Fig. 4-2. Roughness is characterized by the root mean square (RMS) roughness parameter defined as

$$RMS = \sqrt{\frac{1}{N}\sum_{i=1}^{N} Z_i^2} \qquad (4\text{-}1)$$

where N is the number of data points along the interface and Z_i is the current coordinate (height) of the coating surface relative to the mid-section. The RMS values of both polished and grit-blasted bond coat surfaces are around 0.02 μm and 2.6 μm, respectively.

The surface morphology of grit-blasted and polished bond coat is shown in Fig. 4-3. The grit-blasted bond coat has a very rough surface with craters, sharp edges and impurities caused by sand grit. The mean amplitudes of the surface roughness are around and for grit-blasted and polished bond coats, respectively. Fig. 4-4 is the cross-sectional backscattered image showing the microstructure of the bond coat. Before thermal treatment, the bond coat typically has a three-phase microstructure consisting of β(NiAl) and γ(Ni) with a minor amount of α(Cr) precipitates [85]. The polished bond coat surface presented a smooth surface except some small pores on the surface, Fig. 4-3(d). The chemical composition of these two processed bond coats was also determined by EDS, in Table 4-1. It is found that the grit-blasted bond coat has impurity elements of Si, Mg and Ca which may come from the sand grit.

Table 4-1. Bond coat composition

Bond Coat Elements*	Ni	Co	Cr	Al	Y
Fraction (wt.%)	47.3	20.3	21.0	11.0	0.4

*Si, Mg and Ca have been detected in the grit-blasted bond coat surface with the weight percentage of 0.5%, 0.2% and 0.2%, respectively, while these elements are undetectable in the polished surface.

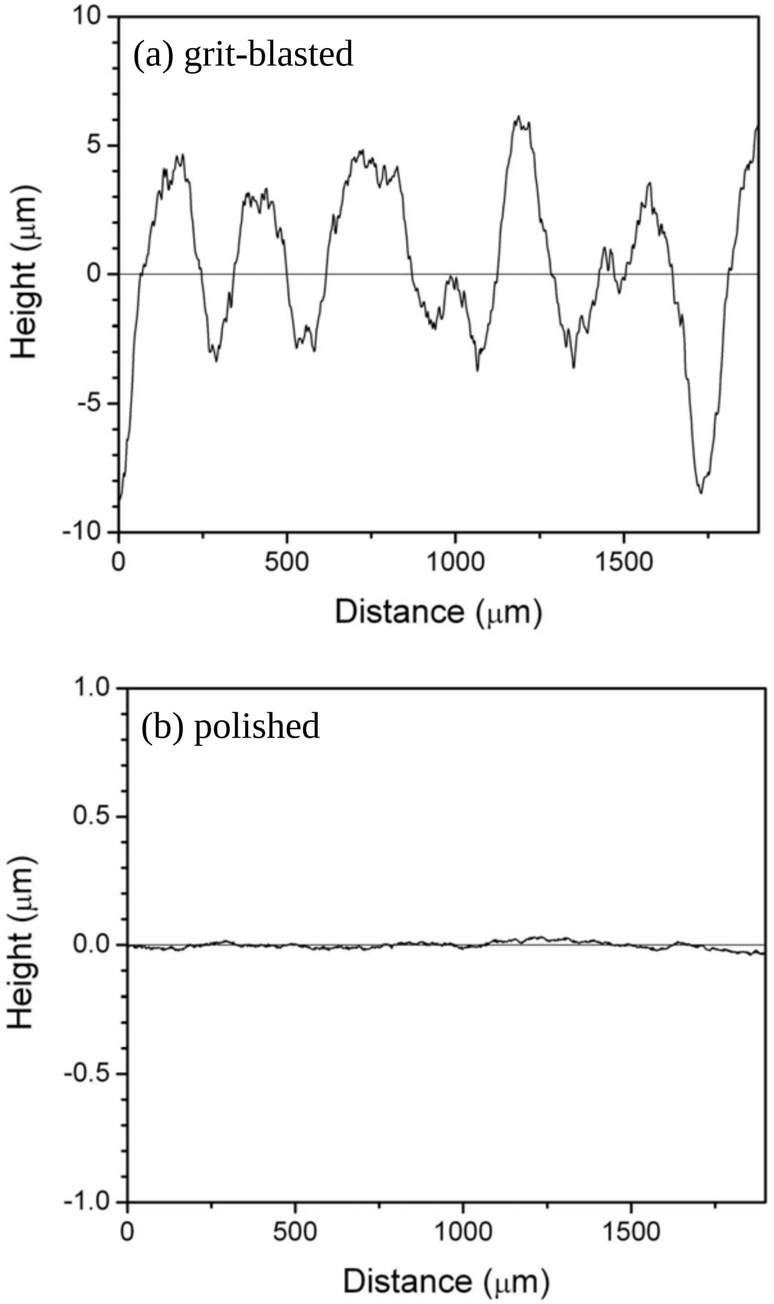

Figure 4-2. Surface roughness profiles of the bond coat surfaces for (a) grit-blasted and (b) polished. Note the difference in scale.

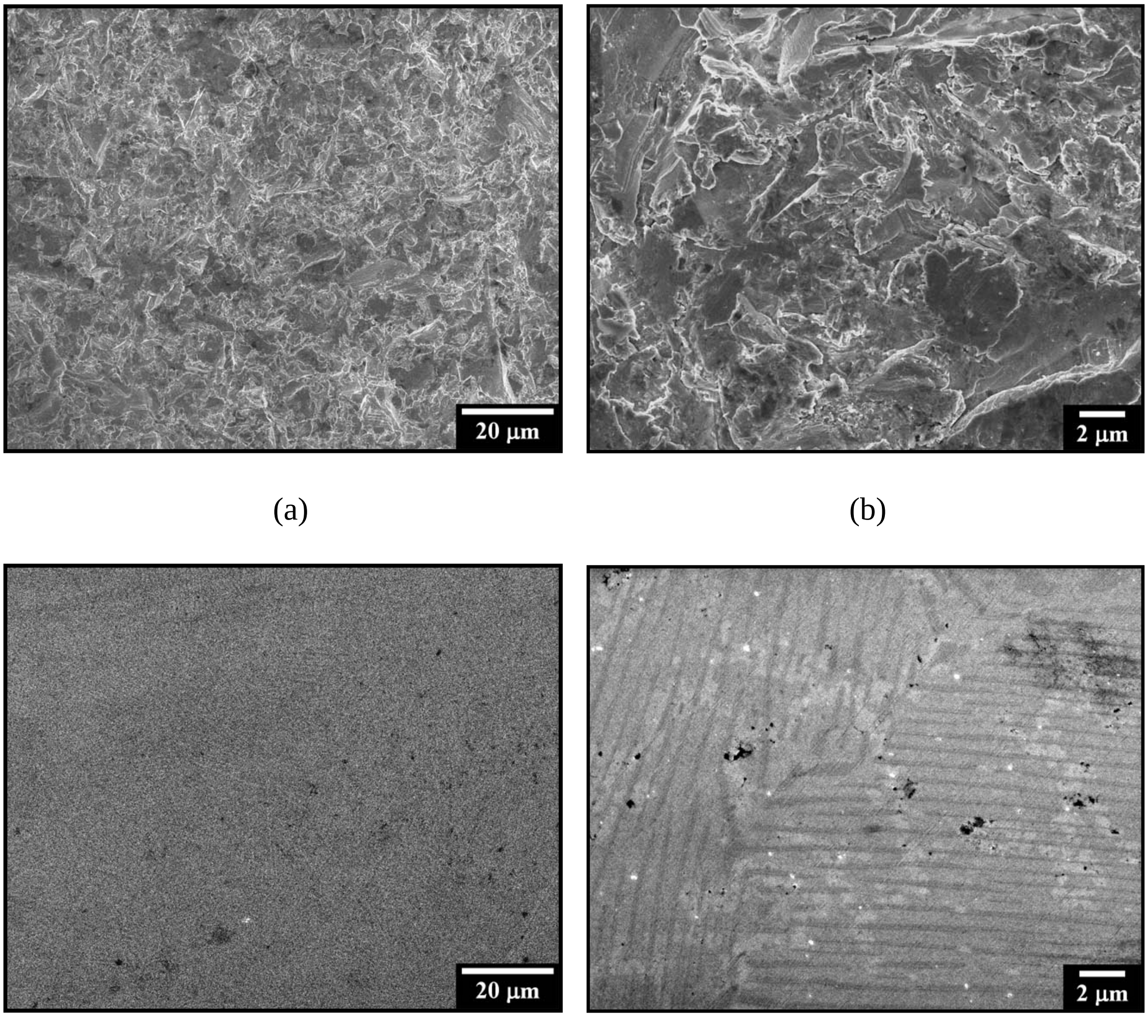

(a) (b)

(c) (d)

Figure 4-3. Surface morphology of bond coat with grit-blasting (a, b) and polishing (c, d)

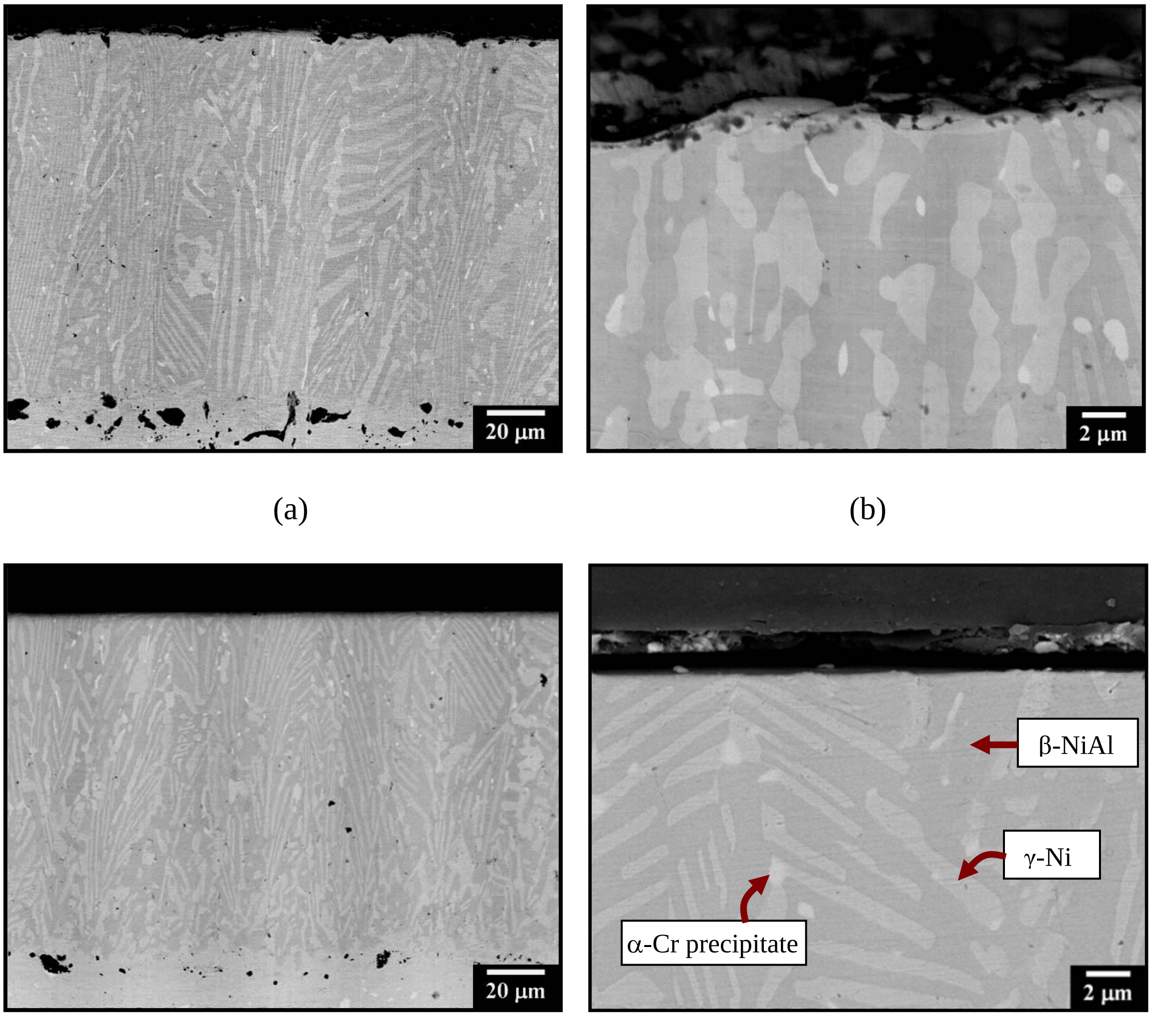

(a) (b)

(c) (d)

Figure 4-4. Cross-section view of grit-blasted (a, b) and polished (c, d) bond coat.

4.3 Coating Characterization Methods

4.3.1 Scanning electron microscopy

A JEOL JSM 6700F scanning electron microscope (SEM) was used to characterize the coating structure and pore morphology. The JSM 6700F is field emission SEM incorporating a cold cathode field emission gun, ultra high vacuum and sophisticated digital technology for imaging. This microscope operates at accelerating voltages ranging from 0.5 to 30 kV and has a very high resolution of 1.0 nm at 15 kV and 2.2 nm at 1 kV. The microscope has secondary electron imaging (SEI) capability utilizing both through-the-lens and in-chamber secondary electron detectors and backscattered electron imaging (BEI) with both compositional and topographical imaging contrast. In addition, it is capable of composition analysis with energy-dispersive X-ray spectroscopy (EDXS) detector.

4.3.2 X-ray diffraction

X-ray diffraction (XRD) was used to determine crystallographic structure of the phases present and to determine if any preferred orientation (or texture) was present in the coating. The texture of the coatings was deduced from X-ray diffraction (XRD) patterns recorded using a XDS 2000 powder diffractometer (Scintag Inc., USA) using CuK_α radiation. The scan angle range 2θ was varied from 10° to 90°, using a step size of 0.02°. A more complete texture analysis (pole figure) was conducted using an X1 Texture instrument (Scintag Inc., USA). The tilt angle α, was varied from 0 to 90° and the sample was rotated 360° around the center. The step size for both rotation and tilting was 5°. Pole figures were plotted with their East-West axis oriented parallel to the rotation axis.

4.4 Thermal Conductivity

Thermal conductivities were measured at 300 K using a laser based, harmonic heating method [135] at the University of California, Santa Barbara. A sketch of the method used here is shown in Fig. 4-5. The principal components include a CO_2 laser, an acoustic-optic modulator, focusing lens and light tunnel. The CO_2 laser operates at a wavelength of 10.6 μm, is used to heat the coating. The modulator attenuates the laser beam and is controlled by a function generator to create harmonic heating. The measurement temperature is controlled with a heated stage connected to a temperature controller. An infrared photovoltaic indium antimonide detector is used to collect thermal emission from the sample. Both the laser signal and the detector signal are measured by a high-speed digitizer and the phase of thermal emission is analyzed to determine coating properties. The resulting temperature field in the sample was interrogated through its thermal time dependent emission. The phase of the thermal emission carries information related to the coating's thermal properties, its thickness and the thermal contrast between the substrate and the coating. A model [135] can be used to relate the phase difference between the laser and the thermal emission and coating properties from which the thermal conductivity can be deduced. The factors that influence the experimental accuracy involved in measurements are temperature and frequency dependence of measurement system as well as the coating thickness measurement. The uncertainties in thermal conductivity associated with this approach were estimated to be less than 10%.

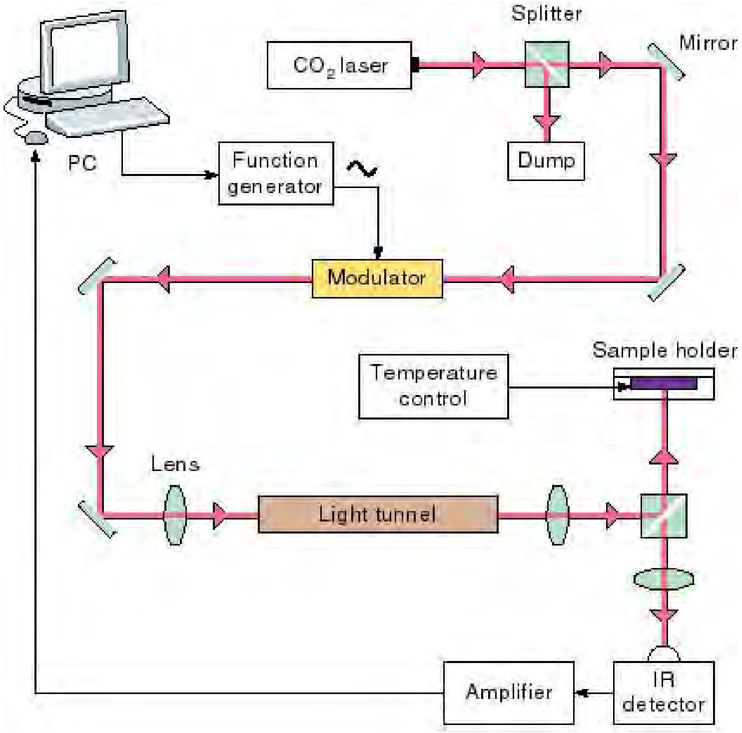

Figure 4-5. Experimental set-up for the measurement of the thermal conductivity [135]

4.5 Density Measurements

Due to the often complex pore geometries present in TBC films, direct measurement has been found to be the most useful approach for determining the coating density. The coating density (ρ) can be obtained by a basic equation:

$$\rho = \frac{W_1 - W_2}{V} \qquad (4\text{-}2)$$

Here, W_1 and W_2 are the weight of the substrate with or without the coating, respectively. V is the coating volume.

The coatings deposited by EB-DVD have in some cases a gradual change in the coating thickness over the area of the substrate. Therefore, it is difficult to determine the true value of the coating thickness. The density may also be varied with the position on the substrate. As a result, the density was measured only for a small area on the substrate for this work.

First of all, a small piece of sample (5mm x 5mm square) was cut from the coupon. Each side of the sample was polished up to #800 grit paper to get a smooth cross section from which the sample dimensions could be determined. The sample was then ultrasonic cleaned with acetone and dried in an oven at 150 °C for a couple of hours to remove the moisture in the coating. At this time, the initial weight of the sample (W_0) was measured using a precision microbalance (Denver Instruments, Arvada, CO). The coating thickness would be observed in the microscope. Next, the sample was attached to the polishing stage with melted crystal bond and then gently polished. During this process, the coating was frequently checked in the microscope. The polishing would be stopped until the coating was almost gone. Finally, the sample was cleaned with acetone again and dried in an oven before measuring the new weight (W_1). The volume (V) of the removed coating could be calculated from the known dimensions. The factors that affect the measurement accuracy mainly come from the coating thickness measurement, the sample dimension measurement and the sample weight measurement. The experiment error is estimated to be less than ± 10%. The greatest errors are expected for the thinnest samples.

4.6 Elastic Modulus Estimates

The measurements of the elastic modulus were performed in Prof. Matthew Begley's group at UVA. Young's modulus is one of the most important properties for TBCs. It has been reported that the nano-indentation method is useful for measuring Young's modulus of thin crystalline films, amorphous films, coatings, glasses and semiconductors [136, 137]. A MTS Instruments nanoindenter used in this work was equipped with a dynamic contact module (DCM) indenter and a triangular Berkovich diamond tip. The shallow cone angle ensured that the indenter contacted a larger lateral region. The indenter load (P) and displacement (h) were continuously and simultaneously recorded during loading and unloading in the indentation process.

A typical load/displacement curve is shown in Fig. 4-6. A simple linear fit through the upper 1/3 of the unloading data intersects the depth axis at h_t. The stiffness, S, is given by the slope of this line. The contact depth, h_c, is then calculated as:

$$h_c = h_m - \varepsilon (h_m - h_t) \quad (4\text{-}3)$$

Where ε depends on the investigated material, h_m is the indenter displacement at peak load. The reduced elastic modulus, E_r, was evaluated from the load displacement data using the following Oliver and Pharr method [138].

$$E_r = \frac{\sqrt{\pi}}{2} \frac{S}{\sqrt{A}} \qquad (4\text{-}4)$$

$$S = \frac{dP}{dh} \qquad (4\text{-}5)$$

Here, A is the projected area of the elastic contact. The area-depth function of a Berkovich indenter tip geometry is typically:

$$A(h_c) = 24.5h_c^2 + C_1h_c^1 + C_2h_c^{1/2} + C_3h_c^{1/4} + ... + C_8h_c^{1/128} \qquad (4\text{-}6)$$

where C_i are constants from curve fitting.

Finally the Young's modulus of the coatings can be derived from the reduced modulus by the following equation:

$$\frac{1}{E_r} = \frac{1-\nu^2}{E} + \frac{1-\nu_i^2}{E_i} \qquad (4\text{-}7)$$

where E and ν are Young's modulus and Poisson's ratio for the specimen and E_i and ν_i are the same parameters for the indenter. Each of the results presented later represent the average of 15-20 indentation measurements, with error bars indicating deviation in the measurement.

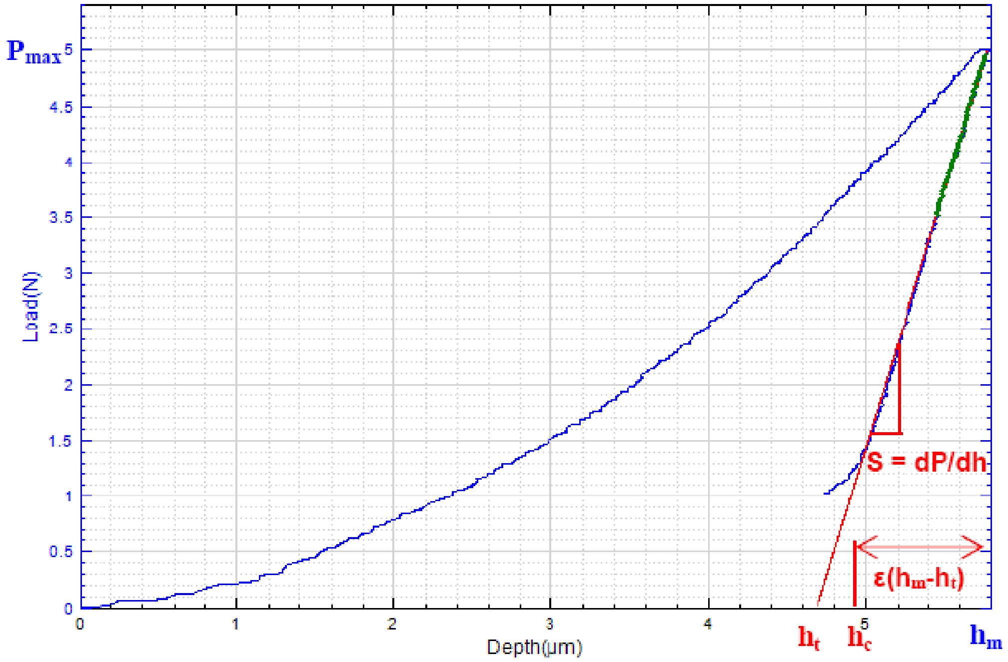

Figure 4-6. A schematic representation of load versus indentation displacement data for an indentation experiment.

4.7 Thermal Cycling

The thermal cycling tests were performed in a top-loading furnace (Fig. 4-6) made by Applied Test Systems, Inc. (Butler, PA). Each cycle consisted of 1-hr holding at 1100 °C and 10-min cooling in forced flowing laboratory air to ~50 °C. The specimens were examined visually every 20 cycles. To better understand the growth of TGO, some samples were taken out for observation and analysis before failure. Failure of the specimens was defined to have occurred when a measurable amount of the TBC had separated from the surface. All spalled specimens were examined using scanning electron microscopy.

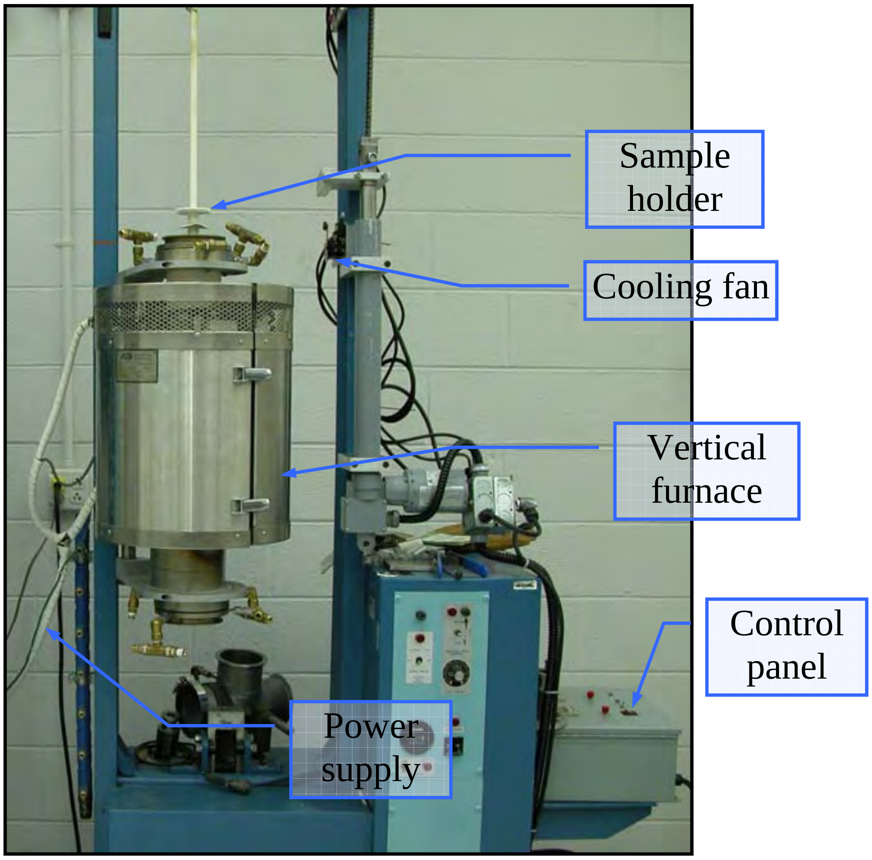

Figure 4-7. Cycling test

Chapter 5

Morphology, Texture and Thermal Conductivity of DVD YSZ

5.1 Overview

A directed vapor deposition process has been used to deposit yttria stabilized zirconia coatings with different substrate rotation rates. The coatings were found to have a variety of morphologies which were dependent upon the processing conditions. The morphologies of DVD YSZ coatings are compared with those deposited using conventional EB-PVD approach. The chapter focuses upon the relationship between pore morphology, thermal conductivity and substrate rotation under high growth pressure conditions. The morphology, texture and pore volume fraction of YSZ films deposited at different rotation rates is systematically investigated and linked to the thermal conductivity and density of the coatings.

5.2 Deposition Conditions

7YSZ coatings were deposited on the Hastelloy-X superalloy coupons with 100-200 μm NiCoCrAlY bond coat at the rotation rate of 0, 0.5, 1, 6, 12, 20 and 30 rpm. The upstream pressure (P_u) is 140 Pa and the downstream pressure (or chamber pressure, P_o) is 16 Pa.

The evaporated flux was entrained in a 10.0 standard litre per minute (slm) helium- 1.0 slm oxygen gas flow. The deposition temperature was set at 1000 °C. The detailed methodology was given in Section 4.1.

5.3 Coating Morphology Characterization

The surface morphology of coatings deposited at rotation rates of 0, 0.5, 1.0, 12, 20 and 30 rpm are shown in Fig. 5-1. There is a distinct difference between the surface topologies of the stationary and the rotated samples. Under stationary deposition, the coating surface is dominated by triangular (three-sided) columns whose tips consisted of three triangular facets, shown in Fig. 5-1(a). This surface morphology is similar to that reported for coatings made by conventional EB-PVD techniques without rotation [79]. The rotated sample surfaces were covered by four-sided square columns that were terminated by four facets, Fig. 5-1(b)-(f). The sides of these pyramids are consistent with {111} facets bounding the tips of <100> oriented growth columns, which would be consistent with EB-PVD observations of coatings grown at 1000 °C with rotation [62, 79]. Increases of the rotation rate reduced the column diameter. However, this trend slowly decreased and the highest rotation rates resulted in coarser columns consisting of several smaller columns each capped by small pyramids with square facets. The growth columns appeared most closely packed together in the sample deposited under stationary conditions.

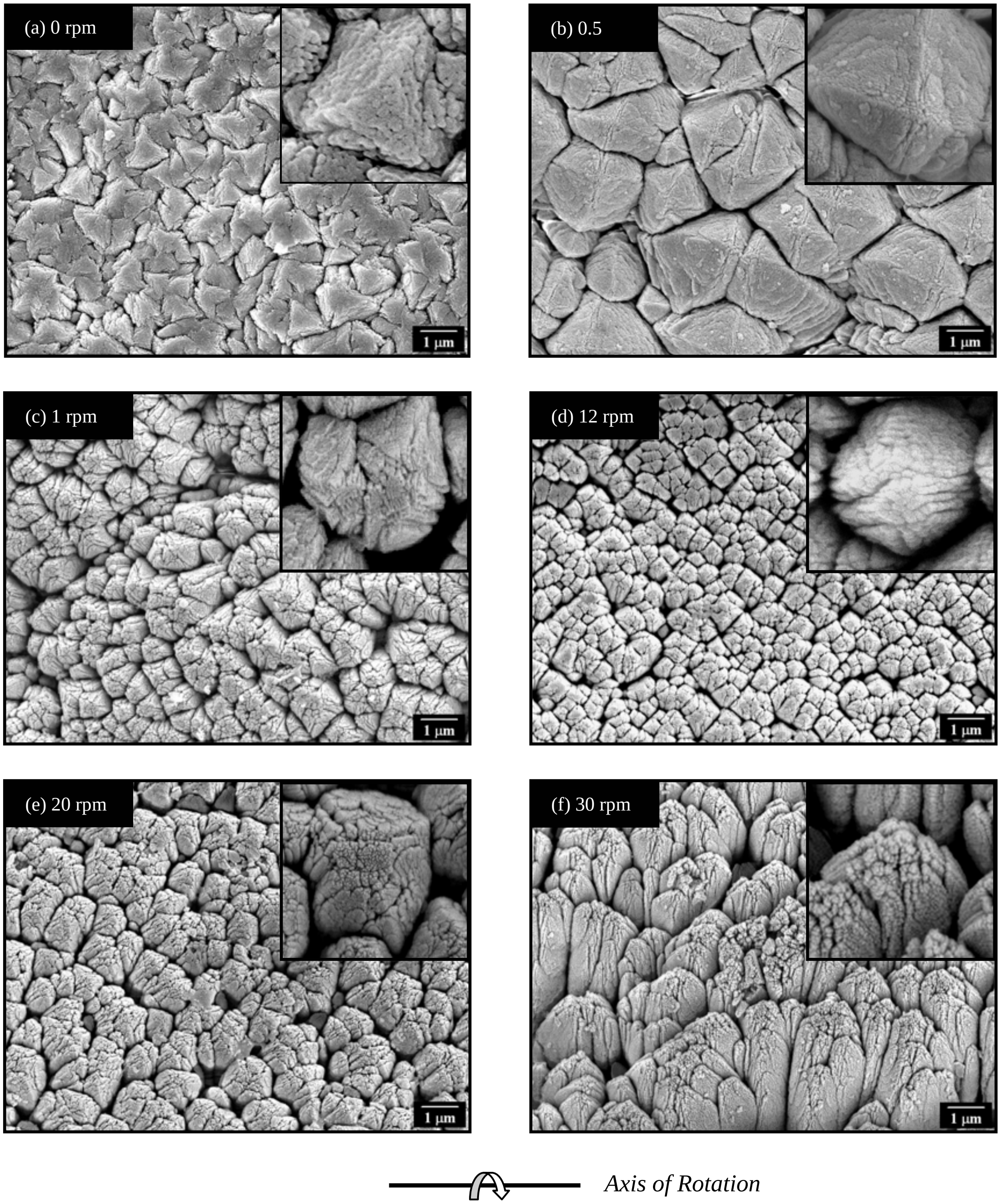

Figure 5-1. Surface morphology of the stationary (a) and rotated (b-f) samples all deposited at 1000 °C

Fig. 5-2 shows cross-sectional views of coating fracture surfaces. The growth direction was vertically upwards in each figure. The cross-sectional morphology of the coatings was very sensitive to the rotation rate. Fig. 5-2(a) shows the structure of a coating deposited onto a stationary substrate whose surface was perpendicular to the vapor plume axis. The growth columns are about 1.5 μm in width, do not change in width with coating depth, and exhibit little intercolumnar porosity. At low rotation rates of 0.5 and 1 rpm, Fig. 5-2 (b) and (c), the prominent feature is the wavy columnar structure (C-shape), which is caused by changes of the vapor flux incidence angle to the substrate. Each wave corresponds to one cycle of substrate rotation. Altering the rotation rate affects both the wavelength and amplitude of the wavy structure. The wavelength of the coating is ~10 μm per cycle at 0.5 rpm and ~4 μm per cycle at 1 rpm. The amplitudes are 2.5 μm and 0.5 μm, respectively. At higher rotation rates of 12, 20 and 30 rpm, the wavelength became so small and hardly seen in the coatings. Thus the wavy structure disappeared and relatively straight column grains were formed in the coating.

The column diameters measured from Fig. 5-2(a)-(f) are 1.5, 7, 4, 0.5, 0.7 and 0.85 μm for 0, 0.5. 1.0, 12, 20 and 30 rpm samples, respectively. The width of the primary growth columns didn’t vary significantly through the coating thickness. The column growth direction was almost parallel to the substrate surface normal. Two types of pores were present in all samples. Type I pores (the gaps between the primary growth columns [63, 74]) can be observed in the micrographs shown in Fig. 5-2. These extend from the bond coat/ceramic interface to the top of the ceramic layer. Those in the slowly rotated samples were not straight, forming a C-shape pattern. Fig. 5-3 shows a much finer, Type II pore morphology present within the growth columns. These Type II pores were feathery structure at the sides of the growth columns. They were oriented perpendicular to the direction of the primary columns growth. Coatings grown with rotation have columns with a more “feathery” structure than those grown under stationary conditions. Type III, spheroidal nanopores were present within the center of growth columns of the stationary and slowly rotated coatings, hardly seen in Fig. 5-3. In the high magnification of polished cross-section view of Fig. 5-4, the Type I, II and III pores were labeled in the image.

The micrographs suggest that the rotated samples have a lower density than the stationary sample. The measured density results support this, see Table 5-1. The stationary sample had the highest density 4.5 g/cm^3, but this is significantly below the theoretical value of 6.0 g/cm^3 for fully dense 7YSZ [43]. The lowest rotation rate sample had a density of 3.38 g/cm^3. The pore volume fraction therefore increased from 26% in the stationary condition to 44% for that rotated at 0.5 rpm. As the rotation rate was increased, the average dwell time for one rotation cycle decreased and this was correlated with an increase of coating density. As shown in Fig. 5-5, samples rotated at 1.0, 12, 20 and 30 rpm had densities of 3.49, 3.58, 3.86 and 4.10 g/cm^3, respectively. These pore fraction trends are in quantitative agreement with kinetic Monte Carlo simulations of deposition onto periodically inclined substrates [139].

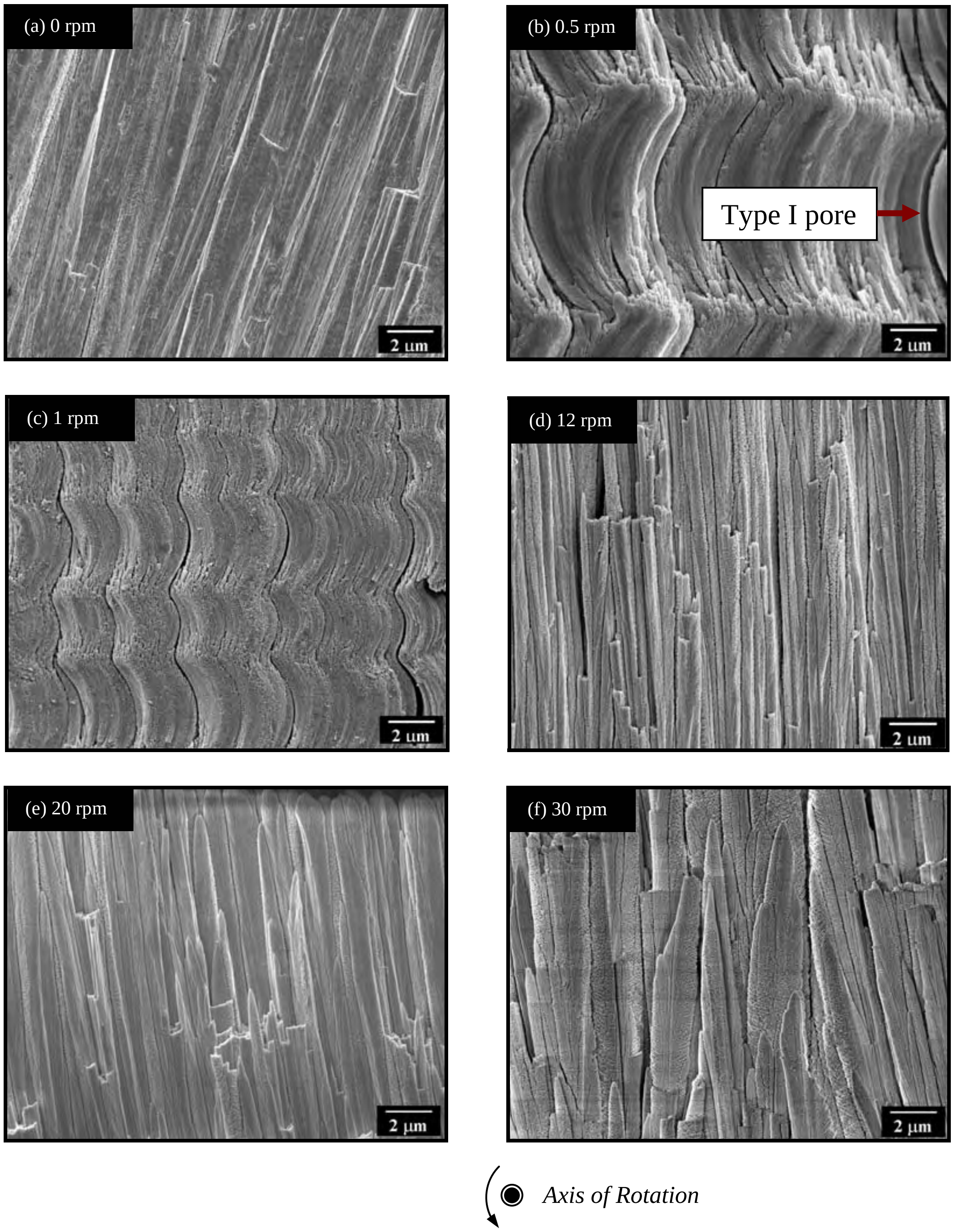

Figure 5-2. Cross-sectional morphology of the samples deposited under stationary and rotated conditions at 1000 °C, Type I pores shown in the image

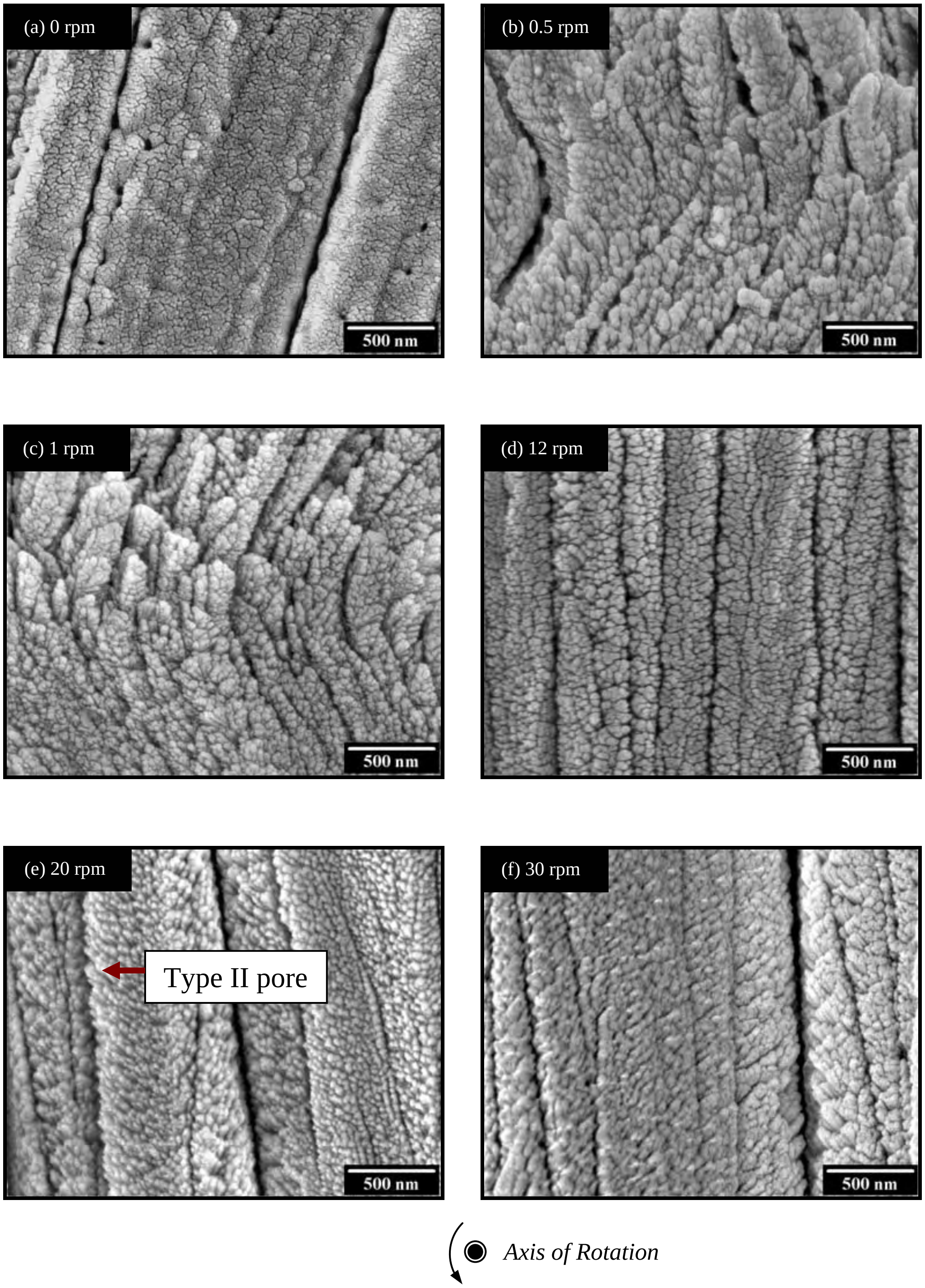

Figure 5-3. Micrographs of samples coated under stationary (a) and rotated (b-f) conditions. Type II pores shown in the microstructure

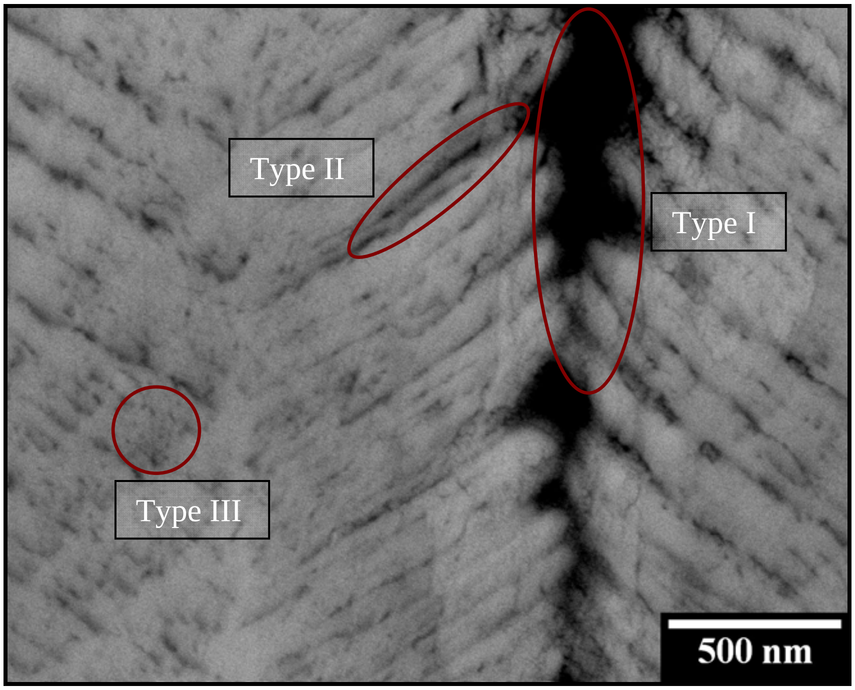

Figure 5-4. Polished cross-section view of YSZ coatings showing the inter- and intra-columnar pores (Type I, II and III)

Table 5-1. Deposition parameters and coating property of the samples

Rotation rate (rpm)	Deposition rate (μm/min)	Column diameter (μm)	Density (g/cm^3)	Pore fraction
0	12	1.5	4.50	25%
0.5	5	7	3.38	44%
1.0	3	4	3.49	42%
6	4	1	3.62	40%
12	4	0.5	3.58	40%
20	3	0.7	3.86	36%
30	3	0.8	4.10	32%

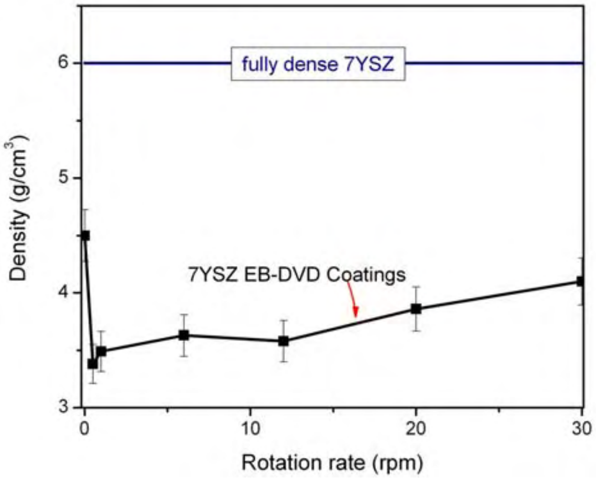

Figure 5-5. The coating density as a function of rotation rate

5.4 Texture Analysis

X-ray diffraction patterns for coatings deposited under the different rotation rates are shown in Fig. 5-6. The diffraction pattern for the stationary substrate coating has very strong {111} type peaks. No {200} peaks were evident in the X-ray pattern of this sample. That implies that the coating was constructed from growth columns whose (111) planes were coplanar with the substrate surface. The growth columns therefore approximately grew in the <111> direction (Note that (111) and [111] are not perpendicular in t-ZrO_2). The observation of three triangular planes terminating the growth columns is consistent with the columns being capped by three {100} type facets.

As the rotation rate was increased, new peaks appeared in the diffraction pattern and the relative intensity of these new peaks rapidly increased. For the lowest rotation rate (0.5 rpm) sample, the crystallographic features of the stationary sample were still evident in the diffraction pattern, Fig. 5-6(b). However, at higher rotation rates, Fig. 5-6(c)-(f), {100} type peaks began to dominate the diffraction pattern and all other peaks gradually disappeared. The growth columns of the rapidly rotated coatings therefore had a large fraction of {100} type planes aligned parallel to the substrate's surface. This is consistent with a <100> type column growth direction and the observation of four triangular facets capping the growth columns is consistent with these here being {111} type planes. Highly textured coatings are therefore created using the EB-DVD technique and either <111> or <100> texture can be selected by choice of the rotation rate at substrate temperature of 1000 °C.

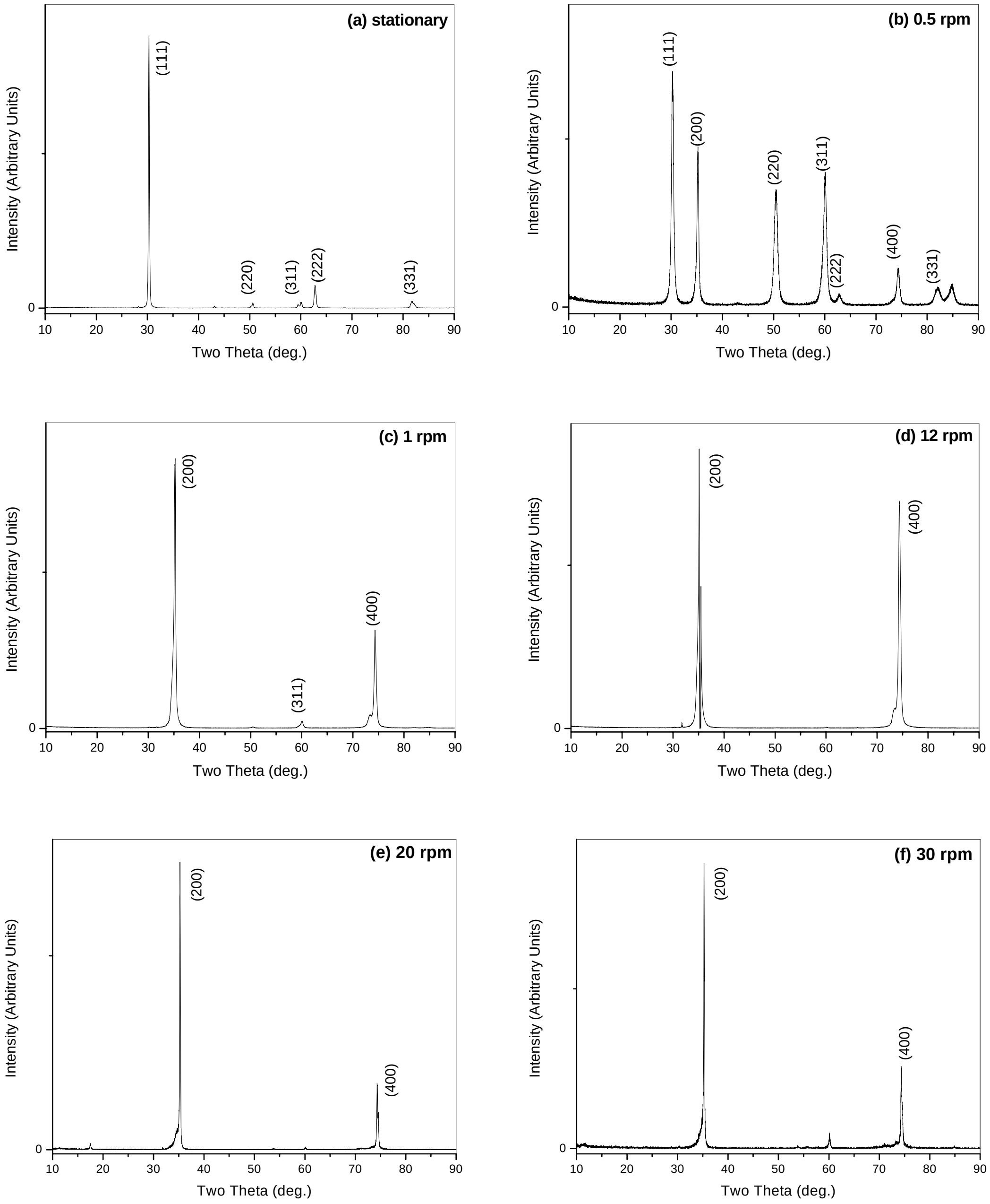

Figure 5-6. XRD patterns of 7YSZ coatings deposited at different rotation rates

Pole figure analyses were also performed on the samples to determine in-plane orientation relationships between the growth columns. Fig. 5-7(a) shows a strong {111} peak located at the center of the pole figure, confirming a preferred <111> through thickness column orientation. The off-axis reflections of the {220} pole figure Fig. 5-7(a), shows a ring pattern of high intensity distributed around the center of the figure. This indicates that no preferred in-plane orientation of the columns developed under stationary deposition. Pole figures for the 0.5 rpm sample are shown in Fig. 5-7(b). A region with strong {200} plane intensity was again located near the center of the pole figure indicating that the majority of the surface planes are parallel to the (100) plane. A distorted ring pattern was evident in the {220} pole figure, again indicating no preferred in-plane orientation. However, as the rotation rate was further increased, Fig. 5-7(c)-(f), a high intensity {100} peak was evident at the center of the {200} pole figure and the off-axis {220} pole figures showed a four-fold symmetry structure around the <100> direction. These observations are indicative of both a well-developed in-plane texture as well as through thickness crystallographic alignment of the growth columns.

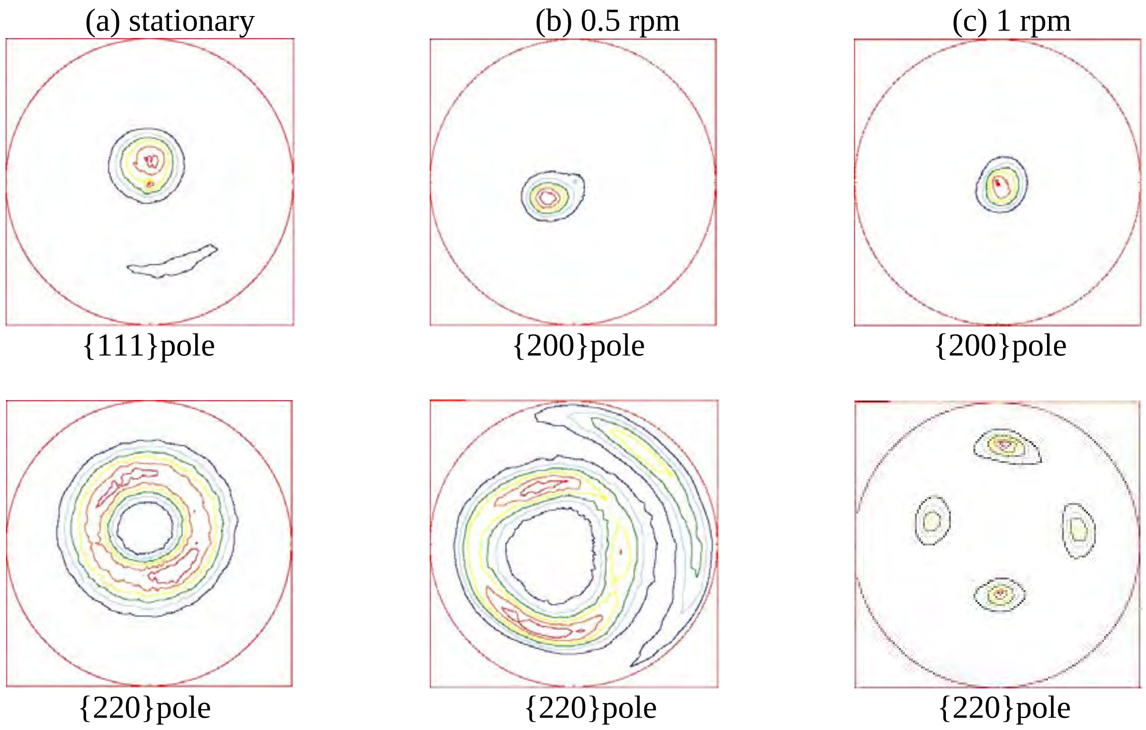

(a) stationary

(b) 0.5 rpm

(c) 1 rpm

{111}pole

{200}pole

{200}pole

{220}pole

{220}pole

{220}pole

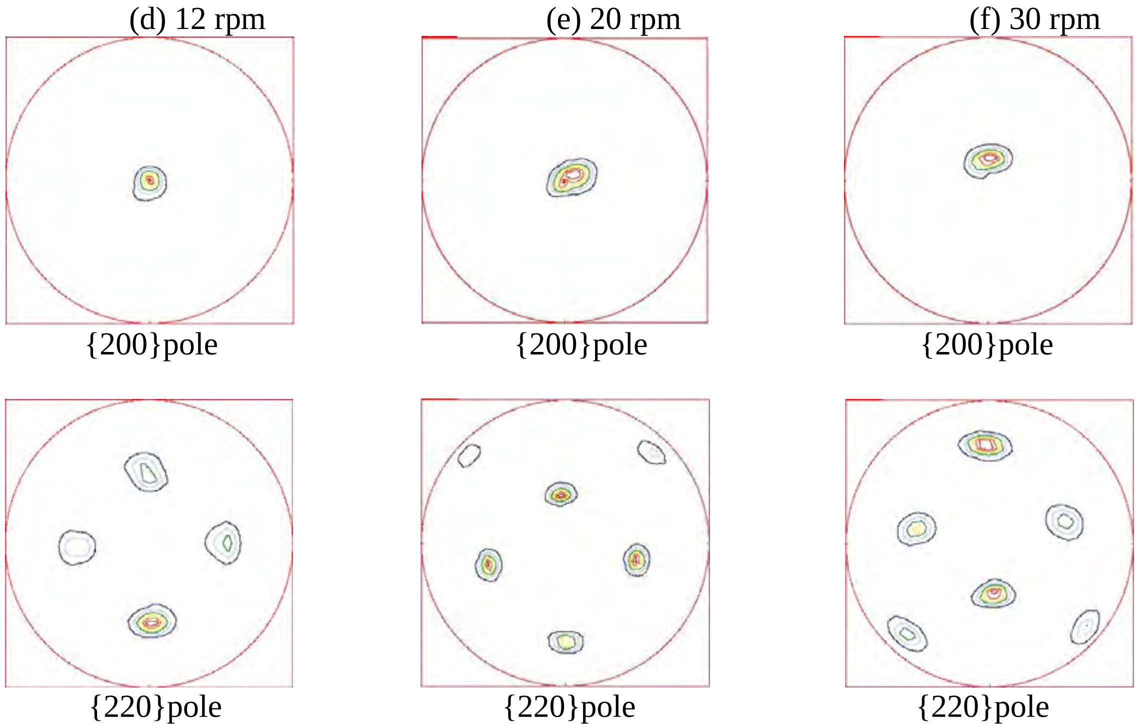

(d) 12 rpm

(e) 20 rpm

(f) 30 rpm

{200}pole

{200}pole

{200}pole

{220}pole

{220}pole

{220}pole

Figure 5-7. Pole figures of the samples at different rotation rates

5.5 Thermal Conductivity

The effect of rotation rate upon the thermal conductivity of the coatings is shown in Fig. 5-8. The stationary sample had the highest thermal conductivity of 1.55 W/mK. This is at the low end of the range reported for conventional EB-PVD samples (1.5-1.9 W/mK). Both growth approaches result in coatings with a much lower thermal conductivity than fully dense 7YSZ (3.0 W/mK at 300 K). The slowly rotated samples had a much lower thermal conductivity than their stationary counterparts (0.8 versus 1.55 W/mK). This very low thermal conductivity is identical to that reported for zigzag structures grown using EB-DVD techniques [74]. As the rotation rates were increased from 0.5 to 30 rpm, the measured thermal conductivities slowly increased from 0.8 to 1.06 W/mK. This trend in thermal conductivity was similar to the variation in coating density, Fig. 5-5. Fig. 5-9 shows the thermal conductivity as a function of the pore fraction. The largest pore fraction coating corresponded with the lowest thermal conductivity. We note that EB-PVD coatings usually have lower pore volume fractions than those reported here [140], and this additional porosity presumably accounts in part for their higher thermal conductivity.

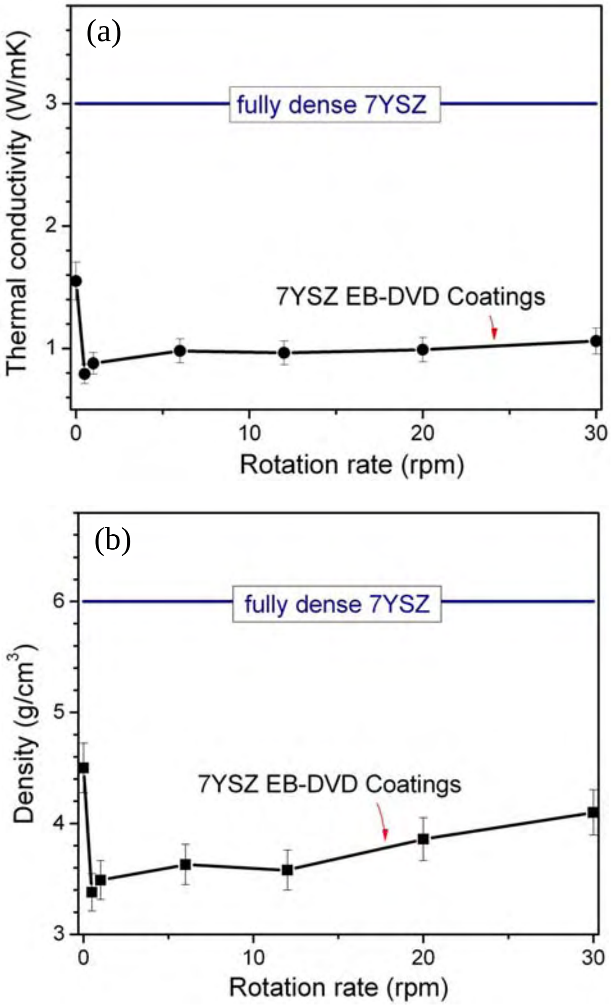

Figure 5-8. The effect of rotation rate on the (a) thermal conductivity and (b) density both measured at 300 K

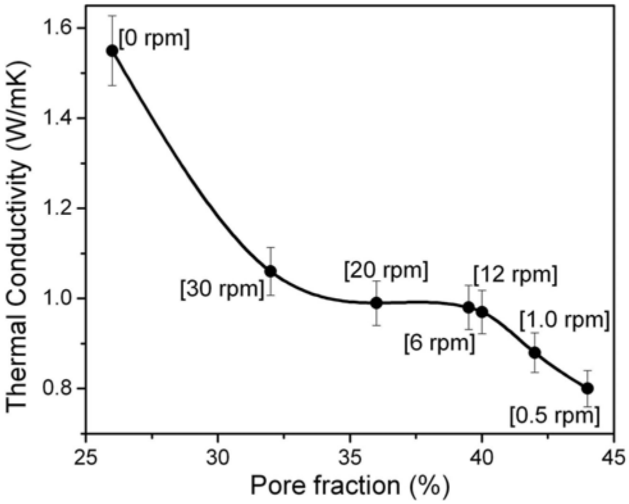

Figure 5-9. Thermal conductivity as a function of pore fraction at 300 K

5.6 Discussion

5.6.1 Pore morphology

Directed vapor deposition processes create a flux with a broader angle of incidence distribution (under stationary substrate conditions) than that associated with EB-PVD deposition (Hass et al.) [141]. This has been shown both experimentally [13] and by kinetic Monte Carlo modeling [139] to enhance the significance of shadowing resulting in coatings with higher pore fractions. When heat is propagated through coatings at low temperatures, only phonon conduction contributes to the heat transport. Phonons are strongly scattered at pore surfaces and conduction across ellipsoidal pores with high aspect ratios introduces a high thermal resistance. The thermal conductivity is therefore strongly dependent on the volume fraction, shape and orientation of pores [142, 143]. Models of the thermal transport in porous 7YSZ coating [63, 144] have shown that this lowers the thermal conductivity of EB-DVD coatings below their EB-PVD counterparts. Substrate rotation at low rotation rates further increases the pore fraction. It also results in wavy columns that are in some respects analogous to the zigzag structures created by alternating the inclination of a substrate [74]. The high porosity level and its favorable orientation for inhibiting heat flow results in slowly rotated coatings having thermal conductivities in the 0.8 W/mK range, which is comparable to that of zigzag EB-DVD and APS coatings.

At low rotation rates, Type I pores are elongated and bent perpendicular to the growth direction making them longer than those in the stationary sample. The width of the pores is also greater. In the slowly rotated samples with wavy columns, the conduction distance is increased contributing to a significant impedance to the heat flow. A recent analytical study of heat conduction across the zigzag structures [63], indicated that inclined Type I pores were highly effective at disrupting through thickness thermal transport. These models suggest that the low thermal conductivity of the C-shaped microstructures is dominated by continuous Type I pores even though their pore fraction is low; Type II and III pores in slowly rotated samples may introduce a relatively smaller effect upon the overall conductivity.

Increasing the rate of rotation significantly reduces the total pore fraction, Fig. 5-5, but the thermal conductivity is restored much more slowly, shown in Fig. 5-8. Fig. 5-9 links the thermal conductivity to the pore volume fraction and indicates that in the 30-40% pore fraction range, the thermal conductivity is a weak function of pore fraction. The rapidly rotated EB-DVD coatings explored here therefore retain a much lower thermal conductivity than their EB-PVD counterparts. The weak dependence of thermal conductivity upon rotation rate in the 5-30 rpm range appears to be the result of a change in the Type III pore morphology with increase in rotation rate.

At higher rotation rate, the Type I pores are vertically aligned and were not greatly affected by the substrate rotation. It is therefore expected that the contribution of these pores to the change in thermal resistance is small. The retention of a low thermal conductivity in the more rapidly rotated samples must therefore be linked to a change in the morphology of Type II and III pores that makes them more effectively at impeding thermal flux transport. By comparing Fig. 5-3(a) and (c), it can be seen that as the rotation rate increased, the pores between feathery structures became aligned transverse to the growth columns in an orientation that would be highly effective at disrupting the flow of heat along the primary growth columns.

5.6.2 Texture

The significant changes in pore morphology that accompanied an increase in rotation rate were also correlated with a change in column growth direction from <111> to <001>. Similar texture changes have been reported for EB-PVD coatings [79]. Schultz, Terry and Levi [62] have developed a competitive facet growth (STL) model to account for these EB-PVD observations. Briefly, during deposition of a thick film, for which growth is characterized by the evolutionary selection process, the structure will be dominated by grains through the thickness of the film having nearly the same “fast growth” axis, resulting in a strong fiber texture to the film.

Stationary samples have the <111> preferred growth direction with growth columns capped by three triangular shaped {100} facets, Fig. 5-10(a). Under constrained surface diffusion conditions, stable columnar growth requires that each of the facets of a column tip receive equal amounts of vapor flux. This condition is referred to as the “equal flux” requirement in the STL model [62, 65]. Unfavorable columnar morphologies which do not satisfy the equal flux condition will be screened out by evolutionary selection. Experiments [65] indicate that stationary samples with oblique vapor incidence angle

(45º) have a (two-sided) rooftop column tip morphology formed by the intersection of two {111} facets. The resulting column axis is then <110> direction. When such a rooftop ridge is parallel to the vapor incidence plane, each {111} facet can receive equal vapor fluxes and growth of such a structure satisfies the “equal flux” condition. Coatings grown with substrate rotation have a <100> column axis orientation with the columns capped by four {111} planes. This is consistent with the STL model, since opposing pairs of facets sequentially receive equal fluxes as the growth columns axis rotates from -90° to 0° and then 0° to 90°, Fig. 5-11. Each period can be likened to an equivalent oblique incidence flux. The two half periods of vapor incidence angle result in equal vapor flux for the period of exposure to a different pair of rooftop column tips bounded by {111} facets with their bisectors then in a <110> direction. Square-pyramidal facet tip columns are formed with a column axis in a <100> direction, Fig. 5-10(b).

During the growth of these columns, the formation of porosity results from flux shadowing and the Type III pore morphology reflects a complicated interplay between the actual flux that intercepts the local growth surface and the fast growth directions of the columns. Substrate rotation broadens the vapor incidence angle distribution and thus promotes the shadowing. The broader flux distribution of the EB-DVD process appears to further enhance this shadowing. The EB-DVD rotated substrate samples therefore have a high volume fraction of “feather-like” Type II pores that can be seen at the edge of columns. They are also orientated in a plane that is highly effective at disrupting thermal conduction along the column axis.

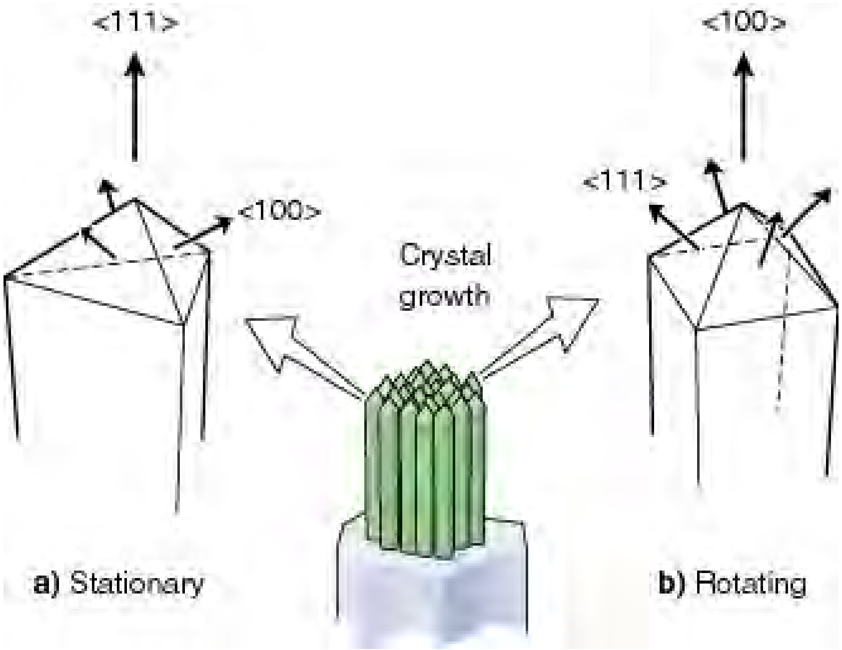

Figure 5-10. Column tip orientation during the column growth

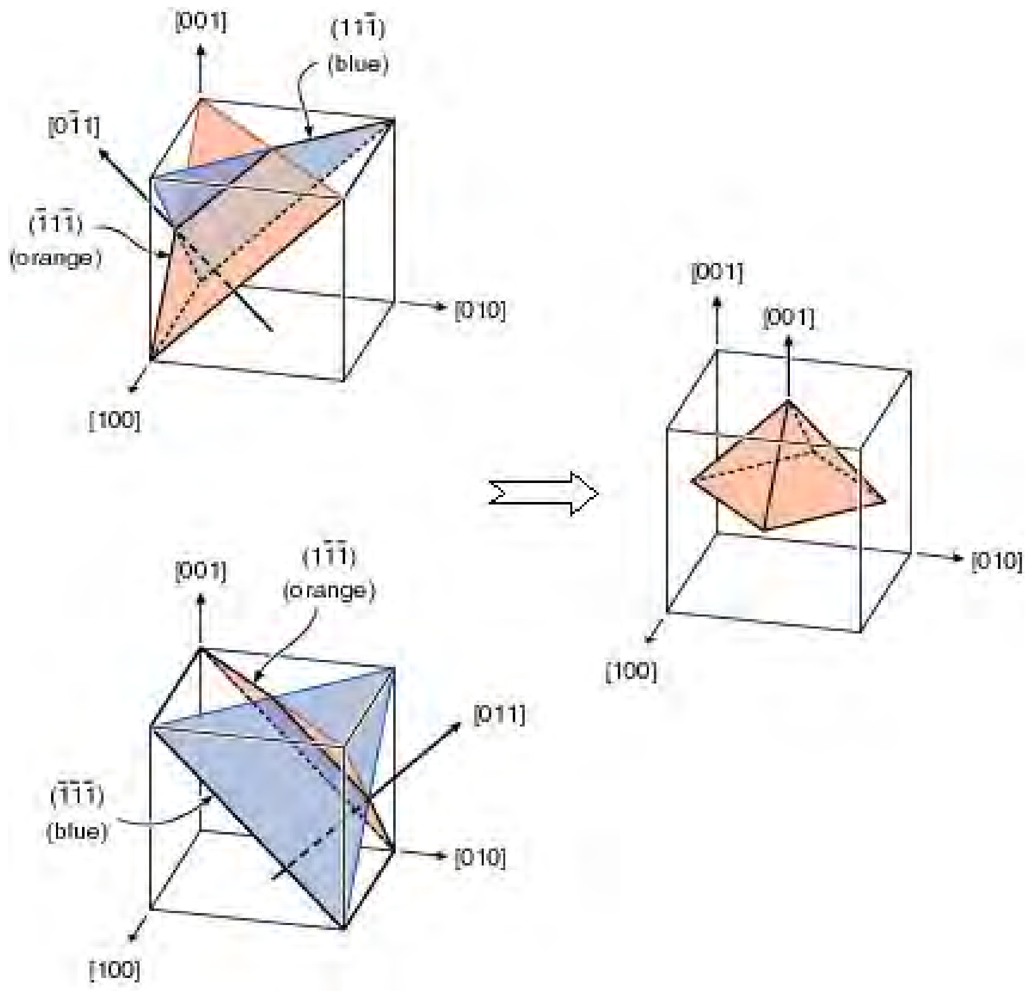

Figure 5-11. Formation of square pyramidal column tip under the condition of rotated substrate

5.7 Summary

YSZ coatings have been successfully deposited on processed bond coat surface using electron-beam directed vapor deposition method. The effect of rotation rate on the coating density, pore morphology, and texture has been investigated and summarized as follows:

During stationary deposition, straight growth columns are formed with triangular faceted column tips. Rotated samples have growth columns with square pyramidal faceted tips. This difference is accompanied by a change in preferred crystallographic growth direction from <111> to <100> as the substrate rotation rate increases. At low rotation rates, wavy columnar structure forms due to the slow rate of change of the incidence angle of the vapor flux to the substrate. The increased conduction distance along the wavy columns combined with a high pore volume fraction results in a very low thermal conductivity of 0.8 W/mK which is well below that of conventionally EB-PVD deposited coatings. At high rotation rates, the wavy columns disappear and relatively straight sided columns are formed in the coating. These coatings have thermal conductivities in the 1 W/mK range which is 50% less than that reported for EB-PVD coatings grown under otherwise similar conditions. The low thermal conductivity of the rotated EB-DVD coatings appears to be a result of an increased volume fraction of Type III nanopores in the primary and secondary growth columns orientated transversely to the heat flow direction.

Chapter 6

Thermal Cycling of DVD YSZ Coatings

6.1 Overview

In this chapter, a cycling test is conducted to understand how the bond coat processing affects the TBC failure lives. The dependence of TBC structure upon the bond coat roughness is presented here. The failure modes are investigated for TBCs on the grit-blasted and polished bond coats. The lifetime and TGO growth rate are compared. In addition, the relation between coating morphology, density and cycling life is also explored. The different failure mechanisms have been presented to explain two distinct failure modes.

6.2 TBC Structure on Grit-blasted Bond Coats

In Chapter 5, the microstructure of TBC on polished bond coats was examined. Here, the YSZ coatings were deposited on grit-blasted bond coats under the same conditions that had been used in the above experiments. The coating surface morphology didn't show any difference with that grown on polished bond coats. However, the cross-section views have a distinct difference. Fig. 6-1 shows the cross-sectional structure of three of the 7YSZ coatings grown at 1000^{o}C at rotation rates of 0.5, 6 and 20 revolutions per minute. At very low rotation rate, the primary growth columns consisted of many smaller fine columns and all had a wavy morphology resulting from the gradual change in angle of incidence of the vapor flux. Fig. 6-1(b) also shows a corn kernel defect in the TBC formed at a depression in the bond coat. These defects form just above concavities in the bond coat by the nucleation of small growth columns which initially grow normal to the concave surface. They eventually terminate in a region of high porosity at the point of impingement of adjacent columns that preferentially collected the incident vapor. Table 6-1 summarizes the coating density data for samples made at various rotation rates upon rough and smooth bond coats. The coatings on rough bond coat have a slightly lower density than those deposited on smooth bond coat due to the many growth defects. Recent assessments of atomic assembly upon rough surfaces during vapor deposition have shown that surface asperities create incident flux shadows resulting in very low density columnar structures [145].

Table 6-1. The coating density vs. rotation rate on different bond coats

Rotation Rate (rpm)		**0.5**	**6**	**20**
Coating Density (g/cm^3)	Rough BC	3.3	3.55	3.98
	Smooth BC	3.38	3.67	4.1

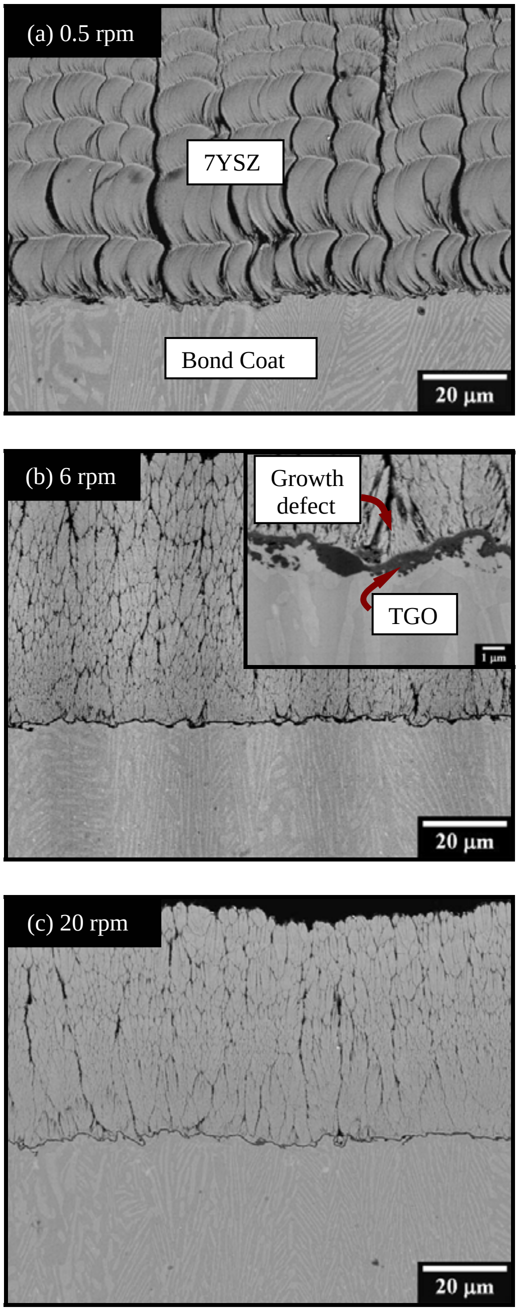

Figure 6-1. The effect of substrate rotation rate on the structure of the coatings grown on the grit-blasted bond coat at a temperature of 1000 °C. The growth columns have a wavy shape at low rotation rates and become straighter as the rotation rate increases. Note the significant undulations of the TGO layer and the presence of TBC growth defects emanating from concavities in the bond coat surface.

6.3 Cycling Test

6.3.1 Grit-blasted bond coat cyclic response

Thermal cycling tests were performed in a top-loading furnace. Each cycle consisted of 1-hr hold at 1100 °C followed by 10-min of cooling in forced flowing laboratory air to a temperature of ~50 °C. The specimens were examined visually every 20 cycles to detect the onset of delamination, with “failure” defined to have occurred when ~20% of the TBC had spalled. To better understand the growth kinetics of the TGO layer, some samples were taken out for observation and analysis before failure. The effects of thermal cycling upon the surface morphology and the cross sectional structure of a coating deposited on a rough bond coat (at 6 rpm) are depicted on Fig. 6-2. Figures 6-2(a) and (e) show the surface and cross-section morphology of a 7YSZ coating deposited with a rotation rate of 6 rpm. The as-deposited coating was composed of square-based pyramidal column tips that had sharp facets. The sides of the growth columns contained feathery pore structures that were inclined at about 45^o to the growth axis. These low density surfaces combined with the intercolumnar gaps are responsible for the low in plane compliance (in both tension and compression) of vapor deposited thermal barrier coatings. Sintering began during the first few cycles, Fig. 6-2(b) and (f). The pyramidal column tips gradually became more rounded and the primary columns locally fused as the thermal cycling continued, Fig. 6-2(b) to (d). Examination of the TBC cross-sections Fig. 6-2(e)-(h) shows that the feathery pore features within the columns suffered rapid sintering and were transformed to relatively spheroidal pores. Significant intracolumnar porosity remained in the coating even after exposure to 630 thermal cycles.

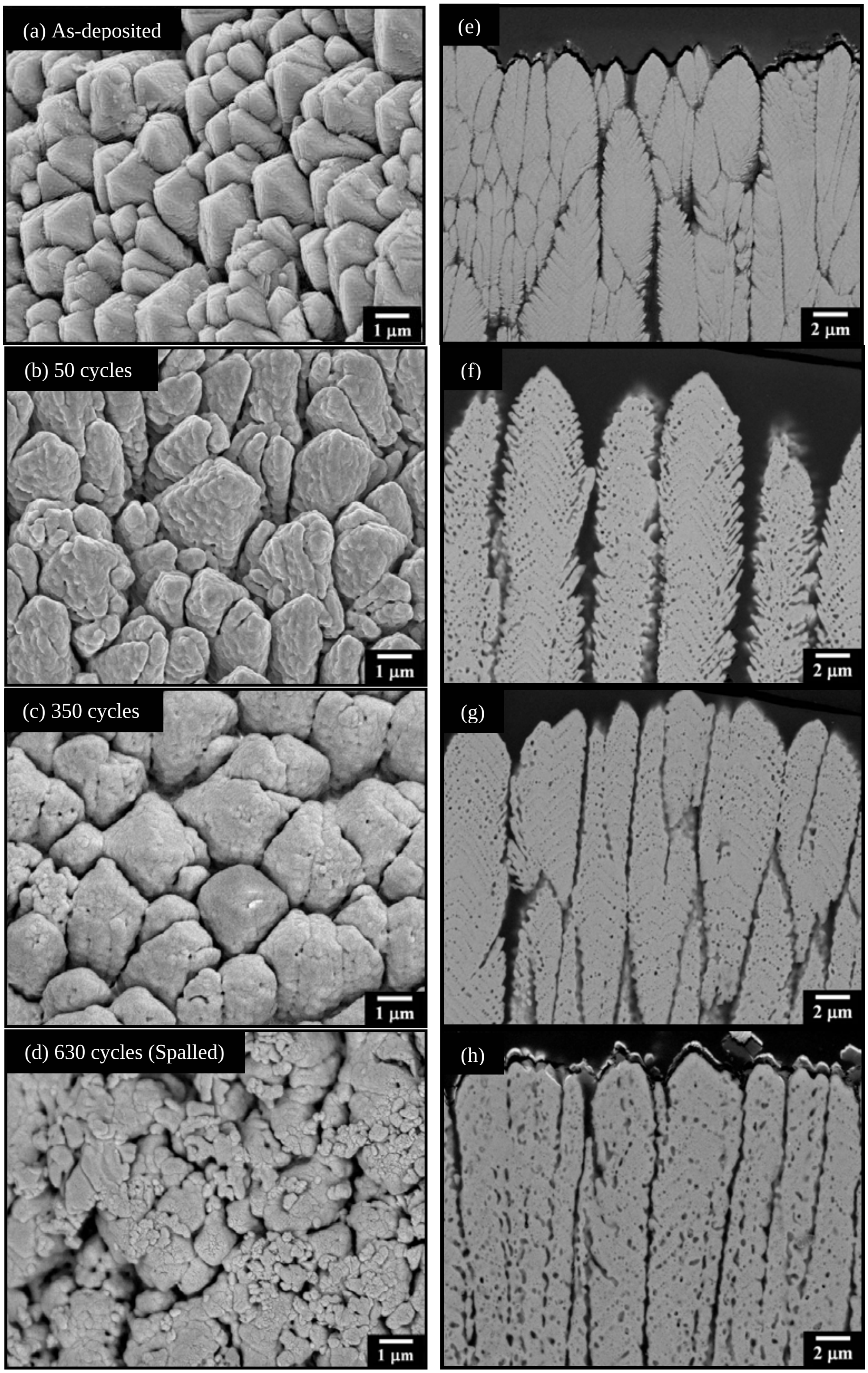

Figure 6-2. Evolution of the coating surface and cross-sectional morphology of a coating during thermal cycling (deposited at 1000°C on a grit-blasted bond coat surface at a rotation rate of 6rpm).

The coatings eventually failed by buckling-delamination during thermal cycling. The spallation started first at the edge of the coupons and then propagated inward across the surface. The variation in the number of thermal cycles to spallation of the 7YSZ coatings is plotted as a function of sample rotation rate in Fig. 6-3. The lifetime slowly decreases as the rotation rate was increased. A data point for the spallation lifetime of EB-PVD 7YSZ coatings deposited on the same NiCoCrAlY bond coat and subjected to similar thermal cycling is included in Figure 6-3 [86]. It suggests that the DVD YSZ coatings have a significantly greater durability than EB-PVD counterparts.

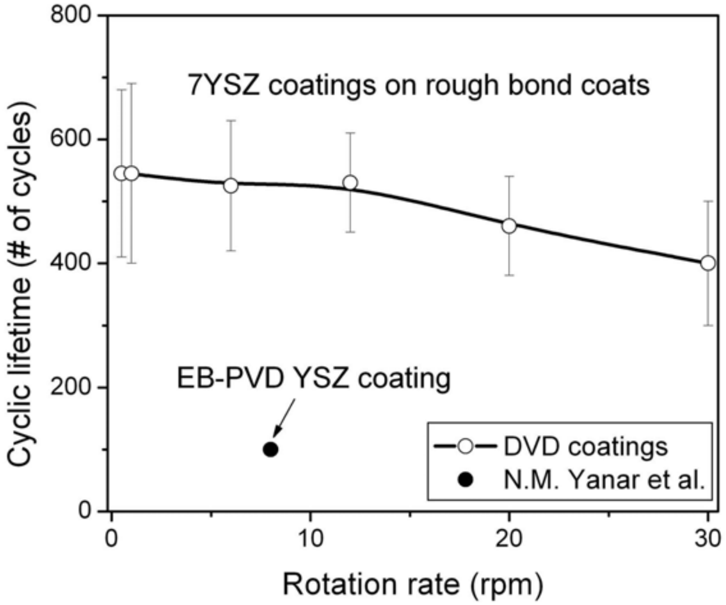

Figure 6-3. Spallation lifetime (number of cycles to macroscopic coating delamination) of 7YSZ coatings as a function of rotation rate. The data are for coatings applied to samples with a grit-blasted (rough surface) bond coat. Data are also shown for an identical composition coating deposited on nominally the same rough bond coat using conventional electron beam physical deposition [86].

The coatings failed by delamination at the TGO/TBC interface. The evolution of the structure at this interface with the cycling is shown in Fig. 6-4. The grit blast process resulted in an initially rough bond coat surface and a thin layer alumina TGO layer had formed the as-deposited coatings, Fig. 6-4(a). When the coatings were subject to thermal cycling at 1100 °C, sintering between columns is evident. The neighboring columns coalesced and shrank, which resulted in the wide intercolumnar gaps, Fig. 6-4(b) through (d). Thermal cycling resulted in an increase of the TGO layer thickness and bond coat rumpling [87]. The differential vertical displacement of the bond coat eventually led to the formation of cracks in the TBC layer very close to the TGO interface. These were initiated at local depressions of the bond coat, Fig. 6-4(b). After 350 cycles, the rumpling wavelength had decreased resulting in many local regions of delamination. As the rumpling amplitude increased these delaminations laterally propagated and interlinked causing eventual spallation of the coating, Fig. 6-4(c) and (d).

Higher magnification views of the TGO/TBC interface reveal details of the delamination process, Fig. 6-5(a) through (b). Thermal cycling caused the TGO layer to thicken, and the amplitude of the undulations to increase by a rumpling mechanism [87], eventually leading to the formation of cracks in the TBC above local depressions in the bond coat shown in Fig. 6-5(b). These regions frequently contained “corn kernel” defects which adhered poorly to the adjacent TBC. As the undulation amplitude increases, these cracks propagate laterally and interlink, causing eventual spallation. The preferred fracture path in the TBC was located within 1-2 μm of the TGO layer and propagated through planes of pores created in the TBC when the vapor incidence angle was most oblique to the surface. Samples subjected to the greatest number of thermal cycles also had small, isolated delamination cracks at the bond coat/TGO interface, Fig. 6-5(d). These did not link up and were not directly responsible for the spallation observed here.

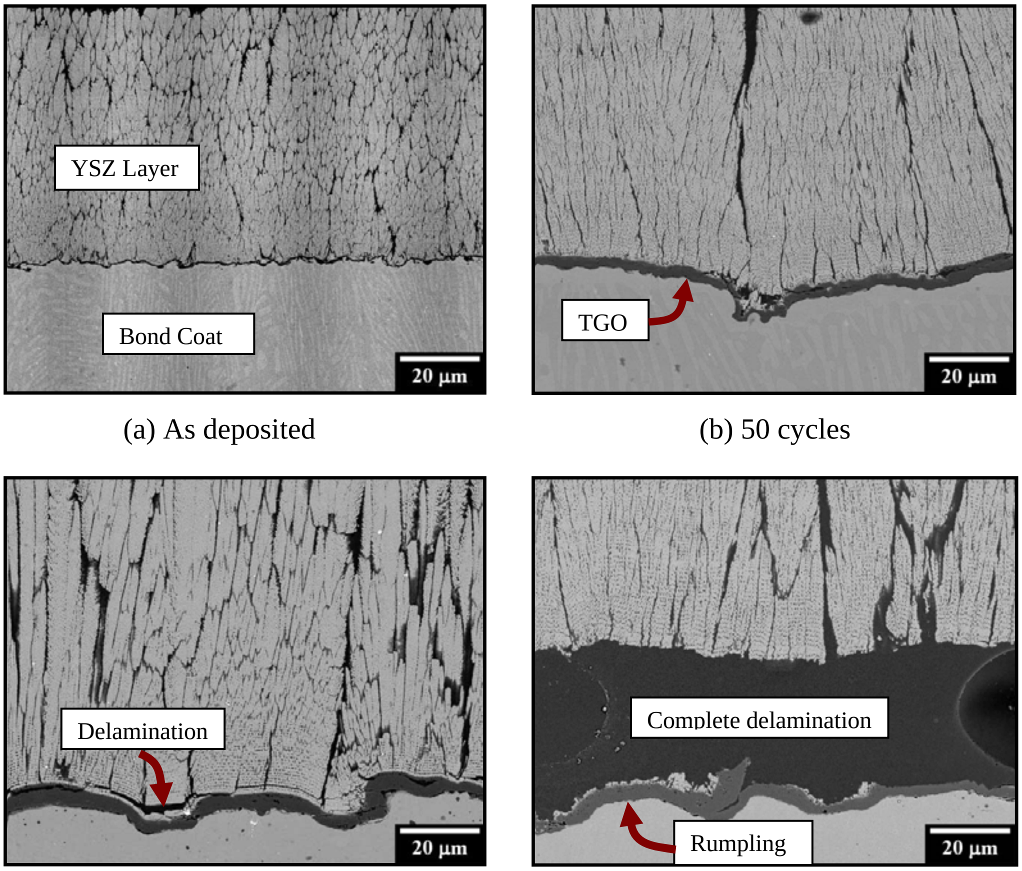

(a) As deposited (b) 50 cycles

(c) 350 cycles (d) 630 cycles (spalled)

Figure 6-4. Evolution of the TGO layer region for a coating deposited on the grit-blasted surface at 6 rpm. A significant increase in rumpling amplitude upon thermal cycling can be seen. Figure (c) shows that the delaminations preferentially penetrated the high porosity bands formed during TBC deposition. Figure (d) shows the spalled interface.

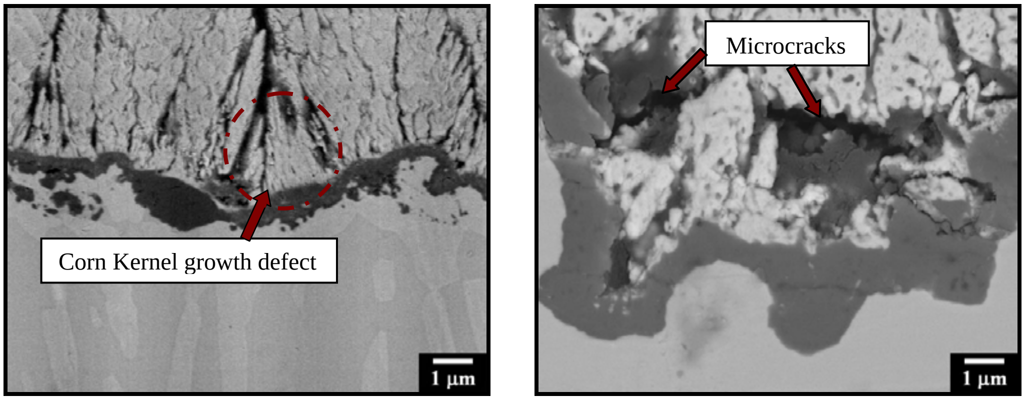

(a) As deposited

(b) 50 cycles

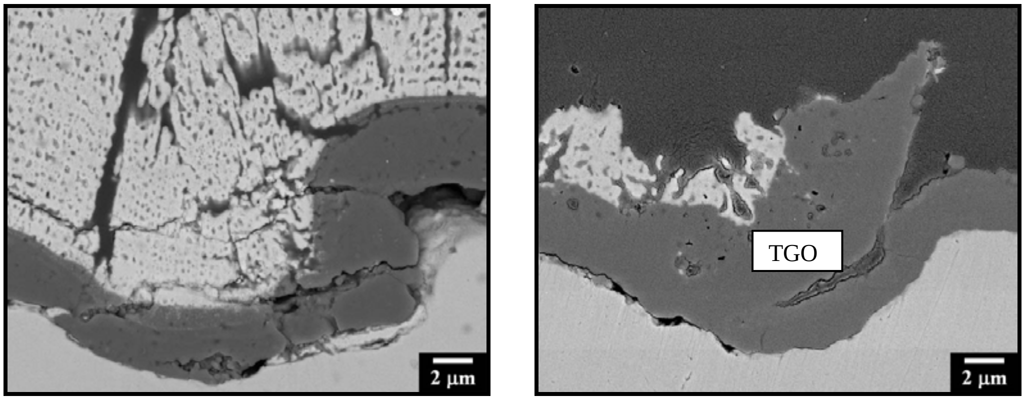

(c) 350 cycles

(d) 630 cycles (spalled)

Figure 6-5. High magnification of the evolution of TGO layer. Figure (b) shows microcracks were initiated in the TBC at TBC-TGO interface in regions where deep rumples formed in the bond coat. Figure (d) shows the appearance of a crack at the bond coat-TGO interface.

The TGO layer increased in thickness with the number of thermal cycles, Fig. 6-6. The TGO growth rate was independent of the TBC rotation rate and approximately parabolic:

$$h^2 = 2k_p t$$

where h is the TGO thickness, t is the hot-time and $k_p \sim 0.025\ \mu m^2/h$.. In the as-grown coatings, there is a thin layer of oxide existing between the TBC and bond coat. The oxide scale reached a critical thickness of ~5 μm when the coating started to exhibit macroscopic spallation. The oxide growth involves counter-diffusion of oxygen and aluminum along the α-Al_2O_3 grain boundaries. The inward diffusion of oxygen and the outward diffusion of Al influences both thickening and elongation.

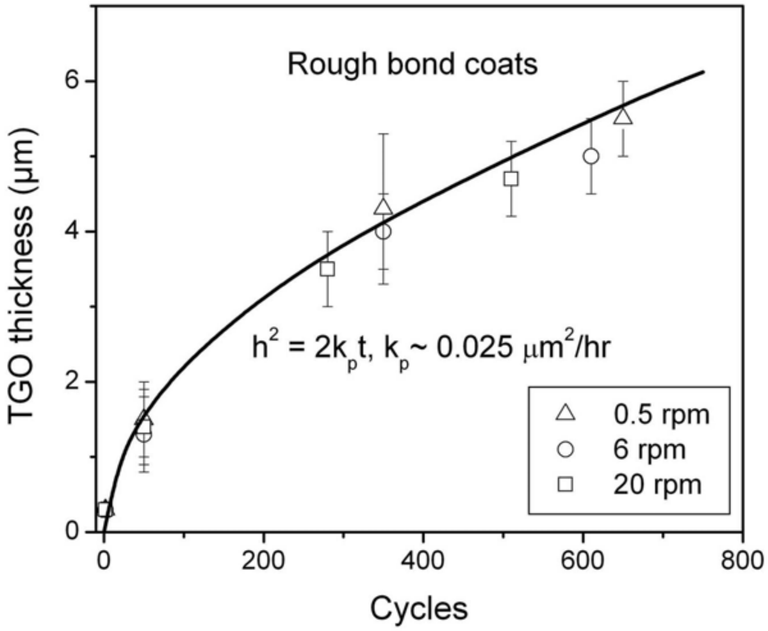

Figure 6-6. TGO layer thickness versus number of (1 hour) thermal cycles at 1100 °C for the DVD 7YSZ coatings

6.3.2 Polished bond coat cyclic response

The cycling behavior of coatings grown on grit-blasted bond coats has been shown above. The results of the coatings grown on polished bond coats under the same cycling condition will be presented next. Fig. 6-7(a) shows the as-processed surface topology of TBC coating deposited on polished bond coat surface at the rotation rate of 6 rpm. Compared with that on grit-blasted bond coat, the column tips were smaller and more uniform. The distinct difference of the coatings on the grit-blasted and polished bond coats is that the latter has no “corn kernel” growth defects, which can be seen in the cross-section structure.

After cycling started, the coatings sintered dramatically. Several small columns combined together to form a relatively larger column. Upon coating failure, the coatings were completely sintered and the originally small columns could hardly be observed in the coating surface, Fig. 6-7(d).

Fig. 6-8 presented the development of coating sintering at different stages of thermal cycles. The columns became wider as the cycling continued. Moreover, the TGO/bond coat interface exhibited significant non-planarity with the increase of cycles. Since the bond coat surface was polished prior TBC deposition, this morphology evidently developed during the cycling. A β-depletion zone can be seen clearly with the progress of cycling. This region developed near the interface, and increased in width from ~0.5 μm in the as deposited condition to ~20 μm when failed.

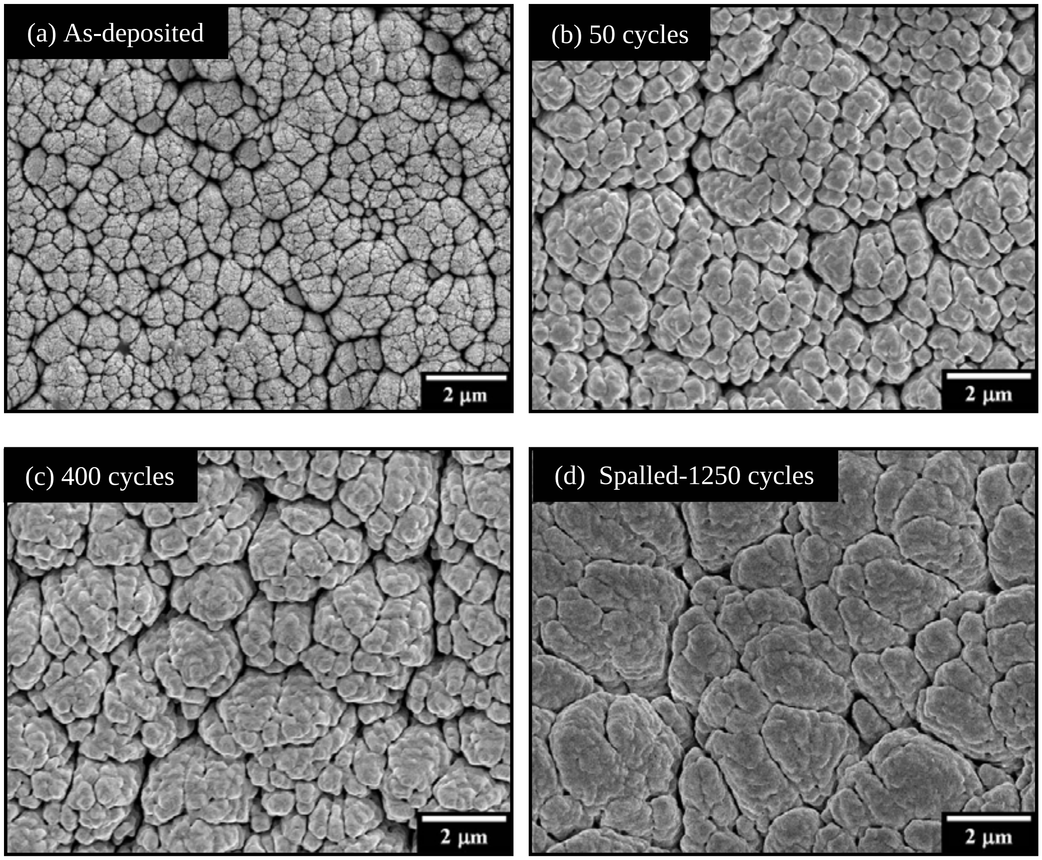

Figure 6-7. Evolution of the coating surface as the coating deposited on a smooth bond coat surface at 6 rpm was thermally cycled.

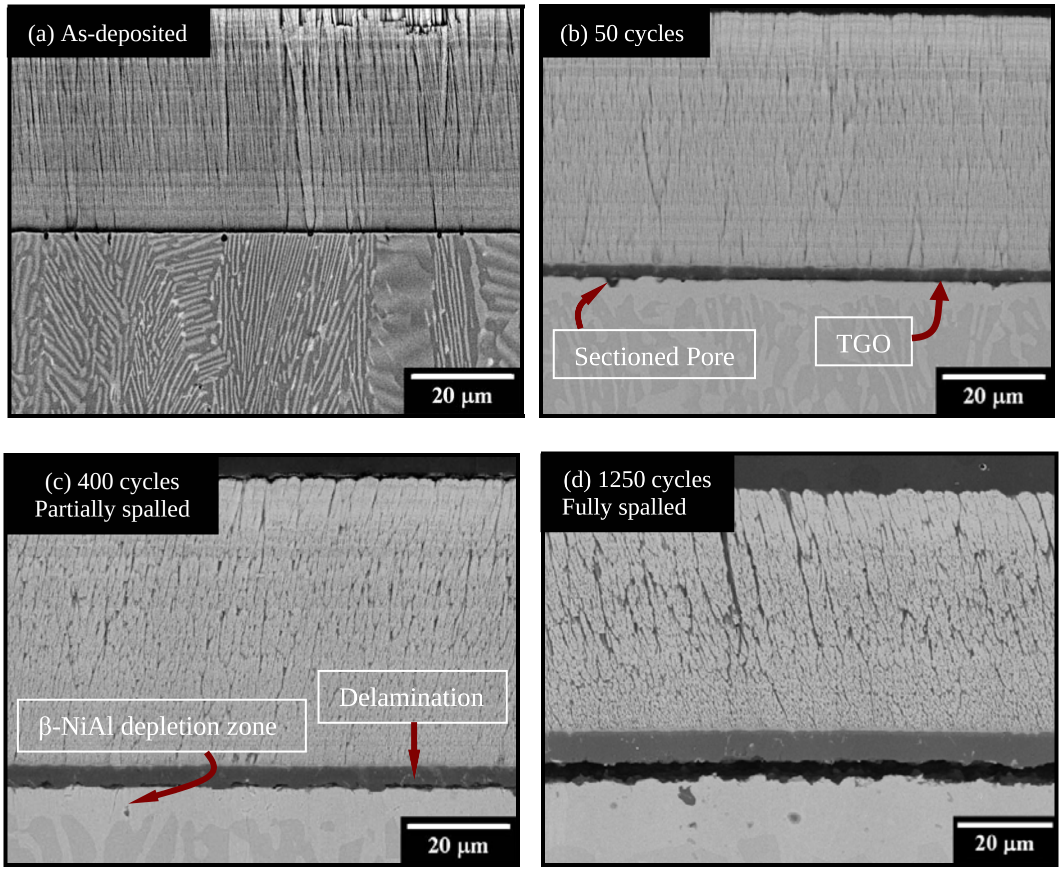

Figure 6-8. Evolution of TBC system deposited on a smooth bond coat surface at 6 rpm during thermal cycling. An increase in the TGO thickness and the TBC intercolumnar gaps with cycling can be seen. Localized delamination occurs at the TGO-bond coat interface in (c). These cracks coalescence and lead to complete spallation in (d).

The failure cycles of EB-DVD 7YSZ coatings tended to decrease with the increasing rotation rate, Fig. 6-9. All of them have the failure times falling between ~900 and ~1350 cycles. The failure lifetime cycles of the coatings grown by EB-PVD were also plotted in the figure. For YSZ coatings grown on smooth NiCoCrAlY bond coat surfaces by varying the rotation rates, almost all of them have more than 1000 cycles to failure, which obviously had more cycles than EB-PVD coatings.

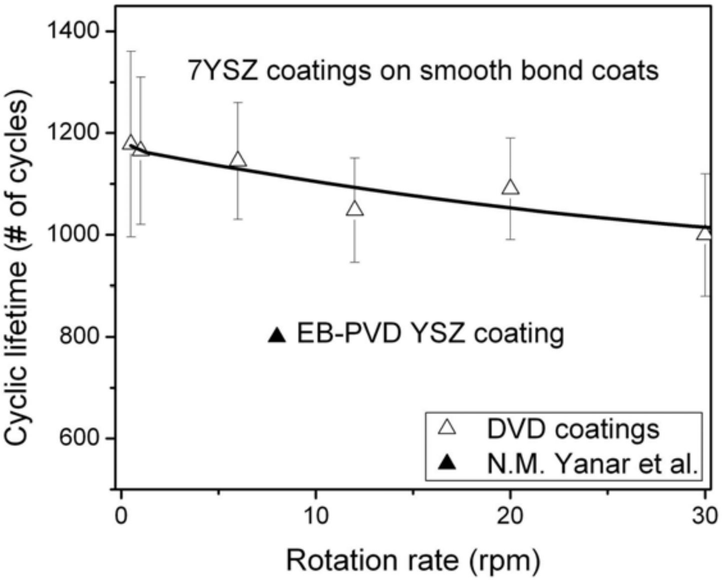

Figure 6-9. The number of cycles for coating delamination versus coating rotation rate for coatings deposited on a smooth bond coat. Data for an EB-PVD coating on a similar polished bond coat [86] is also shown.

The development of TGO layer with the cycles of thermal exposure was shown in Fig. 6-10. Between TBC and bond coat, there is a flat TGO layer with the thickness of ~0.3 μm in the as-deposited condition. The β and γ phases were clearly shown in the bond coat. TGO developed local imperfections (variation in thickness) could also be observed, which could be attributed to the oxidation of the initial surface-connected voids distributed in the bond coat, as well as the emergence of YAG domains (pegs), shown in Fig. 6-10. With further cycling, the oxide layer exhibited significant thickening (~1.5-2 μm). Two distinct layers were revealed in the TGO. The outer layer consisted of an intermixed zone of yttria, zirconia and alumina, and the underlying is aluminum oxide. Moreover, thickness heterogeneities were also presented at the local TGO sites. At 400 cycles, the flat TGO layer became apparent non-planarity. The important observation was the slower TGO growth rate for specimens. The TGO layer is 3 μm thick, 1 μm less than that of 350-cycle grit-blasted counterparts. Fig. 6-10(d) presented the microstructures of samples after failure. The TGO layer was rather thick (5-6 μm). Some reactive element-rich oxides (Y_2O_3/YAG) were shown in the TGO layer, even protruding into the bond coat. The large cracks were found at the interface of TGO/bond coat and extended laterally in the TGO/bond coat, which is also in agreement with the experimental results by Yanar etc. [86].

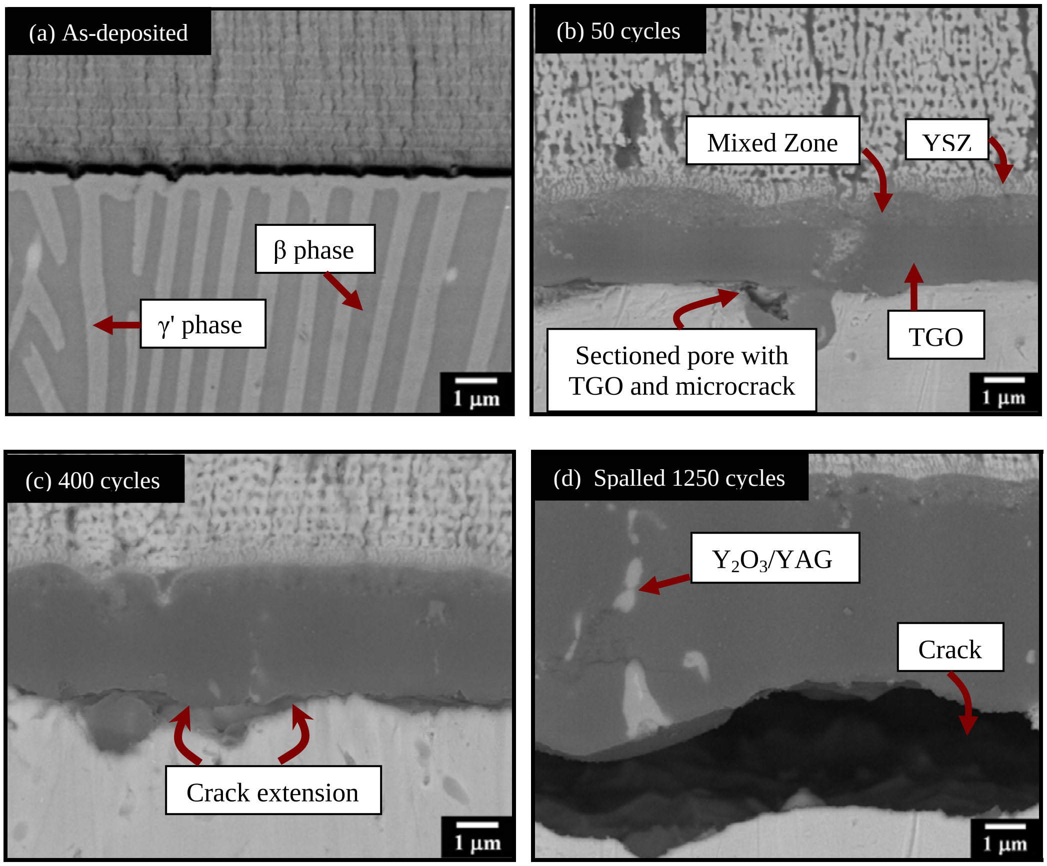

Figure 6-10. The TGO regions as a function of thermal exposure at 1100 °C for coatings deposited on a smooth bond coat surface at the rotation rate of 6 rpm.

Fig. 6-11 presented the trends of TGO thickness with cyclic lifetime for coatings deposited on smooth bond coat surfaces at the rotation rate of 0.5, 6 and 20 rpm. It is noted that all coatings spalled when the TGO layer thickened to ~5.5 μm. The parabolic rate constant k_p was 0.014 $\mu m^2/h$. Compared with the TGO thickness with the cycles for coatings on rough bond coats (Fig. 6-6), the TGO layer had a similar thickness of ~5.5 μm when coating spallation appeared. However, the parabolic rate for the polished bond coat was only half that for the grit-blast bond coat. This is presumed to have occurred because of the presence of the contaminants (Si, Mg, Ca) on the roughened surface [27]. It seems that the polished bond coat surface has removed these contaminants and played an important role in improving the spallation lifetime and slowing the TGO growth rate of a TBC system.

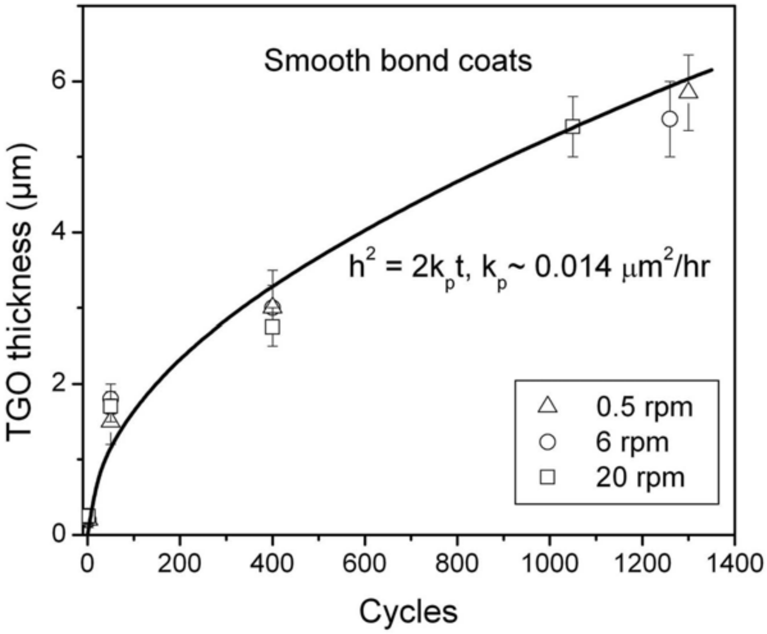

Figure 6-11. TGO layer thickness dependence upon the length of the cyclic high temperature exposure.

6.4 Mechanism Governing Durability

The spallation lifetime of DVD-YSZ coatings on NiCoCrAlY bond coat has been presented in the experimental results. The foregoing measurements indicate that: (*i*) cyclic lifetimes are highly sensitive to the bond coat surface condition; those grown on smooth bond coats have approximately twice the durability of those deposited on grit blasted surfaces and the failure mechanisms are quite different, (*ii)* the durability of the EB-DVD coatings is dependent upon the rate at which it was rotated during deposition.

The failure mechanism of TBC grown on grit-blasted bond coats can be explained in Fig. 6-12. Some initial "Corn Kernel" growth defects occur at the concave regions of the bond coat, resulting from the impact of sand-grit blasting, which can be observed in Fig. 6-5(a). As cycle-by-cycle exposure progresses, the TGO thickening rate was much higher due to the higher oxygen exposed area on rough surface and possible impurities. Concurrently, the TGO growth expands laterally at elevated temperature. Upon cooling, a compressive strain is produced by the lateral growth. Therefore, the strain energy coming from the TGO lateral growth and thermal expansion misfit will be stored in the layer and released by the undulation. The undulation growth is dependent on the high temperature creep strength of the bond coat, the lateral growth strain per cycle and high temperature yield stress of the oxide layer. The development of undulation growth results in the more rumpling TGO layer. As the bond coat rumples, concavities are amplified. The displacements induce tension in the superposed TBC, causing cracks to form (often in "corn kernel" defects) and propagate along planes of lowest local toughness (through planes of small pores). Additionally, it is speculated that small concentrations of impurities/contaminants, such as some Si and Mg oxides from the sand grit, appear to increase the oxidation kinetics and lower the interface toughness of TBC and TGO. Coalescence of a sufficient number of contiguous cracks results in a delamination that exceeds the critical length for buckling [30]. Most systems with MCrAlY bond coats are not prone to such rumpling [30], except upon stepwise cycling [146]. The properties of this particular overlay composition (in terms of thermal expansion and creep strength) must be sufficiently different to allow rumpling. The specifics remain to be ascertained.

Polishing the NiCoCrAlY bond coats resulted in significant improvements in TBC lives. The surface was free of defects such as craters, sharp edges and contaminants after hand polishing. Moreover, the TGO layer formed on these bond coats was very uniform and continuous. Examination of TBC/TGO interface at various stages of cyclic life revealed that the interface was also free of corn kernel growth defects except the thickness heterogeneity at some localized areas (Fig. 6-10). All these indicated that the TBC spallation on polished bond coats should be explained with a different mechanism. Upon polishing, rumpling is suppressed, as expected from the Balint and Hutchinson model [89] and from previous observations [87, 147]. Instead, delamination occurs at the TGO/bond coat interface (Fig. 6-13). Small cracks initiate at the TGO thickness heterogeneities, Fig. 6-10(c). For these to grow and coalesce, the toughness of the intervening interface must be lower than that on pristine interfaces [88, 148] and this appears to be due to the appearance of small flat voids in the intervening regions, possibly in conjunction with sulfur segregation and the embrittlement of this interface

[37, 149]. Hf is found to effectively getter S and inhibit segregation to the interface, thereby enhancing the adhesion between the TGO and bond coat [150]. However, no Hf is doped into the bond coat studied here. This may result in the formation of small flat voids in some regions.

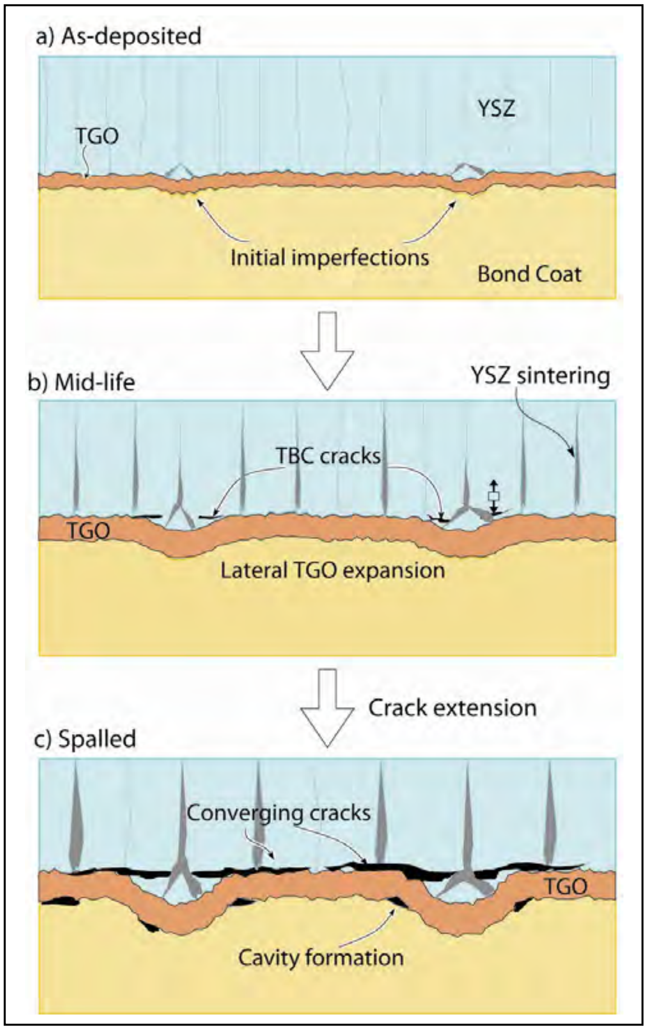

Figure 6-12. Spallation failure mechanism for DVD TBC coatings deposited on rough surface bond coat susceptible to rumpling. (a) Shows initial (corn kernel) growth defects near depressions in the surface of the as-deposited coatings. (b) Shows rumpling and TBC microcrack initiation near initial depressions in the bond coat. (c) Shows microcrack convergence and coating spallation. Note that the TGO layer thickness and rumpling amplitude both increase with cycling for this bond coat.

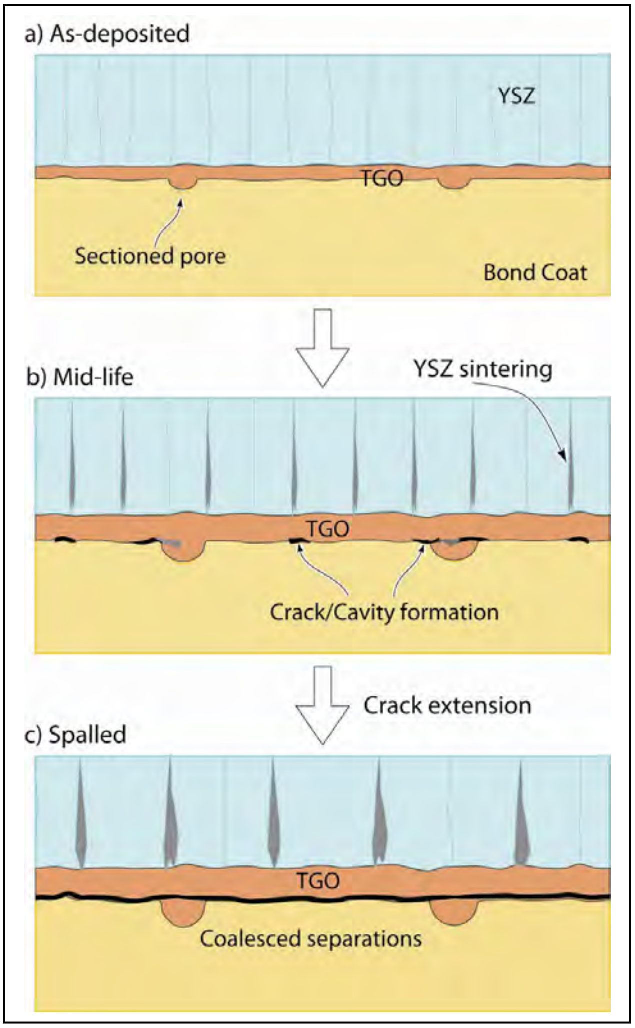

Figure 6-13. Schematic illustration of spallation mechanism for DVD TBC coatings deposited on a polished bond coat. The absence of initial undulations greatly slows the bond coat rumpling rate. Fracture was initiated at surface intersecting voids whose interior oxidation produced locally thickened TGO. These coalesced with simultaneously forming flat voids at the bond coat – TGO interface to cause delamination failure of the coating.

The increase in spallation life as the rotation rate during deposition is decreased is similar for coatings applied to both surface conditions. The lifetime of the DVD coatings on both surfaces are also significantly greater than EB-PVD coatings applied on the same bond coat system. While there are many morphological differences in the coatings that might be invoked to account for these observations, the most fundamental is the significant difference in coating density. Experiments have shown that the DVD TBCs are less dense than EB-PVD TBCs, which means DVD coatings have more porosity in the columnar microstructure. It is also noted, Fig. 6-14, that the elastic modulus of as-deposited coatings increases with coating density. If the spallation data are plotted against coating density, Fig. 6-15(a), it is apparent that the lifetime decreases for both bond coats and the data from the EB-PVD experiments falls on the same trend line. The thickness of the TGO layers at which spallation occurs also decreases as the density increases (Fig. 6-15b). The enhanced durability relative to EB-PVD coatings, as well as the trend with rotation rate, is attributed to the lower coating density.

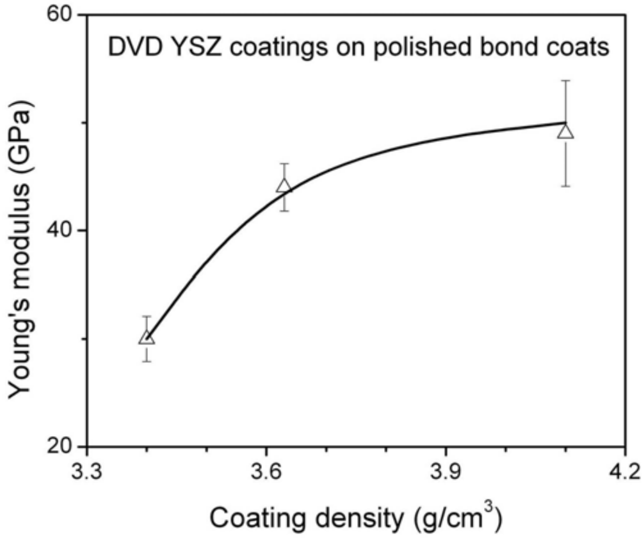

Figure 6-14. Young’s modulus of the coatings as a function of the coating density

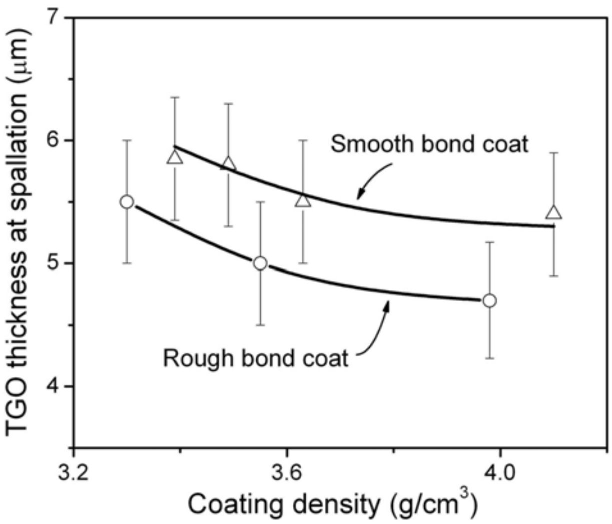

(a) TBC cyclic life

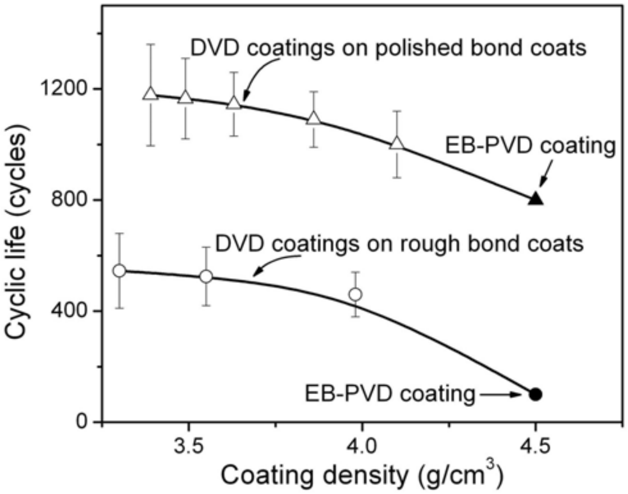

(b) TGO critical thickness

Figure 6-15. (a) TGO thickness at spallation and (b) Cyclic life of the coatings as a function of the coating density. Note that in (b), the EB-PVD YSZ coatings are estimated to have the density of 4.5 g/cm^3 from reports of their pore fraction of 20-25% [86].

If the spalling is deemed to occur by edge delamination at the TGO/bond coat interface (as for the polished specimens), shown in Fig. 6-16, the process is governed by the steady-state energy release rate. Hutchinson et al [87, 151] have shown that for a TGO/TBC bilayer, the steady state energy release rate is given by:

$$G_{ss} = \frac{(E_1'h_1(1+\upsilon_1)\varepsilon_{1r} + E_2'h_2(1+\upsilon_2)\varepsilon_{2r})^2}{2(E_1'h_1 + E_2'h_2)} - \frac{M\Delta\kappa}{2} \qquad \text{(4-1)}$$

with the net moment acting on the bilayer coating, given by

$$M = \frac{E_1'E_2'h_1h_2(h_1+h_2)[(1+\upsilon_2)\varepsilon_{2r} - (1+\upsilon_1)\varepsilon_{1r}]}{2(E_1'h_1 + E_2'h_2)} \qquad \text{(4-2)}$$

and the net curvature change of the bilayer upon decohesion:

$$\Delta\kappa = \frac{6[(1+\upsilon_2)\varepsilon_{2r} - (1+\upsilon_1)\varepsilon_{1r}]}{h_1h_2}\left(\frac{h_1+h_2}{\xi}\right) \qquad \text{(4-3)}$$

with the non-dimensional function ξ given by:

$$\xi = \frac{E_1'}{E_2'}\left(\frac{h_1}{h_2}\right)^2 + \frac{E_2'}{E_1'}\left(\frac{h_2}{h_1}\right)^2 + 4\left(\frac{h_1}{h_2}\right) + 4\left(\frac{h_2}{h_1}\right) + 6 \qquad \text{(4-4)}$$

and

$$E_1' = \frac{E_1}{1-\upsilon_1^2} \qquad E_2' = \frac{E_2}{1-\upsilon_2^2} \qquad \text{(4-5)}$$

The subscripts 1 and 2 refer to the TGO and TBC, respectively. The quantities ν, h, ε_r and E are the Poison ratio, thickness, residual strain and Young's modulus in each layer, respectively. The residual strain is dominated by the thermal expansion mismatch, $\Delta\alpha$, between the coating and substrate and by ΔT, the temperature drop from the peak temperature, $\varepsilon_{2r} = \Delta\alpha\Delta T \approx -0.0026$. The critical TGO thickness can calculated upon equating G_{ss}, to the mode II interfacial toughness. If this toughness is assumed to be the same value for all of the coatings (80 J/m^2) [85, 151], and assuming $\upsilon_1 = 0.2$,

$\upsilon_2 = 0.3$, $\varepsilon_{1r} \approx -0.0076$, $E_1 = 380GPa$ and $h_2 = 80\mu m$, the relationship between the critical thickness and TBC modulus is plotted on, Fig. 6-17(a). These estimated thickness levels are comparable to those measured at “failure” for the coatings on the polished samples and they predict the same critical thickness dependence upon TBC density found in the experiments, Fig. 6-15(b).

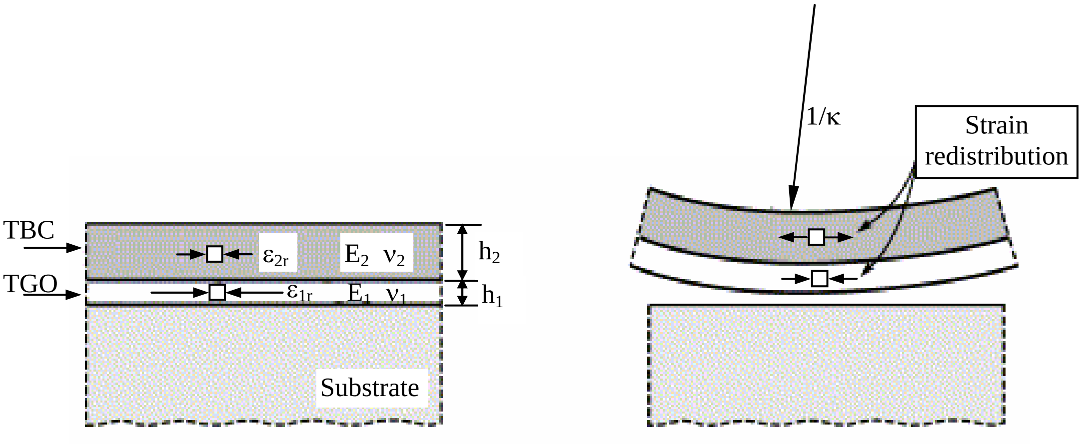

(a) TBC/TGO attached to substrate

(b) Detached

Figure 6-16. Illustration of the curvature induced delamination of the TBC/TGO layer from the substrate.

The result in Fig. 6-17(a) indicates that the critical TGO thickness (and therefore the spallation lifetime) has a maximum value (of ~6 μm) at a coating modulus of ~25 GPa. For the coatings grown here, it increases as the TBC density is decreased and this trend is evident in the experimental data shown in Fig. 6-15. The analysis also highlights the importance of the coating thickness, Fig. 6-17(b) and interface toughness, Fig. 6-17(c). It is interesting to note that even modest increases of toughness (from 80 to 90 Jm^{-2}) are predicted to increase the critical thickness of a TBC with a 30 GPa Young's modulus by about 1 μm and therefore increase the lifetime of a coating on a polished bond coat from 1330 to 1770 cycles. While changes to the coating thickness are predicted to have little effect upon the life, they do affect the optimum density (modulus) for maximum life: with thicker coatings requiring the use of a lower coating density (modulus). Xu et al. [152] mentioned that larger in-plane modulus or greater thickness increases the energy release rate G and thus reduces the durability, which is shown in the similar trends seen in Fig. 6-17.

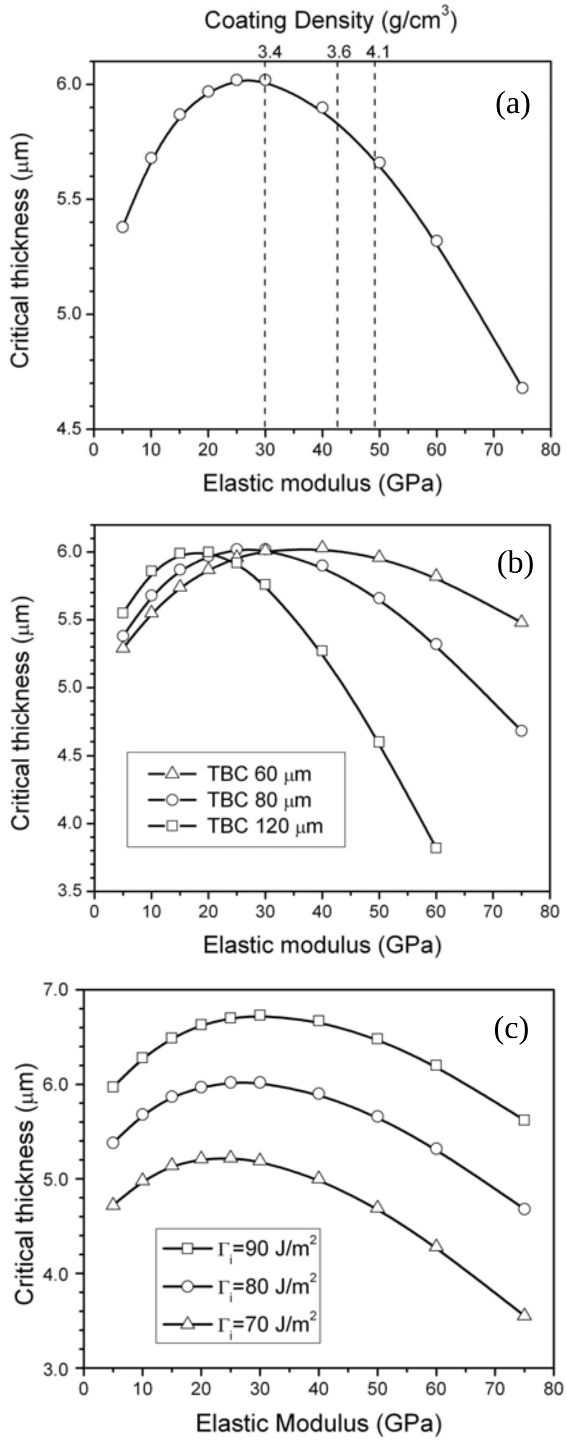

Figure 6-17. (a) Predicted critical TGO thickness for TBC buckling delamination failure as a function of TBC Young’s modulus assuming (i) an interfacial toughness of 80 J/m^2 and a coating thickness of 80 μm. The coating density – Young’s modulus correlation of Figure 15 was used to obtain the modulus values. (b) Shows the effect of varying the TBC thickness while maintaining the toughness constant at 80 J/m^2. (c) The effect of interfacial toughness upon the critical TGO thickness for 80 μm thick coatings.

6.5 Summary

In this chapter, the effect of rotation rate and bond coat processing on the coating density, pore morphology, and cycling behavior has been investigated. It is found that rough (Grit-blasted) bond coat has more surface defects (such as craters, sharp edges and impurities etc.) than smooth (hand-polished) one, which will produce a significant effect on the following TBC deposition. Coatings grown on grit-blasted bond coats have only half the lifetime of those deposited on polished bond coats. The bond coat surface also governs the mechanism of spallation failure. The lifetimes of coatings applied to rough bond coats are governed by bond coat rumpling whereas those for the polished bond coat coatings is dictated by interface delamination. The critical TGO thickness at coating failure is shown to decrease with increase in coating density consistent with a steady state strain energy release model. The lower critical TGO thicknesses of the rough bond coat surfaces are consistent with a reduced interfacial toughness. Measurements of the coatings elastic modulus confirm a reduction in coating modulus as the pore content of the coatings increases and therefore a reduction in the stored elastic strain energy available to drive interfacial failure.

The results and strain energy release rate models indicate that spallation lifetimes can be optimized by (*i*) controlling the deposition process so that the in-plane Young’s modulus of an 80 μm TBC coating is 25-30 GPa (the optimum modulus decreases as the coating thickness is increased), (*ii*) reducing the amplitude of initial undulations on the bond coat surface and (*iii*) using bond coat chemistries that have reduced propensity for void formation in the bond coat adjacent to the TGO.

Chapter 7

Morphology and Texture of DVD $Sm_2Zr_2O_7$ Coatings

7.1 Overview

Yttria stabilized zirconia is normally used for the TBC layer because it has a low thermal conductivity at its use temperature [153], exhibits good erosion and foreign object damage resistance [54], has sufficient toughness to support the operational stresses in the presence of the various growth defects and has excellent thermochemical stability when in contact with α-alumina [50]. Nevertheless, significant further reductions in superalloy surface temperatures (or ceramic coating thicknesses) could be achieved if lower thermal conductivity ceramic coating compositions were substituted for this material. Interest in raising the gas turbine engine operating temperatures (to enhance engine cycle efficiency) has also exposed a potential weakness of the YSZ system. If 7YSZ is heated above 1200 °C, it undergoes a phase transformation from the metastable *t′*-phase to a mixture of the equilibrium tetragonal (t) and cubic (c) phases [21]. During subsequent cooling, the t phase transforms to a monoclinic (m) structure with a significant (~4.5 vol.%) volume expansion which promotes coating failure [21]. New ceramic compositions that do not suffer phase changes over the temperature range of this future applications are therefore of interest.

Finally, it has also been realized that the sintering rate of ytrria stabilized zirconia rapidly increases with temperature [21]. This decreases the pore volume fraction in the coating and facilitates diffusion bonding of the vertical cracks and pores [50]. These effects increase the coatings thermal conductivity and its in-plane modulus. The former leads to a more rapid TGO growth and the latter to an increase in the strain energy within the TBC layer which is then available to drive interfacial (delamination) failure [23]. These issues have motivated a search for alternative ceramics with lower thermal conductivity, improved high temperature phase stability, better sintering resistance, and an erosion and foreign object impact resistance comparable to the current material [43, 93].

Samarium zirconate (ZrO_2-33 mol% Sm_2O_3) is of particular interest for TBC applications since this pyrochlore appears to be phase stable up to its melting point 2200 °C, shown in Fig. 7-1 [121]. Its thermal conductivity (at 700 °C) is reported to be ~1.5 W/mK which is very low compared with that of 7 wt% Y_2O_3 stabilized zirconia (~2.3 W/mK). Its thermal expansion coefficient is 10.8×10^{-6}/°C which is comparable with that of 7YSZ. Preliminary experimental studies of sintering also indicate it has a low sintering rate at least up to a temperature of 1400 °C [122].

Samarium zirconate also appears to be amenable to deposition by electron beam evaporation techniques. However, the high cost of the rare earth element requires its efficient use during vapor deposition. Gas jet based evaporation techniques such as electron-beam directed vapor deposition (EB-DVD) have been shown to have a high material deposition efficiency under some conditions [76]. Their multi-source capability also facilitates the deposition of multilayers (eg. 7YSZ/zirconate coatings) that might be needed to avoid thermochemical incompatibilities with alumina [95, 119]. Here, we describe the deposition of samarium zirconate coatings using a DVD approach and investigate the effects of substrate rotation rate and deposition temperature on the coatings density, pore morphology, texture and microstructure. Their influence upon the coatings thermal conductivity and thermal cycling is also assessed. The observations are contrasted with those reported recently for identically grown and characterized 7YSZ coatings [134].

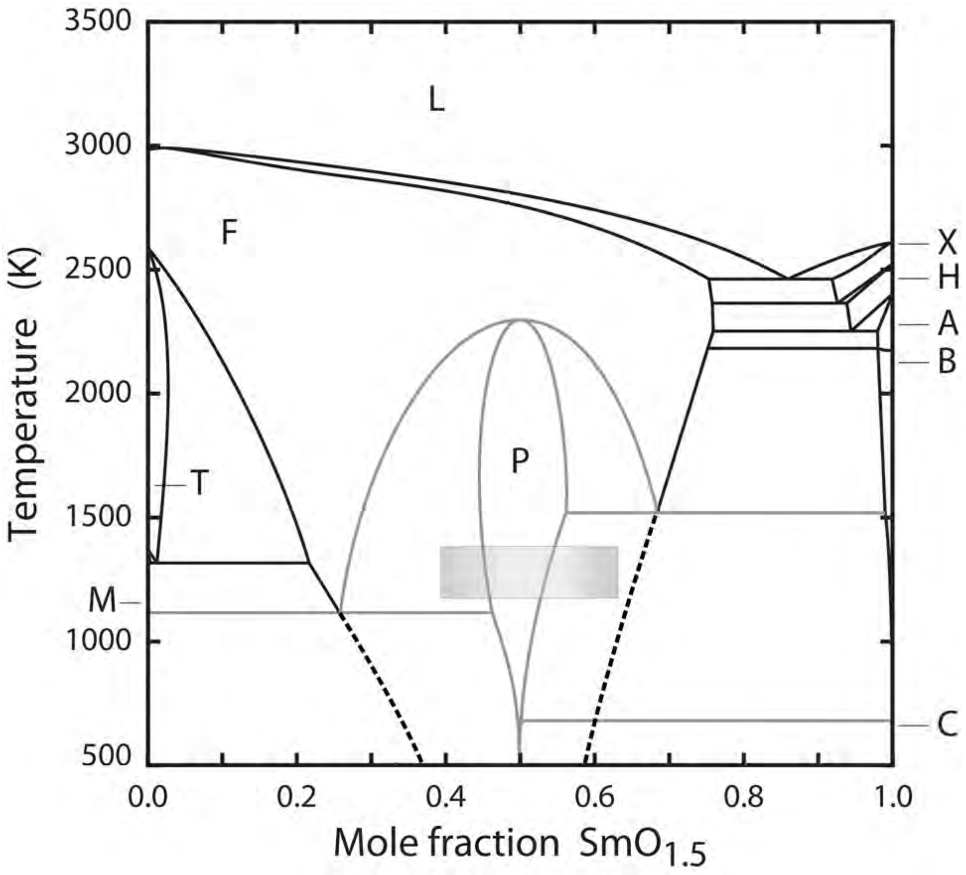

Figure 7-1. The ZrO_2-$SmO_{1.5}$ phase diagram (adapted from reference [117]). When pyrochlore (P) phase ordering is kinetically suppressed, as in the current work, the extended fluorite solid solution would be bound by the extrapolated M + F and F + B boundaries (denoted by the dashed lines). The shaded area in the middle of the metastable fluorite field shows the deposition temperature range and the maximum variation in $SmO_{1.5}$ observed in the experiments. Note that the minimum fluctuation observed (±5%) would fall mostly within the single phase pyrochlore upon ordering, whereas larger fluctuations could lead to two-phase F+P and P+B mixtures.

7.2 Experimental Setup

Samarium zirconate coatings were deposited on both stationary and rotated substrates using an EB-DVD technique at the rotation rate of 0, 0.5, 1, 6, 12 and 20 rpm. The deposition conditions were nominally identical to those used for 7YSZ which are described elsewhere [134]. The evaporation source was a 12.5 mm diameter SZO rod (TCI Ceramics Inc., MD). The chemical composition of the rod measured by energy-dispersive X-ray spectroscopy (EDS) was $48ZrO_2$-$52SmO_{1.5}$ (in mole percent). The substrate temperature was monitored and maintained at a prescribed level during deposition using a thermocouple placed very close to the substrate. We note that there is a difference between the actual temperature of the deposition surface and that measured by the thermocouple, but for the purposes of this comparative analysis they are assumed to be the same. A systematic investigation of the effect of the putative substrate temperature (900-1100°C) and rotation rate (0-20 rpm) upon the coating morphology, density and thermal conductivity was then conducted. The deposition rate was 10±2 μm/min for the samples deposited without rotation and approximately 3-4 μm/min for all others.

7.3 Results

Typical microstructures of the EB-DVD SZO coatings are illustrated in Fig. 7-2. Measured thicknesses ranged from ~65 to 110μm. The average bulk composition was $Sm_{2.1}Zr_{1.9}O_7$: slightly off stoichiometry but relatively consistent with that measured for the source rod. In contrast, the backscattered electron images in Fig. 7-2 reveal fluctuations from the average $SmO_{1.5}$ content within each coating. The amplitude of these fluctuations varied from sample to sample. The lowest variation of ±5% was found for a non-rotated specimen, Fig. 7-2(a), but some of the rotated coatings had higher variations (up to ±12% for the specimen rotated at 20 rpm) Fig. 7-2(b). There was no apparent correlation between the deposition conditions and the extent of compositional heterogeneity. Rather, it appears that the significant vapor pressure difference of the constituent cations has created melt instabilities leading to unsteady evaporation of the two species. As with 7YSZ, the texture and morphology of the SZO coatings grown by DVD were highly sensitive to the growth conditions. The salient observations are described below.

7.3.1 Deposition temperature effects

The morphology of the SZO coatings was strongly affected by the substrate temperature during deposition. Figure 7-3 shows surface and through thickness fracture surface images of coatings deposited at 900°, 1000° and 1100°C using a fixed substrate rotation rate of 6 rpm. All three coatings were composed of relatively tightly packed growth columns with faceted tips. At the higher temperatures, Fig. 7-3(c), the tips had a well-defined 4-sided pyramidal shape typical of fluorite derivative structures and were similar to those seen in 7YSZ [65, 154] and other zirconates [155]. The growth columns had a strong $\langle 200 \rangle$ preferred orientation. As the deposition temperature decreased, secondary crystals started to appear on the growth surface, e.g. Fig. 7-3(b), and these became sufficiently numerous at 900°C to make the shape of the tips appear rough and indistinct, Fig. 7-3(a).

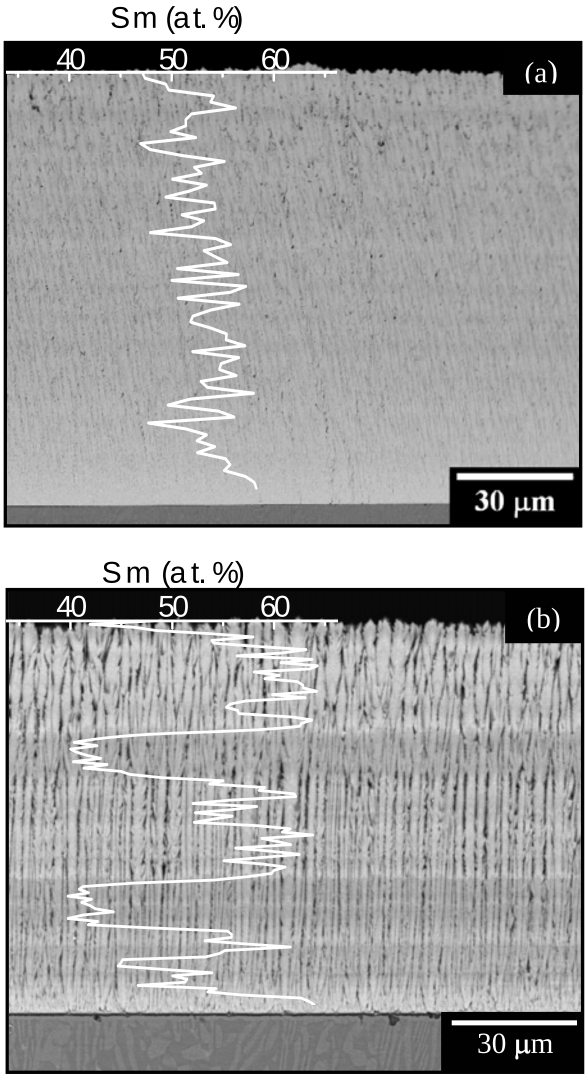

Figure 7-2. Back scattered electron images of typical SZO coating microstructures deposited at 1000°C with superposed composition profiles determined by EDS. The banding is a manifestation of variation in the samarium content through the thickness. (a) Coating deposited without rotation, exhibiting a samarium fluctuation of < ±5 at%Sm. (b) A coating deposited at a high rotation rate where the fluctuation was up to ±12 at%Sm.

Examination of the through-thickness fracture surfaces, Figs. 7-3(d-f), reveals a fairly typical columnar structure for coatings grown at the higher temperatures. These are again reminiscent of those seen in EB-PVD coatings [62]. The structure formed at 1100°C, Fig. 7-3(f), appears more regular than one might infer from the top view, Fig. 7-3(c), with columns separated by distinct intercolumnar gaps and well-developed feathery pores within the columns. These have been designated in earlier papers as Type I and II porosity respectively [74, 134]. As the temperature decreases to 1000°C the fracture surface reveals incipient branches growing off the column sides, Fig. 7-3(e), but the main columns are still clearly identifiable. Further reduction in deposition temperature to 900°C, however, leads to highly branched columns with an apparent loss of the feathery morphology. The distinction between intra- and intercolumnar pores on the fracture surface also becomes blurred, as seen by comparing Figs. 7-3(d) and (f). One might envisage the structure in Fig. 7-3(d) as containing two main columns each consisting of multiple sub-columns oriented on average along the vertical axis. Examination of polished cross sections corresponding to this sample revealed that the scale of the branching increased with distance from the substrate (Fig. 7-4). Even so, some of the coarser “branches” under the surface still exhibited the fine feathery pore structure associated with a high through thickness thermal resistance. Fig. 7-5 shows high magnification micrographs of the columns to more clearly reveal the feathery structures.

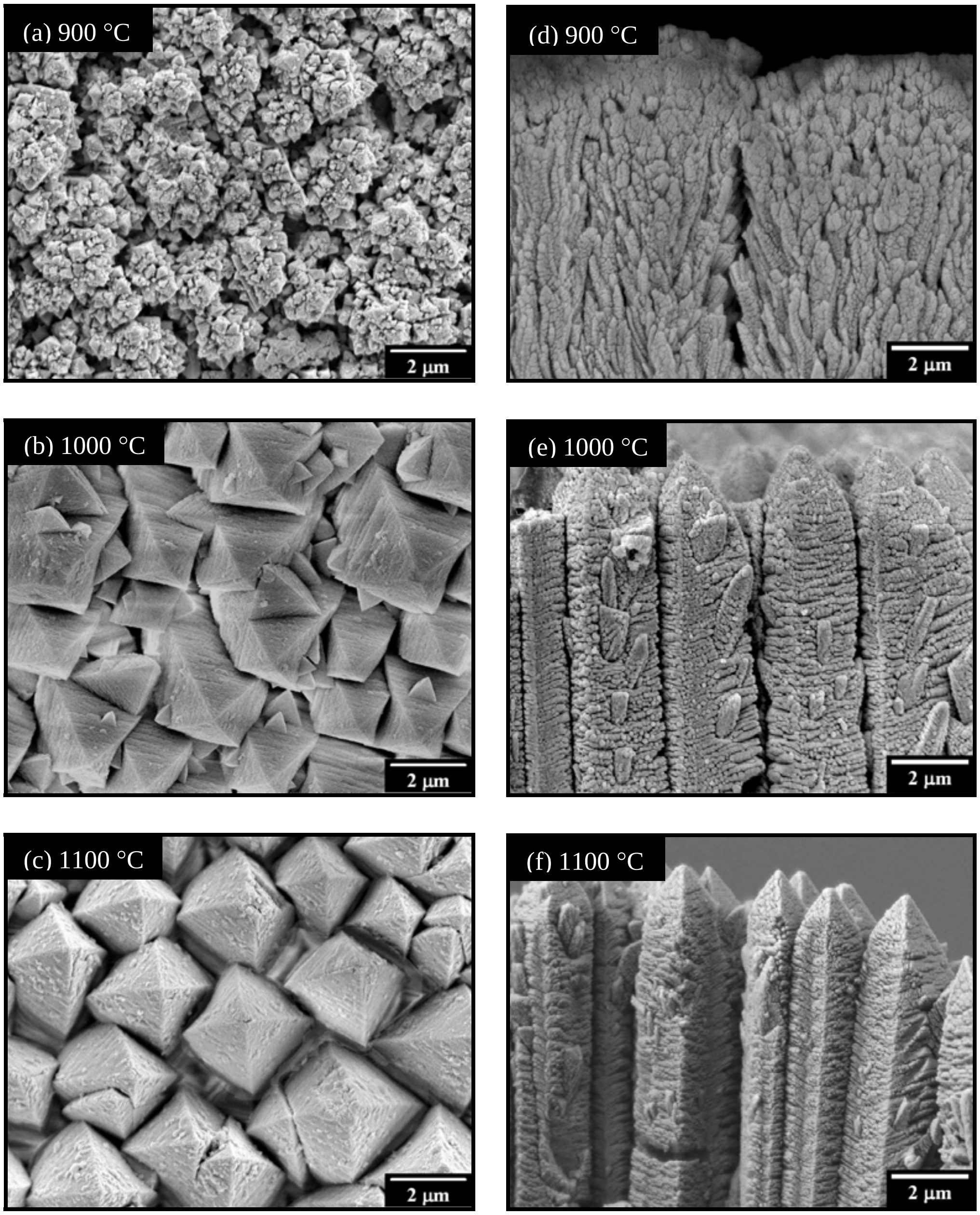

Figure 7-3. Surface topology (a-c) and through thickness fracture surface images (d-f) of SZO coatings deposited at temperatures of (a and d) 900°, (b and e) 1000° and (c and f) 1100°C on substrates rotated at 6 rpm. Note the increase propensity for growth column branching as the deposition temperature is reduced.

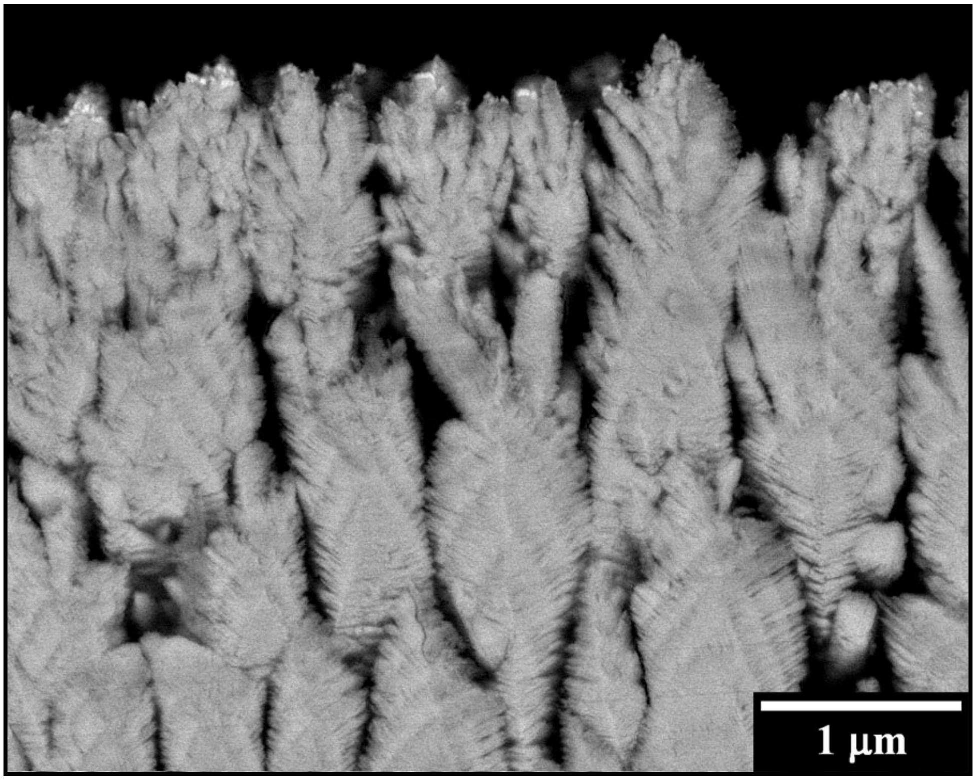

Figure 7-4. A polished cross-section of the sample deposited at 900^{o}C that shows the multiply branched columns near the coating surface. Fine scale “feathery” porosity within the growth columns is responsible for the chevron shading.

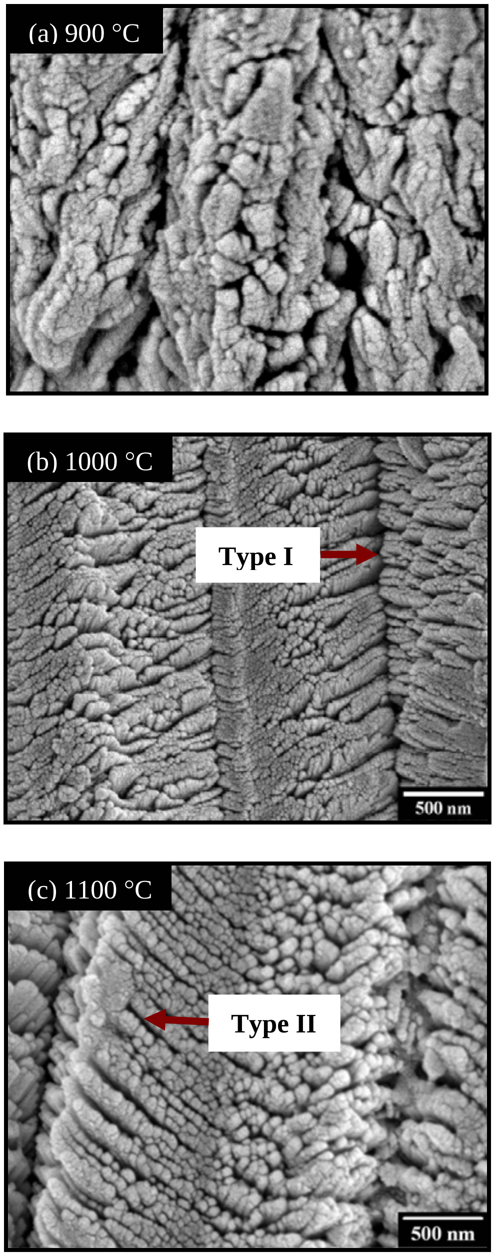

Figure 7-5. Cross-sections of $Sm_2Zr_2O_7$ coatings deposited at temperatures of 900°, 1000° and 1100 °C on substrates rotated at 6 rpm. Note the increase in growth column widths as the temperature of deposition was increased. The intercolumnar (Type I) and feathery (Type II) pore structures are also shown.

XRD patterns of coatings deposited at the different substrate temperatures (all at 6 rpm) are shown in Fig. 7-6. All of the peak positions are consistent with the fluorite (disordered) form of $Sm_2Zr_2O_7$ [156] with a lattice parameter 0.5285 nm. When doubled to account for the ordering in the pyrochlore structure, this is slightly lower than the reported value of 1.0594 nm for samarium zirconate [156]. The peak intensities reveal a predominant $\langle 200 \rangle$[1] out of plane texture at all temperatures, with minor amounts of secondary orientations present at the higher temperatures (most notably $\langle 111 \rangle$). The consistency of the strong $\langle 200 \rangle$ texture across the temperature range is rather remarkable in the context of the substantial changes in the columnar structure in Fig. 7-3. Pole figures also suggested preferred in-plane orientations but these are less distinct than those reported for conventional EB-PVD 7YSZ [62, 65] and gadolinium zirconate [123].

---

[1] Crystallographic notation referred to the fluorite structure. The equivalent pyrochlore planes have doubled indices, i.e. $\{200\}_F = \{400\}_{Py}$.

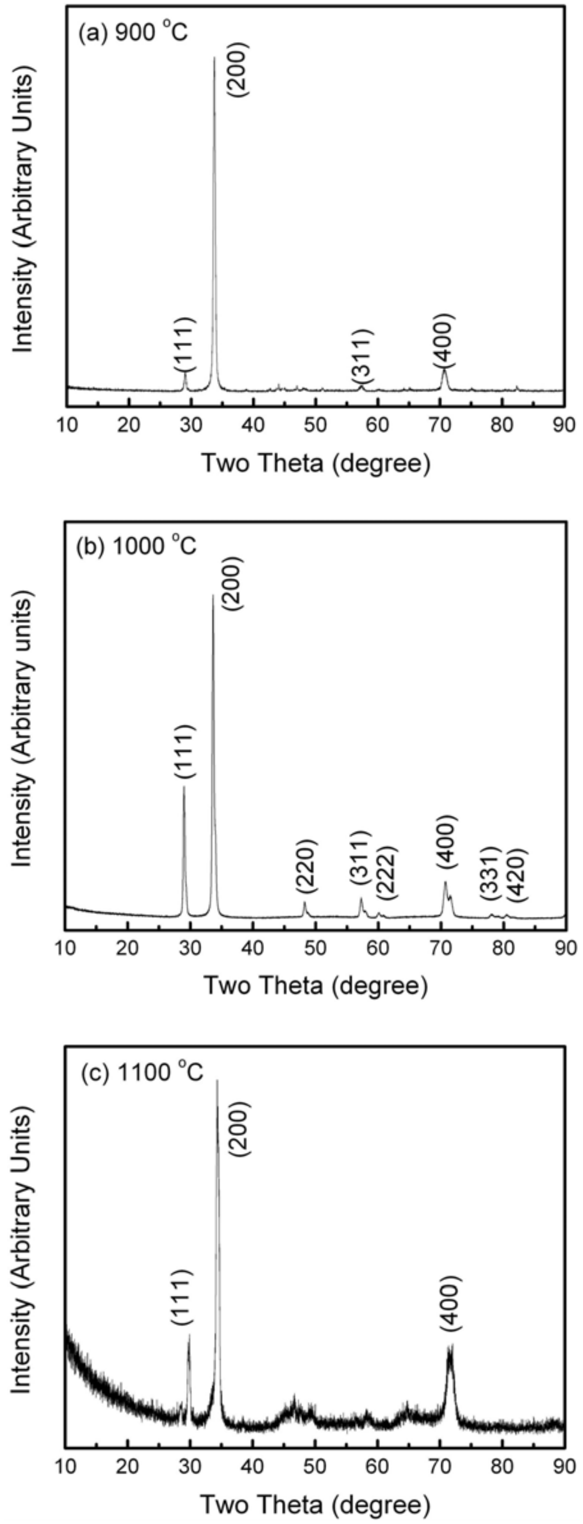

Figure 7-6. X-ray diffraction patterns for SZO coatings deposited at nominal substrate temperatures of (a) 900°, (b) 1000° and (c) 1100°C. The rotation rate was 6 rpm.

The density (ρ) and through thickness thermal conductivity (k) of the SZO coatings were measured as a function of the deposition temperature and are compared on a normalized basis with data for similarly grown 7YSZ coatings in Fig. 7-7. The conductivities (k_o) of the theoretically fully dense (ρ_o) 7YSZ and SZO at ambient temperature are taken as 3 and 2 $W \cdot m^{-1}K^{-1}$ based on [43]. Both normalized properties for SZO are lower than for 7YSZ, by ~5% for ρ/ρ_0 and ~8% by k/k_0. The porosity content of the zirconate is therefore slightly higher and slightly more effective at hindering heat transport in the through thickness direction. One should note, however, that these differences are close to the typical scatter of the measurement techniques utilized [157]. Both properties increase with coating deposition temperature, reflecting a concomitant decrease in porosity. However, the relative conductivity for SZO rises comparatively faster than its relative density with increasing deposition temperature. Relative conductivities after aging (Fig. 7-7b) are also lower for the zirconate, and it is notable that the values for the higher temperature are now distinctly separated, whereas those for the lower temperature are closer together.

7.3.2 Rotation rate effects

Examples of the morphology of columnar coatings grown at 1000°C on stationary substrates as well as those corresponding to the slowest (0.5 rpm) and highest (20 rpm) rotation rates are shown in Fig. 7-8. (Those for 6 rpm were shown in Figs. 7-3b and e). Polished cross sections are chosen for Fig. 7-8(d-f) instead of fracture surfaces (cf. Fig. 7-3(d-f)) because the latter were less informative, especially for the lowest rotation rate.

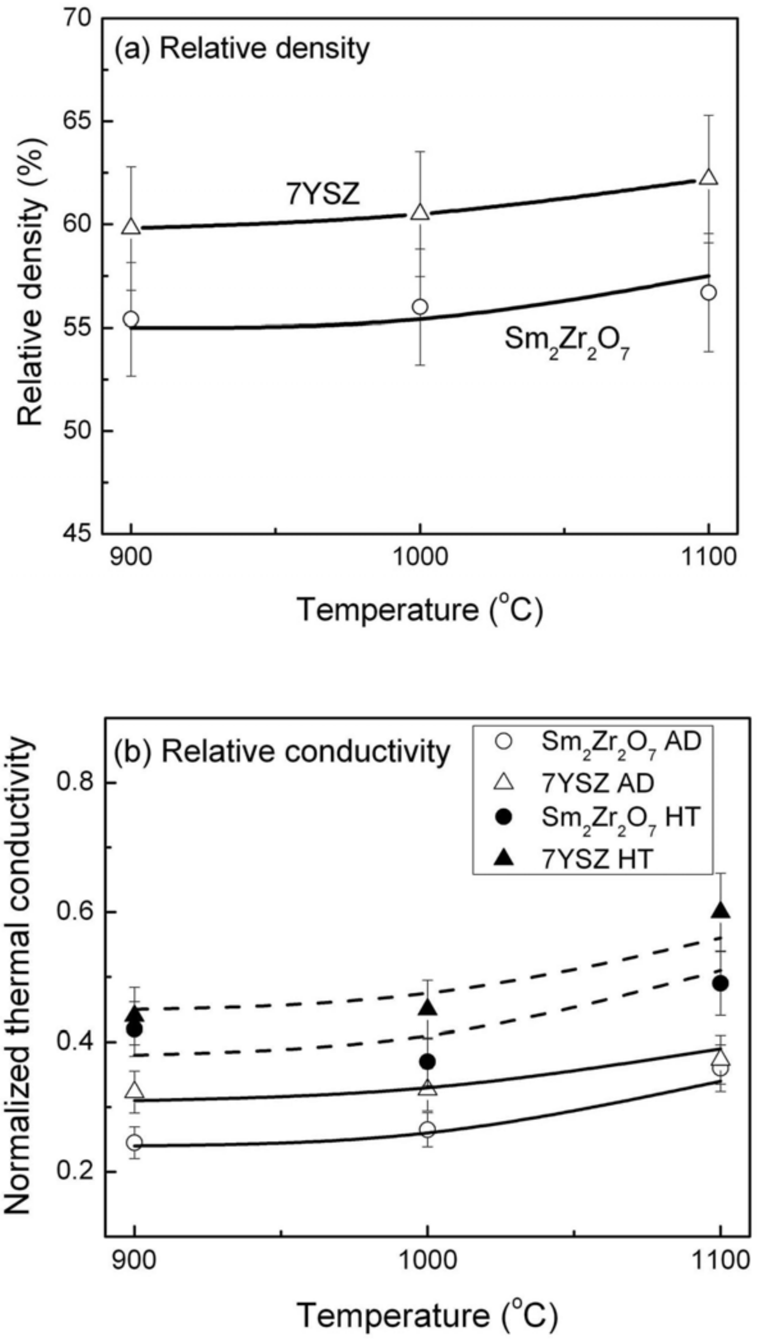

Figure 7-7. Effect of deposition temperature on the (a) density and (b) thermal conductivity of SZO DVD coatings, compared with those of YSZ deposited under the same conditions. The properties are normalized in both cases by those of the dense oxides. The rotation rate was 6 rpm. AD and HT denote as-deposited and heat treated for 10h at 1100°C.

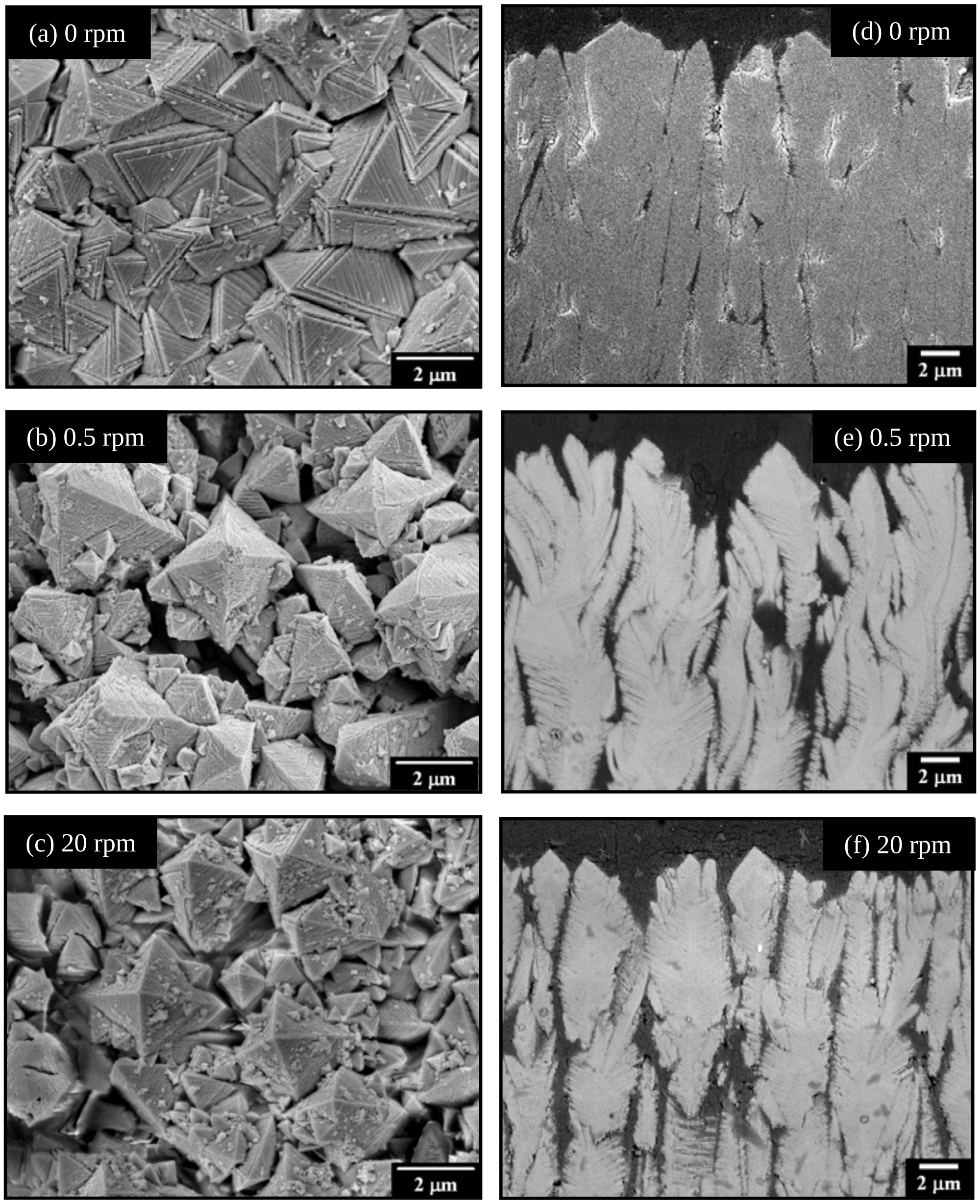

Figure 7-8. Surface topology (a-c) and polished cross section (d-f) of SZO coatings deposited at rotation rates of (a and d) zero, (b and e) 0.5 and (c and f) 20 rpm at a substrate temperature of 1000°C.

When the coatings were grown on stationary substrates under nominally normal incidence, as in Fig. 7-8(a), the growth surface was composed of column tips bound by triangular facets and was much more planar than those observed in YSZ grown under the same conditions [134], or on the samarium zirconate coatings grown with rotation, Figs. 7-8(b) and (c), which exhibited square-based pyramidal column tips bound by curved triangular faces. Some pyramidal tips are also evident in Fig. 7-8(a), but the majority of the triangular facets were oriented closer to the plane of the substrate. It is also noted that these facets show ledge-like features predominantly parallel to one of the sides. Highly magnified images of the ledges reveal the presence of fine scale pores extending into the interior of the of the growth columns, Fig. 7-9.

The cross sectional views in Fig. 7-8 show that the coating grown without rotation comprises closely packed columns with much narrower intercolumnar gaps than those grown with rotation. Interestingly, the columns in Fig. 7-8(d) still show “feathery” branches that are more similar to those found in rotated EB-PVD coatings than to those grown with stationary substrates [65]. These branches can be seen clearly in Fig. 7-9(a). These feathery pores appear to have formed as the ledges on the facet tips are laterally across the facet shadowing the material below, Fig. 7-8.

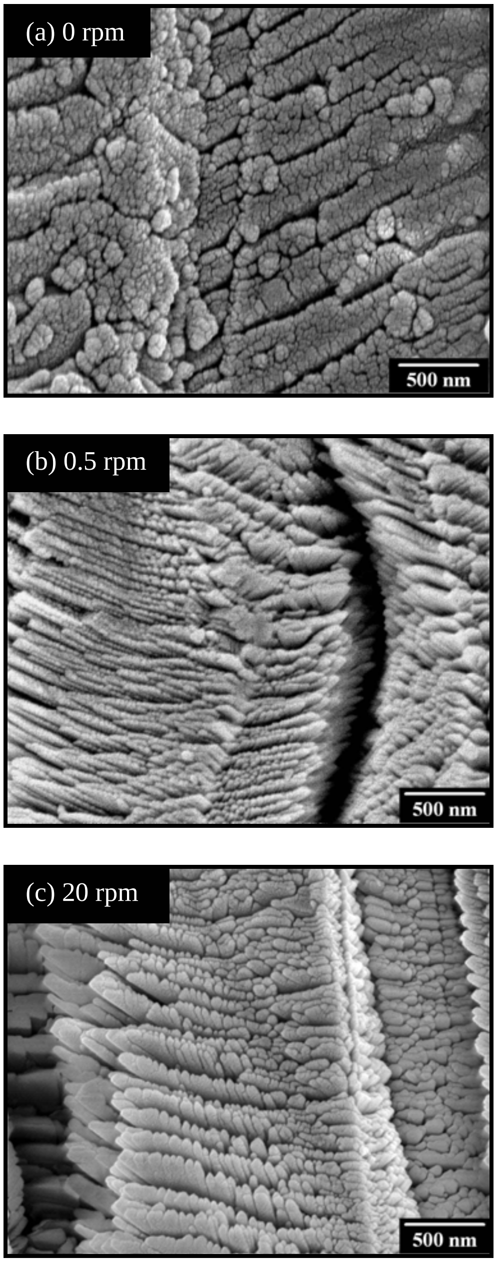

Figure 7-9. High magnification views of $Sm_2Zr_2O_7$ coatings growth columns grown (a) with no rotation, (b) at rotation rate of 0.5 rpm and (c) at 20 rpm. The coatings were deposited at a temperature of 1000 °C

Slow rotation at 0.5 rpm resulted in pronounced C-shaped columnar structures with a wavelength of ~10.8μm and similarly shaped intercolumnar gaps, Fig. 7-8(e). The wavelength is consistent with the rate of deposition and the period of a single revolution of the substrate. The columns are clearly defined and very thin near the substrate, but they become less distinct as they grow. This is a result of the concomitant widening and segmentation of the column tips, evident in Fig. 7-8(e), apparently occurring as the vapor flux orientation transitions from the “sunset” to “sunrise” part of the next rotation cycle [62]. With increasing rotation rate the C-shaped features become smaller and rapidly lose their identity as the growth front moves away from the substrate. The columns then adopt the more typical structure, as shown for the 20 rpm case in Figs. 7-2(b) and 7-8(f). The intercolumnar gaps are aligned close to the substrate normal, with typical feathery pores within each column.

XRD patterns in Fig. 7-10 are again indexable to the (disordered) fluorite form of the zirconate, regardless of the rotation rate. However, the relative intensity of the diffraction peaks changed with rotation rate, indicative of a change in the out-of-plane texture. Coatings grown on stationary substrates exhibit a dominant ⟨111⟩ peak, consistent with prior observations on similarly grown 7YSZ coatings [134] but with significant amounts of ⟨220⟩ and ⟨311⟩ reflections, which were not present in the latter. The implication is that the texture is mixed, as suggested by the top views of the growth surface in Fig. 7-8(a). The ⟨200⟩ reflections are much smaller in this case, but grow in intensity relative to ⟨111⟩ as the rotation rate increases, while the ⟨220⟩ and ⟨311⟩ peaks rapidly disappear. This was accompanied by a change in surface morphology from triangular facets in Fig. 7-8(a) to the pyramidal column tips characteristic of ⟨200⟩ growth in 7YSZ under similar conditions [134].

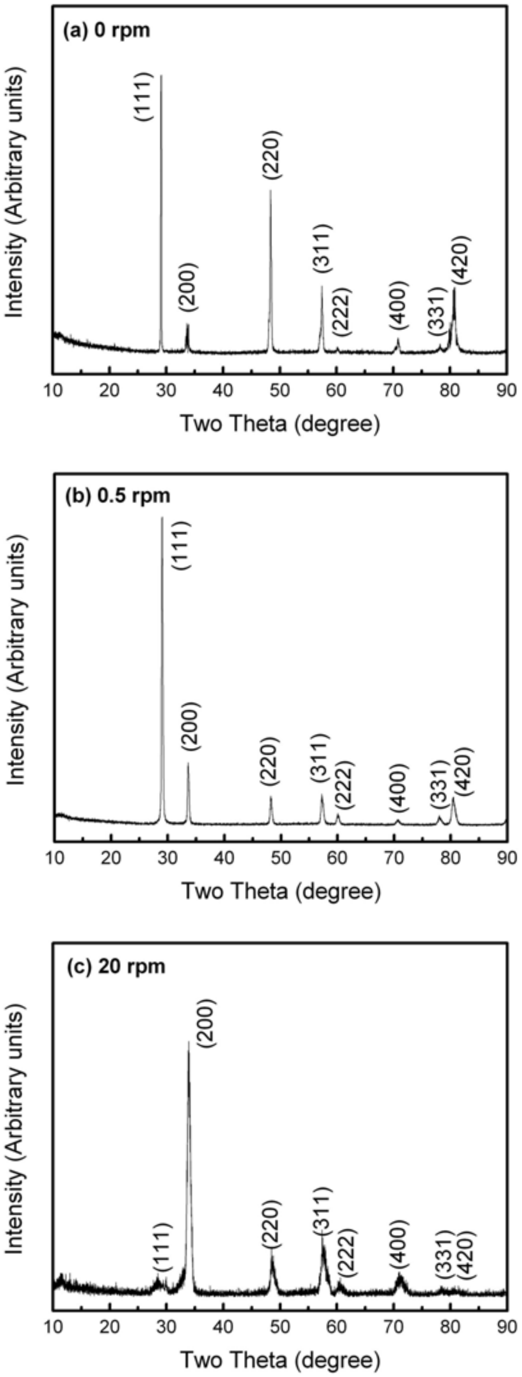

Figure 7-10. X-ray diffraction patterns of SZO coatings deposited at a temperature of 1000°C with rotation rates of (a) 0 rpm, (b) 0.5 rpm, and (c) 20 rpm. Compare also with coatings deposited at 6 rpm in Fig. 6(b).

The relative density and normalized thermal conductivity for the SZO coatings are shown as a function of the rotation rate in Fig. 7-11, and compared with similar data for 7YSZ [134]. Both materials exhibit similar trends with rotation rate in the as-deposited condition, with the individual property values being consistently lower for the zirconate for all rotation rates, (although we note that some of the differences are within the error of the measurements). The relative order seems to be reversed for the stationary samples, but the differences in conductivity are within the experimental scatter. The differences in conductivity are somewhat reduced after heat treatment (Fig. 7-11c) but the same trends persist.

7.4 Discussion

Salient findings from this study include; (i) confirmation that SZO can be deposited by DVD with microstructures suitable for thermal barrier coating applications albeit with some composition variability that requires further study; (ii) SZO is deposited with a metastable fluorite structure instead of the stable pyrochlore form; (iii) there exists overall similarity in crystallographic texture with 7YSZ grown under comparable conditions but the pore morphology appears to be more sensitive to deposition temperature in SZO; (iv) there are differences in porosity content and its evolution during high temperature aging that impact the thermal conductivity; and (v) there are no obvious difference in the lifetime of the SZO coating which were deposited on the polished and grit-blasted bond coats, which means the bond coat processing is not an important factor that affect the TBC failure. These findings are further discussed below.

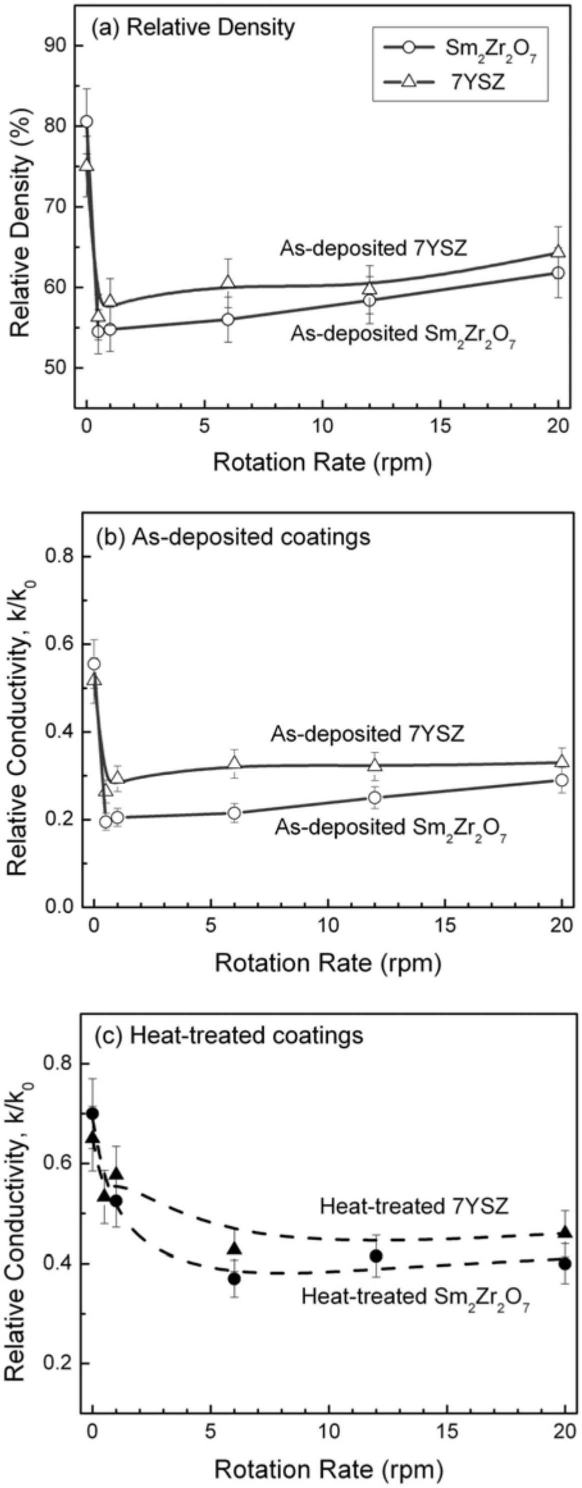

Figure 7-11. Effect of rotation rate on the (a) density, and thermal conductivity of (b) as-deposited coatings and (c) coatings heat-treated 10h at 1100°C. Values for 7YSZ and SZO coatings deposited at the same substrate temperature (1000°C) are compared, normalized by the corresponding property for the dense oxide.

7.4.1 Coating composition

In principle, the composition of a multi-component vapor should be different from that of the melt from which it emanates, as dictated by the vapor pressures of the pure components and their activities in the melt. In the case of oxides, there are additional concerns about dissociation reactions, e.g. the vapor of a ZrO_2-$MO_{1.5}$ (M = Y or rare earth) alloy may contain Zr, ZrO, ZrO_2, M, MO, O and O_2 [158]. It is also known that one may establish a steady state evaporation condition wherein a solid is continuously fed into its melt and the vapor forming from the melt has the same composition as the solid, albeit not that of the melt. This is claimed to be feasible as long as the vapor pressures of the components are not too dissimilar (reportedly by no more than two orders of magnitude) [159].

Information on the vapor pressures of the relevant species over ZrO_2-M_xO_y melts is generally not available in the literature, although estimates could be made based on data for the corresponding solids. (The slope should change moderately at the melting point but the curve should be essentially continuous.) The available (calculated) data for the relevant solids is summarized in Fig. 7-12, plotted as ratios to the total vapor pressure of the two dominant Zr bearing species, i.e. $p_{MO}/p_{(ZrO+ZrO_2)}$. It is reported that for all the other oxides in this figure the dominant species is the sub-oxide MO [158]. Also plotted are the vapor pressures of MO and ZrO over two equi-molar compositions, namely $Zr_{0.5}M_{0.5}O_{1.75}$, where M = Y, La. (La occurs as a pyrochlore compound that melts congruently, whereas the equivalent Y composition is a fluorite solid solution and melts incongruently.) The relevant temperature range is above the liquidus, T_L, which is marked in Fig. 7-12 for 7YSZ and the three zirconates that have attracted the most interest for TBC technology.[2]

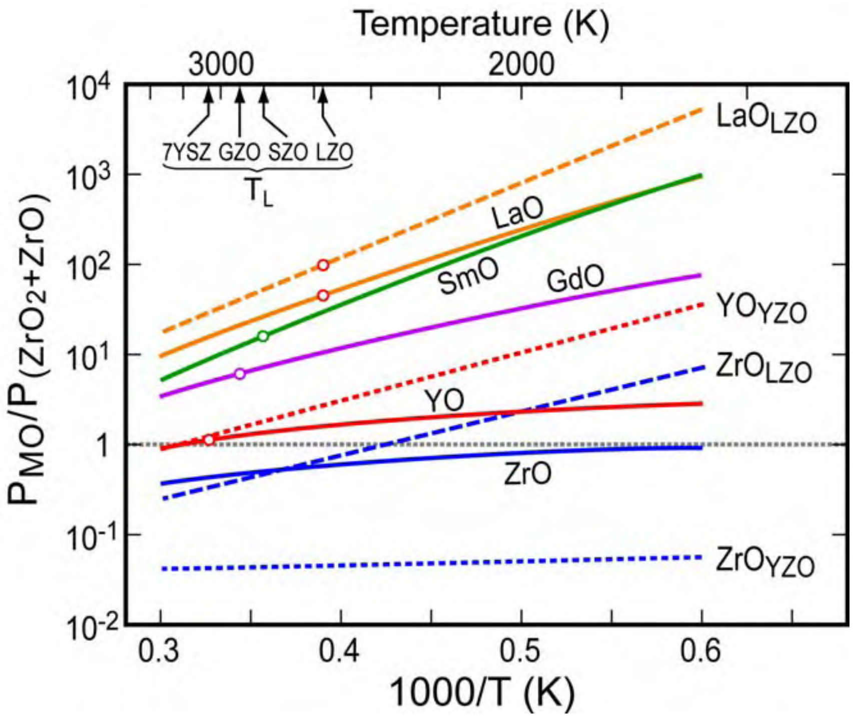

Figure 7-12. Reported vapor pressures for oxide species expected during evaporation of Y and rare-earth oxides of interest and the corresponding zirconates.

Figure 7-12 reveals that the partial pressure of the dopant monoxide is usually higher than the total of the Zr-bearing species, but is within a factor of $\leq 10^2$ for the relevant temperature range, and also that $p_{MO}/p_{(ZrO+ZrO_2)} \rightarrow 1$ for all MO at some critical temperature above T_L. The implication is that it should be possible, to evaporate and

---

[2] Note that the curve for LaO_{LZO} does not bend at the liquidus temperature of LZO, suggesting the calculation in [158] Jacobson NS. Thermodynamic Propertities of Some Metal Oxide-Zirconia Systems. NASA Technical Memorandum 102351. Cleveland, Ohio: Lewis Research Center, 1989. p.62. ignores the solid/liquid transition.

deposit combinations of these oxides with ZrO_2 and preserve the original composition. Upon closer examination it is evident that $p_{MO}/p_{(ZrO+ZrO_2)}$ ~1 for Y at the 7YSZ liquidus but diverges progressively from unity in the order YO < GdO < SmO < LaO. This is qualitatively consistent with the observed difficulty in preserving composition uniformity during deposition here and elsewhere [119, 155]. The reality is, however, more complicated. Note that p_{MO} diverges more from $p_{(ZrO+ZrO_2)}$ for the $Zr_{0.5}M_{0.5}O_{1.75}$ compositions than for MO above the pure M_2O_3 oxides, suggesting a significant effect of the relative activities of the oxide/sub-oxide species in the melt. Concomitantly, there is a change in the relative populations of ZrO and ZrO_2 with the addition of the second oxide. Unfortunately, the paucity of thermodynamic information precludes any further analysis of the $Zr_{0.5}Sm_{0.5}O_{1.75}$ system. Moreover, while a full steady state is arguably not achieved, further understanding is needed of the interplay between melting and evaporation with variations in the beam power input and/or ingot feeding to explain the oscillations in composition along the thickness noted in Fig. 7-2. Process models that capture the complexity of the phenomena involved are necessary for this but do not exist at the present time.

7.4.2 Metastable fluorite structure

Deposition of SZO from the vapor occurs in a temperature range where the stable structure should be the ordered pyrochlore, as evident in Fig. 7-1(b), even when accounting for some deviation from stoichiometry as in the present case. However, XRD reveals no signs of ordering in the as-deposited material, Figs. 7-6 and 7-10, although the characteristic pyrochlore reflections (331, 511, etc.) are relatively weak and could be further obscured by texturing. This behavior is similar to that observed during EB-PVD deposition of GZO [123]. Absent cation ordering, the structure is a metastable defect fluorite, as shown by removing the pyrochlore phase field from Fig. 7-1 and extending the relevant phase boundaries of the fluorite field. Note that in spite of the compositional heterogeneity the coatings can all be single phase fluorite, although only those with narrower fluctuations can eventually order to single phase pyrochlore.

The lack of ordering may be understood from consideration of the atomic arrangements needed to generate the pyrochlore structure during growth, Fig. 7-13, and the relevant kinetic constraints. Regardless of texture, active growth takes place on {111} facets and the behavior is broadly similar to that observed in 7YSZ [57, 62, 65, 134], with some important differences. One is that 7YSZ grows directly in the t’ form, where all {111} planes are equivalent (although slightly asymmetric because of the tetragonality). In contrast, the cubic pyrochlore structure has two types of {111} planes with different stoichiometry, namely A_3B_1 and A_1B_3, Fig. 7-13(a,b). The pyrochlore pattern is established by stacking six alternating A_3B_1 and A_1B_3 planes in a specific sequence, normal to the $\langle 111 \rangle$ directions. When growing along the $\langle 100 \rangle$ axes with a pyramidal habit, Fig. 7-13(c,d), three of the four {111} facets bounding the tip have one stoichiometry while the fourth has the conjugate composition. The distribution is then reversed for each alternating set of layers. Because the vapor is in principle stoichiometric, A and B atoms (with their bound oxygen’s) arrive in equal proportions at the surface. For the pyrochlore pattern to evolve, the crystallization mechanism must involve the cooperative growth of several layers and concomitant diffusional rearrangement of the cations. The XRD results indicate that these processes are kinetically insufficient within the time scale of the deposition. It is possible that some local short-range ordering occurs, whereupon the as-deposited columns would be conglomerates of small coherent domains with different degrees of partial order.

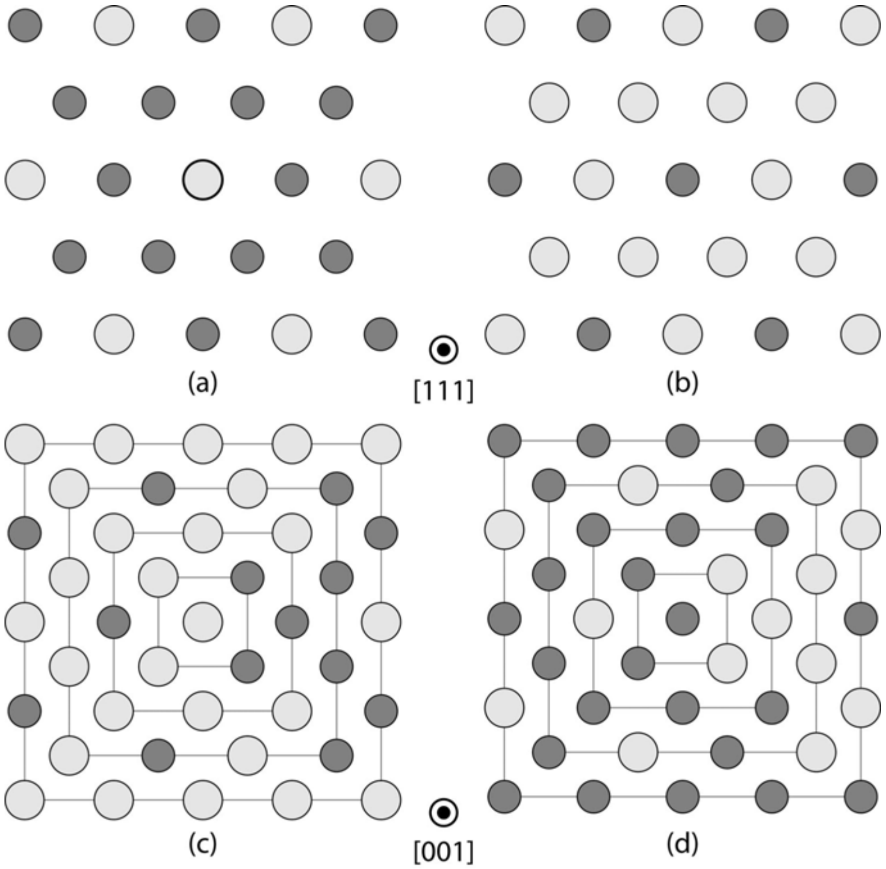

Figure 7-13. Atomic arrangement on the two types of (111) planes present in the pyrochlore structure (a, b), and the alternating configurations of (111) planes forming the pyramidal column tips for growth along the (001) direction. The darker circles represent the larger (Sm^{3+}) cations, and the lighter ones are the (Zr^{4+}) cations. Oxygens are omitted for clarity. Note that the stacking sequence along the (111) direction in the fully ordered pyrochlore involves 6 alternating planes of the types in (a, b) with different in-plane shifts.

7.4.3 Texture and morphology

In general, the crystallographic aspects of the texture developed in DVD SZO coatings resemble those reported for DVD 7YSZ [134], and PVD GZO [123] albeit not for LZO [155, 160]. The latter, however, were affected by much larger compositional heterogeneity (up to ±40%) and atypical columnar structures, so they are not suitable for comparison. DVD SZO coatings rotated at conventional rates (≥6rpm) exhibit predominantly ⟨200⟩ out-of-plane textures that have been explained in YSZ as a result of evolutionary selection [78] of special orientations wherein the tip facets can capture equal amounts of flux from the vapor during a rotation cycle [62, 65]. These coatings also exhibit preferred ⟨002⟩ in-plane orientations, justifiable on similar grounds. The texture of the rotated SZO coatings was generally less developed than that observed for YSZ at the same temperatures and rotation rates, i.e. minor amounts of other orientations were found mixed in with the dominant ⟨200⟩ columns. It is likely that this is due to the significantly smaller thickness of the SZO coatings, ~70±5% of their 7YSZ counterparts, implying that the evolutionary selection process was more advanced in the latter and the minor orientations had been screened out.

Texture selection under stationary deposition is less understood and more sensitive to temperature than in rotated specimens. Earlier work on PVD 7YSZ revealed the changes in the population of orientations from ⟨111⟩>>⟨220⟩ at 900°C to ⟨111⟩>>⟨220⟩>⟨311⟩ at 1000°C, to ⟨220⟩>>⟨311⟩>⟨111⟩ at 1100°C [65]. By comparison, the stationary DVD YSZ deposited at 1000°C had a predominant ⟨111⟩ texture [134], closer to that seen in

PVD coatings at 900°C, while SMO deposited under the same conditions exhibits nearly the same pattern of orientations as PVD YSZ at 1000°C. Some of the variability in 7YSZ might be ascribed to differences in the experimental set up, but it is more likely to result from the higher deposition rate of DVD that arguably has a similar effect on the time available for rearrangements at the surface than a lower temperature.[3] The same argument could not be used for the differences between DVD 7YSZ and SZO, but in this case the coating is significantly thinner in the zirconate, suggesting that the texture is not as developed as that in 7YSZ, an observation also made in the rotated specimens.

The samples deposited at very low rotation rates represent a special case because of the adjustments that are needed at the column tip facets as the growth direction changes over a 180° range and a long wavelength each revolution of the substrate. The tips (Fig. 7-8e) undergo exacerbated segmentation because the features on one facet build up substantially on the “sunrise” part of the cycle before the “sunset” portion occurs, biasing the shadowing process. The evolutionary selection process is arguably delayed, and the segmentation adds complexity to the possible spectrum of orientations at the surface.

Branching of the columns, particularly evident at the lower deposition temperatures (Fig. 7-3) also complicates texture development. Similar effects have been observed in LZO deposition [155] and ascribed to the occurrence of re-nucleation, but the coatings in that case did not appear to have any preferred orientation. That is certainly not the case here,

---

[3] Note that the concept of a “homologous” temperature does not work well here since the melting temperature of SZO is significantly lower than that of 7YSZ, so the same substrate temperature would imply a higher T/T_M and “faster” diffusion. The argument is obviously too simplistic because diffusion is slower in the pyrochlore, but one must remember that the structure growing is fluorite, where the cation arrangement is random and therefore the effects on diffusion should be diminished.

although there are obviously multiple smaller crystallites often observed on the tips of columns, e.g. Figs. 7-8(b) and (c). Several scenarios are then possible. In one, the "nuclei" form by cluster condensation in the vapor and subsequent landing on the growth surface. In that case the clusters may give rise to mis-oriented branches that are occluded by the growth of the larger columns, cf. Figs. 7-3(b) and (c). Alternatively, the clusters may be able to re-orient themselves shortly after landing on the surface and give rise to a new but oriented growth center, producing a branch because of shadowing but still being competitive in an evolutionary selection process. Finally, it is also possible that there is heterogeneous nucleation of a new crystal with a twin orientation, but that would require local ordering to develop as a separate growth center.

7.4.4 Porosity and thermal conductivity

With the exception of the coatings on stationary substrates, the relative density (and pore fraction) depends rather weakly on deposition temperature, Fig. 7-7(a) and rotation rate, Fig. 7-11(a). However, the thermal conductivities of both SZO and 7YSZ exhibit a quite strong, nonlinear dependence upon pore volume fraction, Fig. 7-14(a). The SZO coatings grown here have thermal conductivities that range from 0.4 to 1.1 W/m·K; much lower than that of identically grown 7YSZ coatings. Data for the thermal conductivity of EB-PVD YSZ coatings is shown on Fig. 7-14(a) as a comparison [135, 140]. Most of these coatings have a higher density and thermal conductivity than the EB-DVD coatings even though similar deposition temperatures were used. The differences in conductivity appear to arise almost entirely from the substantially different intrinsic thermal conductivities of the two materials. To illustrate this, the thermal conductivity dependence upon pore fraction has been fitted to an expression of the form:

$$k_{coating} = K \cdot k_{int\,rinsic} \cdot (1 - f)^{n} \tag{1}$$

where, $\kappa_{coating}$ is the coating thermal conductivity, $\kappa_{intrinsic}$ is the intrinsic thermal conductivity of the material from which it is made [43], f is the pore volume fraction and n is an exponent. The ambient temperature thermal conductivity of fully dense SZO has been measured to be ~2.0 W/mK [43], while that for bulk 7YSZ is ~3.0 W/mK [43]. Combining DVD and PVD data, it is found that the 7YSZ and SZO behaviors in Fig. 7-14(a) are best fitted by an exponent, n = 2.5.

A plot of the K factor against the pore fraction, Eq. (1), is shown in Fig. 7-14(b). It clearly reveals that K is reasonably is close to unity for both materials, from which one may infer that the differences in the measured conductivity to first order arise from $k_{intrinsic}$. The separation of the two curves in Fig. 7-14(b) as the pore fraction increases is likely the result of the sensitivity of the pore morphology to temperature and rotation rate. Note, for example, that the lowest density (highest porosity) corresponds to the lowest rotation rate in Fig. 7-11(a), wherein the heavily curved columns near the bottom provide much larger barriers to heat transfer than the straight intercolumnar gaps in conventional structures.

Finally, it is worth noting that the heat treatment seems to have as strong an effect upon the density and thermal conductivity of the SZO DVD coatings as it does on their 7YSZ counterparts. In principle, this is inconsistent with the reportedly higher resistance to sintering of zirconates [161]. The implication is that the driving force for sintering must be dominant, presumably because of a substantially higher initial porosity contents introduced by the DVD process (cf. Figs. 7-7 and 7-11).

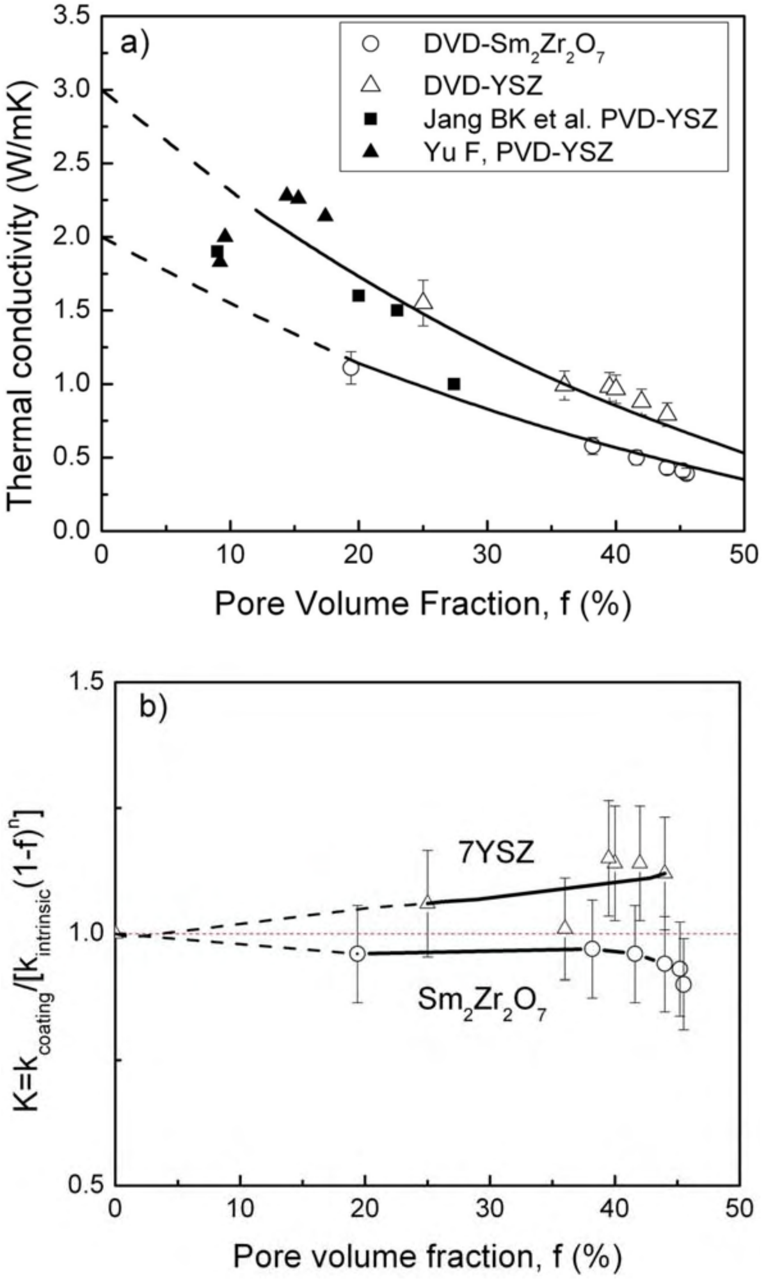

Figure 7-14. (a) The thermal conductivity and (b) the K factor in Equation (1) as a function of pore volume fraction (*f*) for SZO and 7YSZ coatings. The data for 7YSZ coatings are from references [135, 140].

7.5 Summary

$Sm_2Zr_2O_7$ coatings with microstructures suitable for thermal barrier coatings have been successfully synthesized by EB-DVD. The coatings exhibit compositional variation across the thickness of up to ±12%$SmO_{1.5}$, indicative of source instabilities induced in part by the difference in vapor pressures of the constituent oxides.

SZO coatings grow with a metastable fluorite structure due to kinetically constrained cation ordering within the time scale of the deposition process. This observation is in agreement with observations on other rare earth zirconates. The coating morphology is broadly consistent with those produced in 7YSZ and GZO by EB-DVD and EB-PVD, respectively, but becomes increasingly atypical with decreasing deposition temperature and/or at low rotation rates, both of which induce extreme branching of the columns. The origin of the branching is associated with shadowing in the low rotation specimens, but is less clear in the case of the lower deposition temperature.

The thermal conductivity of SZO DVD coatings is substantially lower than that measured on DVD 7YSZ or on EB-PVD Gd zirconate. The former is primarily due to the lower intrinsic conductivity of the SZO, whereas the latter is a result of the much higher porosity content produced by the DVD process. This high level of porosity, however, appears to drive pore reconfiguration during high temperature exposure at the same rate in SZO and 7YSZ, notwithstanding the expected lower diffusional rates in SZO.

Implementation of DVD SZO in thermal barrier systems appears viable but is likely to require improved control of the composition during growth, as well as a study of the optimum levels of porosity and the processing parameters needed to achieve them.

Chapter 8

Thermal Cycling of $Sm_2Zr_2O_7$ Coatings

8.1 Overview

As we presented in Chapter 7, a series of SZO coatings were grown using different rotation rates at 1000 °C on the NiCoCrAlY bond coated Hastelloy-X substrates. Some of these samples were grown on rough (grit-blasted) bond coats. The remainders were deposited on smooth (polished) bond coats. All the SZO coated samples were cycled between ambient temperature and 1100 °C under the same conditions that were used for the lifetime test of the 7YSZ samples (Chapter 6). As for the 7YSZ case, the thermal cycling lifetime was measured for the SZO coatings applied to both grit-blasted and polished NiCoCrAlY bond coats. The effect of the rotation rate upon the SZO coating lifetime has also been investigated.

8.2 Thermal Cycling Results

8.2.1 Rough bond coats

We begin by examining the cycling response of a ~70 μm thick SZO coating grown using a rotation rate of 6 rpm at 1000 °C on a rough bond coat surface. Figure 8-1 shows the evolution of the SZO coating as it was progressively cycled. Figures 8-1(a) and (d) shows the as deposited coatings morphology of its top surface and cross-section, respectively.

The coating has well-defined pyramidal column tips and a column width of 1-2 μm in the surface. In cross-section, it can be seen that the columns were initially parallel sided and began to side branch in the top 25 μm of the coating. The as deposited coating has a very thin ~0.3 μm TGO layer which is difficult to resolve in the cross-section view. It can be clearly seen in a higher magnification view, Fig. 8-2(a). The rough interface resulting from “grit blasting” between the SZO and the bond coat is also evident shown in the Fig. 8-1(d) and 8-2(a). Growth defects (“corn kernel” defects) have been circled in the figure and like the YSZ case appeared in locally depressions of the bond coat. These conical TBC imperfections, which form due to shadowing effects at interface irregularities during SZO deposition, are poorly bonded to the rest of SZO. As mentioned in the thermal cycling of 7YSZ (Chapter 6), these defects are preferred sites for ratcheting to initiate when the specimens are subjected to thermal cycling test.

After exposure to 50 cycles of thermal cycling at 1100 °C, significant sintering between the columns was evident in the coating, Fig. 8-1(b). The TGO layer also rapidly thickened to ~2.2 μm. Some Y-Al oxide pegs were also found in the TGO layer. These can be seen in Fig. 8-1(e) at low magnification. They are more easily recognized at higher magnification Fig. 8-2(b). As the cyclic oxidation continued, the SZO coating grown using a rotation rate of 6 rpm failed at ~250 cycles. Examination of the coating at this point, Fig. 8-1 (c) and (f), indicated that the neighboring growth columns had begun to sinter together and the surfaces of the faceted pyramidal tips had been smoothened. A large delamination crack can be observed at the interface of the SZO and TGO, in Fig. 8-1(f) and Fig. 8-2(c). A ~4 μm thick TGO layer was rapidly formed on the bond coat surface. Once again, it can be seen to contain some Y-Al oxide pegs. These pegs deeply penetrated into the bond coat. A “β-NiAl depletion zone” formed in the regions below the TGO layer is also evident, Fig. 8-1(f). It was also noticed that some small cracks appeared inside the TGO and these cracks propagated through some Y-Al oxide pegs, shown in Fig. 8-2(c).

Examination of Fig. 8-1(d)-(f) also showed that the pore volume fraction had decreased as the cycling continued, i.e. the columns reduced their surface area due to the sintering. Some bright and quite dense regions were marked in the coating (white spots). A linescan EDS analysis of the spalled sample is shown in Fig. 8-3. The coating still demonstrates a composition fluctuation of ±9 at%Sm., which is corresponding to the composition fluctuation discussed in Chapter 7. It is also noticed that those bright and dense regions correspond to places of relatively higher Sm content.

The effect of the rotation rate upon the cyclic lifetime of the SZO coatings is shown in Fig. 8-4(a). It can be seen that the SZO coatings have a short cyclic failure life compared to equivalently grown YSZ coatings; it was well below 300 cycles for most of specimens. The lifetime was again rotation rate dependent. As the rotation rate increased, the lifetime cycles slowly decreased like YSZ coatings. The coating density increases with the increasing rotation rate and thus the coating modulus, which will increase the strain energy in the coating and lead to the coating failure. All the SZO coatings spalled and detached just above the TGO layer.

As deposited

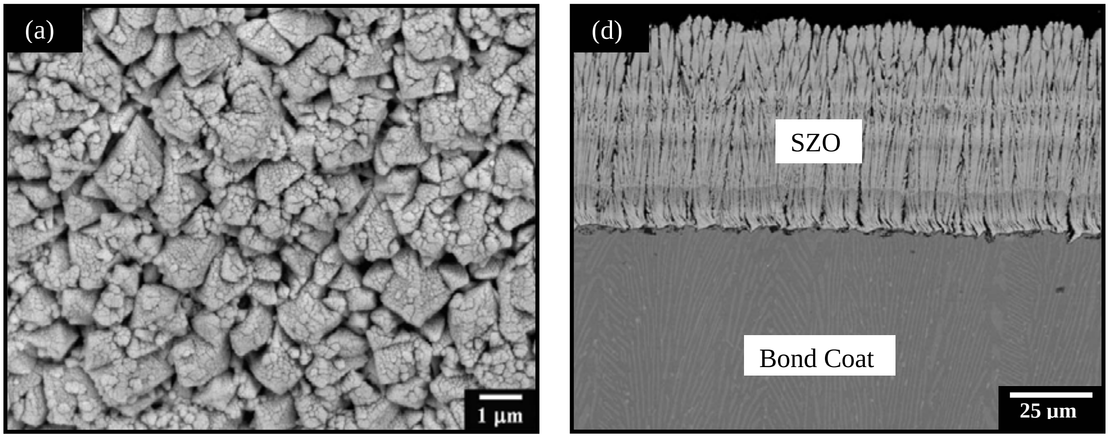

50 cycles@ 1100 °C

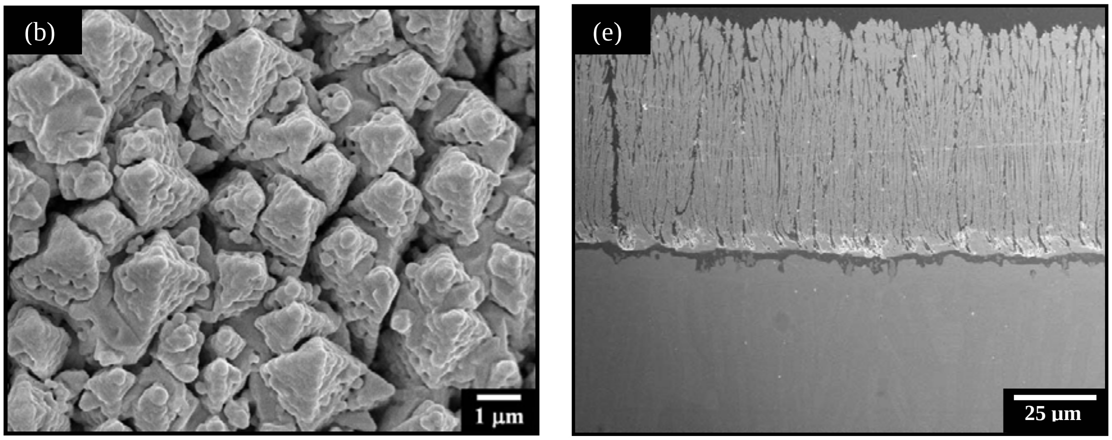

Spalled ~250 cycles

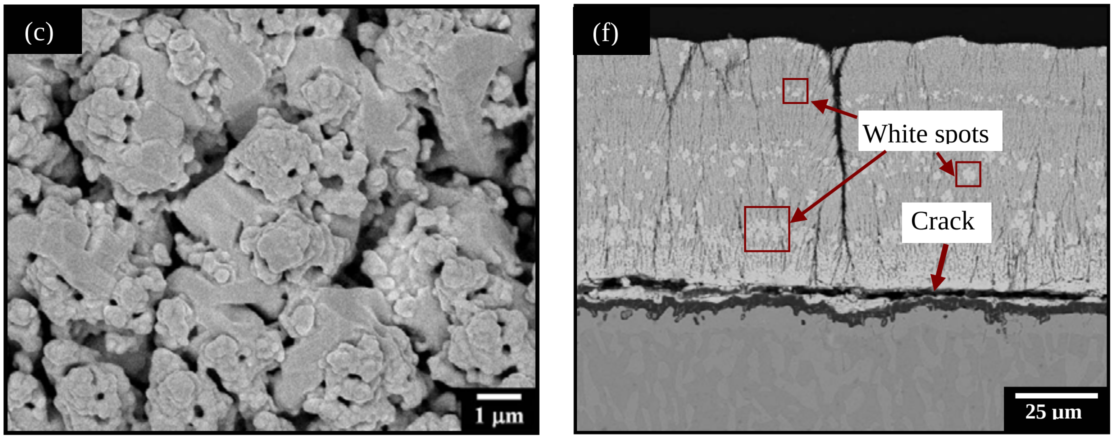

Figure 8-1. The morphology of an SZO coating on rough bond coat evolved with thermal cycling: (a, d) as-deposited, (b, e) after 50 thermal cycles and (c, f) after spallation. The coating was deposited at 1000 °C with a rotation rate of 6 rpm.

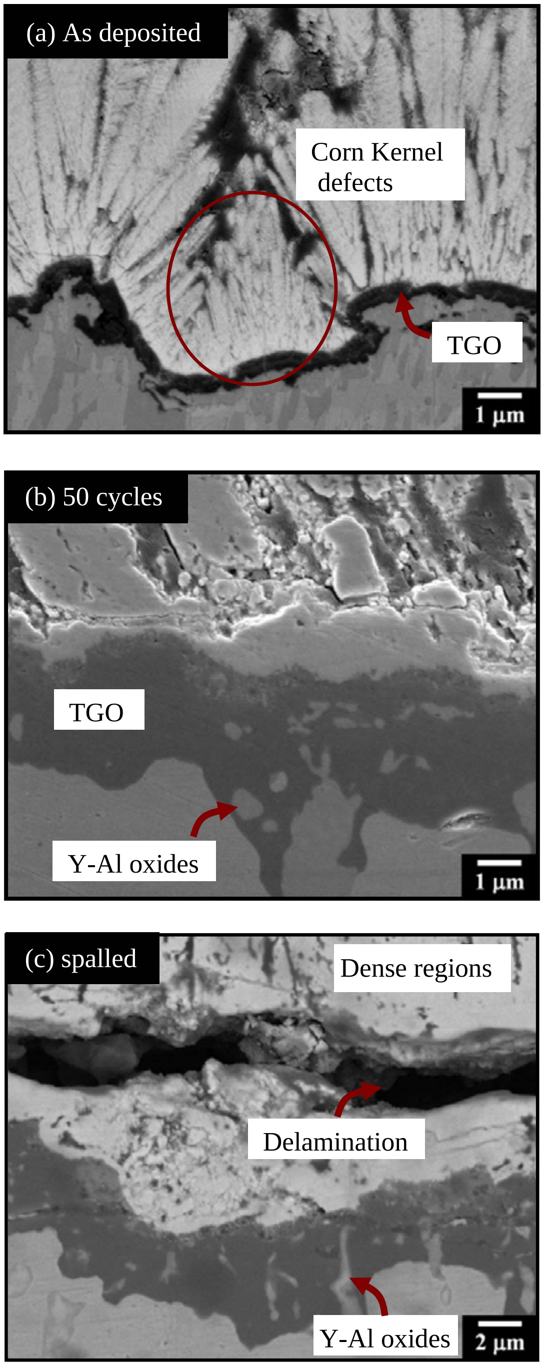

Figure 8-2. The TGO layer evolved with the thermal cycles: (a) as-deposited, (b) 50 thermal cycles and (c) the spallation at ~250 cycles.

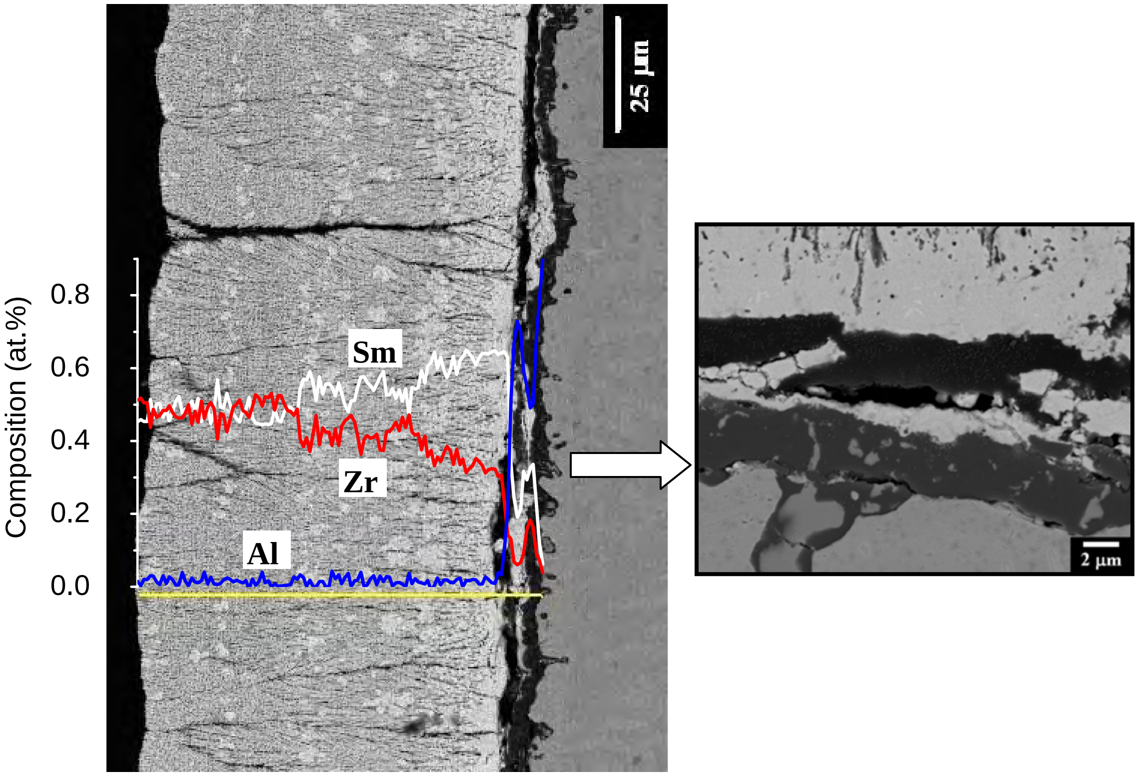

Figure 8-3. The linescan analysis of the spalled SZO sample. The coating still exhibits a samarium fluctuation of ±9 at%Sm after ~250 thermal cycles. White, red and blue lines represent the composition profiles of Sm, Zr and Al, respectively.

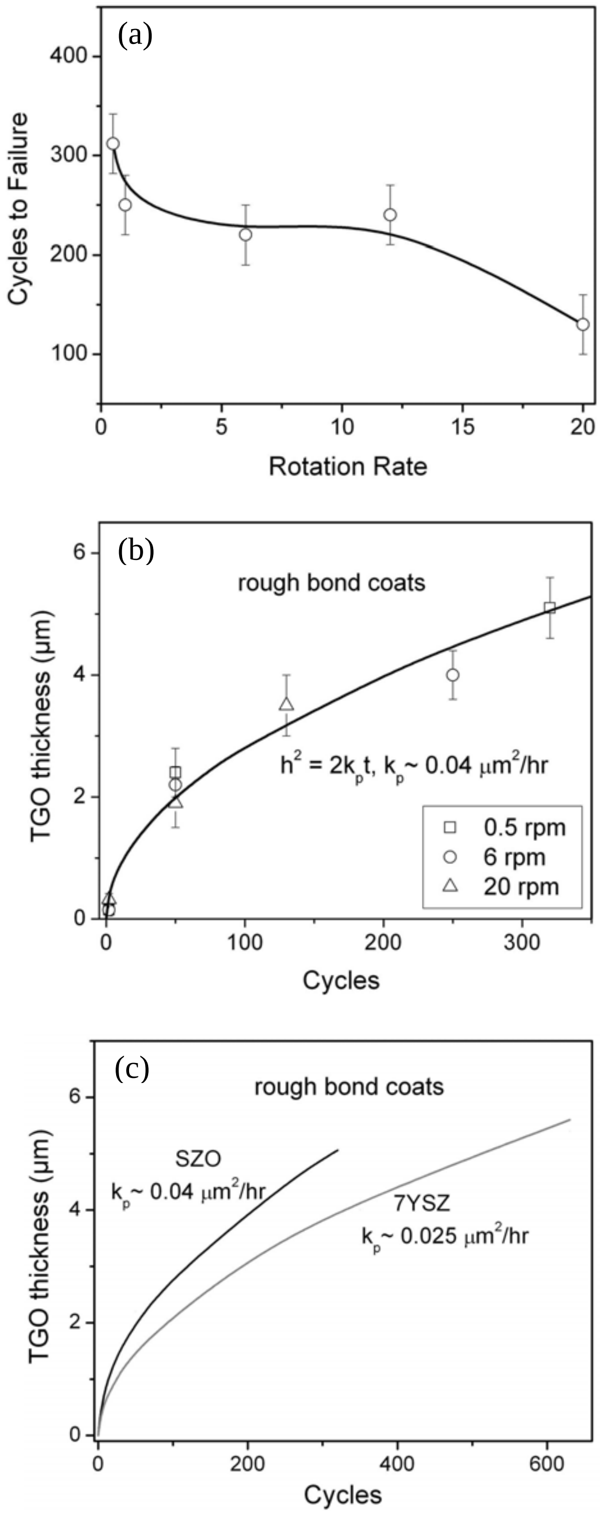

Figure 8-4.Thermal cycling data for SZO coatings on a rough bond coat: (a) Cyclic lifetime vs. rotation rate, (b) TGO thickness vs. cycles and (c) a comparison of TGO growth rate between SZO and YSZ.

The dependence of TGO thickness upon the number of cycles is shown in Fig. 8-4(b). The data is well fitted by a parabolic expression. The parabolic growth rate is around 0.04 μm^2/hour, which is a little larger than that of the YSZ coatings (0.025 μm^2/hour) on grit-blasted bond coats. For comparison purposes, the evolution of the TGO thickness of both the SZO and YSZ coatings with the number of exposure cycles is plotted in the figure 8-4(c). The thicker TGO layer of SZO coatings (compared to YSZ), may be a result of a reaction between the SZO and the alumina rich TGO as discussed below.

8.2.2 Smooth bond coats

Samples with SZO coatings deposited at various rotation rates on a polished bond coat were thermally cycled, and their microstructural changes examined. Representative micrographs of top surfaces and cross-sections are shown in the figure 8-5. Like the coatings grown on rough bond coats, clear pyramidal column tips were observed in the top view, Fig. 8-5(a). As cycling began, the sharp edges of the column tips became smoothened.

Examination of cross-section views Fig. 8-5 (d)-(f) shows rapid increases in TGO thickness with thermal exposure. A ~0.4 μm thin TGO layer was formed during deposition of the SZO layer, clearly shown in higher magnification view of Fig. 8-6(a). With increasing high temperature exposure time, the TGO thickness increases to ~4 μm, Fig. 8-5(f) and Fig. 8-6(c). At ~300 cycles, the coating develops the spallation at the interface of TBC/TGO. In the thick TGO layer, the Y-Al oxide pegs distribute and protrude into the bond coat. In Fig. 8-6(b), an inter-mixed zone is found to be present in the top TGO layer. The thickness of the mixed zone and regular TGO is 0.5 and 2 μm, respectively. In the mixed zone, the elements of Sm, Zr, Al and other bond coat elements (Ni, Co, Cr, in low atomic percentage) are detected by the EDS analysis.

A comparison of the evolution of sintering of fractured columns between the SZO and YSZ coatings was shown in Fig. 8-7. It is evident that the open feathery microstructure features at the edge of the columns in both as-deposited coatings. As thermal cycling progresses, the reduction in the surface energy is the driving force for sintering and induces the changes in the pore morphology. Examination of 50-cycle SZO sample demonstrates that the feather-arm features become coarser in comparison with those in the as-received state, while the feathery arms disappear and the neighboring columns neck in the YSZ coating due to the atomic diffusion to reduce the surface area. When the SZO coatings spall at ~300 cycles, the open feathery microstructure of the columns breaks up into closed porosity that can be observed within the columns. For the 350-cycle YSZ sample, the columns sinter together with less intracolumnar pores.

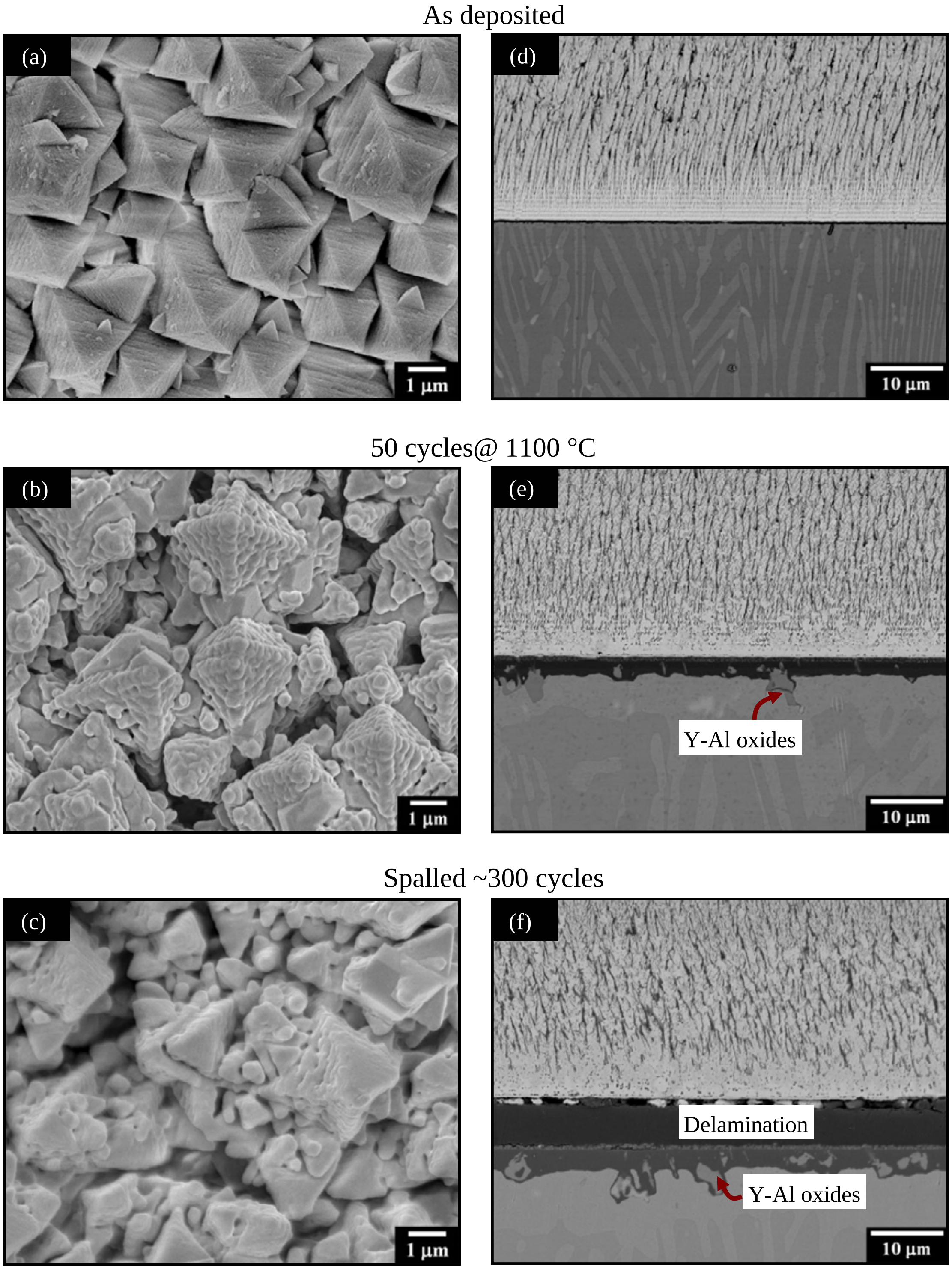

Figure 8-5. The evolution of the morphology of SZO coatings with the number of thermal cycles: (a, d) as-deposited, (b, e) 50 cycles and (c, f) the spallation. The SZO coatings were deposited on smooth bond coats at 1000 °C at the rotation rate of 6 rpm.

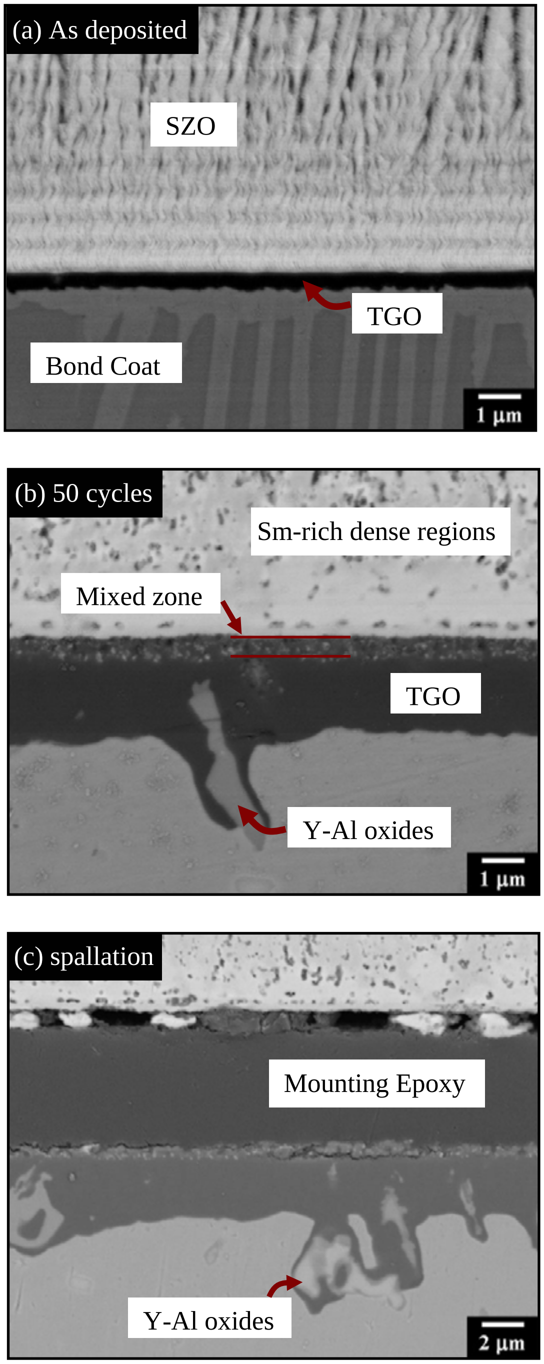

Figure 8-6. The evolution of TGO layer with thermal cycles. The SZO coatings were deposited at 1000 °C using a rotation rate of 6 rpm.

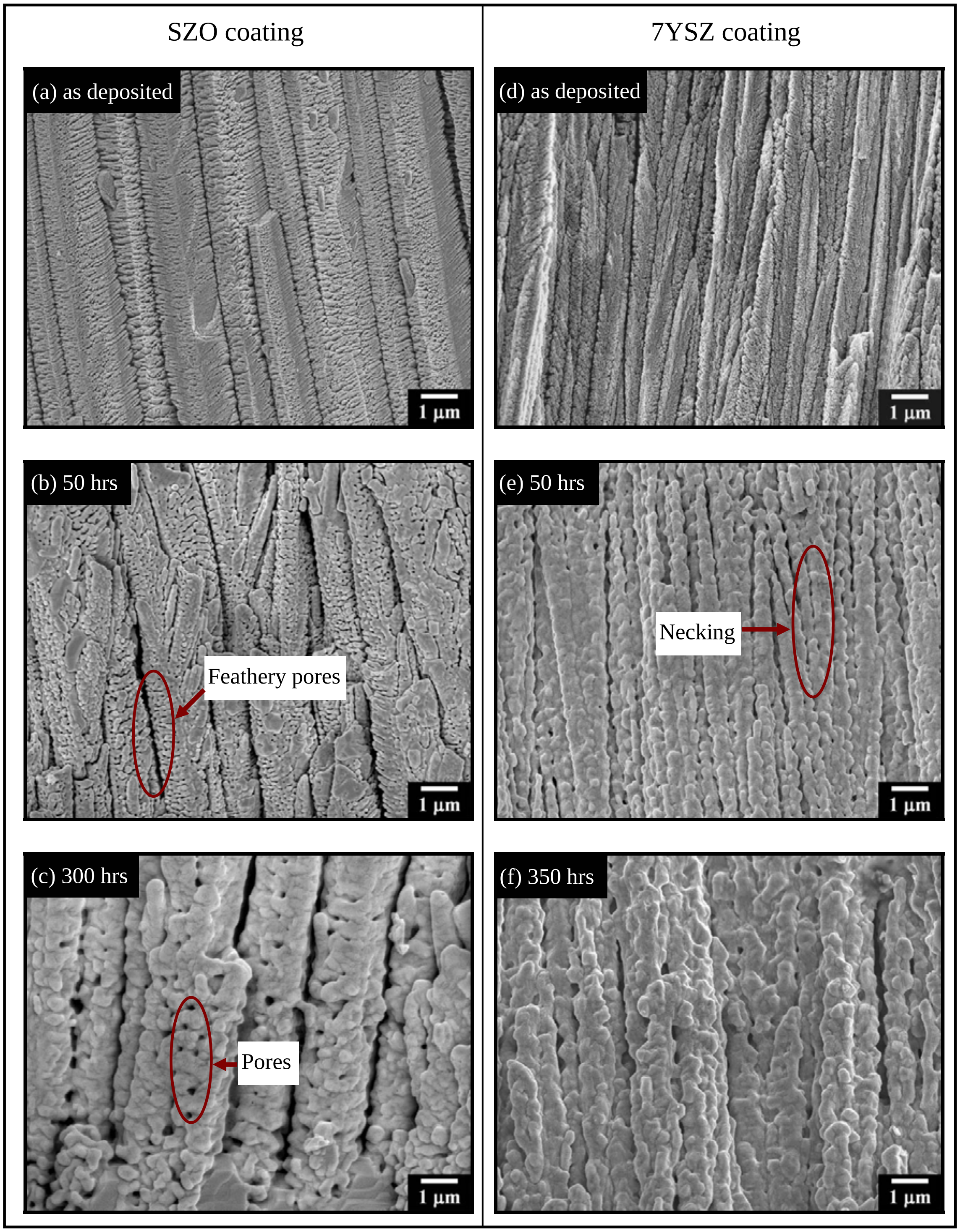

Figure 8-7. A comparison of the sintering between SZO and 7YSZ for as-deposited coatings (a, d), 50-hr cycled coatings (b, e) and over 300-hr cycled coatings (c, f). All images were shown in fractured cross-section views.

The spalled sample with the attached SZO coating was scanned by XRD. The result in Fig. 8-8(a) corresponds to diffraction from the top surface of the SZO layer. Compared to the equivalent XRD pattern of the as-deposited coating (Fig. 7-6b), small peaks are present in the thermally cycled coating. These peaks have been labeled and found to be the reflections of the ordered pyrochlore structure. This indicates that the fluorite structure of as-deposited SZO coating had transformed to the pyrochlore structure by atomic diffusion after exposure to high temperature for 300 hours.

After the SZO coating detached from the underlying substrate, the TGO covered bond coat without the top SZO coating were also examined by X-ray scan. The XRD spectrum is shown in Fig. 8-8(b). The peaks from SZO coating are still dominant in the spectrum, which indicates that some remnant SZO coating remains attached to the TGO despite the coating delamination. The distinct ordering peaks for the pyrochlore SZO is still evident in the pattern. In addition to the peaks from the SZO, some new peaks have appeared in the XRD data. Many of them correspond to the reflections of $SmAlO_3$, which implies that Sm_2O_3 and Al_2O_3 have reacted to form samarium aluminate ($SmAlO_3$).

Fig. 8-9(a) displays the dependence of the cyclic lifetime upon rotation rate for SZO coatings applied to polished bond coats. Unlike 7YSZ coatings, the number of cycles to failure for the SZO coatings is approximately the same as that of the coatings applied to grit-blasted bond coats. The coatings also have the same trend with the rotation rate. As the rotation rate increases, the lifetime slowly decreases from ~350 to ~150 cycles.

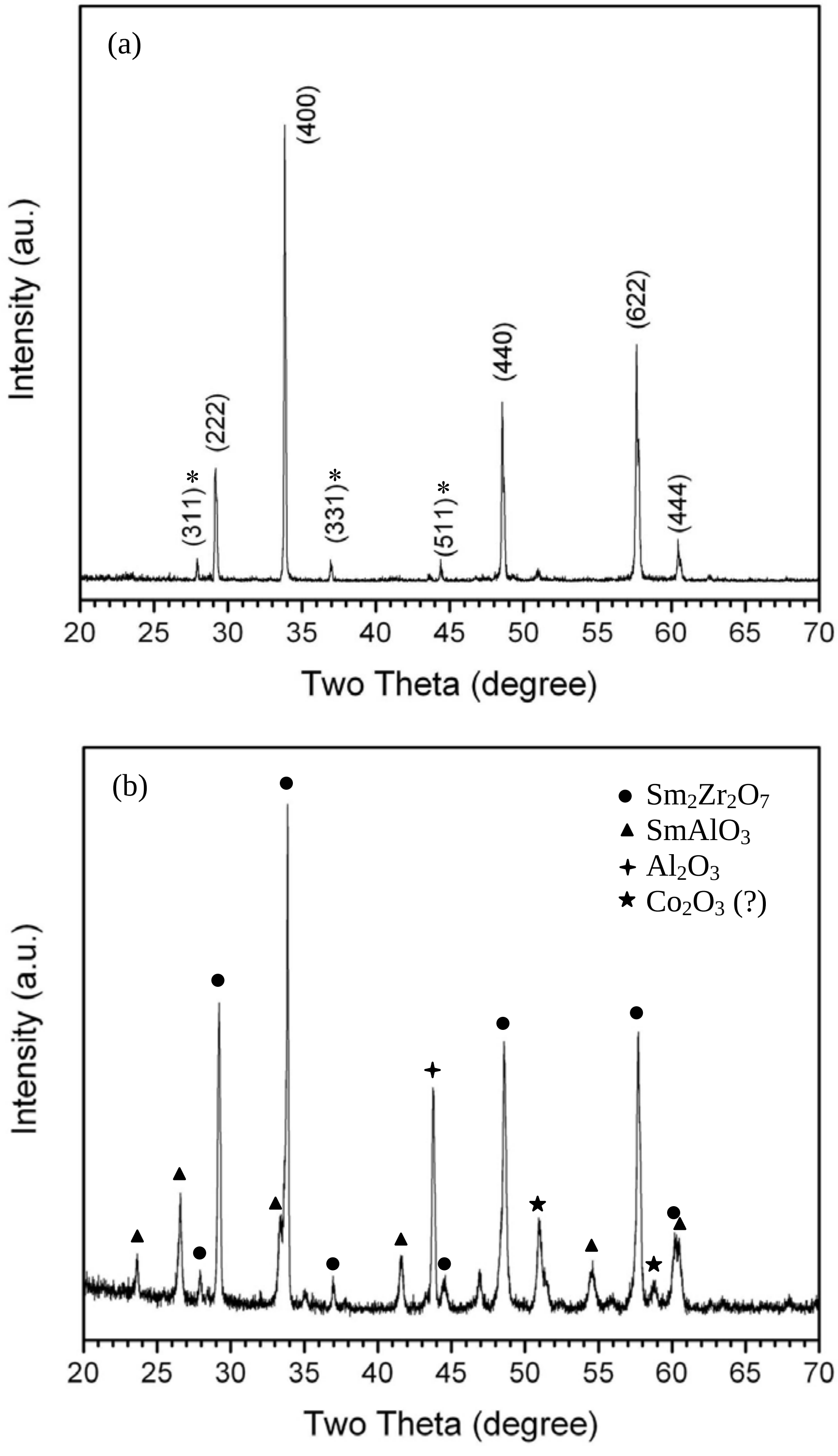

Figure 8-8. X-ray diffraction data for the spalled sample (shown in Fig. 8-4c). (a) with SZO coating still attached to the bond coat, and (b) without SZO coating.

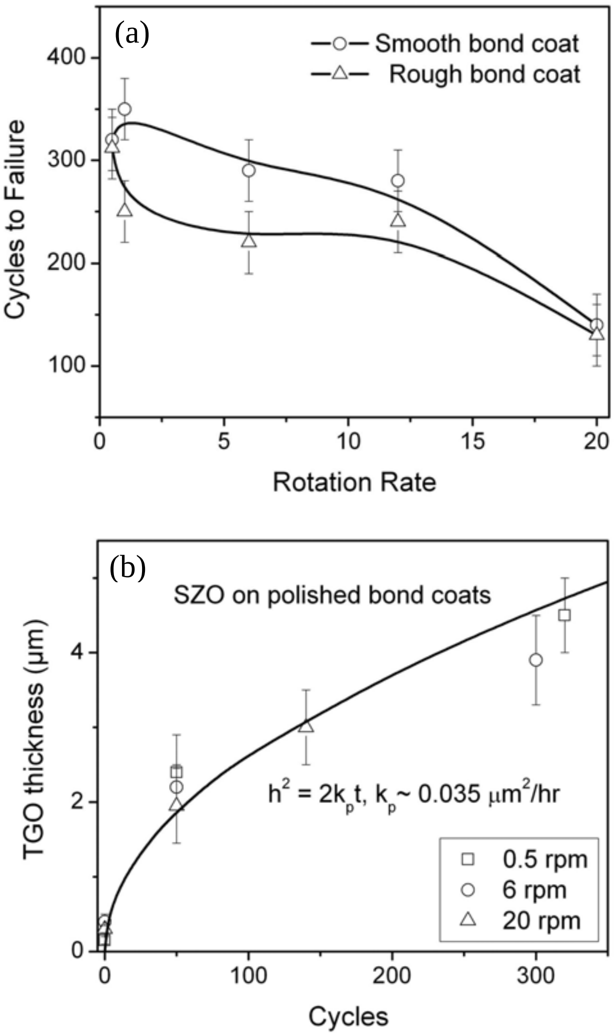

Figure 8-9. Cycling data for SZO coatings on smooth bond coats: (a) Lifetime vs. rotation rate and (b) the TGO growth rate.

The development of TGO thickness with thermal cycling is shown in the figure 8-9(b). The data fit a parabolic growth law with a parabolic rate constant of 0.035 μm^2/hour. In order to compare with the YSZ coatings deposited on the same bond coats and the same conditions, The TGO thickness with thermal cycling for both coatings are plotted in Fig. 8-10(a). It can be clearly seen that SZO coatings have a higher TGO growth rate than YSZ. The lifetime has a distinctive difference between these two coatings. YSZ coatings have much longer lifetime cycles than SZO coatings, shown in Fig. 8-10(b). Both coatings have the decreasing lifetime as the coating density is increased, but the lifetime in this case is unaffected by the initial surface condition of the bond coat.

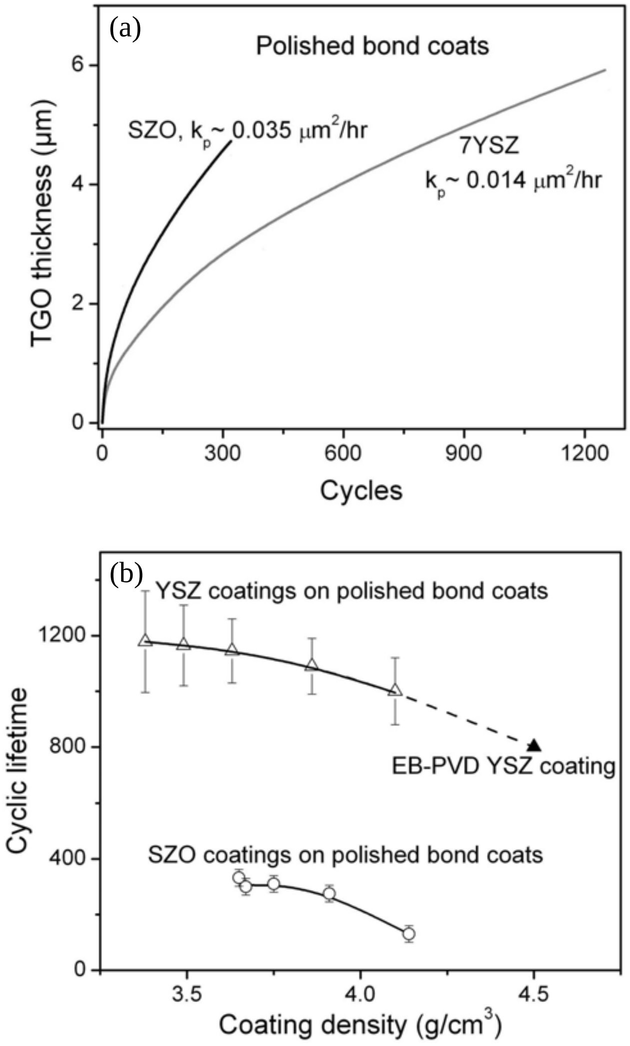

Figure 8-10. (a) A comparison of TGO growth rate for SZO and YSZ coatings on polished substrates, (b) The relation between lifetime and density for YSZ and SZO coatings. For the same density, the SZO coating has more pore fraction than 7YSZ because the fully dense SZO and 7YSZ materials have the density of 6.7 and 6.0 g/cm^3, respectively.

8.3 Discussion

The experimental results above indicated that the spallation lifetime of SZO coatings on NiCoCrAlY bond coats is independent of the bond coat surface condition. These lifetimes are as much as a factor of four less than YSZ coatings deposited identically on the same bond coats. The SZO coatings all fail by delamination at TBC/TGO regardless of the bond coat surface condition. The lifetimes do depend upon rotation rate and therefore coating density, implying the strain energy stored in the coating plays a role in the onset of failure. However, the chemical characteristics of the interface appear to have a deciding effect on the failure of SZO coatings.

As discussed in chapter 6, the bond coat surface governs the spallation failure mechanism of 7YSZ coatings. The lifetimes of coatings applied to rough bond coats are governed by bond coat rumpling whereas those for the polished bond coats are dictated by interface delaminations. For the rough bond coats, the creep of the bond coat exacerbates the amplitude of the rumpling, causing cracks to form in the vicinity of “corn kernel” defects. The contaminants due to the grit blasting result in the low interface toughness of TBC/TGO. These cracks propagate along the planes of lowest local toughness and finally delaminate at the interface of TBC/TGO. For the smooth bond coats, rumpling was suppressed upon polishing. Small cracks initiate at the local TGO thickness heterogeneities. The appearance of small flat voids and the sulfur segregation to the interface of TGO/bond coat embrittle the interface. The delamination finally happens between the TGO and bond coat when the strain energy release rate is greater than the interface toughness of TGO/bond coat.

The TGO rumpling is evident in the examination of Fig. 8-1(d)-(f). Like YSZ coatings on rough bond coats, much higher strain energy will be stored in the TGO layer during cycling, resulting from the thermal expansion mismatch with the substrate and the TGO lateral growth. The release of this energy leads to the undulation growth which is dependent upon the bond coat rumpling. It appears that this rumpling mechanism is not the sole reason for the earlier failure of SZO coatings on rough NiCoCrAlY bond coats. Many experiments have shown that rare earth zirconates react with alumina in the TGO layer. Leckie et al. has found that Gd_2O_3 reacts with Al_2O_3 when exposure at high temperature [119]. In their case, the reactive oxide $GdAlO_3$ appear to greatly lower the interface toughness of TBC/TGO. The phase diagram of binary Sm_2O_3-Al_2O_3 system [2] is presented in Fig. 8-11(a). A compound, $SmAlO_3$, which has a perovskite-like structure, forms at 50 mol% Sm_2O_3. This compound is phase stable up to 2100 °C. Thermodynamic behavior of ternary Sm_2O_3-ZrO_2-Al_2O_3 system at 1250 °C has been shown in Fig. 8-11(b). From the previous results, it is known that the fluorite structure of as-deposited SZO coatings develop into a ordered pyrochlore structure due to the enhanced atomic diffusion at high temperature. The pyrochlore SZO and the interphase $SmAlO_3$ are found to co-exist in the range of pyrochlore compositions. As one of the rare-earth zirconates, it is believed that $SmO_{1.5}$ will react with Al_2O_3 and form $SmAlO_3$. The findings of the peaks of $SmAlO_3$ in the XRD pattern have verified this prediction.

As mentioned for YSZ spallation in Chapter 6, the critical TGO thickness can be calculated by Hutchinson's theory [151]. If we assume that the SZO coating has the same fracture mode as YSZ and the interfacial toughness between TGO and bond coat is also considered to be 80 J/m^2. It is noticed that the SZO has a Poisson's ratio of 0.28 [162], slightly different from YSZ. Fig. 8-12 has shown the variation of the calculated critical TGO thickness with the coating modulus. It is known that both fully dense YSZ and SZO materials have the Young's modulus of ~ 230 GPa with similar poisson's ratios of 0.3 (YSZ) and 0.28 (SZO) [162].Consequently the as-deposited SZO coating is expected to have the similar elastic modulus in the range of 10-50 GPa as YSZ has. It is also anticipated that the SZO sample failure happens at the TGO thickness of more than 5.5 μm. However, it is noted that the spallation of SZO coatings occurs when the TGO thickness approaches ~4 μm. This can be explained in two ways. First and foremost, the reaction product oxide might also play a significant role in the failure like $GdAlO_3$. This oxide may embrittle the interface of SZO/TGO and dramatically lower the interface toughness. This also leads to the rapid failure of the coating. Secondly, the coating modulus increases with the sintering. The SZO coating has quite dense regions close to the TGO layer with higher content of Sm. These dense regions may result in higher elastic modulus and thus higher strain energy stored in the system, which partly contributes to earlier spallation by reducing the critical TGO thickness. Consequently, the shorter lifetimes of SZO coatings can be primarily attributed to the lower interface toughness at SZO/TGO resulting from the damage of $SmAlO_3$, as well as the higher coating modulus due to the dense regions just above the TGO layer.

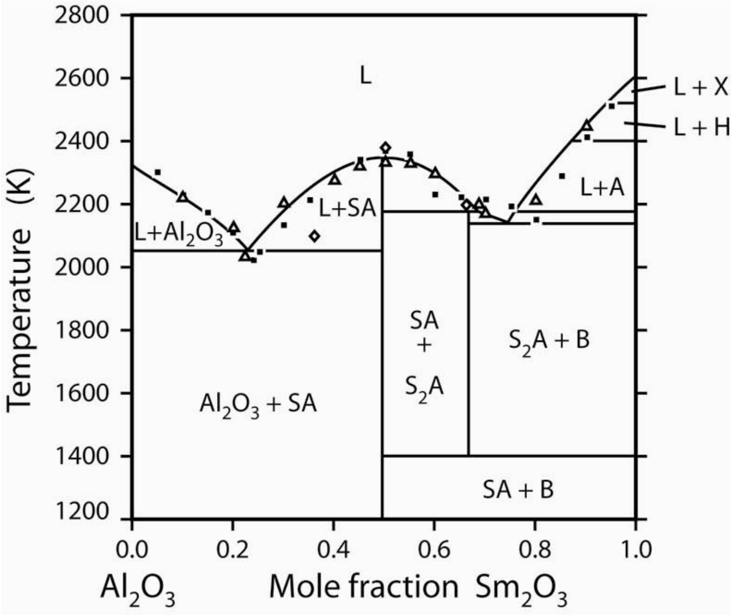

(a) Phase diagram of binary Sm_2O_3-Al_2O_3 system

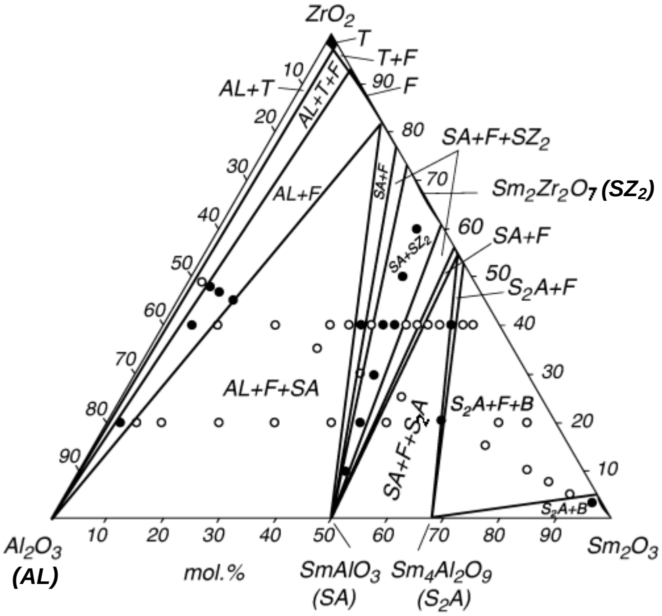

(b) Ternary Sm_2O_3-ZrO_2-Al_2O_3 system at 1250 °C

Figure 8-11. Thermodynamic behavior of samaria, zirconia and alumina. (a) Phase diagram of Sm_2O_3-Al_2O_3 (calculated [2] and experimental data [3-5]). (b) The compounds of $SmAlO_3$ (SA) and $Sm_4Al_2O_9$ (S_2A) have perovskite and monoclinic structure, respectively. A, B, H and X represent different types of Sm_2O_3 oxides. T and F are tetragonal and fluorite structure of ZrO_2.

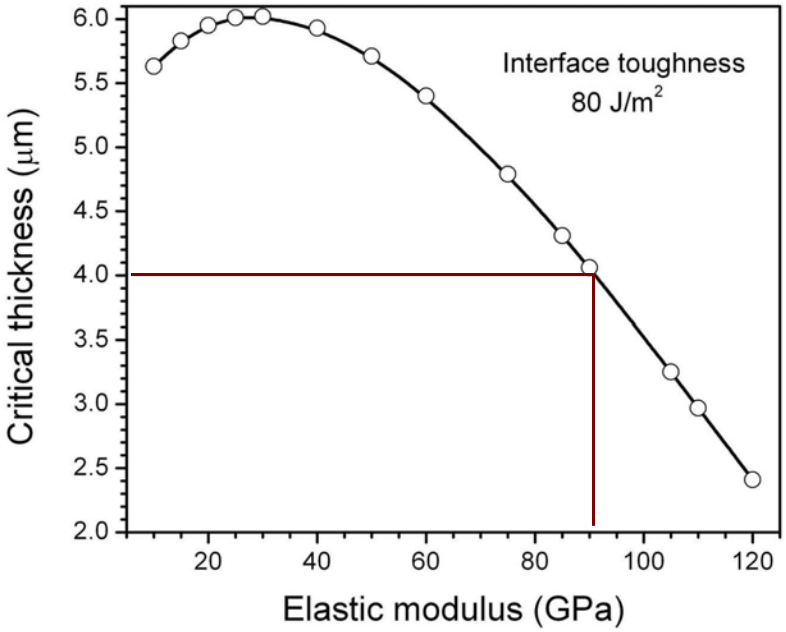

Figure 8-12. The variation of estimated TGO critical thickness with the elastic modulus of SZO coatings. Here it is assumed that the SZO sample has the same interfacial toughness 80 J/m^2 at TGO/bond coat. The thickness of the SZO coating is 80 μm and the poisson's ratio is 0.28. The equations for the model used here are given in Chapter 6.

8.4 Summary

In this chapter, the cycling experiments have been conducted on the SZO coatings grown on grit-blasted and polished NiCoCrAlY bond coats. The SZO coating itself appears to resist sintering in comparison with equivalent times of exposure to 1100 °C for 7YSZ coating. The fluorite phase of as-deposited SZO coatings transforms to the ordered pyrochlore structure after thermal cycling. Samaria tends to react with TGO to form the new compound $SmAlO_3$ in the mixed zone. The SZO coatings have much shorter lifetime of 100-300 cycles, regardless of the bond coat condition. This earlier failure of the SZO coating is primarily attributed to the chemical reaction between SZO and TGO. The reaction product $SmAlO_3$ interphases might lower the interface toughness and decrease the adhesion between SZO and TGO and thus lead to earlier TBC spallation at the interface. The rumpling mechanism is also responsible for the spallation of SZO coatings grown on rough bond coats.

Chapter 9

7YSZ/ $Sm_2Zr_2O_7$ Bilayer Coating

9.1 Overview

Samarium zirconate coatings deposited by the DVD method have been shown to have a through thickness thermal conductivity approximately one half that of YSZ deposited in the same manner. In Chapter 8, the samarium zirconate coatings also appear to have better sintering resistance than YSZ. However, their cycling lifetime is much shorter than that of YSZ. The primary reason is that samarium zirconate is thermodynamically unstable when placed in contact with aluminum oxide at all application temperatures of interest (≥1000 °C). The reaction between these two coatings forms the new $SmAlO_3$ interphases, which may damage the interface and reduce the toughness. A durable $Sm_2Zr_2O_7$ TBC should not be in direct contact with the TGO at the conditions expected in engine operation. One approach to potentially address this problem is to use an intermediate layer that is compatible with both alumina and SZO and that acts as a diffusion barrier between them. Such a material must also retain the strain tolerance needed for thermal cyclic durability. The most obvious candidate is 7YSZ whose cyclic durability as a TBC material and compatibility with the TGO are well established. Such an approach has been shown successfully in gadolinium zirconate (GZO) system [123].

This chapter first focuses on the deposition of YSZ/SZO bilayer coating using DVD approach and then morphology and cycling performance of this bi-layer coating is investigated. One goal was to understand the characteristics of the interface between the layers. A second objective was to assess the thermal cycling lifetime of the bi-layer.

9.2 Experimental Methodology

Bi-layer (7YSZ/$Sm_2Zr_2O_7$) coatings were deposited on rotated substrates using the EB-DVD technique. Here, two-rod crucible was used in the DVD system, shown in Fig. 4-1. 7YSZ and $Sm_2Zr_2O_7$ rods were placed in the crucible at the same time. When the substrates were heated to 1000 °C, 7YSZ coatings were first deposited, followed by deposition of a $Sm_2Zr_2O_7$ layer by moving the electron beam to the second source rod without breaking the vacuum. The substrates were rotated at 6 rpm during the deposition. Helium/oxygen was fed into the chamber at a rate of 10slm/1slm. The upstream pressure is 140 Pa and the downstream pressure 16 Pa. The deposition rate is 4±1 μm/min.

The thermal cycling behavior of bilayer coatings was investigated in an identical manner to that used earlier, i.e. by a thermal cycling from ambient to 1100 °C for 60 holding minutes and followed by with forced air cooling for 10 minutes. The sample can be cooled to around 50 °C. The coatings were characterized by scanning electron microscopy and energy dispersive X-ray analysis. Samples were taken out for the examination at 50 cycles, 350 cycles and upon spallation.

9.3 Coating Microstructure

The microstructure of the as-deposited bi-layer coatings presented in Fig. 9-1 shows the polished cross-section, including $Sm_2Zr_2O_7$, 7YSZ, bond coat and substrate. The top view has the silimar surface morphology as the typical $Sm_2Zr_2O_7$ coatings deposited on polished NiCoCrAlY bond coats (seen in Fig. 7-3b). The thickness of the samarium zirconate is around 80 μm and 7YSZ ~10 μm. A thin layer of TGO (~ 0.5 μm) formed at the interface of 7YSZ and bond coat. It is apparently a flat layer. β-NiAl phase and γ-Ni phase are clearly shown in the bond coat, close to the interface, Fig. 9-1(c). Like the SZO layer coatings on rotated substrates, the SZO layer in the bilayer has a dominant orientation of <100> normal to the substrate, which can be seen in the XRD result Fig. 9-2. This indicates that the top SZO layer has a preferred column growth direction of <100> which is the same as that of the SZO only layer grown on the substrate. In addition, there are no pyrochlore ordering reflections in the XRD pattern, which implies that the deposited $Sm_2Zr_2O_7$ is a fluorite solid solution consistent with the earlier observations.

The polished cross-section in Fig. 9-3 provides additional insight into the near-interface microstructures of the 7YSZ/$Sm_2Zr_2O_7$ bi-layer. Examination of the 7YSZ/SZO interfaces in the two coatings shows that the transition from 7YSZ to SZO occurred seamlessly, without disruption of the feathery columnar structure. The continuity of the pre-existing 7YSZ columnar growth pattern and the following $Sm_2Zr_2O_7$ coating is apparent at all relevant length scales, from the intercolumnar gaps to the intracolumnar feathers, shown in Fig. 9-3. This indicates that the as-deposited 7YSZ/SZO retained the strain-tolerant inter-columnar void structure. The relatively small lattice misfit between t′-YSZ (a=0.5111 nm and c=0.5169 nm) [22] and fluorite cubic SZO (a=0.5295 nm) [156] ensures the continuous growth of the SZO layer on 7YSZ.

To investigate the interdiffusion between two oxides, the chemical composition by EDS spot analysis under back-scattered electron imaging mode was recorded from areas close to the bilayer interface. Spots on Line 1 are on the 7YSZ columns, about 0.5 μm away from the SZO, while spots on Line 2 on the SZO columns, 0.5 μm away from the 7YSZ. The result for the average composition is shown in Table 9-1. It is noticed that Sm is detected in the YSZ coating but Y is not detectable in the SZO coating. This indicates that SZO diffused into the YSZ coating along the intercolumnar gaps during the deposition. However, the Sm signal is not detected close to the interface 7YSZ/TGO, which means 7YSZ layer still plays a role in preventing SZO from diffusion to the TGO. The diffusion of Sm in 7YSZ is limited to the scale of the interface.

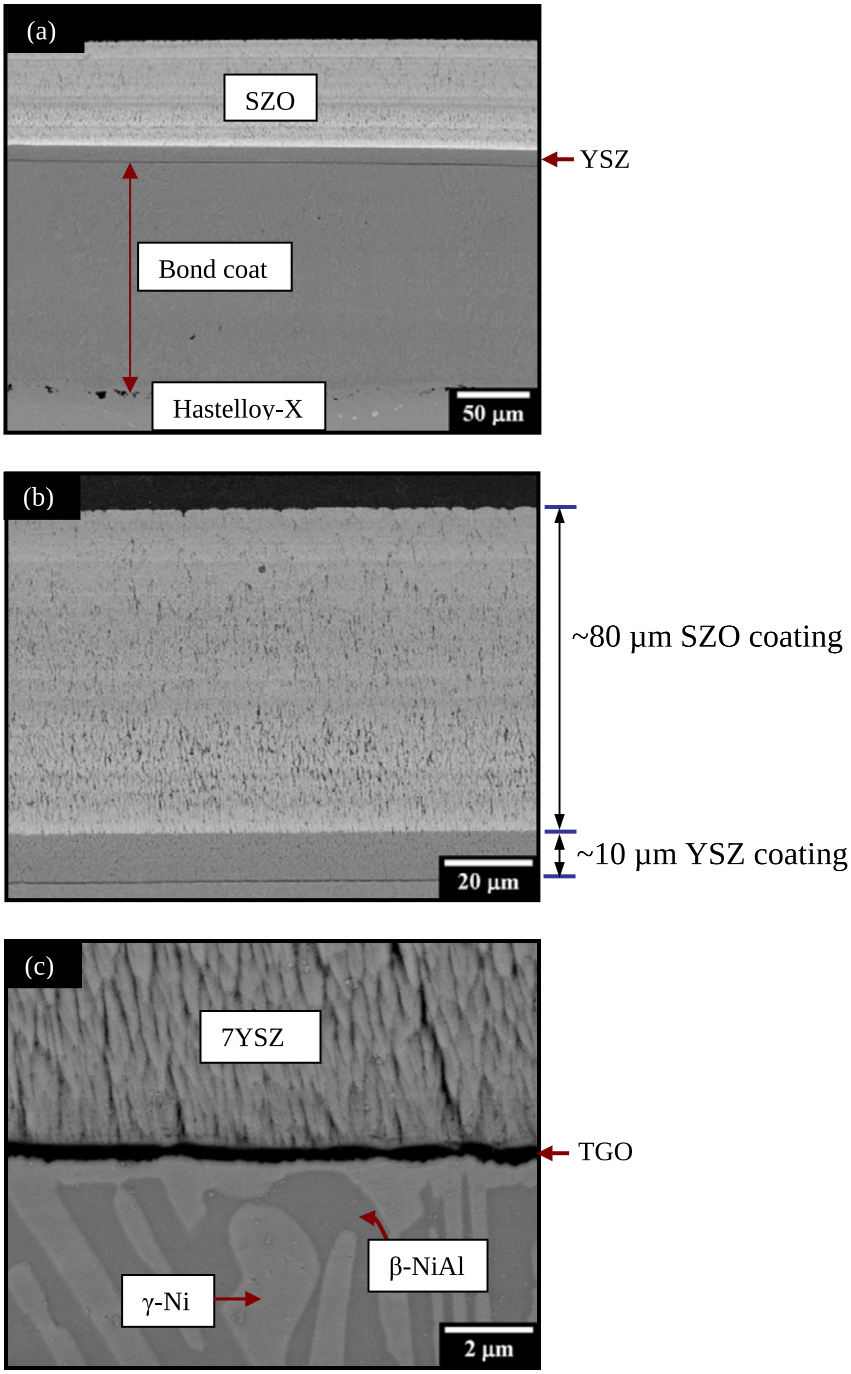

Figure 9-1. Microstructure of as-deposited bi-layer coatings at increasing magnification. The bilayer was deposited on polished NiCoCrAlY bond coat at 1000 °C using a rotation rate of 6rpm.

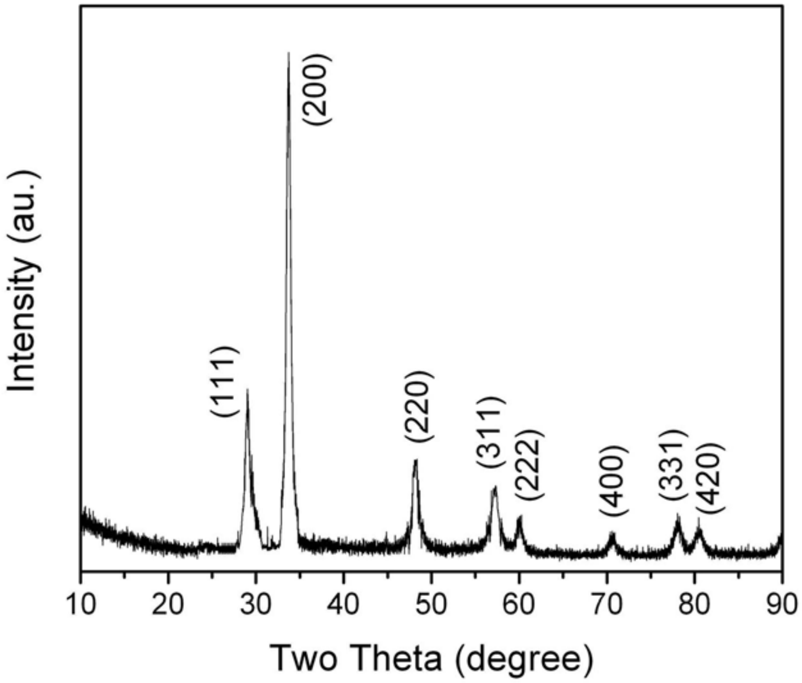

Figure 9-2. XRD pattern of the top SZO surface of an as-deposited bi-layer coating coated on NiCoCrAlY bond coat at 1000 °C.

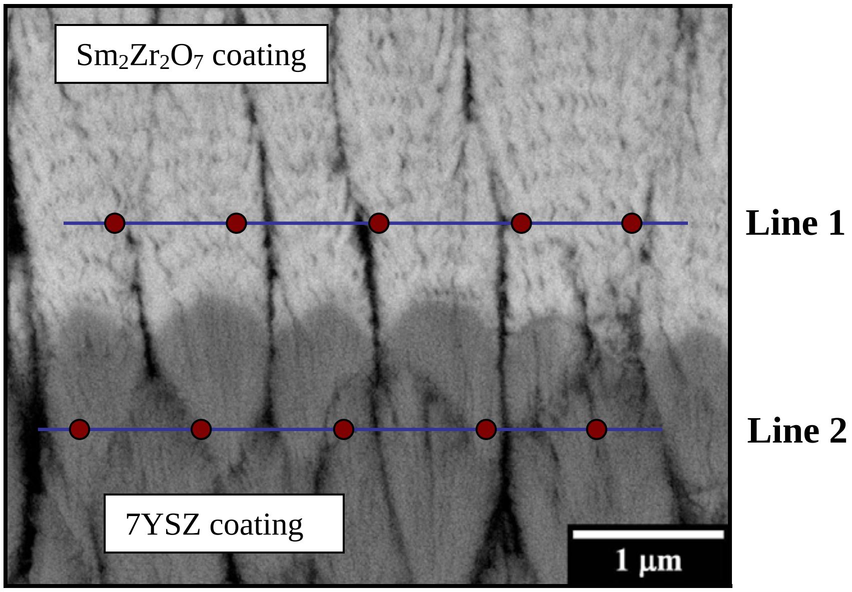

Figure 9-3. The polished cross-section of SZO coating on 7YSZ coating. Small colored circles represent different positions where EDS measurements were recorded.

Table 9-1. EDS analysis for Lines 1 and 2

Position	Sm (at.%)	Y (at.%)	Zr (at.%)
Line 1	60.2	0	39.8
Line 2	4.7	6.9	88.4

9.4 Thermal Cycling

9.4.1 After 50 thermal cycles

After 50 cylces, it is found that the TGO layer has a similar behavior as a single 7YSZ layer coating on NiCoCrAlY bond coat. The TGO layer becomes thick (around 1.5 μm) due to the oxidation of Al and other elements in the bond coat. The oxide precipitates appears in the BEI image of the TGO layer, in Fig. 9-4. The EDS analysis indicates that the precipitates contain comparable amounts of Y and Al, which are probably Y_2O_3/YAG mixed phase. There is no evidence of localized interface separations between the 7YSZ layer and SZO layer. After 50 cycles, it is observed that the feathery structure on the column lateral surfaces is smoothened, especially on 7YSZ. The $Sm_2Zr_2O_7$ feathery structure appears to have slower evolution, which is observed in the similar 7YSZ/$Gd_2Zr_2O_7$ bi-layer coating [123]. In addition, a mixed zone including YSZ and alumina is also observed at the interface of 7YSZ/TGO. As mentioned in the background (Chapter 2.2), YSZ is first solvable in metastable (gamma and theta) alumina and then precipitates when metastable alumina transforms to alpha alumina.

The interface of 7YSZ/SZO is of particular interest in Fig. 9-4(c). Although the top SZO coating is intact attached to the 7YSZ, there is a dense region occurred at the interface within the SZO coating. Similar phenomena are observed in the thermal cycling of single SZO coating on the bond coat in Chapter 8. This observation is consistent with the banding structure of the SZO coating. The line scan analysis (Fig. 9-5) was conducted to investigate the diffusion of Sm in YSZ layer. The result shows that Sm has diffused into the YSZ coating, but not reached the interface of YSZ/TGO.

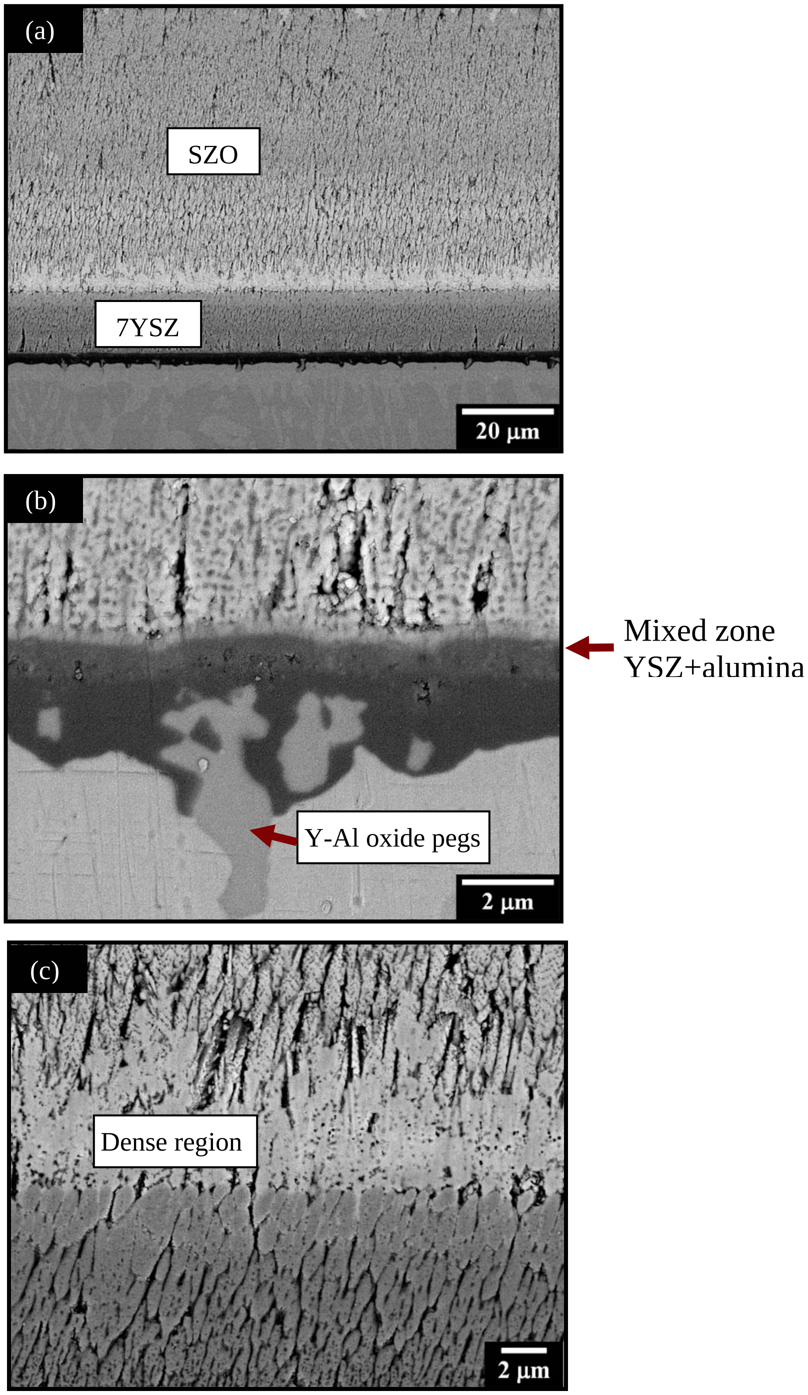

Figure 9-4. Coating morphology after 50 thermal cycles. The bilayer coating was deposited at 1000 °C using a rotation rate of 6rpm.

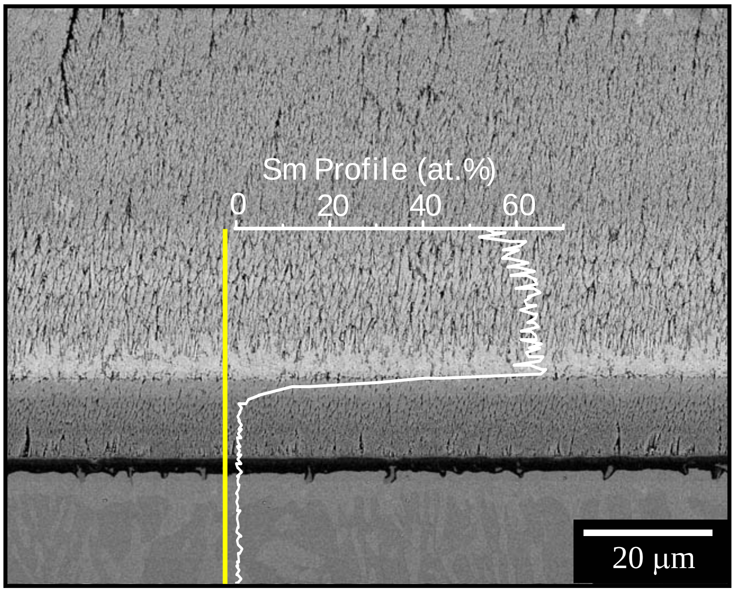

Figure 9-5. Line scan analysis of Sm composition for the bilayer coating after 50 thermal cycles. The coating was grown at 1000 °C using a rotation rate of 6rpm.

9.4.2 After 350 thermal cycles

The bi-layer samples continued cycling in the furnace. The samples were then taken out for analysis when they reached 350 cycles. The small voids occur at local TGO regions, in Fig. 9-6(b). However, the bilayer coating is still attached to the TGO layer. The TGO thickness increases to ~3.5 μm due to the continuous oxidation of Al from the bond coat. Like the sample of 50 thermal cycles, the separation or detachment is not found at the interface of 7YSZ/$Sm_2Zr_2O_7$, Fig. 9-6(c). Due to the 350-hour thermal exposure, the diffusion distance of Sm into the YSZ coating increases with time. EDS measurement detects low content of Sm (< 1 at.%) near the TGO. Line scan analysis was also shown in the figure 9-7. It can be seen that the signal of Sm is detectable through the YSZ coating, which is consistent with the EDS analysis of the interface of YSZ/TGO.

It might be explained from the specific microstructure of DVD YSZ coating. It is known that DVD YSZ coating is less dense than PVD YSZ coating, which means DVD YSZ coating has more pores and gaps (inter- and intra-columnar pores). This might promote Sm to migrate into YSZ coatings along the grain boundaries and gaps. Another possible reason is that YSZ layer is too thin (~10 μm). Although the diffusion coefficient of Sm in 7YSZ is not available, the diffusivity of Y in YSZ is reported to be ~10^{-16} m^2s^{-1} [163]. If the diffusivity of Sm in YSZ is assumed to have the same order of magnitude (~10^{-16} m^2/s), it can be estimated that the characteristic diffusion length ($\sqrt{D\tau}$) is ~10 μm after almost 300 hours. This value is consistent with the observation in the experiment.

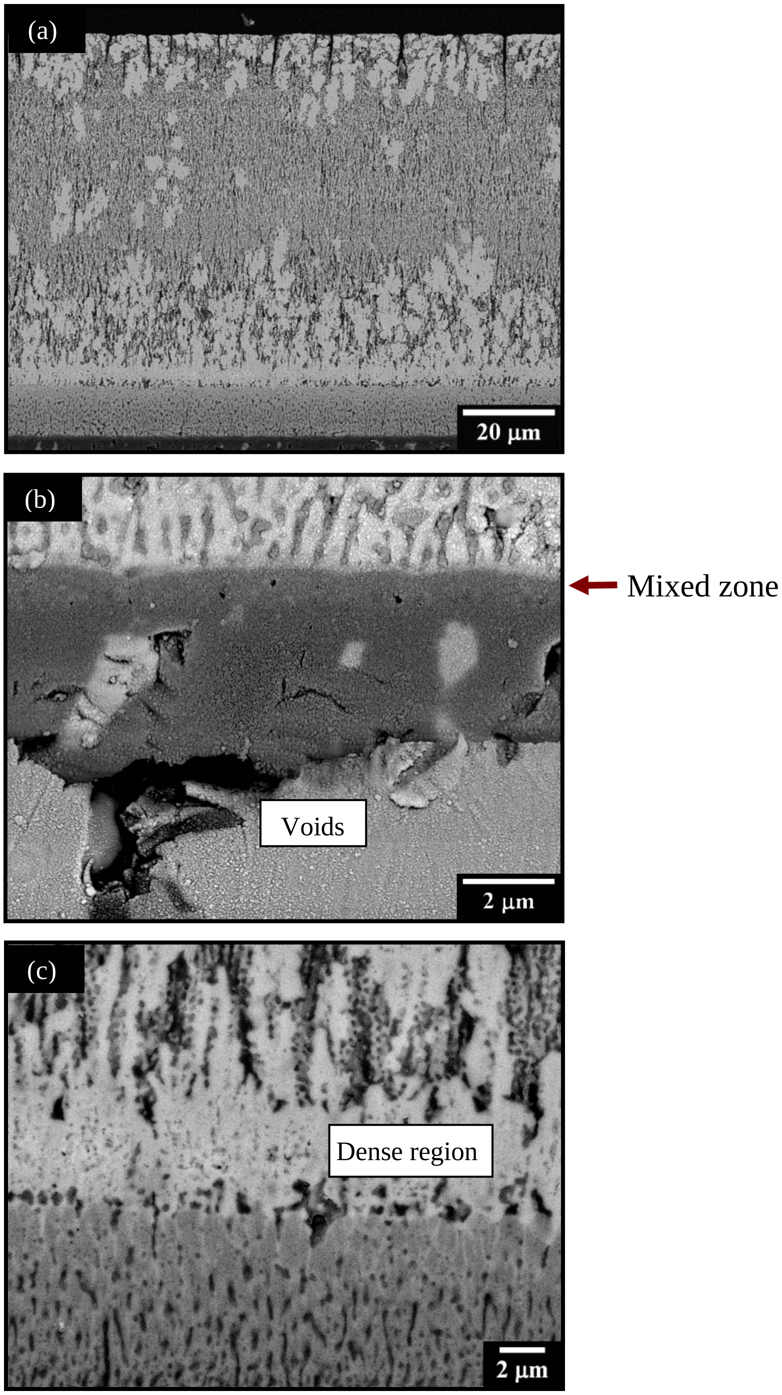

Figure 9-6. Coating morphologies after 350 thermal cycles. The bilayer coating was deposited at 1000 °C using a rotation rate of 6rpm.

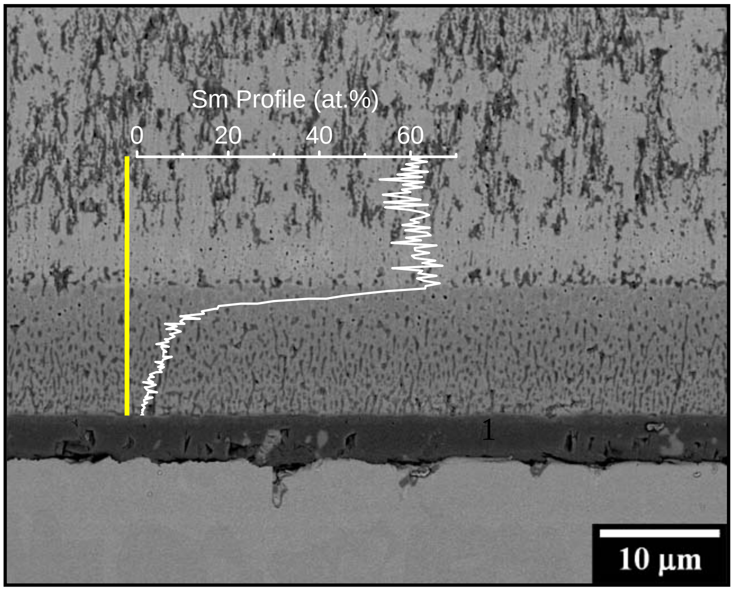

Figure 9-7. Line scan analysis of Sm composition for the bilayer coating after 350 thermal cycles. The coating was deposited at 1000 °C using a rotation rate of 6rpm.

9.4.3 Spallation

The cycling was continued for these bilayer samples. The spallation happened from 1000 cycles to 1150 cycles. The coating delaminates from the interface between the TGO layer and the bond coat, in Fig. 9-8. The TGO thickness is ~6.2 μm. It is also noted that the wider inter-columnar gaps due to sintering penetrate deeply into the coatings, Fig. 9-8(a). Until spallation, these two ceramic coatings are perfectly compatible with each other. Mixed zone is still observed at the interface of YSZ/TGO (Fig. 9-8b). Due to the diffusion of Sm from the top SZO coating, it might include $SmAlO_3$ in the mixed zone. Fig. 9-8(c) also provides a comparison of sintering between SZO and YSZ. It appears that SZO still have the columnar structure while the columns of YSZ coating almost disappear. This again indicates that SZO appears to have a better resistance to sintering than YSZ.

Fig. 9-9 displays the thickening of the TGO layer with thermal cycling. The parabolic growth rate constant is ~0.018 $\mu m^2/hr$, which is slightly larger than that of single 7YSZ coating on polished bond coats. A comparison of the lifetime among 7YSZ, $Sm_2Zr_2O_7$ and bilayer is shown in Table 9-2. All the samples experienced the same cycling history, i.e. they were heated at 1100 °C for an hour and then followed by 10-min forced air cooling. The results indicate that both 7YSZ and bilayer coating have comparable failure lifetime, which is much longer than that of $Sm_2Zr_2O_7$. Therefore, the bilayer coating maximized the benefits of 7YSZ and $Sm_2Zr_2O_7$. It has inherited the long lifetime from 7YSZ while having the good resistance to sintering and CMAS attack.

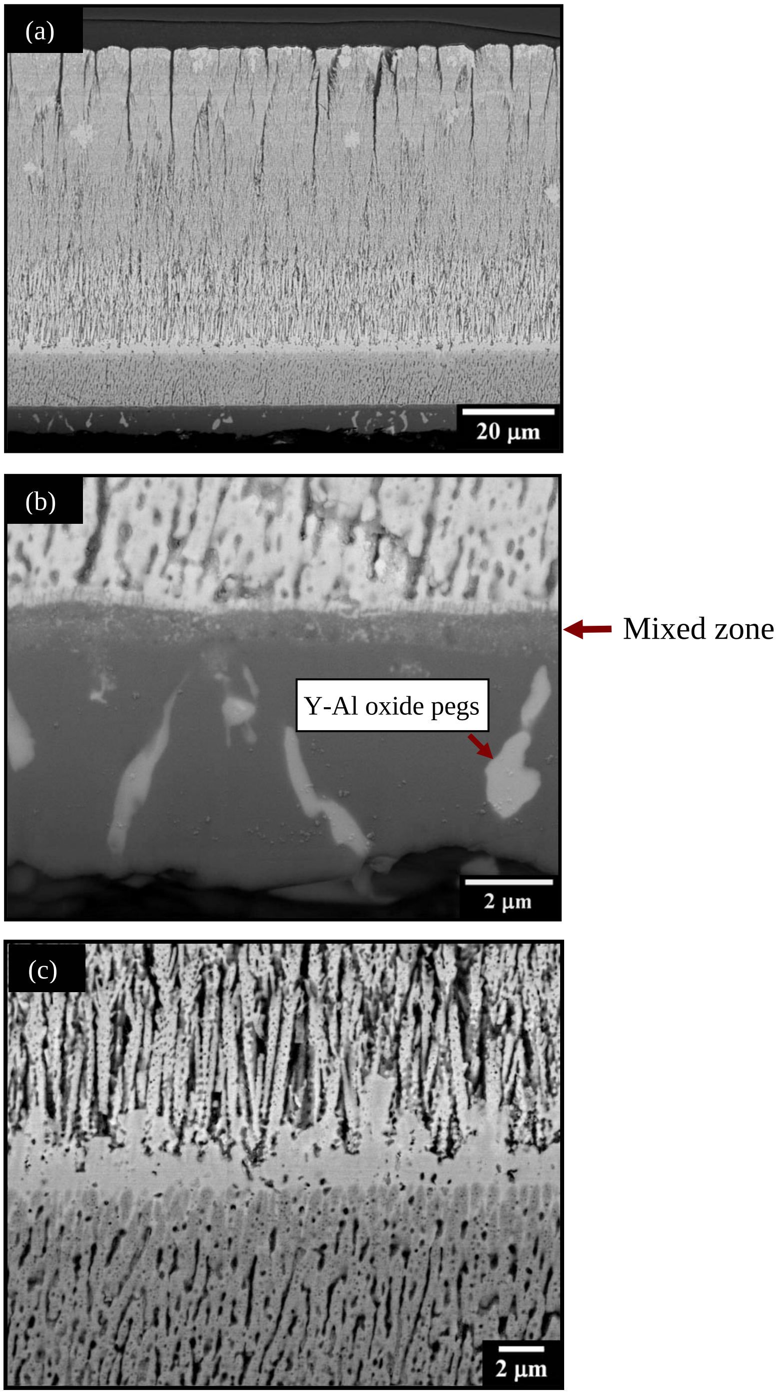

Figure 9-8. The coating morphology after spallation (~1000 cycles). The coating was deposited at 1000 °C using a rotation rate of 6rpm.

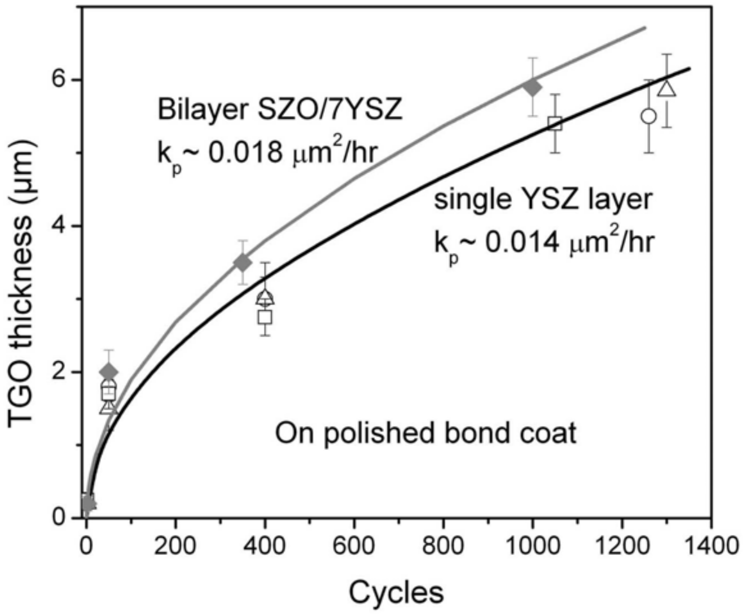

Figure 9-9. The evolution of the TGO thickness with thermal cycles for the bilayer and 7YSZ samples. Both coatings were grown on polished bond coats at 1000 °C.

Table 9-2. Comparison of lifetime of three different coatings

Coatings	**Bond coat Condition**	**Rotation rate (rpm)**	**Failure cycles**
7YSZ	Polished NiCoCrAlY	6	1140 ± 110
SZO			300 ± 30
Bilayer 7YSZ/SZO			1075 ± 75

9.5 Discussion

The high temperature cycling exposure results indicate that 7YSZ is a successful candidate for a diffusion barrier between the $Sm_2Zr_2O_7$ and the TGO even in the presence of open column gaps as needed for preserving strain tolerance. The interdiffusion between $Sm_2Zr_2O_7$ and YSZ happened during the exposure, which has been justified by the detection of Sm in the YSZ coating with the increasing thermal cycles. The morphological evolution of the feathery columnar structure of the coatings is primarily driven by surface diffusion and is an important factor that determines the performance and durability of TBCs. During the cycling, there are some specific features, such as smoothening of the feathery columns, fusion of neighboring columns by neck formation, and coarsening and removal of internal porosity [23]. These processes degrade the insulating capacity and compliance of the TBC. The bi-layer TBC provides an opportunity to compare two candidate TBC materials with the same starting microstructure. After the spallation at 1100 °C, Fig. 9-8(c), the columns of $Sm_2Zr_2O_7$ appear to be rougher than those of YSZ. This indicates that the $Sm_2Zr_2O_7$ is more capable of retaining porosity in the microstructure than 7YSZ.

In this work, 7YSZ layer plays a certain role in acting as a diffusion barrier between SZO and TGO during thermal exposure, but not completely. Sm is still detectable near the TGO during hundreds of hours of cycling. The primary reason is that the 7YSZ coating is not thick enough for the diffusion barrier. The characteristic diffusion distance of Sm in 7YSZ is over 10 μm (7YSZ thickness) after 300 hours. It can be estimated that the minimum thickness of YSZ layer should be more than 20 μm when the coatings have 1000 thermal cycles. More porous structure of YSZ coatings might have the minor effect on the Sm diffusion to TGO. Increasing the 7YSZ coating thickness is a desirable choice for the practical application.

An intriguing observation in the experiment is that some bright dense bandings occur in the coating during exposure. In these regions, the columns are fully sintered with fewer pores. It is also found that much higher content of Sm exists in these regions than the normal columns, which is somewhat consistent with the banding structure observed in Chapter 7. The idea ratio of Sm:Zr in the SZO coating is 50:50. The coating has a compositional fluctuation of Sm during the deposition due to the big difference in vapor pressure of samaria and zirconia. This fluctuation can reach up to ±(5~12)% through the thickness. It can be inferred that very high Sm (usually >60 at.%) in the coating contributes to the fast sintering of the columns. The surface diffusion of Sm in SZO has been dramatically promoted under the condition of much higher Sm concentration, which leads to the faster necking and sintering of the columns. The separate deposition of samaria and zirconia is a best way to control the composition during the deposition.

The bilayer TBC spalled at the interface of TGO/bond coat in a similar way as a single layer YSZ on polished NiCoCrAlY bond coat. This can be explained by the same mechanism that has been discussed in chapter 6. The small cracks were initiated at local thickness heterogeneities and propagated through the low interface toughness of TGO/bond coat caused by some small voids and sulfur diffusion. As mentioned in the experimental results, the TGO growth rate for the bilayer sample is a little faster than that for 7YSZ sample. This is probably attributed to the Sm migration to the TGO layer. The chemical reaction between samaria and alumina leads to the thicker TGO and thus the slight decrease of the lifetime.

CMAS test will be investigated in the future research direction. Experimental data and calculations by Krämer indicate that CMAS can penetrate EB-PVD 7YSZ coatings on very short time scales [24]. Studies of the interaction between $Gd_2Zr_2O_7$ and CMAS [119, 123] also suggests the possibility of a bi-layer architecture with 7YSZ as a mitigating solution. Gadolinium zirconate has demonstrated the potential resistance to CMAS attack. $Gd_2Zr_2O_7$ is effective because it reacts with CMAS more rapidly and the solid reaction products block the intercolumnar pores, stopping the further penetration of the melts. The use of $Gd_2Zr_2O_7$ as a protective barrier against CMAS attack holds significant promise and highlights the importance of microstructure to the implementation of the concept. It is expected that $Sm_2Zr_2O_7$ has the same feature as $Gd_2Zr_2O_7$ due to their similar microstructure.

9.6 Summary

The 7YSZ/ $Sm_2Zr_2O_7$ bilayer coatings have been successfully grown by two-rod DVD system. The analysis of the microstructure reveals that the $Sm_2Zr_2O_7$ coatings continuously grow on the pre-existing 7YSZ columns, retaining the same intercolumnar structures. This indicates that $Sm_2Zr_2O_7$ grows on YSZ column tips along the YSZ column direction. The thickness of the 7YSZ layer is demonstrated to be a critical parameter for a diffusion barrier layer against samaria interaction with alumina. The morphological changes of 7YSZ and $Sm_2Zr_2O_7$ are compared after thermal exposure. $Sm_2Zr_2O_7$ still appears to have the rough column structure while the columns of YSZ become smoothened. The faster TGO growth rate for the bilayer contributes to the slightly decrease of lifetime compared with a single YSZ coating on the same bond coat.

Chapter 10

Discussion

In this dissertation, an electron beam directed vapor deposition technique was investigated as a means for depositing the thermal barrier coatings onto the superalloy substrates with the EB-PVD deposited bond coats. An intensive study of the effect of process condition changes on the composition, morphology, texture and performance of TBCs was conducted to seek to identify the relations between these parameters. These can be described in the following aspects:

10.1 Coating Composition

In this work, two kinds of ceramic materials (7YSZ and $Sm_2Zr_2O_7$) have been investigated as the thermal barrier coatings. Their ideal source composition are 7.6 at.% $YO_{1.5}$- ZrO_2 and 50 at.% $SmO_{1.5}$-ZrO_2, respectively. The coating compositions have been examined after the deposition. The as-deposited 7YSZ coating basically remains to be very close to the source while the SZO coating has a composition fluctuation up to ±12%.

In principle, the composition of a multi-component vapor should be different from that of the melt from which it emanates, as dictated by the vapor pressures of the pure components and their activities in the melt. In the case of oxides, there are additional concerns about dissociation reactions, e.g. the vapor of a ZrO_2-$MO_{1.5}$ (M = Y or rare earth alloy) may contain Zr, ZrO, ZrO_2, M, MO, O and O_2 [158]. For the rare earth oxide M_xO_y, it is reported that the dominant species is the sub-oxide MO [158]. It is also known that one may establish a steady state evaporation condition wherein a solid is continuously fed into its melt and the vapor forming from the melt has the same composition as the solid, albeit not that of the melt. This is claimed to be feasible as long as the vapor pressures of the components are not too dissimilar (reportedly by no more than two orders of magnitude) [159].

In Chapter 7, the ratio of vapor pressure $p_{MO}/p_{(ZrO+ZrO_2)}$ in the ZrO_2-M_xO_y melt was plotted in Fig. 7-13. The data for 7YSZ and the three zirconates that have attracted the most interest for TBC technology have been demonstrated. Figure 7-13 reveals that the partial pressure of the dopant monoxide is usually higher than the total of the Zr-bearing species, but is within a factor of $\leq 10^2$ for the relevant temperature range. This implies that it should be possible, to evaporate and deposit combinations of these oxides with ZrO_2 and preserve the original composition. Upon closer examination it is evident that $p_{MO}/p_{(ZrO+ZrO_2)} \sim 1$ for Y at the 7YSZ liquidus but diverges progressively from unity in the order YO < GdO < SmO < LaO. This is quite consistent with the observations in the DVD experiments. 7YSZ coating is much more close to its source material than the SZO coating. It is also noted that p_{MO} diverges more from $p_{(ZrO+ZrO_2)}$ for the $Zr_{0.5}M_{0.5}O_{1.75}$ compositions than for MO above the pure M_2O_3 oxides, suggesting a significant effect of the relative activities of the oxide/sub-oxide species in the melt. Concomitantly, there is a change in the relative populations of ZrO and ZrO_2 with the addition of the second oxide. Unfortunately, the paucity of thermodynamic information precludes any further analysis of the $Zr_{0.5}Sm_{0.5}O_{1.75}$ system.

10.2 Coating Morphology and Texture

In general, both DVD YSZ and SZO coatings have the triangular column tips during the stationary deposition, while they have the pyramidal tips when the substrate rotates. XRD spectra and pole figures demonstrate that <111> texture dominates in the growth direction of the stationary coatings and the conventionally rotated (≥6 rpm) coatings have the strong textured <100> orientation. Due to the lack of ordering reflections in the XRD spectra, both 7YSZ and SZO exist as a metastable defect phase (t′ phase for 7YSZ, cubic fluorite for SZO) in the coatings rather than their original tetragonal and pyrochlore phases.

The periodic bond chain [80] analysis predicts the preferred growth facets of fluorite to have a {111} habits. The stationary coating has the stable equilibrium <111> texture under normal vapor incidence. The <100> out-of-plane texture for rotated coatings can be explained as a result of evolutionary selection [78] of special orientations wherein the tip facets can capture equal amounts of flux from the vapor during a rotation cycle [62, 65]. The texture of the rotated SZO coatings was generally less developed than that observed for YSZ at the same temperatures and rotation rates, i.e. minor amounts of other orientations were found mixed in with the dominant ⟨100⟩ columns. Probably it result from the significantly smaller thickness of the SZO coatings, ~70±5% of their 7YSZ counterparts, implying that the evolutionary selection process was more advanced in the latter and the minor orientations had been screened out.

At very low rotation rates (0.5 rpm), the sample has a mixed spectrum from stationary and rotated samples. It is because of the adjustments that are needed at the column tip facets as the growth direction changes over a 180° range and a long wavelength each revolution of the substrate. The tips undergo exacerbated segmentation because the features on one facet build up substantially on the "sunrise" part of the cycle before the "sunset" portion occurs, biasing the shadowing process. The evolutionary selection process is arguably delayed, and the segmentation adds complexity to the possible spectrum of orientations at the surface.

10.3 Coating Morphology and Thermal Conductivity

There are three types of pores characterized in the coatings. Type I pores are the wide and elongated intercolumnar gaps. Type II pores occur at the edge of the columns with the feature of "feathery structure". Type III pores have the smallest scale which are hardly seen in the normal view of images. They are nano-sized spheroid pores distributed in the center of a column.

Porosity in the coating generally occurs through the process of shadowing coupled with insufficient surface diffusion. Geometric features in the path of vapor cast shadows on the growing film surface due to the line-of-sight nature of the deposition process. The growth of the voids created by the shadowing process is dependent on the competition with the void elimination by surface diffusion. Intercolumnar gaps originate from vapor phase condensation and operation of macroscopic shadowing caused by the curved column tips, triggered by rotation of the parts during deposition. The feathery pores are a consequence of shadowing by growth steps on the column tips near the center of a column. The growth steps of the column tips act as shadowing centers, leading to mostly open porosity aligned under angles between 35-50° towards the main column axis. These open feathery pores might partly transform into the closed nano-sized spheroid pores during the deposition. These nano pores are found more often in the center area of a column.

When heat is propagated through coatings, phonon conduction primarily contributes to the heat transport. Phonons are strongly scattered at pore surfaces and conduction across ellipsoidal pores with high aspect ratios introduces a high thermal resistance. The thermal conductivity is therefore strongly dependent on the TBC microstructure, including volume fraction, shape and orientation of pores [142, 143]. Normally Type I pores are almost perpendicular to the substrate and are less effective at impeding the heat flux to the below substrate. However, in the slowly rotated samples with C-shaped columns, the conduction distance is increased contributing to a significant impedance to the heat flow. This is justified by an analytical study of heat conduction across the zigzag structures [63], which indicated that inclined Type I pores were highly effective at disrupting through thickness thermal transport. Type II and III pores are inclined to the column growth direction with high aspect ratio, which are quite resistant to the heat transport.

It is found in the experiments that the SZO coatings have thermal conductivities that range from 0.4 to 1.1 W/m·K; much lower than that of identically grown 7YSZ coatings.

The differences in conductivity appear to arise almost entirely from the substantially different intrinsic thermal conductivities of the two materials. The ambient temperature thermal conductivity of fully dense SZO has been measured to be ~2.0 W/mK [43], while that for bulk 7YSZ is ~3.0 W/mK [43]. This big difference leads to the disparate values of two coating with the similar microstructure,

10.4 TBC Failure Mechanisms

In this work, TBC density and microstructure are effected by the substrate rotation rate and substrate surface roughness. Concomitantly the TBC failure is strongly dependent upon the density and microstructure. This causes the different failure mechanisms for 7YSZ coatings deposited on grit-blasted and polished substrates.

The “Corn Kernel” growth defects occur at the concave regions of the bond coat when YSZ is grown on grit-blasted bond coats. As the bond coat rumples during cycling, concavities are amplified. The displacements induce tension in the superposed TBC, causing cracks to form (often in “corn kernel” defects) and propagate along planes of lowest local toughness (through planes of small pores). Coalescence of a sufficient number of contiguous cracks results in a delamination that exceeds the critical length for buckling [30]. Most systems with MCrAlY bond coats are not prone to such rumpling [30], except upon stepwise cycling [146]. The properties of this particular overlay composition (in terms of thermal expansion and creep strength) must be sufficiently different to allow rumpling. The specifics remain to be ascertained.

Upon polishing, rumpling is suppressed, as expected from the Balint and Hutchinson model [89] and from previous observations [87, 147]. Instead, delamination occurs at the TGO/bond coat interface (Fig. 13). Small cracks initiate at the TGO thickness heterogeneities, Fig. 10(c). For these to grow and coalesce, the toughness of the intervening interface must be lower than that on pristine interfaces [88, 148] and this appears to be due to the appearance of small flat voids in the intervening regions, possibly in conjunction with sulfur segregation and the embrittlement of this interface [37, 149]. Hf is found to effectively getter S and inhibit segregation to the interface, thereby enhancing the adhesion between the TGO and bond coat [150]. However, no Hf is doped into the bond coat studied here. This may result in the formation of small flat voids in some regions.

The spallation life is increased as the rotation rate during deposition is decreased. The lifetime of the DVD coatings on both surfaces are also significantly greater than EB-PVD coatings applied on the same bond coat system. While there are many morphological differences in the coatings that might be invoked to account for these observations, the most fundamental is the significant difference in coating density. It is noted that the elastic modulus of as-deposited coatings increases with coating density. Through the calculations from the Hutchinson’s theory [151], the thickness of the TGO layers at which spallation occurs also decreases as the density increases. The enhanced durability relative to EB-PVD coatings, as well as the trend with rotation rate, is attributed to the lower coating density.

Although YSZ has good thermal cyclic durability, the high temperature phase instability limits its further use for future TBC operation at even higher temperature to increase engine efficiency. SZO coatings with low thermal conductivity attract the interest for the potential TBC application. In spite of that, the cycling performance precludes its direct use as the TBC. The earlier failure of the SZO coatings is independent of bond coat conditions. The thermochemical instability between samaria and alumina is a significant reason for the earlier spallation. The experiments have found that the chemical reaction happens at the interface of SZO/TGO during thermal cycling:

$$Sm_2O_3 + Al_2O_3 \rightarrow 2SmAlO_3$$

Thus, the reaction product $SmAlO_3$ is expected to lower the interface toughness and lead to the earlier failure. It remains to be investigated about the extent to which the $SmAlO_3$ damages the interface.

In spite of shorter lifetime, SZO coatings appear to show a promising sintering resistance in comparison to YSZ. Under this circumstance, the bilayer 7YSZ/SZO is created and investigated. The slight difference of lattice parameters between these two oxides leads to relatively small lattice misfit, which provides an opportunity for SZO to grow continuously on the 7YSZ column tips. 7YSZ layer is deposited as a barrier layer against the samaria diffusion to the underlying alloy. However, the surfaces of intercolumnar pores provide a diffusion path for Sm to the 7YSZ columns, and then to the TGO. When the thickness of 7YSZ layer is 10 μm, Sm is detected at the interface of YSZ/TGO after 350 thermal cycles by EDS analysis. The YSZ thickness becomes a significant factor for fulfilling the function of a diffusion barrier. The minimum thickness of YSZ layer estimated from characteristic diffusion length $\sqrt{D\tau}$ is ~ 20 μm when the bilayer has at least 1000-hr thermal cycles.

Chapter 11

Conclusions

In this dissertation, an electron beam directed vapor deposition approach was used as a means for systematically investigating the effect of substrate rotation and deposition temperature on the coating composition, structure, pore morphology and texture. The relation between pore morphology and coating density and thermal conductivity was also examined. The failure lifetime of the coatings could be effected by varying the bond coat condition. Two types of TBC materials (7YSZ and $Sm_2Zr_2O_7$) are studied in this work. Some specific conclusions can be drawn:

During stationary deposition of YSZ coatings, straight sided growth columns are formed with triangular column faceted tips. Rotated samples have growth columns with square pyramidal faceted tips. This difference is accompanied by a change in preferred crystallographic growth direction from <111> to <100> as the substrate rotation rate increases. Low rotation rates lead to wavy columnar structure due to the slow rate of change of the incidence angle of the vapor flux to the substrate, resulting in a very low thermal conductivity of 0.8 W/mK. At high rotation rates, relatively straight columns in the coating still have low thermal conductivities in the 1 W/mK range. The low thermal conductivity of the rotated EB-DVD coatings appears to be a result of an elongated Type I intercolumnar gaps and an increased volume fraction of inclined feathery Type II pores and Type III spheroid nanopores in the primary growth columns.

The effect of rotation rate and bond coat processing on the density, pore morphology, and cycling behavior of 7YSZ coatings has been investigated. It is found that rough (Grit-blasted) bond coat has more surface defects (such as craters, sharp edges and impurities etc.) than smooth (hand-polished) one, which will produce a significant effect on the following TBC deposition. Coatings grown on grit-blasted bond coats have only half the lifetime of those deposited on polished bond coats. The lifetimes of coatings applied to rough bond coats are governed by bond coat rumpling whereas those for the polished bond coat coatings is dictated by interface delamination. The critical TGO thickness at coating failure is shown to decrease with increase in coating density consistent with a steady state strain energy release model. Measurements of the coatings elastic modulus confirm a reduction in coating modulus as the pore content of the coatings increases and therefore a reduction in the stored elastic strain energy available to drive interfacial failure.

Due to phase instability, fast sintering rate and CMAS attack of YSZ materials at high temperatures, a promising candidate material of $Sm_2Zr_2O_7$ with low thermal conductivity and good phase stability was investigated using an EB-DVD approach. Experiments have found that SZO coatings made by EB-DVD exhibit compositional variation through the coating thickness of up to ±12%$SmO_{1.5}$, indicative of source instabilities induced in part by the difference in vapor pressures of the constituent oxides. A metastable fluorite structure forms in the SZO coatings due to kinetically constrained cation ordering within the time scale of the deposition process. The thermal conductivity of DVD SZO coatings is substantially lower than that of the counterpart DVD 7YSZ. The former is primarily due to the lower intrinsic conductivity of the SZO, whereas the latter is a result of the much higher porosity content produced by the DVD process. The cycling tests have shown that SZO coatings have very short lifetime regardless of the bond coat conditions. It primarily results from the thermochemical instability between $SmO_{1.5}$ and $AlO_{1.5}$ as well as the densely sintering regions above the TGO layer. The reaction between them forms the interphase $SmAlO_3$ that may embrittle the interface and reduce the lifetime of the coatings. SZO coating appears to show a better sintering resistance than YSZ coating during the equivalent exposure to high temperature.

The 7YSZ/ $Sm_2Zr_2O_7$ bilayer coatings have been successfully grown by DVD approach. Examination of the interface of bilayer shows that SZO coatings continuously grow on the pre-existing 7YSZ columns, retaining the same intercolumnar structures. The effectiveness of the 7YSZ layer as a diffusion barrier layer against samaria interaction with alumina is strongly dependent upon the thickness of YSZ coating. Finally the bilayer system has a comparable lifetime with a single YSZ coating on the same bond coat.

When the SZO coating is deposited from a single SZO rod, the composition fluctuation of Sm in the coating is undesirable. This fluctuation leads to the rapid sintering in the dense regions of high content of Sm. The reason remains to be identified and explored by future work. It is still not clear how higher atomic percentage of Sm promotes the fast sintering and how the reaction product $SmAlO_3$ between samaria and alumina damages the interface. The CMAS performance of the YSZ/SZO bilayer coating also needs to be investigated in the future.

References:

[1] Levi CG. Metastability and microstructure evolution in the synthesis of inorganics from precursors. Acta Materialia 1998;46:787.

[2] Fabrichnaya O, Seifert HJ. Assessment of thermodynamic functions in the ZrO_2-Sm_2O_3-Al_2O_3 system. Journal of Alloys and Compounds;In Press, Corrected Proof.

[3] Budnikov PP, Kushakovskii VI, Belevantsev VS. Acad. Sci. USSR Dokl. Chem. 1965;165:1177.

[4] Mizuno M, Yamada T, Noguchi T. Yogyo Kyokaishi 1977;85:374.

[5] Bondar IA, Toropov NA. Bull. Acad. Sci. USSR, Div. Chem. Sci. 1966;2:195.

[6] Reed RC. The Superalloys: Fundamentals and Applications: Cambridge University Press, 2006.

[7] Dutta S. Fracture toughness and reliability in high-temperature structural ceramics and composites: Prospects and challenges for the 21st Century. Bulletin of Materials Science 2001;24:117.

[8] Richerson DW. Ceramics for turbine engines. Mechanical Engineering, September 1997.

[9] Miller RA. Thermal barrier coatings for aircraft engines: history and directions. Journal of Thermal Spray Technology 1997;6:35.

[10] Peters M, Leyens C, Schulz U, Kaysser WA. EB-PVD Thermal Barrier Coatings for Aeroengines and Gas Turbines. Advanced Engineering Materials 2001;3:193.

[11] Miller RA. Current status of thermal barrier coatings -- An overview. Surface and Coatings Technology 1987;30:1.

[12] Groves JF. Directed Vapor Deposition. Department of Materials Science and Engineering, vol. Ph.D. Charlottesville, VA: University of Virginia, 1998.

[13] Hass DD. Thermal Barrier Coatings via Directed Vapor Deposition. Department of Materials Science and Engineering, vol. Ph.D. Charlottesville, VA: University of Virginia, 2001.

[14] Gell M, Duhl DN, Gupta DK, Sheffler KD. Advanced Superalloy Airfoils. Journal of Metals 1987;39:11.

[15] Chen X, Wang R, Yao N, Evans AG, Hutchinson JW, Bruce RW. Foreign object damage in a thermal barrier system: mechanisms and simulations. Materials Science and Engineering A 2003;352:221.

[16] Rhys-Jones TN, Toriz FC. Thermal barrier coatings for turbine applications in aero engines. High Temperature Technology 1989;7:73.

[17] Wellman RG, Nicholls JR. Erosion, corrosion and erosion-corrosion of EB PVD thermal barrier coatings. Tribology International 2008;41:657.

[18] Tabakoff W, Shanov V. Erosion rate testing at high temperature for turbomachinery use. Surface and Coatings Technology 1995;76-77:75.

[19] Becker WT, Shipley RJ. ASM Handbook: Volume 11: Failure Analysis and Prevention, 2002.

[20] Padture NP, Gell M, Jordan EH. Thermal Barrier Coatings for Gas-Turbine Engine Applications. Science 2002;296:280.

[21] Schulz U. Phase Transformation in EB-PVD Yttria Partially Stabilized Zirconia Thermal Barrier Coatings during Annealing. Journal of the American Ceramic Society 2000;83:904.

[22] Lughi V, Clarke DR. Transformation of Electron-Beam Physical Vapor-Deposited 8 wt% Yttria-Stabilized Zirconia Thermal Barrier Coatings. Journal of the American Ceramic Society 2005;88:2552.

[23] Lughi V, Tolpygo VK, Clarke DR. Microstructural aspects of the sintering of thermal barrier coatings. Materials Science and Engineering A 2004;368:212.

[24] Krämer S, Yang J, Levi CG, Johnson CA. Thermochemical Interaction of Thermal Barrier Coatings with Molten CaO-MgO-Al_2O_3-SiO_2 (CMAS) Deposits. Journal of the American Ceramic Society 2006;89:3167.

[25] Stecura S, Liebert, CH. Thermal barrier coating system. US Patent 4055705: The United States of America as represented by the Administrator of the (Washington, DC), 1977.

[26] Streiff R, Cerclier O, Boone DH. Structure and hot corrosion behavior of platinum-modified aluminide coatings. Surface and Coatings Technology 1987;32:111.

[27] Tolpygo V, Clarke D, Murphy K. The effect of grit blasting on the oxidation behavior of a platinum-modified nickel-aluminide coating. Metallurgical and Materials Transactions A 2001;32:1467.

[28] Stecura S. Advanced thermal barrier system bond coatings for use on nickel-, cobalt- and iron-base alloy substrates. Thin Solid Films 1986;136:241.

[29] Fox AC, Clyne TW. Oxygen transport by gas permeation through the zirconia layer in plasma sprayed thermal barrier coatings. Surface and Coatings Technology 2004;184:311.

[30] Evans AG, Mumm DR, Hutchinson JW, Meier GH, Pettit FS. Mechanisms controlling the durability of thermal barrier coatings. Progress in Materials Science 2001;46:505.

[31] Stott FH, Wood GC. Growth and adhesion of oxide scales on Al_2O_3-forming alloys and coatings. Materials Science and Engineering 1987;87:267.

[32] Stiger MJ, Yanar NM, Topping MG, Pettit FS, Meier GH. Thermal barrier coatings for the 21st century. Z. Metallkd 1999;90:1069.

[33] Evans AG, Clarke DR, Levi CG. The influence of oxides on the performance of advanced gas turbines. Journal of the European Ceramic Society 2008;28:1405.

[34] Levi CG, Sommer E, Terry SG, Catanoiu A, Rühle M. Alumina Grown during Deposition of Thermal Barrier Coatings on NiCrAlY. Journal of the American Ceramic Society 2003;86:676.

[35] Tolpygo VK, Clarke DR. Microstructural study of the theta-alpha transformation in alumina scales formed on nickel-aluminides. Materials at High Temperatures 2000;17:59.

[36] Rybicki GC, Smialek JL. Effect of the θ-α-Al_2O_3 transformation on the oxidation behavior of β-NiAl + Zr. Oxidation of Metals 1989;31:275.

[37] Smeggil JG. Some comments on the role of yttrium in protective oxide scale adherence. Materials Science and Engineering 1987;87:261.

[38] Reddy A, Hovis D, Heuer A, Paulikas A, Veal B. In Situ Study of Oxidation-Induced Growth Strains In a Model NiCrAlY Bond-Coat Alloy. Oxidation of Metals 2007;67:153.

[39] Lipkin DM, Clarke DR. Measurement of the stress in oxide scales formed by oxidation of alumina-forming alloys. Oxidation of Metals 1996;45:267.

[40] Fabrichnaya O, Aldinger F. Assessment of the thermodynamic parameters in the system ZrO_2-Y_2O_3-Al_2O_3. Zeitschrift für Metallkunde 2004;95:27.

[41] Schulz U, Saruhan B, Fritscher K, Leyens C. Review on Advanced EB-PVD Ceramic Topcoats for TBC Applications. International Journal of Applied Ceramic Technology 2004;1:302.

[42] Miller R, Smialek, JL, Garlick, RG. Advances in Ceramics **3**, Science and Technology of Zirconia I: American Ceramic Society, Columbus, Ohio, 1981.

[43] Wu J, Wei X, Padture NP, Klemens PG, Gell M, Garcia E, Miranzo P, Osendi MI. Low-Thermal-Conductivity Rare-Earth Zirconates for Potential Thermal-Barrier-Coating Applications. Journal of the American Ceramic Society 2002;85:3031.

[44] Morrell P, Taylor R. Thermal diffusivity of thermal barrier coatings of ZrO_2 stabilized with Y_2O_3. High Temp. High Press. 1985;17:79.

[45] Klemens PG. Theory of heat conduction in nonstoichiometric oxides and carbides. High Temp. High Press. 1985;17:41.

[46] Wu J, Padture NP, Klemens PG, Gell M, García E, Miranzo P, Osendi MI. Thermal conductivity of ceramics in the ZrO_2-$GdO_{1.5}$ system. Journal of Materials Research 2002;17:3193.

[47] Wu J, Padture NP, Gell M. High-temperature chemical stability of low thermal conductivity ZrO_2-$GdO_{1.5}$ thermal-barrier ceramics in contact with [alpha]-Al2O3. Scripta Materialia 2004;50:1315.

[48] Clarke DR. Materials selection guidelines for low thermal conductivity thermal barrier coatings. Surface and Coatings Technology 2003;163-164:67.

[49] Jones R. Thermal Barrier Coatings in Metallurgical and Ceramic Protective Coatings. London: Chapman & Hall, 1996.

[50] Clarke DR, Levi CG. Materials Design For The Next Generation Thermal Barrier Coatings. Annual Review of Materials Research 2003;33:383.

[51] Jayaram V, Levi CG, Whitney T, Mehrabian R. Characterization of Al_2O_3---ZrO_2 powders produced by electrohydrodynamic atomization. Materials Science and Engineering: A 1990;124:65.

[52] Balmer ML, Lange FF, Levi CG. Metastable Phase Selection and Partitioning for $Zr_{(1-x)}Al_xO_{(2-x/2)}$ Materials Synthesized with Liquid Precursors. Journal of the American Ceramic Society 1994;77:2069.

[53] Murphy KS, More KL, Lance MJ. As-deposited mixed zone in thermally grown oxide beneath a thermal barrier coating. Surface and Coatings Technology 2001;146-147:152.

[54] Nicholls JR, Deakin MJ, Rickerby DS. A comparison between the erosion behaviour of thermal spray and electron beam physical vapour deposition thermal barrier coatings. Wear 1999;233-235:352.

[55] Jones RL, Williams CE. Hot corrosion of Co---Cr---Al---Y by molten sulfate-vanadate deposits. Materials Science and Engineering 1987;87:353.

[56] Strangman TE. Thermal barrier coatings for turbine airfoils. Thin Solid Films 1985;127:93.

[57] Schulz U, Schmucker M. Microstructure of ZrO_2 thermal barrier coatings applied by EB-PVD. Materials Science and Engineering A 2000;276:1.

---

[58] Ruckle DL. Plasma-sprayed ceramic thermal barrier coatings for turbine vane platforms. Thin Solid Films 1980;73:455.

[59] Nicholls JR, Lawson KJ, Johnstone A, Rickerby DS. Methods to reduce the thermal conductivity of EB-PVD TBCs. Surface and Coatings Technology 2002;151-152:383.

[60] Taylor TA. Thermal barrier coating for substrates and process for producing it. United States Patent 5073433: Technology Corporation (Danbury, CT) 1991.

[61] Padture NP, Schlichting KW, Bhatia T, Ozturk A, Cetegen B, Jordan EH, Gell M, Jiang S, Xiao TD, Strutt PR, Garcia E, Miranzo P, Osendi MI. Towards durable thermal barrier coatings with novel microstructures deposited by solution-precursor plasma spray. Acta Materialia 2001;49:2251.

[62] Schulz U, Terry SG, Levi CG. Microstructure and texture of EB-PVD TBCs grown under different rotation modes. Materials Science and Engineering A 2003;360:319.

[63] Lu TJ, Levi CG, Wadley HNG, Evans AG. Distributed Porosity as a Control Parameter for Oxide Thermal Barriers Made by Physical Vapor Deposition. Journal of the American Ceramic Society 2001;84:2937.

[64] Leamy HJ, Gilmer GH, Dirks AG. "The Microstructure of Vapor Deposited Thin Films" in Current Topics in Materials Science
North-Holland, Amsterdam, 1980.

[65] Terry SG. Evolution of Microstructure during the growth of thermal barrier coatings by electron-beam physical vapor deposition. Materials Department, vol. Ph. D. Santa Barbara: University of California, 2001.

[66] Thornton JA. Influence of substrate temperature and deposition rate on structure of thick sputtered Cu coatings. Journal of Vacuum Science and Technology 1975;12:830.

[67] Rigney DV, Viguie, R, Wortman, DJ, Skelly, DW. Thermal Barrier Coating Workshop 1995. vol. 3312: NASA Conference Publication, 1995. p.135.

[68] Rossnagel SM, Nichols C, Hamaguchi S, Ruzic D, Turkot R. Thin, high atomic weight refractory film deposition for diffusion barrier, adhesion layer, and seed layer applications. Journal of Vacuum Science & Technology B: Microelectronics and Nanometer Structures 1996;14:1819.

[69] Robbie K, Friedrich LJ, Dew SK, Smy T, Brett MJ. Fabrication of thin films with highly porous microstructures. Journal of Vacuum Science & Technology A: Vacuum, Surfaces, and Films 1995;13:1032.

[70] Muller K-H. Dependence of thin-film microstructure on deposition rate by means of a computer simulation. Journal of Applied Physics 1985;58:2573.

[71] Zhou XW, Johnson RA, Wadley HNG. Vacancy formation during vapor deposition. Acta Materialia 1997;45:4441.

[72] Yang YG, Johnson RA, Wadley HNG. A Monte Carlo simulation of the physical vapor deposition of nickel. Acta Materialia 1997;45:1455.

[73] Cho J, Terry SG, LeSar R, Levi CG. A kinetic Monte Carlo simulation of film growth by physical vapor deposition on rotating substrates. Materials Science and Engineering A 2005;391:390.

[74] Hass DD, Slifka AJ, Wadley HNG. Low thermal conductivity vapor deposited zirconia microstructures. Acta Materialia 2001;49:973.

[75] Robbie K, Brett MJ, Lakhtakia A. First thin film realization of a helicoidal bianisotropic medium. Journal of Vacuum Science & Technology A: Vacuum, Surfaces, and Films 1995;13:2991.

[76] Groves JF, Wadley HNG. Functionally graded materials synthesis via low vacuum directed vapor deposition. Composites Part B: Engineering 1997;28:57.

[77] Unal O, Mitchell TE, Heuer AH. Microstructures of Y_2O_3 -Stabilized ZrO_2 Electron Beam-Physical Vapor Deposition Coatings on Ni-Base Superalloys. Journal of the American Ceramic Society 1994;77:984.

[78] van der Drift A. Evolutionary selection, a principle governing growth orientation in vapour-deposited layers. Philips Research Reports 1967;22:267.

[79] Wada K, Yamaguchi N, Matsubara H. Effect of substrate rotation on texture evolution in ZrO_2-4 mol.% Y_2O_3 layers fabricated by EB-PVD. Surface and Coatings Technology 2005;191:367.

[80] Hartman P, Perdock WG. On the relations between structure and morphology of crystals. Acta Crystallographica 1955;8:49.

[81] Hartman P. On the crystal habit of fluorite: Bulg. Acad. Sci., Sofia, 1974.

[82] Klemens PG, Gell M. Thermal conductivity of thermal barrier coatings. Materials Science and Engineering A 1998;245:143.

[83] Mumm DR, Evans AG, Spitsberg IT. Characterization of a cyclic displacement instability for a thermally grown oxide in a thermal barrier system. Acta Materialia 2001;49:2329.

[84] Yanar NM, Meier GH, Pettit FS. The influence of platinum on the failure of EBPVD YSZ TBCs on NiCoCrAlY bond coats. Scripta Materialia 2002;46:325.

[85] Mumm DR, Evans AG. On the role of imperfections in the failure of a thermal barrier coating made by electron beam deposition. Acta Materialia 2000;48:1815.

[86] Yanar N, Pettit F, Meier G. Failure characteristics during cyclic oxidation of yttria stabilized zirconia thermal barrier coatings deposited via electron beam physical vapor deposition on platinum aluminide and on NiCoCrAlY bond coats with processing modifications for improved performances. Metallurgical and Materials Transactions A 2006;37:1563.

[87] Spitsberg IT, Mumm DR, Evans AG. On the failure mechanisms of thermal barrier coatings with diffusion aluminide bond coatings. Materials Science and Engineering A 2005;394:176.

[88] Chen MW, Ott RT, Hufnagel TC, Wright PK, Hemker KJ. Microstructural evolution of platinum modified nickel aluminide bond coat during thermal cycling. Surface and Coatings Technology 2003;163-164:25.

[89] Balint DS, Hutchinson JW. An analytical model of rumpling in thermal barrier coatings. Journal of the Mechanics and Physics of Solids 2005;53:949.

[90] Peng X, Clarke DR. Piezospectroscopic Analysis of Interface Debonding in Thermal Barrier Coatings. Journal of the American Ceramic Society 2000;83:1165.

[91] Tolpygo VK, Clarke DR. On the rumpling mechanism in nickel-aluminide coatings: Part I: an experimental assessment. Acta Materialia 2004;52:5115.

[92] Mercer C, Faulhaber S, Evans AG, Darolia R. A delamination mechanism for thermal barrier coatings subject to calcium-magnesium-alumino-silicate (CMAS) infiltration. Acta Materialia 2005;53:1029.

[93] Clarke DR, Phillpot SR. Thermal barrier coating materials. Materials Today 2005;8:22.

[94] Cao XQ, Vassen R, Stoever D. Ceramic materials for thermal barrier coatings. Journal of the European Ceramic Society 2004;24:1.

[95] Levi CG. Emerging materials and processes for thermal barrier systems. Current Opinion in Solid State and Materials Science 2004;8:77.

[96] Thornton J, Majumdar A, McAdam G. Enhanced cerium migration in ceria-stabilised zirconia. Surface and Coatings Technology 1997;94-95:112.

[97] Brandon JR, Taylor R. Thermal properties of ceria and yttria partially stabilized zirconia thermal barrier coatings. Surface and Coatings Technology 1989;39-40:143.

[98] Jones RL, Reidy RF, Mess D. Scandia, yttria-stabilized zirconia for thermal barrier coatings. Surface and Coatings Technology 1996;82:70.

[99] Jones RL, Mess D. Improved tetragonal phase stability at 1400°C with scandia, yttria-stabilized zirconia. Surface and Coatings Technology 1996;86-87:94.

[100] Padture NP, Klemens PG. Low Thermal Conductivity in Garnets. Journal of the American Ceramic Society 1997;80:1018.

[101] Zhu D, Miller RA. Sintering and creep behavior of plasma-sprayed zirconia- and hafnia-based thermal barrier coatings. Surface and Coatings Technology 1998;108-109:114.

[102] Yoshiba M, Abe K, Aranami T, Harada Y. High-temperature oxidation and hot corrosion behavior of two kinds of thermal barrier coating systems for advanced gas turbines. Journal of Thermal Spray Technology 1996;5:259.

[103] Schulz U, Fritscher K, Leyens C. Two-source jumping beam evaporation for advanced EB-PVD TBC systems. Surface and Coatings Technology 2000;133-134:40.

[104] Friedrich CJ, Gadow R, Lischka MH. Lanthanum hexaaluminate thermal barrier coatings. The 25th Annual International Conference on Composites, Advanced Ceramics, Materials, and Structures: B. Cocoa Beach, Florida: American Ceramic Society, Westerville, OH, USA, pp. 372-375, 2001.

[105] Vassen R, Cao X, Tietz F, Basu D, Stover D. Zirconates as New Materials for Thermal Barrier Coatings. Journal of the American Ceramic Society 2000;83:2023.

[106] Kittel C. Introduction to Solid State Physics: John Wiley and Sons, Inc., New York, 1953.

[107] Dugdale JS, MacDonald DKC. Lattice Thermal Conductivity. Physical Review 1955;98:1751.

[108] Lawson AW. On the high temperature heat conductivity of insulators. Journal of Physics and Chemistry of Solids 1957;3:155.

[109] Cahill DG, Pohl RO. Heat flow and lattice vibrations in glasses. Solid State Communications 1989;70:927.

[110] Maloney MJ. Thermal barrier coating systems and materials. United States Patent 6177200: United Technologies Corporation (Hartford, CT), 2001.

[111] Suresh G, Seenivasan G, Krishnaiah MV, Murti PS. Investigation of the thermal conductivity of selected compounds of lanthanum, samarium and europium. Journal of Alloys and Compounds 1998;269:L9.

[112] Lehmann H, Pitzer D, Pracht G, Vassen R, Stover D. Thermal Conductivity and Thermal Expansion Coefficients of the Lanthanum Rare-Earth-Element Zirconate System. Journal of the American Ceramic Society 2003;86:1338.

[113] Suresh G, Seenivasan G, Krishnaiah MV, Srirama Murti P. Investigation of the thermal conductivity of selected compounds of gadolinium and lanthanum. Journal of Nuclear Materials 1997;249:259.

[114] Schelling PK, Phillpot SR, Grimes RW. Optimum pyrochlore compositions for low thermal conductivity. Philosophical Magazine Letters 2004;84:127

[115] Cao XQ, Vassen R, Jungen W, Schwartz S, Tietz F, Stover D. Thermal Stability of Lanthanum Zirconate Plasma-Sprayed Coating. Journal of the American Ceramic Society 2001;84:2086.

[116] Catchen GL, Rearick TM. O-anion transport measured in several $R_2M_2O_7$ pyrochlores using perturbed-angular-correlation spectroscopy. Physical Review B 1995;52:9890.

[117] Wang C. Experimental and Computational Phase Studies of the ZrO2-based Systems for Thermal Barrier Coatings. Max-Planck-Institut für Metallforschung, vol. Ph.D. Stuttgart, 2006.

[118] Kraftmakher Y. Equilibrium vacancies and thermophysical properties of metals. Physics Reports 1998;299:79.

[119] Leckie RM, Kramer S, Ruhle M, Levi CG. Thermochemical compatibility between alumina and ZrO_2-$GdO_{3/2}$ thermal barrier coatings. Acta Materialia 2005;53:3281.

[120] Maloney MJ. Thermal barrier coating systems and materials. United States Patent 6117560: United Technologies Corporation (Hartford, CT), 2000.

[121] Bevan DJM, Summerville E. Mixed Rare Earth Oxides, 1979.

[122] Subramanian R. Thermal barrier coating having high phase stability. US Patent 6258467: Siemens Westinghouse Power Corporation (Orlando, FL), 2001.

[123] Leckie RM. Fundamental issues regarding the implementation of Gd zirconate in thermal barrier systems. Doctoral Dissertation in Materials. Santa Barbara, CA: University of California, Santa Barbara, 2006.

[124] Hass DD, Parrish PA, Wadley HNG. Electron beam directed vapor deposition of thermal barrier coatings. Journal of Vacuum Science & Technology A: Vacuum, Surfaces, and Films 1998;16:3396.

[125] Kim YG, Wadley HNG. Plasma-assisted deposition of lithium phosphorus oxynitride films: Substrate bias effects. Journal of Power Sources 2009;187:591.

[126] Schiller S, Heisig U, Panzer S. Electron Beam Technology: John Wiley & Sons, New York, 1982.

[127] Arata Y. Plasma, Electron, and Laser Beam Technology: Metals Park, OH, ASM, 1986.

[128] Yu Z, Hass DD, Wadley HNG. NiAl bond coats made by a directed vapor deposition approach. Materials Science and Engineering A 2005;394:43.

[129] Wang B, Chakoumakos BC, Sales BC, Kwak BS, Bates JB. Synthesis, Crystal Structure, and Ionic Conductivity of a Polycrystalline Lithium Phosphorus Oxynitride with the [gamma]-Li3PO4 Structure. Journal of Solid State Chemistry 1995;115:313.

[130] Hass DD, Wadley HNG. Gas jet assisted vapor deposition of yttria stabilized zirconia. Journal of Vacuum Science & Technology A: Vacuum, Surfaces, and Films 2009;27:404.

---

[131] Jensen P, Bardotti L, Hoareau A, Treilleux M, Cabaud B, Perez A, Cadete Santos Aires F. Diffusion and aggregation of large antimony and gold clusters deposited on graphite. Surface Science 1996;367:276.

[132] Besson D, Bardotti L, Hoareau A, Prevel B, Treilleux M, Esnouf C. Spontaneous alloying on HOPG by successive deposition of Sb clusters and Au atoms. Materials Science And Engineering B 1999;60:51.

[133] Thornton JA. Influence of apparatus geometry and deposition conditions on the structure and topography of thick sputtered coatings. Journal of Vacuum Science and Technology 1974;11:666.

[134] Zhao H, Yu F, Bennett TD, Wadley HNG. Morphology and thermal conductivity of yttria-stabilized zirconia coatings. Acta Materialia 2006;54:5195.

[135] Yu F. The Nondestructive Evaluation of Thermal Barrier Coatings: Measurements of Thermal Properties and Associated Defects. Department of Mechanical and Environmental Engineering, vol. Ph. D. Santa Barbara: University of California, 2005.

[136] Jang B-K, Matsubara H. Hardness and Young's modulus of nanoporous EB-PVD YSZ coatings by nanoindentation. Journal of Alloys and Compounds 2005;402:237.

[137] Wellman RG, Dyer A, Nicholls JR. Nano and Micro indentation studies of bulk zirconia and EB PVD TBCs. Surface and Coatings Technology 2004;176:253.

[138] Oliver WC, Pharr GM. An improved technique for determining hardness and elastic modulus using load and displacement sensing indentation experiments. Journal of Materials Research 1992;7:1564.

[139] Yang YG, Hass DD, Wadley HNG. Porosity control in zig-zag vapor-deposited films. Thin Solid Films 2005;471:1.

[140] Jang BK, Matsubara H. Influence of rotation speed on microstructure and thermal conductivity of nano-porous zirconia layers fabricated by EB-PVD. Scripta Materialia 2005;52:553.

[141] Hass DD, Marciano Y, Wadley HNG. Physical vapor deposition on cylindrical substrates. Surface and Coatings Technology 2004;185:283.

[142] Furmanski P, Floryan JM. A thermal barrier with adaptive heat transfer characteristics. Trans. ASME, J. Heat Transfer 1994;116:302.

[143] Hasselman DPH. Effect of Cracks on Thermal Conductivity. Journal of Composite Materials 1978;12:403.

[144] Gu S, Lu TJ, Hass DD, Wadley HNG. Thermal conductivity of zirconia coatings with zig-zag pore microstructures. Acta Materialia 2001;49:2539.

[145] Hass DD, Yang Y, Wadley HNG. Pore Evolution During High Pressure Atomic Vapor Deposition. 2008 (submitted).

[146] Mercer C, Hovis D, Heuer AH, Tomimatsu T, Kagawa Y, Evans AG. Influence of thermal cycle on surface evolution and oxide formation in a superalloy system with a NiCoCrAlY bond coat. Surface and Coatings Technology 2008;202:4915.

[147] Yanar NM, Kim G, Hamano S, Pettit FS, Meier GH. Microstructural characterization of the failures of thermal barrier coatings on Ni-base superalloys. Materials at High Temperatures 2003;20:495.

[148] Jiang Y, Smith JR, Evans AG. First principles assessment of metal/oxide interface adhesion. Applied Physics Letters 2008;92:141918.

[149] Smialek JL, Jayne DT, Schaeffer JC, Murphy WH. Effects of hydrogen annealing, sulfur segregation and diffusion on the cyclic oxidation resistance of superalloys: a review. Thin Solid Films 1994;253:285.

[150] Smith JR, Jiang Y, Evans AG. Adhesion of the γ-Ni(Al)/α-Al_2O_3 interface: a first-principles assessment. International Journal of Materials Research 2007;98:1214.

[151] Begley MR, Mumm DR, Evans AG, Hutchinson JW. Analysis of a wedge impression test for measuring the interface toughness between films/coatings and ductile substrates. Acta Materialia 2000;48:3211.

[152] Xu T, He MY, Evans AG. A Numerical Assessment of the Propagation and Coalescence of Delamination Cracks in Thermal Barrier Systems. Interface Science 2003;11:349.

[153] Hasselman DPH, et al. Thermal diffusivity and conductivity of dense polycrystalline ZrO_2 ceramics: a survey. American Ceramic Society Bulletin 1987;66:799.

[154] Schulz U, Oettel H, Bunk W. Texture of EB-PVD Thermal Barrier Coatings Under Variable Deposition Conditions. Z. Metalkd. 1996;87:488.

[155] Saruhan B, Francois P, Fritscher K, Schulz U. EB-PVD processing of pyrochlore-structured $La_2Zr_2O_7$-based TBCs. Surface and Coatings Technology 2004;182:175.

[156] Subramanian MA, Aravamudan G, Subba Rao GV. Oxide pyrochlores -- A review. Progress in Solid State Chemistry 1983;15:55.

[157] Bennett TD, Yu F. A nondestructive technique for determining thermal properties of thermal barrier coatings. Journal of Applied Physics 2005;97:013520.

[158] Jacobson NS. Thermodynamic Propertities of Some Metal Oxide-Zirconia Systems. NASA Technical Memorandum 102351. Cleveland, Ohio: Lewis Research Center, 1989. p.62.

[159] Partridge PG, Ward-Close CM. Processing of advanced continuous fibre composites - Current practice and potential developments. International Materials Reviews 1993;38:1.

[160] Xu Z, Zhong X, Zhang J, Zhang Y, Cao X, He L. Effects of deposition conditions on composition and thermal cycling life of lanthanum zirconate coatings. Surface and Coatings Technology 2008;202:4714.

[161] Vassen R, Traeger F, Stöver D. New Thermal Barrier Coatings Based on Pyrochlore/YSZ Double-Layer Systems. International Journal of Applied Ceramic Technology 2004;1:351.

[162] Shimamura K, Arima T, Idemitsu K, Inagaki Y. Thermophysical Properties of Rare-Earth-Stabilized Zirconia and Zirconate Pyrochlores as Surrogates for Actinide-Doped Zirconia. International Journal of Thermophysics 2007;28:1074.

[163] Oishi Y, Ando K, Sakka Y. Lattice and Grain-Boundary Diffusion Coefficients of Cations in Stabilized Zirconias. Advances in Ceramics: Additives and Interfaces in Electronic Ceramics, vol.7. Columbus (OH): The American Ceramic Society, 1983.